

UNIVERSITY OF STRATHCLYDE

DOCTORAL THESIS

---

**MEMS enabled miniaturisation of  
Photoacoustic Imaging and Sensing  
systems**

---

*Author:*  
Jonas KUSCH

*Supervisor:*  
Prof. Deepak  
UTTAMCHANDANI & Dr.  
Gordon M.H. FLOCKHART

*A thesis submitted in fulfilment of the requirements  
for the degree of Doctor of Philosophy*

*in the*

Centre for Microsystems and Photonics  
Electronic & Electrical Engineering

August 31, 2021

## Declaration of Authorship

I, Jonas KUSCH, declare that this thesis titled, “MEMS enabled miniaturisation of Photoacoustic Imaging and Sensing systems” and the work presented in it are my own. I confirm that:

- This thesis is the result of the author’s original research. It has been composed by the author and has not been previously submitted for examination which has led to the award of a degree.
- Where I have consulted the published work of others, this is always clearly attributed.
- I have acknowledged all main sources of help.
- Where the thesis is based on work done by myself jointly with others, I have made clear exactly what was done by others and what I have contributed myself.

The copyright of this thesis belongs to the author under the terms of the United Kingdom Copyright Acts as qualified by University of Strathclyde Regulation 3.50. Due acknowledgement must always be made of the use of any material contained in, or derived from, this thesis.

Signed:

---

Date:

---



UNIVERSITY OF STRATHCLYDE

## *Abstract*

Faculty Name  
Electronic & Electrical Engineering

Doctor of Philosophy

### **MEMS enabled miniaturisation of Photoacoustic Imaging and Sensing systems**

by Jonas KUSCH

This work presents multiple advances toward miniaturised photoacoustic imaging systems. Miniaturising the system is done in two steps. Firstly, by using novel custom arrays of piezoelectric miniaturised ultrasound transducers. The arrays were fabricated using a cost-efficient multi-user process. The achievable upper frequency limits were restricted by the design limitations of the multi-user process. The designs comprised of a single frequency and two frequency staggered arrays. They were characterised using laser Doppler velocimetry, pitch and catch technique as well as photoacoustic excitation. Additionally, the arrays were compared to commercial bulk ultrasound transducers. The custom-made PMUT arrays perform well compared to commercial transducer, despite their significantly smaller (two orders of magnitude) detection area. Secondly, an optical resolution photoacoustic microscope consisting of MEMS based excitation - using a fast-scanning micro-mirror for Q-switching - and detection schemes is built and used to image synthetic targets and phantoms. Furthermore, a simulation model of the system is developed to evaluate influences of the miniaturised elements on the photoacoustic signal generation and received spectra and signal strength. Finally, a novel photoacoustic excitation scheme based on CW - laser excitation and a MEMS based fast-scanning micro-mirror is presented and its performance relative to pulsed excitation photoacoustic imaging is evaluated. Here, the photoacoustic excitation is not due to fast pulsed laser excitation, but caused by scanning a focused CW - beam over a sample.



## *Acknowledgements*

In the course of this Ph.D. project I received a great deal of support and assistance.

Firstly, I would like to thank my supervisors Prof. Deepak Uttamchandani and Dr. Gordon Flockhart, whose guidance and expertise helped me formulate the underlying research question and further my project. Your ideas and constructive feedback helped me advance and improve my research project.

I would also like to thank Dr. Ralf Bauer. Your reliable and ever available help, ideas and insights helped me choose the right direction and complete my dissertation successfully.

Finally, I would not have been able to complete this Ph.D. without the help and support of my family and Ms. Aisling Egan. Thank you, for putting up with me during these times!





# Contents

<b>Abstract</b>	<b>v</b>
<b>Acknowledgements</b>	<b>vii</b>
<b>1 Introduction</b>	<b>1</b>
1.1 How Light generates Sound . . . . .	2
1.1.1 Pathway of the Light to the absorber . . . . .	3
1.1.2 The photoacoustic Effect . . . . .	3
1.1.3 Propagation of the PA wave . . . . .	5
1.1.4 Light in, Sound Out . . . . .	6
1.2 Devices used in PA systems in the literature . . . . .	7
1.2.1 Laser Sources used in PA Systems . . . . .	7
1.2.2 Photoacoustics in Biomedicine . . . . .	8
1.2.3 Transducers . . . . .	9
1.3 Detection Schemes for PA imaging . . . . .	11
1.3.1 Reconstruction Algorithms . . . . .	13
1.4 Photoacoustic Trace and signal power . . . . .	14
1.4.1 Photoacoustic Wave . . . . .	14
1.4.2 Calculating the PA Signal Power . . . . .	15
1.4.3 Interpolation of the Frequency Content . . . . .	15
1.5 Discussion and Conclusion . . . . .	17
<b>2 Simulations of Photoacoustic Signals</b>	<b>19</b>
2.1 Introduction to k-wave . . . . .	20
2.2 Setting up the simulations . . . . .	21
2.2.1 Influence of Pulse Width . . . . .	22
2.2.2 Influence of the Spot Size of the Laser . . . . .	25
2.3 Near Field Distance for Detection . . . . .	27
2.4 Discussion . . . . .	30
<b>3 Preliminary Photoacoustic Setup</b>	<b>33</b>
3.1 Photoacoustic test setup . . . . .	33
3.2 Laser characteristics . . . . .	35
3.2.1 Maximum laser power and beam spot size . . . . .	35
3.2.2 Pulse width & Pulse to pulse repeatability . . . . .	37
3.3 Phantom preparation . . . . .	38
3.3.1 Estimation of Speed of Sound in Gelatin . . . . .	39

3.3.2	Electromagnetic Interference . . . . .	40
3.4	Commercial Ultrasound Transducers . . . . .	41
3.5	Photoacoustic scans . . . . .	43
3.5.1	Ink Targets . . . . .	44
3.5.2	Scans of polyimide coated Fibre . . . . .	46
3.6	Discussion . . . . .	49
<b>4</b>	<b>Miniaturisation of Piezoelectric Ultrasound Transducers</b>	<b>51</b>
4.1	Design of the PMUT arrays . . . . .	51
4.1.1	Design of single-element membrane transducers . . . . .	52
4.1.2	Design of multi-type transducer array . . . . .	56
4.1.3	Design of bar transducers . . . . .	59
4.1.4	Fabrication of the PMUT arrays . . . . .	62
4.1.5	Fabrication Process . . . . .	63
4.2	Inspection of microfabricated PMUT arrays . . . . .	64
4.2.1	SEM results . . . . .	64
4.2.2	Optical Profiler Examination . . . . .	67
4.2.3	X-Ray Diffraction results . . . . .	69
4.3	Characterisation of the PMUT arrays . . . . .	71
4.3.1	Characterisation using LDV . . . . .	71
4.3.2	Characterisation using PCT . . . . .	74
4.3.3	Characterisation using PE . . . . .	75
4.4	SNR measurements . . . . .	82
4.4.1	Estimation of the SNR of the PMUT arrays . . . . .	82
4.4.2	Comparison of the PMUT arrays and the commercially available single-element transducers . . . . .	84
4.5	Application of PMUT arrays to PA detection . . . . .	86
4.6	Verification of Simulation . . . . .	88
4.7	Discussion . . . . .	90
<b>5</b>	<b>Miniaturisation of the Laser Source using MEMS micromirrors</b>	<b>93</b>
5.1	MEMS Micromirrors . . . . .	94
5.2	Pulse Width and PRF . . . . .	96
5.3	Maximum Pulse Energy and Power . . . . .	99
5.4	Laser Spot size and Focal point size . . . . .	101
5.5	Discussion and Conclusion . . . . .	103
<b>6</b>	<b>All MEMS based PA system</b>	<b>105</b>
6.1	Performance of the PA generation using the MEMS laser . . . . .	105
6.1.1	Single-type Array . . . . .	106
6.1.2	Multi-type Array . . . . .	107
6.1.3	Beam-Type Array . . . . .	107
6.1.4	Commercial Transducers . . . . .	108
6.1.5	Comparison of SNRs . . . . .	110
6.2	Analysis of the PA wave train . . . . .	111

6.3	Target imaging . . . . .	113
6.3.1	Fibre scans . . . . .	113
6.3.2	Ink soaked thread . . . . .	120
6.4	Discussion and Conclusion . . . . .	124
<b>7</b>	<b>Scanning laser beam PA</b>	<b>127</b>
7.1	Basic Principle . . . . .	127
7.2	Simulation . . . . .	129
7.2.1	Pulse Energy and Pulse Width . . . . .	129
7.2.2	Expected PA signal . . . . .	130
7.2.3	Minimum Discernible Target Distance . . . . .	132
7.3	Reconstruction Algorithm . . . . .	133
7.4	Experiments . . . . .	133
7.4.1	Pulse width . . . . .	133
7.4.2	Output Power . . . . .	135
7.4.3	Test setup . . . . .	137
7.4.4	Experimental Verification . . . . .	137
7.5	Discussion . . . . .	139
<b>8</b>	<b>Conclusion and Future Work</b>	<b>141</b>
8.1	Simulations of Photoacoustic Signals . . . . .	141
8.2	Miniaturisation of the photoacoustic scanning system . . . . .	142
8.3	Scanning laser beam photoacoustic . . . . .	145
	<b>Bibliography</b>	<b>147</b>



# List of Figures

1.1	Pathway of Light and generation of an acoustic wave . . . . .	2
1.2	Optical windows in tissue . . . . .	9
1.3	Typical PA trace . . . . .	14
1.4	Frequency content derived by applying FFT . . . . .	16
1.5	Comparison of estimation methods for interpolating FFT results . . . . .	17
2.1	k-Wave simulation running . . . . .	22
2.2	Pulse widths used in k-wave simulation and trend of main frequency . . . . .	23
2.3	Spectral Maps and PSDs from simulations (pulse widths) . . . . .	25
2.4	Beam diameter used in simulations and evolution of main frequencies . . . . .	26
2.5	PSDs at specific distances derived from beam diameter simulations . . . . .	27
2.6	Sepctral Maps derived from beam diameter simulations . . . . .	28
2.7	Visualisation of near field effects on detection . . . . .	29
2.8	NFD: normalised Signal Strength over diameter at fixed distance . . . . .	29
2.9	Evaluated NFDs in attenuating and un-attenuating media . . . . .	30
3.1	PA setup varieties . . . . .	34
3.2	Commercial Nd:YAG : Laser Spot Size . . . . .	37
3.3	Commercial Nd:YAG : Laser pulse shape . . . . .	38
3.4	Results: Speed of sound experiments . . . . .	41
3.5	Electromagnetic Interference . . . . .	42
3.6	Setup: schematic setup for Photoacoustic Excitation . . . . .	43
3.7	Result of PE for 2.25 MHz transducer . . . . .	44
3.8	Result of PE for 10 MHz transducer . . . . .	44
3.9	Graph of Cross scan of ink injection . . . . .	45
3.10	Size of single-mode fibre and PCF compared . . . . .	46
3.11	Cross-section of PCF imaged using the PA setup . . . . .	48
3.12	Traces and PSDs of imaged PCF . . . . .	48
3.13	Topscan of PCF . . . . .	49
4.1	COMSOL: resonance frequency for clamped discs . . . . .	53
4.2	Design of single-type PMUT array . . . . .	53
4.3	Diagram Membrane element . . . . .	55
4.4	Design of multi-type PMUT array . . . . .	58
4.5	Sketch for calculation of area for bar transducer . . . . .	60
4.6	COMSOL: resonance frequency for bar transducers . . . . .	60
4.7	Design of bar-type PMUT array . . . . .	62

4.8	Whole Chip design	63
4.9	MEMS fabrication process	64
4.10	SEM imaging of single-type transducer array	65
4.11	SEM imaging of multi-type transducer array	66
4.12	SEM imaging of bar-type transducer array	66
4.13	SEM close up of undercut	67
4.14	Optical Profiler results	69
4.15	X-Ray Diffraction Results	70
4.16	Laser Doppler Velocimetry Setup	72
4.17	Laser Doppler Velocimetry Results: single-type array	72
4.18	Laser Doppler Velocimetry Results: multi-type array	73
4.19	Pitch-Catch technique setup	75
4.20	Pitch-Catch technique Results: single and multi-type array	76
4.21	Characterisation by photoacoustic Excitation setup	78
4.22	Characterisation by photoacoustic Excitation Results single-type array	78
4.23	Characterisation by photoacoustic Excitation multi-type array	79
4.24	Characterisation by photoacoustic Excitation bar-type array	81
4.25	Commercial Laser: SNR for single-type array	83
4.26	Commercial Laser: SNR for multi-type array	84
4.27	Commercial Laser: SNR for bar-type array	85
4.28	Commercial Laser: comparison of transducers	86
4.29	Phased array application: setup	87
4.30	Phased array application: results	88
4.31	Verification of Simulation results	89
5.1	MEMS Q-switched Laser Cavity	94
5.2	MEMS micromirror	95
5.3	Micromirror deflection angle	97
5.4	Micromirror deflection modes	97
5.5	MEMS Laser pulse shape and frequency content	98
5.6	MEMS Laser pulse train	99
5.7	MEMS Laser start up behaviour	100
5.8	MEMS Laser Beam Profile	101
5.9	MEMS Laser Focal Spot	102
6.1	MEMS Laser: SNR for single-type array	106
6.2	MEMS Laser: SNR for multi-type array	107
6.3	MEMS Laser: SNR for bar-type array	108
6.4	MEMS Laser: SNR for commercial 2.25 MHz	109
6.5	MEMS Laser: SNR for commercial 10 MHz	109
6.6	MEMS Laser: SNR comparison	110
6.7	Comparison MEMS vs commercial laser	111
6.8	MEMS Laser: PA train evaluation	112
6.9	MEMS laser based OR PAM Setup Sketch	113
6.10	PCF cross-section imaged with single-type array	115

6.11	PCF cross-section imaged with multi-type array . . . . .	116
6.12	PCF cross-section imaged at low-energies . . . . .	117
6.13	PCF cross-section imaged with single-type array in scattering medium . . . . .	118
6.14	PCF in scattering medium - traces and PSDs . . . . .	119
6.15	Topscan of PCF imaged with All-MEMS ORPAM system . . . . .	120
6.16	Size of suture threads compared to PCF . . . . .	121
6.17	Imaging PCF and suture threads, coated and uncoated . . . . .	122
6.18	Image cross of suture threads . . . . .	123
6.19	Cross of suture threads - traces and PSDs . . . . .	124
7.1	Principle of scanning beam PA system . . . . .	128
7.2	Schematic: Scanning beam setup principle . . . . .	129
7.3	Scanning speed of laser spot . . . . .	130
7.4	Effect of target width on pulse width for scanning beam PA . . . . .	131
7.5	Expected frequency content for various target sizes for scanning beam PA . . . . .	132
7.6	Consideration concerning the lateral resolution . . . . .	133
7.7	Pulse widths measured at different scanline positions . . . . .	134
7.8	Laser diode bar power output . . . . .	135
7.9	Laser diode bar power output . . . . .	136
7.10	Power output achievable with scanning beam PA . . . . .	137
7.11	Schematic: Scanning beam test setup . . . . .	138
7.12	Laser diode bar power output at a duty cycle of 12.5 % . . . . .	139
7.13	Scanning beam PA recorded traces . . . . .	139
7.14	Scanning beam PA recorded traces . . . . .	140
8.1	New PMUT Design . . . . .	145





# List of Tables

1.1	The weights $W$ , the means $\mu$ and the standard deviations $\sigma$ used to create the PSD. . . . .	16
3.1	The measured dimensions of the marks on the laser alignment paper in x- & y- direction of the beam spots. . . . .	36
4.1	The resonance frequencies are shown for the different modes and their respective shapes. . . . .	54
4.2	The Bessel's functions zero-crossing $j_{m,n}$ and the relative (to the first mode) resonance frequency is shown for the first four modes. . . . .	56
4.3	The resonance frequency, surface area for each element and in total and the number of elements are shown for each transducer sub-array. . . . .	59
4.4	The average and standard deviation of the measured ROCs (in $mm$ ) of the sub-arrays. The sub-arrays exhibit both convex and concave curvatures. . . . .	68
4.5	The table shows the centre frequencies and bandwidths (FWHM), as well as the relative bandwidth for the different transducer groups of the single-type PMUT array as well as the multi-type array. . . . .	74
4.6	The resonance frequencies of the single-type and the multi-type PMUT arrays. . . . .	80
4.7	The designed 1 <sup>st</sup> resonance frequencies of the single-type and the multi-type PMUT arrays are compared with the results from the characterisation. The bracketed number shows the error compared to the designed values. . . . .	81
4.8	The active surface areas of the custom-made PMUT arrays and the commercial transducers are shown. . . . .	85
5.1	The table shows the maximum deflection angle of the micromirror at their first and second resonance frequency. * These values were measured at a separate experiment . . . . .	96
7.1	The pulse widths and the pulse energies increase with target dimensions and with distance from the centre of the scanline. The values shown here result from a simulation using a CW-laser with 1 W power output. . . . .	130



# List of Abbreviations

<b>ARPAM</b>	<b>Acoustic Resolution PhotoAcoustic Microscopy</b>
<b>FFT</b>	<b>Fast Fourier Transform</b>
<b>ORPAM</b>	<b>Optic Resolution PhotoAcoustic Microscopy</b>
<b>PA</b>	<b>PhotoAcoustic</b>
<b>PAT</b>	<b>PhotoAcoustic Tomography</b>
<b>PCF</b>	<b>Polyimide Coated optical Fiber</b>
<b>PRF</b>	<b>Pulse Repetition Frequency</b>
<b>PSD</b>	<b>Power Spectral Density</b>
<b>US</b>	<b>UltraSound</b>
<b>TOF</b>	<b>Time of Flight</b>



# List of Symbols

$a, l, d, h$	distance	m
$r$	radius	m
$m$	mass	g
$E$	energy	J
$P$	power	W ( $\text{J s}^{-1}$ )
$V$	voltage	V
$V_{pp}$	peak-to-peak voltage	V
$f$	frequency	Hz
$PRF$	pulse repetition frequency	Hz
$\omega$	angular frequency	rad
$\tau$	pulse width	s
$t$	time	s
$\lambda$	wavelength	m
$OD$	optical density	1
$R$	reflectivity	1



## Chapter 1

# Introduction

Over the past decade photoacoustic (PA) imaging has received increased interest. Applications of photoacoustic sensing and imaging were demonstrated for non-destructive testing and in clinical settings, where it shows promise as an imaging technique for deep tissue investigations. The main application in a clinical setting so far has been breast cancer imaging as PA imaging can easily map blood oxygenation and image vasculature, key indicator of malignant tissue [1]–[5]. For mammography PA imaging systems showed to have an imaging depth of 4 cm [6] and are also in use for post-biopsy classification [7]. Additionally, PA imaging is used for dermal imaging, e.g. imaging of dermal papilla, and skin layer differentiation [8], [9]. As with breast cancer, it is also used for skin cancer detection, preoperative imaging as well as intra-operative control [10]–[12]. Furthermore, it offers improved detection of metastasising melanomas in the lymph nodes [13]. Apart from identifying malignant tissue it is applied to identifying inflammatory skin diseases such as eczema and psoriasis, due to increased vascularisation and changes in vascular physiology [14], [15]. Additionally, it is also used in vascular imaging of major blood vessels (externally and internally) [16], [17], such as the carotid arteries and micro-vasculature [18], [19]. Furthermore, PA imaging is applied to gastrointestinal imaging and functional measurements of inflammatory diseases such as Crohn's disease [20]. Here, the level of severity of the inflammation can be imaged up to a depth of 35 mm [21].

The available systems still suffer from their bulkiness, which limits their applicability in clinical settings. A reduction of the size and cost of the systems will make photoacoustic system more widely available. The potential of a size and cost reduction by looking at MEMS sensors and actuators in multiple sections of the PA systems will be investigated in this thesis.

The introduction will give an overview of how the photoacoustic (PA) effect works and how it is applied to imaging and sensing applications. Furthermore, different photoacoustic excitation sources (aka lasers) will be discussed as will be ultrasound detection schemes. There are two main types of imaging techniques using the photoacoustic effect; laser ultrasonics and photoacoustic sensing. The former uses the PA effect to create a ultrasonic (US) wave with desired frequency and pulse shape. This shaped acoustic wave then travels through the medium, where it is reflected.

The acoustic wave then propagates to the transducer, where it is detected. The contrast in laser ultrasonics is based on mechanical properties (e.g. elasticity, acoustic impedance) and the acoustic wave propagates through the medium twice. PA imaging utilises the difference in absorbing spectra for sensing / imaging a target. Here, the target is irradiated (usually) by a pulsed laser beam and an acoustic wave is generated at the location of the object due to the photoacoustic effect. Thus, its optical properties are used as contrast. The generated PA wave then propagates to the acoustic transducer, where it is detected. Thus, using PA the acoustic wave propagates through the medium only once. The research described here is about photoacoustics.

## 1.1 How Light generates Sound

The conversion of optical electro-magnetic energy into acoustic energy via the photoacoustic effect is described in this section. For this purpose, the propagation of the optical wave (light) to the absorber over a pathlength  $l$  (see Fig. 1.1), the photoacoustic effect and the propagation of the generated acoustic wave along the spatial dimensions  $x$  (comprising of the  $x$ ,  $y$  and  $z$  direction) are described using the example of a short-pulsed laser focused onto a target embedded in an optical attenuating medium. Other PA detection schemes will be described in section 1.3.1.

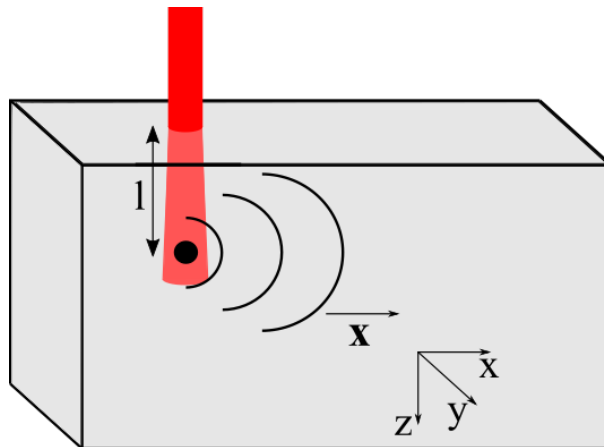


FIGURE 1.1: The laser (red) is emitted into the scattering medium (grey). This causes broadening of the beam over the pathlength  $l$  to the absorber (black). Here, the light is absorbed and an acoustic wave is generated. This photoacoustic wave propagates along the spatial dimensions  $x$  (comprising of the  $x$ ,  $y$  and  $z$  direction).



### 1.1.1 Pathway of the Light to the absorber

Light travelling through a non-transparent medium is subject to scattering and absorption. In both cases particles of the medium absorb a photon, but while in the latter the energy of the photon is absorbed, in a scattering process a photon of equal (elastic scattering) or lower (inelastic scattering) energy is re-emitted. Only elastic scattering is considered here, as inelastic scattering, such as spontaneous Raman scattering, shows very low incidence rates (1 in  $10^8$  photons [22]). The absorptivity of a medium is described as a spatial frequency ( $1/cm$ ) using the absorption coefficient  $\mu_A$ . The ratio of non-absorbed photons  $T_A$  over a pathlength  $l$  can be calculated as:

$$T_A = e^{-\mu_A l} \quad (1.1)$$

Scattering is denoted similarly as  $\mu_S$ . In scattering the re-emission of the photon happens at a random deflection angle  $\gamma$  from the initial pathway of the photon. The distribution of the deflection angle depends on the medium's anisotropy, denoted as the mean of the cosine of the deflection angle  $g = \langle \cos(\gamma) \rangle$  [23]. A photon scattered in a medium with  $g = 0$  is equally likely to be re-emitted into any direction, where as in a medium with  $g = 1$  the photon is re-emitted along its initial pathway. Thus, the anisotropy is compensated for in the scattering factor using:

$$\mu'_S = (1 - g) \cdot \mu_S \quad (1.2)$$

Similarly to eq. 1.1, the ratio of non-scattered photons  $T_S$  over a pathlength  $l$  while compensating for the anisotropy can be calculated as:

$$T_S = e^{-\mu'_S l} \quad (1.3)$$

A unidirectional beam of light with an initial optical energy per unit area, i.e. the fluence rate,  $F_0$  travelling over a pathlength  $l$  in an absorbing and scattering medium is thus reduced according to the Beer-Lambert law as:

$$F = F_0 e^{-(\mu'_S + \mu_A) l} \quad (1.4)$$

To characterise the penetration depth of light in tissue, the effective attenuation is used. It is derived from diffusion theory as  $\mu_{eff} = \sqrt{3\mu_A(\mu'_S + \mu_A)}$  [24], [25]. While a scattered photon will still travel through the medium and might be scattered back towards the mean path of the light, an absorbed photon will not. Thus, the effective attenuation coefficient is not calculated as a linear summation of the scattering coefficient and the absorption coefficient. The resulting mean free pathlength in soft tissue is approximately 1 mm [26].

### 1.1.2 The photoacoustic Effect

Consider that the beam with fluence rate  $F(\mathbf{x}, t)$  reaches an absorber, which absorbs energy in accordance with its local absorptivity. This absorbed energy causes a rise in the local temperature, which in turn increases the local pressure. This initial pressure

$p_0$  can be described in terms of the (constant) Grüneisen parameter  $\Gamma$  and the heating function  $H(x)$  under the assumption of a delta function like laser pulse [26]. The Grüneisen parameter  $\Gamma$  is dimensionless and describes the energy-specific pressure changes [27]. It can be described using the thermal coefficient of volume expansion  $\beta$ , the specific heat capacity at constant volume  $C_V$ , the heat isothermal compressibility  $\kappa$  and the density  $\rho$  as [28]:

$$\Gamma = \frac{\beta}{\kappa \rho C_V} \quad (1.5)$$

If a more realistic non-delta function laser pulse is assumed the heating function is not only dependent on spatial parameters ( $\mathbf{x} = (x, y, z)$ ) but also on temporal parameters. The initial pressure can thus be calculated as:

$$p_0(\mathbf{x}, t) = \Gamma \cdot H(\mathbf{x}, t) \quad (1.6)$$

The heating function is calculated from the fluence rate and the absorption coefficient  $\mu_A(\mathbf{x})$ , the latter is assumed as constant in the area of the focal point, thus  $H(\mathbf{x}, t) = F(\mathbf{x}, t) \cdot \mu_A$ . The fluence rate can be subdivided into a scaling maximum value  $F_{max}$ , a normalised temporal intensity fluctuation  $I(t)$  (i.e. the laser pulse shape, constant over  $\mathbf{x}$  and a spatial intensity fluctuation  $S(\mathbf{x})$  (i.e. the laser beam profile, constant over  $t$ ):

$$H(\mathbf{x}, t) = F_{max} S(\mathbf{x}) I(t) \cdot \mu_A(\mathbf{x}) \quad (1.7)$$

Combining equations 1.6 and 1.7, and with  $H_{max} = F_{max} \cdot \mu_A$ , the laser induced pressure can be calculated as:

$$p_0(\mathbf{x}, t) = \Gamma F_{max} \mu_A S(\mathbf{x}) I(t) \quad (1.8)$$

If a volume is continually exposed to a constant laser beam, it will only heat up and the energy will dissipate via radiative processes. To create the necessary expansion and relaxation, which generates the desired pressure wave, a change in the temporal profile  $I(t)$  is required. Thus, for effective PA generation using short-pulsed lasers, the temporal profile of the laser must adhere to the thermal and stress confinements [29]. The latter states, that the pulse width  $\tau$ , the width of the temporal profile  $I(t)$  (FWHM), is small compared to the volume expansion. This can be described as:

$$\tau < \frac{d_{res}}{v_S} \quad (1.9)$$

with the speed of sound  $v_S$  and the desired resolution  $d_{res}$ . The desired resolution describes the maximum achievable resolution of the system. To achieve this resolution the requirements described in equations 1.9 and 1.10 need to be fulfilled. The thermal confinement compares the thermal diffusion to the pulse width and can be described as [28]:

$$\tau < \frac{d_{res}^2}{4\alpha_t} \quad (1.10)$$

with  $\alpha_t$  as the thermal diffusivity.

### 1.1.3 Propagation of the PA wave

The ultrasonic (US) wave generated at the absorber propagates as a spherical wavefront at the speed of sound of the medium from its point of origin. Thus, for a given receiver area  $A$  the initial amplitude  $p_0$  reduces according to inverse square law with increasing distance. Additionally, in attenuating media, the US wave is subject to complex lossy processes such as structural and vibrational relaxation and the effects of the viscosity of the medium [30]. These processes are highly frequency dependent and lead to experimentally verified description of the attenuation  $\alpha$  as:

$$\alpha = \alpha_0 \omega^y \quad (1.11)$$

with  $\alpha_0$  as the attenuation coefficient,  $\omega$  as the angular frequency and  $y$  as the power law exponent, which is typically in the region of  $1 < y < 1.5$  for soft-tissue [30]. This frequency dependency causes the high frequency content to be attenuated at a greater rate. Thus, an attenuating medium acts as a low-pass filter on the US wavefront. Another property of the medium affecting the propagation of US is the ratio of speed of the pressure wave and the particle speed of the fluid. This is called the acoustic impedance  $Z$  and can be rewritten using the density  $\rho$  of the medium and its speed of sound  $v_s$  [31]:

$$Z = \frac{\rho}{v_s} \quad (1.12)$$

The acoustic impedance can be used to calculate the ratio of the transmitted and the reflected part of the US wave at an interface of media. The reflected part  $R$  of a US wave can be calculated from the acoustic impedance of the originating medium  $Z_1$  and the medium it is moving into  $Z_2$  as [32]:

$$R_{aco} = \left( \frac{Z_2 - Z_1}{Z_2 + Z_1} \right)^2 \quad (1.13)$$

The transmitted part  $T$  can be calculated similarly to eq. 1.13 as:

$$T_{aco} = 1 - \left( \frac{Z_2 - Z_1}{Z_2 + Z_1} \right)^2 \quad (1.14)$$

Values for the acoustic impedance range from 1.34 *MRayl* to 1.71 *MRayl* for soft-tissue, 0.18 *MRayl* for lung tissue and 7.8 *MRayl* for bone [32].

### 1.1.4 Light in, Sound Out

Combining the aforementioned effects results in the initial fluence rate  $F_0$  of the laser used to create the PA response being reduced to  $F$  by scattering and absorption as shown in eq. 1.4. Additionally, the free space focal point of a focused laser is widened due to scattering effects. Thus eq. 1.8 can be rewritten as:

$$p_0(x, t) = \Gamma F_0 e^{-(\mu'_{S,med} + \mu_{A,med})l} \mu_{A,abs} S(x) I(t) \quad (1.15)$$

with the penetration depth of the light  $l$ ,  $\mu_{A,abs}$  as the absorption coefficient of the absorber and  $\mu'_{S,med}$  and  $\mu_{A,med}$  as the reduced scattering and the absorption coefficient of the medium, respectively. The generated pressure wave with its initial pressure is then reduced by attenuation and transmission losses for the  $m$  media it is travelling through:

$$p_{end} = p_0 \prod_{n=1}^m \left(1 - \left(\frac{Z_n - Z_{n-1}}{Z_n + Z_{n-1}}\right)^2\right) \cdot \alpha_{0,n} \omega^y l_n \quad (1.16)$$

with  $Z_0$  as the impedance of the medium in which the PA response is generated and  $l_n$  the length of the pathway through the respective medium. The acoustic impedance  $Z$  is measure of the flexibility and stiffness of a medium [32]. It is given in Rayl, which has SI units of  $\frac{kg}{m^2 s}$ , and ranges for tissue 1.34 *MRayl* for fatty tissue to 1.71 *MRayl* for muscular tissue [32]. The acoustic impedance is calculated from the density  $\rho$  and the speed of sound  $v_S$  as:

$$Z = \rho v_S \quad (1.17)$$

On an interface of two media with different acoustic impedances  $Z_1$  and  $Z_2$  part of the acoustic wave is reflected. The transmission  $T$ , which is the complement of the reflection loss  $R$ , i.e.  $T = 1 - R$ . It can be calculated as:

$$T = 1 - \frac{(Z_1 - Z_2)^2}{(Z_1 + Z_2)^2} \quad (1.18)$$

The process in eq. 1.15 occur instantaneously compared to the process described in eq. 1.16, since  $c \gg v_S$ . For a maximum fluence rate-specific PA signal strength the term  $\mu'_{S,med} + \mu_{A,med}$  should be minimal, while  $\mu_{A,abs}$  should be maximal. The generated PA wave should travel through as few as possible layers with closely matching acoustic impedances. Additionally, these layers should be narrow. Thus, with the attenuation of both light (in the optical window, see 1.2.2) and US in biological tissue a 10 MHz PA signal is attenuated by approximately one order of magnitude per centimetre [26].

As the axial resolution of an acoustic wave is dependent on its frequency, the low-pass filtering qualities of an attenuating medium on an acoustic wave, as described in eq. 1.11, it is dependent on the length of the pathway through the medium [31]. The lateral resolution depends on the diameter of the excitation beam at the absorber.

Thus, the lateral resolution is affected by the initial beam width, the beam shaping optics and the scattering of the probed medium.

## 1.2 Devices used in PA systems in the literature

In general, PA systems consists of a light source, typically a short-pulsed laser, to create a PA response in a target absorber as described above, as well as a transducer to detect the generated acoustic wave. Here, a general overview over available systems in each category is given.

### 1.2.1 Laser Sources used in PA Systems

Solid state Q-switched lasers, such as Nd:YAG lasers, have been widely used in photoacoustic imaging, both for soft-tissue and dental imaging [33]–[35]. Their wide usage is due to their typical high pulse energies of  $E > 800 \text{ mJ}$  and short pulse widths with  $\tau < 10 \text{ ns}$  [33], [34], [36], [37]. Their drawback is their low pulse repetition frequency (PRF), which usually is in the tens of Hz range, as well as their spatial and energy requirements. The last point can be overcome by using diode-pumped lasers with  $PRF < 50 \text{ Hz}$ ,  $E > 80 \text{ mJ}$  with a footprint and weight at around 5% of a flash-lamp-pumped Nd:YAG laser [37]. The bulkiness and the low PRF limit their usage in clinical setups. A way to compensate for the low PRF of traditional Q-switched solid state lasers is to use Au - coated fast resonant MEMS scanning mirrors to open and close a laser cavity around a side-pumped gain medium [38]. These MEMS Q-switched lasers offer short pulse lengths ( $\tau \geq 28 \text{ ns}$ ), high PRFs ( $PRF \leq 8 \text{ kHz}$ ) and pulse energies of  $E \leq 7.9 \mu\text{J}$ . The pulse energy can be increased by 550 % using a dielectric coating instead of a Au-coating on the micro-mirrors [39].

A widely used laser source, especially in handheld PA imaging devices, are pulse laser diodes (PLDs) [40], [41]. PLDs usually offer pulse lengths in the range of tens of ns to 200 ns with pulse energies ranging up to several mJ [40]–[45]. They are also commercially available (e.g. Lumibird - Quantel Lasers, France) with pulse widths of  $\tau = 30 \text{ ns}$  with a pulse energy  $E = 4 \text{ mJ}$  and  $PRF = 6 \text{ kHz}$  available at wavelengths of 808 nm, 915 nm, 940 nm or 980 nm. The pulse width can even be reduced to 3 ns at  $PRF < 500 \text{ kHz}$  at reduced energies ( $E > 1 \mu\text{J}$ ) (Illuminator, Lumibird - Quantel Lasers, France). The wavelengths of the PLDs applied for PA imaging are usually in the range of 785 nm to 950 nm, since these are the wavelengths that high pulse power PLDs are easily commercially available. CW - laser diodes offer a wider range of available wavelengths, but need special driving circuits. These are often developed for LIDAR applications [46]. When using these driving circuits and thus exceeding the current maxima for CW - operation short pulse widths ( $\tau \approx 10 \text{ ns}$ ) and very high PRF ( $\leq 600 \text{ kHz}$ ) can be achieved for low pulse energies ( $E \leq 200 \text{ nJ}$ ) [47]. As a laser beam entering a strongly attenuating medium such as soft tissue is scattered and the beam defocused, another light source currently investigated for PA imaging is LEDs [48], [49]. These offer pulse energies of  $E \leq 200 \mu\text{J}$ ,  $PRF \leq 4 \text{ kHz}$  and pulse widths

$\tau > 50 \text{ ns}$ . As they are not as tightly focused as laser beams, they are used for volume excitation.

The combined use of several wavelengths (multi-spectral optoacoustics) offers a higher specificity for biomedical applications, as the absorption spectra differ between tissue types. This can be used for differentiating melanomas [50]. Here, the PA response generated at  $\lambda_1 = 584 \text{ nm}$  is used to image the surrounding blood vessels and  $\lambda_2 = 764 \text{ nm}$  is used to image the depth of the melanoma, where  $\lambda_1$  is already too heavily attenuated. Other systems based on PLDs and tuneable solid state lasers have been developed for clinical applications [41], [51].

Additionally, Mid IR lasers are used in PA imaging setups [52], [53]. Here, the wavelengths coincide with the overtones of the  $\text{CH}_2$  groups found in lipids. They are therefore often used for imaging of lipid layers, e.g. atherosclerotic plaque [52]. UV laser sources are used for PA microscopy, as the beam can be focused more tightly due to the lower wavelength [54], [55]. The PA signal strength can be increased by applying a heating pulse with pulse lengths of up to 1 ms before the probe pulse. This rise in temperature increases the Grüneisen factor  $\Gamma$ , and thus the generated PA response [56], [57].

Femtosecond lasers offer very short pulse widths - as the name suggests - in the femtosecond range (30 fs to 235 fs) [58]–[61]. They usually generate pulses with energies ranging from 15 nJ to 2  $\mu\text{J}$  at PRFs ranging from 5 MHz to 1 kHz. Recent development has yielded increased pulse energies of 100  $\mu\text{J}$  to 23 mJ at PRFs of 100 kHz to 25 kHz [60], [61]. The drawback of these short pulsed lasers is their broadband output of  $\approx 20 \text{ nm}$  [60]. Due to their small pulse widths these laser generate high frequency US waves. Thus, they are mainly used in non-attenuating media or for very short pathlengths, as the low-pass filtering property of attenuating media quickly decreases the signal beyond the noise threshold.

### 1.2.2 Photoacoustics in Biomedicine

There is a wide variety of lasers available with wavelengths ranging from 157 nm ( $\text{F}_2$  excimer laser [62]) to 699.5  $\mu\text{m}$  (for methyl alcohol lasers [63]). Although such a large bandwidth of laser wavelength is available, not all are feasible for application in PA imaging, as the tissue is strongly absorbent. The main attenuators of light in a biomedical context, i.e. human tissue, are water and haemoglobin (oxygenated and deoxygenated) [64]. For wavelengths  $< 850 \text{ nm}$  haemoglobin is the most prominent absorber. It decreases from a local maximum at 400 nm with  $\mu_{A,400} = 3000 \frac{1}{\text{cm}}$  to  $\mu_{A,650} = 5 \frac{1}{\text{cm}}$  at 650 nm [64]. Thus, wavelengths with  $\lambda < 650 \text{ nm}$  are not feasible for PA imaging due to absorption by haemoglobin. For wavelengths with  $\lambda > 900 \text{ nm}$  water is the dominant absorber. In general, the absorption of light in water increases in the range of 650 nm to 950 nm to local maximum, followed by a decrease in absorption. The absorption steadily increases to maximum  $\mu_{A,3000} = 10000 \frac{1}{\text{cm}}$  at

$\lambda = 3\mu\text{m}$  [65]. Thus, laser with wavelengths  $\lambda < 650\text{ nm}$  and  $\lambda > 950\text{ nm}$  are not feasible for PA imaging. This range is called the first optical window [52], [66]. Due to local minima in the absorption of water the second ( $1100\text{ nm} < \lambda_2 < 1350\text{ nm}$ ) and third ( $1600\text{ nm} < \lambda_3 < 1850\text{ nm}$ ) NIR window are located between local spikes of absorption by water [52], [66]. The optical windows are shown in Fig. 1.2 (reproduction from [52]), with the first and second NIR windows combined. The inherent low absorption rate of biological tissue in these windows facilitates deep imaging, especially for the second NIR window. Here, the lower absorption rate of haemoglobin and a reduced scattering coefficient allow for deeper imaging [67]. While the inherent contrast will be low, this can be improved by using contrast agents such as nano-particles tuned to the desired wavelengths [68].

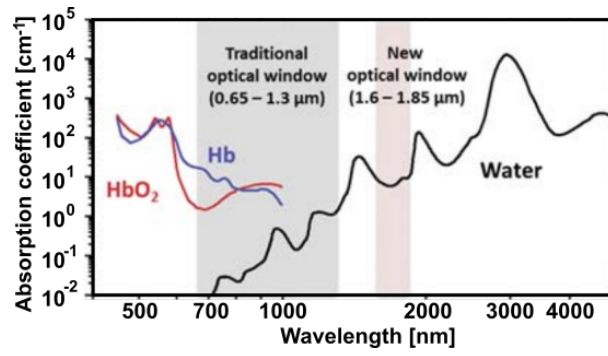


FIGURE 1.2: The main absorbers in biological tissue, oxygenated and deoxygenated haemoglobin, as well as water, show regions with lower absorption rates. These regions form the optical windows at  $650\text{ nm}$  to  $900\text{ nm}$  and  $1100\text{ nm}$  to  $1350\text{ nm}$  (combined, grey) and  $1600\text{ nm}$  to  $1850\text{ nm}$  (red). This graph is a reproduction from [52].

### 1.2.3 Transducers

Conventional ultrasound transducers are fabricated from crystalline piezoelectric materials and consist of either a single element or an array of elements. Single element transducer are commercially available with a planar surface or with a curved surface. This curvature of a radius  $R$  causes the received beams to be collected around the focal point. This focal point is situated at a focal length  $F = R$  [31]. Acoustic waves originating from the focal Fraunhofer zone are detected at a focal gain  $G_f$ , calculated for a circular symmetric transducer as:

$$G_f = \frac{\pi r^2}{\lambda F} \quad (1.19)$$

with the radius  $r$  and the wavelength  $\lambda$  [31]. Whereas acoustic waves originating in the near and far Fresnel zones reduce the detected signal in a similar fashion as described for planar transducers in section 2.3. Transducer arrays are manufactured

using the dice and fill method. Here, a plate of piezoelectric ceramic – such as lead zirconate titanate (PZT) – is diced into an array and the created trenches are filled with a polymer or an epoxy. This limits the shape of the array's elements. Miniaturisation of ultrasound detector arrays involving microfabrication techniques similar to those used in manufacturing integrated circuits (ICs) offers the possibility of a higher degree of control over the shape of the individual elements. In the move towards miniaturisation of photoacoustic systems a variety of ultrasound transducers have become available. Those consist of capacitive micro-machined ultrasound transducers (CMUT), piezoelectric micro-machined ultrasound transducers (PMUT) and optical ultrasound transducers, e.g. micro ring resonators. The application of miniaturised MEMS based sensors has the potential to result in smaller and better sensor systems at reduced unit-costs [69].

CMUTs detect ultrasound by measuring changes in capacitance. These MEMS capacitors are created by etching a cavity in a silicon substrate [70]. Thus, a thin film is created on the top side of the cavity onto which a metal layer is deposited; creating the top electrode. The bottom electrode of the capacitor is a doped silicon layer underneath the cavity. The cavity height varies from 50 nm to 650 nm, but is typically  $\approx 600$  nm [70]–[73]. A bias voltage is applied between the electrodes in order to generate a capacitance dependent current signal [71]. The capacitance is changed by incoming acoustic waves displacing the thin film acting as top electrode of the capacitor. CMUTs have been reported with centre frequencies of up to 29 MHz at 100 % relative bandwidth [73], [74] and offer high sensitivity [72], [75]. This is achieved by decreasing both the element size and the distance of the capacitor plates to as low as 20  $\mu\text{m}$  and 55 nm [71]. In addition to the small element size, the CMUT's parameters are achieved by operation at high bias voltages (of up to 100 V [75]) near or in collapsed mode. Here, the bias voltage is large enough to pull the top electrode partially into contact with the bottom electrode [76]. This operation puts the transducer at risk of failure and is, due to the high voltages, potentially problematic in biomedical applications.

PMUTs detect acoustic waves due to pressure induced deflection and deformation of a piezoelectric membrane. This membrane is sandwiched between a top electrode, usually made from aluminium or gold, and the device layer as bottom electrode, made from doped silicon. The device layer is set upon the handle wafer, with an electrically isolating oxide layer in between. The piezo-electric thin film materials used in PMUTs are inorganic, such as ZnO, AlN and PZT, or organic, such as silk fibroin [77], [78]. The use of thin film materials and comparably simple manufacturing process allows for higher degrees of flexibility with regards to transducer shapes. Arrays of dome transducers of different ellipticity have been fabricated, the difference in dome dimensions allows for higher overall bandwidths while the dome shape gives the array mechanical stability [79]. Furthermore, it allows the transducer membrane to be produced without a Si-layer, thus increasing electro-mechanical coupling. Beam-shaped transducers have been fabricated which



utilise higher order resonance modes to increase the overall bandwidths of the transducer [80]. PMUTs are passive (i.e. no electrical supply or bias voltage is required) miniaturised acoustic sensors which can outperform CMUTs with relative bandwidths of  $\leq 165\%$  [79].

Micro ring resonators (MRR) consist of a ring waveguide close ( $< 1 \mu m$ ) to a bus waveguide. The light from the bus waveguide evanescently couples into the ring waveguide and vice versa. The output amplitude is dependent on the effective refractive index of the MRR. A change in pressure changes the effective refractive index by deforming the ring's shape and altering the material's refractive index due to localised stress. This allows MRRs to have wide bandwidths ( $BW \leq 350$  MHz), low noise equivalent pressures ( $NEP \geq 21.4$  Pa) and higher saturation thresholds compared to conventional piezoelectric ultrasound transducers [81]–[83]. The drawbacks of MRR systems are that they have to be fibre coupled to a narrow band laser source and actively interrogated, and function purely as detector, i.e. they cannot be used as a source for acoustic waves. A Fabry-Perot etalon is another example of optical US transducers. Here, a Fabry-Perot cavity is formed by two mirrors spaced using a transparent material [84], [85]. A free-space optics approach to interrogating the Fabry-Perot cavity is required. This allows for scanning the interrogation beam over the etalon, rather than using an x-y-stage, facilitating scan speed. Compared to MRRs they offer worse noise equivalent pressures ( $210$  Pa to  $2.1$  kPa) and bandwidths ( $20$  MHz to  $100$  MHz) [84], [85].

When using transducer schemes that require the transducer to be in contact with the interrogated medium, the acoustic impedance of both needs to be carefully matched, to minimise acoustic reflection losses. Non-contact optical US transducers are not affected by this. Using for example two-wave mixing interferometry (TWMI), the signal weakening effects of scattering on rough surfaces and low reflectivity can be overcome. In TWMI a probe beam is reflected off of a specimen and guided back to a photorefractive crystal, to which a strong DC voltage is applied (several kV) [86], [87]. A reference beam from the probe laser interferes with the probe beam in the photorefractive crystal, low-pass filtering and amplifying the signal. These systems are reported with bandwidths of  $> 100$  MHz [86], [87].

### 1.3 Detection Schemes for PA imaging

Due to their large bandwidths optical transducers - both contact and contactless - are appropriate for photoacoustic microscopy (PAM). PAM is one of two main test setups for PA imaging, the other being photoacoustic tomography (PAT). In PAM the resolution depends on the focus of the laser, this sub-class is called optical resolution PAM (OR PAM), or the resolution of the transducer, aptly called acoustic resolution PAM (AR PAM).

The simplest OR PAM test consists of a US transducer detecting the PA signals generated by a tightly focused laser beam [88], [89]. Here, the optical axis is orthogonal to the acoustic axis. The specimen is then scanned by either moving the specimen using a motion stage or by scanning the laser beam using galvo-mirrors [89], [90]. Using OR PAM the minimum achievable lateral resolution  $R_L$  depends on the wavelength  $\lambda$  and the numerical aperture of the focusing optics  $NA$  with  $R_L = 0.51 \frac{\lambda}{NA}$  [91]. In this setup the focal region of the laser and the acoustic sensor do not match very well, reducing the field of view and its depth. Thus, other setups overlap the laser and transducer focal region by using a coaxial arrangement [89], [92], [93]. These setups can be used for both OR and AR PAM. For AR PAM the lateral resolution  $R_L$  depends on the frequency  $f$ , the speed of sound  $v_s$  and the numerical aperture of the transducer  $NA$  with  $R_L = 0.71 \frac{c}{NAf}$  [90]. The axial resolution  $R_A$  depends for both systems on the bandwidth of the acoustic transducer  $BW$  with  $R_A = 0.88 \frac{v_s}{BW}$  [90]. OR PAM imaging systems rely on a tightly focused beam to image targets with a high resolution. They can be only used for an imaging depth of up to a few mean free path lengths, as the beam becomes weaker and more diffuse, and thus the focal spot gets bigger. While the signal gets weaker with depth for AR PAM systems too (especially at higher frequencies), the focal spot size is not strongly affected as it is determined by the acoustic properties.

The physical limitations of the focal spot size result in different applications. OR PAM is mainly used for imaging of fixed cells, such as haemoglobin [94], [95], or superficial microvasculature [92]. It achieves lateral resolutions of down to 120 nm - 270 nm [94], [95]. While AR PAM only achieves lateral resolutions of  $> 20 \mu m$  it does so at larger depth of focus of up to 2 mm [89], [93], [96]. Furthermore, by changing the transducer the imaging depth can be adjusted at the cost of lateral resolution, e.g. 85  $\mu m$  resolution at a depth of up to 3.5 mm to 590  $\mu m$  for  $> 10 mm$  [93]. Thus, AR PAM is used to image small animal, both in part (vasculature) and whole body [89], [93], [97].

While both AR and OR PAM achieve good resolutions, they lack the imaging depths and the imaging speed required for use in many biomedical applications. Here, PAT is most widely used. In PAT short pulses from a defocused laser irradiate a target volume and generated a PA response on the absorbers within. Here, a variety of light sources are used, e.g. solid state lasers, PLDs and LEDs [42], [98], [99]. One or several US transducers are moved around the target volume to detect the generated PA response. The transducer axis is either in excitation mode, i.e. perpendicular to the optical axis [42], [98], or in transmission mode, i.e. co-axial with the laser [99]. Instead of rotating a transducer around the volume, the image acquisition speed can be vastly improved by using transducer arrays in the shape of half-ring [100], rings [6] or hemispheres [101], [102]. These systems offer resolutions ranging from 0.2 mm to 1 mm for imaging depths of 15 mm and  $> 22 mm$ , respectively [101], [102]. Furthermore, the PAT approach allows for real-time imaging of up to 10 volumetric frames per second [102] and is used clinically in applications such as breast imaging

and arthritis examinations [6], [100], [101], [103].

In the recent years super-resolution PA imaging has been developed to increase the resolution past the acoustic and the optical diffusion limits, for the diffusive region ( $> 1\text{mm}$  penetration depth) and the ballistic region ( $< 1\text{mm}$  penetration depth), respectively. In PA imaging the acoustic diffusion limit can be surpassed by illuminating the region of interest (ROI) with a sequence of random speckle patterns [104]. For this, a diffusor is placed in the optical path. The resolution can be enhanced by a factor of 1.4 by analysing the variance of the detected PA signals [104]. This can be further increased to a factor of 2.4 by also applying the acoustic transducer inherent point-spread function for the deconvolution of the signal [105]. To surpass the optical diffusion limit, two consecutive Gaussian laser pulses are used to illuminate the ROI [94]. As the first pulse photobleaches it, the signal generated in the centre of the focal spot is greatly reduced. Taking the differential of these two signals results in the PA signal generated in the centre of the focal spot. Using this method the lateral resolution can be decreased to  $80\text{ nm}$  [94].

### 1.3.1 Reconstruction Algorithms

AR and OR PAM operate similarly by point-wise scanning of a target using an interrogation beam. Here, either the target is moved or the beam scanned using beam steering elements such as mirrors. Thus, the individual positions are always known and a PA response value is calculated. The simplest reconstruction per pixel is using time-of-flight method (TOF), by calculating the distance from the detector  $d_{SD}$  using the arrival time  $t$  as  $d_{SD} = v_s t$ . Thus, the signal strength can be evaluated for each distance. This causes different absorbers at the same distance to be not distinguishable.

By scanning the target and using a delay-and-sum algorithm on adjacent pixels a large synthetic aperture can be created [106]. This technique is called synthetic aperture focusing technique (SAFT) and can distinguish targets that were previously (using TOF) indistinguishable due to being at the same distance. The algorithm can be further improved by utilising the signal coherence [106]. Furthermore, by extending the delay-and-sum algorithm to a delay-multiply-and-sum algorithm the focal depth can be increased. increasing the overall imaging depths per pixel [89].

Data acquired using a PAT system with transducer positions in a (semi-) circle or semi-sphere around the target can be reconstructed using filtered back-projection, by applying an inverse Radon-transform to the acquired sinograms [107], [108]. This process can be improved by using a delay-and-sum algorithm [109]. In a second step the calculated signals are deconvoluted to rebuild the pressure waves before reconstructing the volumetric image [101]. While the data acquisition is reasonably fast using PAT, the image reconstruction is computationally intense.

## 1.4 Photoacoustic Trace and signal power

This section will discuss the considerations taken to analyse the recorded acoustic signal, reconstruct the power spectral density (PSD) and calculate the signal power.

### 1.4.1 Photoacoustic Wave

A typical trace of a photoacoustic wave detected in experiments as described in the following chapters in this thesis is shown in Fig. 1.3. This trace has two features; the detected PA signal (green box) and an initial response (red box) which is caused by electro-magnetic interference. The electromagnetic interference is caused by photoacoustic or photoelectric effects generated by the scattered laser light impinging on the transducers; it is shown experimentally in subsection 3.3.2. The time delay  $T$  between these two features is the time the generated PA wave propagates through the medium. Thus, the distance between the source and the detector  $d_{SD}$  can be calculated from the delay  $T$  and the speed of sound in the medium  $v_s$  as:

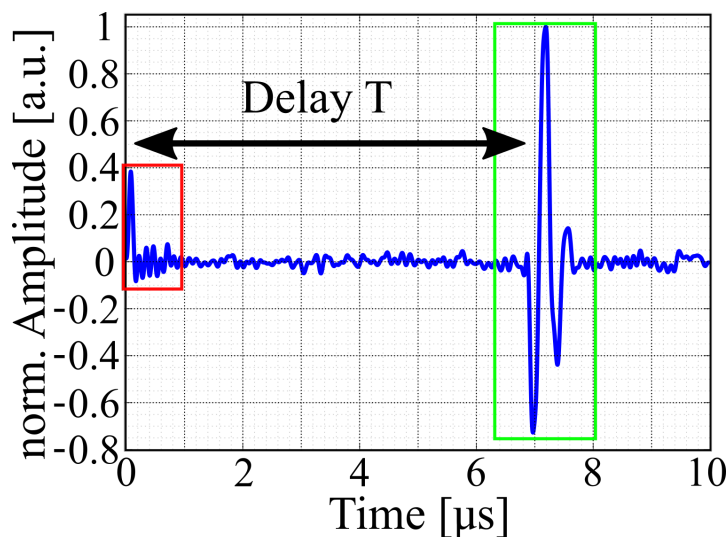


FIGURE 1.3: The generated photoacoustic wave was detected using an Olympus 2.25 MHz transducer and averaged over 256 samples. The PA signal is shown in the green box, whereas the red box shows an initial response coinciding with the laser trigger.

$$d_{SD} = v_s T \quad (1.20)$$

For example with a speed of sound in tissue of  $v_s = 1540 \text{ m/s}$  and a delay of  $T = 7 \mu\text{s}$  the distance of the transducer to the source can be calculated using the TOF approach as:

$$d_{SD} = 1540 \text{ m/s} \cdot 7 \mu\text{s}$$

$$d_{SD} = 10.78 \text{ mm}$$

### 1.4.2 Calculating the PA Signal Power

The power  $P_S$  of a time-domain signal  $S(t)$  is calculated as the integral over the signal's power spectral density (PSD), which is calculated by applying the Fourier transform to the signal [110]:

$$P_S = \int \mathfrak{F}(S(t)) df \quad (1.21)$$

Equation 1.21 is adjusted according to the requirements for analysing the recorded data. Firstly, since the transducer only has a finite bandwidth from  $f_{low}$  to  $f_{high}$  the integral is limited as well. Secondly, as the time-domain signal  $S(t)$  is digitised at a sampling frequency  $f_s$  by recording the data, it is turned into a discrete signal  $S[n]$ . The discrete signal is filtered using a high-pass filter with a cut-off frequency of  $f_{cut} = 50 \text{ kHz}$  to reduce noise. It is then windowed over the PA response (see Fig. 1.3, green box) using a Hamming window. This was done to reduce the noise power as only the windowed part contains the relevant information of the PA wave. The PSD is calculated by applying the Fast-Fourier-transform (FFT) to the windowed signal (see Fig. 1.4, red crosses). Since this results in a set of discrete values, cubic spline interpolation (see Fig. 1.4, blue dotted line) was used to reduce estimation errors of the interpolated signal (see chapter 1.4.3) and thus the calculated integral. The integral for a continuous signal is calculated as the sum of the discrete interpolated values over the frequency range dictated by the transducer's bandwidth (FWHM, see Fig. 1.4, green solid lines). Thus equation 1.21 changes to:

$$P_S = \sum_{f_{low}}^{f_{high}} \mathfrak{F}(S[n]) \quad (1.22)$$

### 1.4.3 Interpolation of the Frequency Content

Using the FFT the frequency content is calculated for a set of discrete frequencies  $F[n]$ . The spacing of these values depends on the sampling frequency, with higher sampling frequencies resulting in smaller spacings. Often the limits of the integral do not coincide with the values of  $F[n]$ . Thus, in order to calculate the integral the frequency content for frequencies  $F[n] < F[f] < F[n + 1]$  have to be estimated. Here, three estimation strategies are compared. A nearest-neighbour strategy is considered, in which  $F[f]$  assumes the value of the nearest  $F[n]$ , as well as linear interpolation and cubic spline interpolation. The comparison of the three approaches is done on a pseudo-PSD consisting of the superposition of three weighted Gaussian distributions described by equation 1.23:

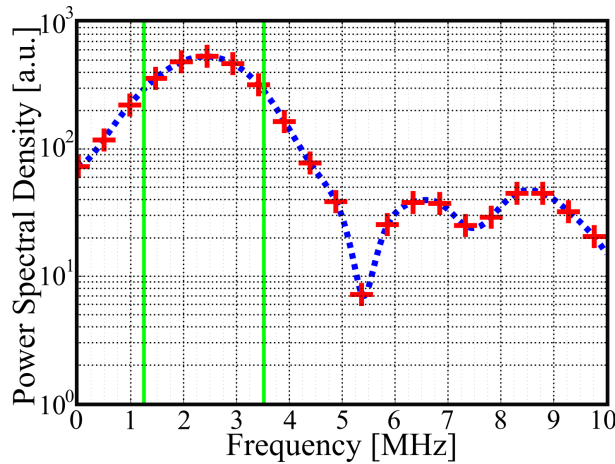


FIGURE 1.4: The PSD calculated using the FFT of a discrete signal  $S[n]$  is shown as red crosses. Its cubic spline interpolation is shown as a blue dotted line. The signal power is calculated as the integral over the latter in the limits marked by the solid green lines.

$$f(x) = \frac{1}{\sigma\sqrt{2\pi}} e^{-\frac{(x-\mu)^2}{2\sigma^2}} \quad (1.23)$$

TABLE 1.1: The weights  $W$ , the means  $\mu$  and the standard deviations  $\sigma$  used to create the PSD.

No.	$W$	$\mu$	$\sigma$
1	0.75	0.9	0.25
2	1.5	2.25	0.5
3	1	4	0.75

Their respective weights  $W$ , means  $\mu$  and standard deviations  $\sigma$  are shown in table 1.1. The mean denotes the centre frequency and the standard deviation describes the bandwidth in this pseudo PSD. The generated PSD (see Fig. 1.5, black solid line) is then sampled (see Fig. 1.5, a, black x). From these discrete frequencies the PSD is reconstructed using nearest neighbour method (see Fig. 1.5, a, green solid line), linear interpolation (see Fig. 1.5, a, blue dotted line) and cubic spline interpolation (see Fig. 1.5, a, red dotted line). The nearest neighbour approach only shows good agreement close to  $F[n]$ . Both the linear interpolation and the cubic spline interpolation show good agreement with the original pseudo PSD, while the former deviates on sharp spikes. This is visualised in the error graph (see Fig. 1.5, b). Here, the estimation error of the nearest neighbour approach (green) fluctuates wildly, while the linear interpolation (blue) peaks at the location of the local maxima and minima of the original pseudo PSD. The spline interpolation (red) shows a low error over the whole

frequency band.

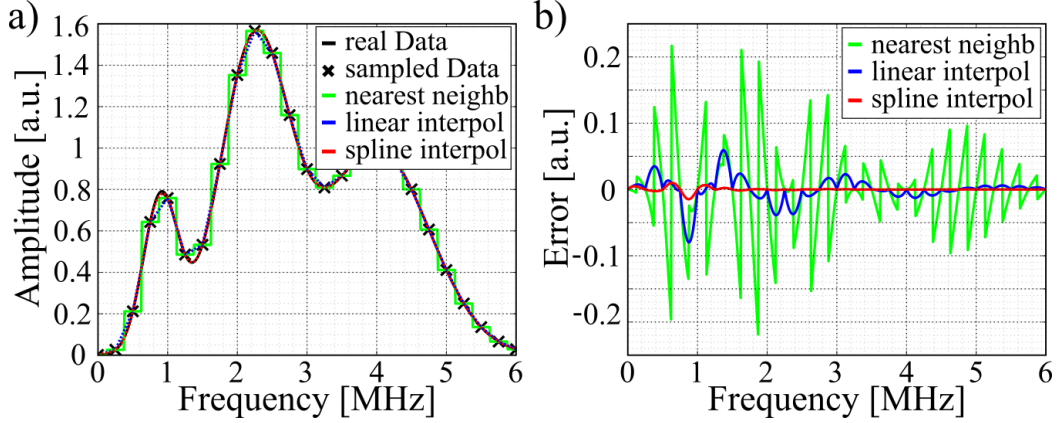


FIGURE 1.5: a) The sampled data points (black x) were used to estimate the pseudo PSD (solid line, black) using nearest neighbour estimation (solid line, green), linear interpolation (dotted line, blue) and cubic spline interpolation (dotted line, red). The latter resulted in the lowest estimation errors (b).

Using this pseudo PSD and the estimation of the three approaches the root-mean-square errors (RMSE) were calculated as:

$$RMSE = \sqrt{\frac{1}{N} \sum_{i=1}^N (X_i - Y_i)^2} \quad (1.24)$$

with the number of data points  $N$ , the estimated value  $X$  and the true value  $Y$ . The nearest neighbour approach yielded  $RMSE_{NN} = 0.0619$ , linear interpolation yielded  $RMSE_{lin} = 0.0190$  and cubic spline interpolation  $RMSE_{SP} = 0.0028$ . As the cubic spline interpolation yielded the lowest estimation errors, it was chosen as estimation method.

## 1.5 Discussion and Conclusion

PA imaging is based on the photoacoustic effect, where US signals are generated by an absorber and detected using conventional US transducers. Unlike in US imaging it is not the elasticity that is mapped but the absorption at the laser wavelength of the imaged media. Therefore, US and PA imaging can be used as complementary imaging techniques, especially considering that a PA system already consists of US transducers.

PA imaging systems appear in two forms, PAT and PA microscopy, i.e. OR PAM and AR PAM. PA microscopy is used mostly for imaging on a cellular level and microvasculature studies, as its penetration depth is severely constricted by the

ballistic optical pathlength (OR PAM) and high US attenuation (AR PAM). For imaging at larger depths and at larger (greater than cells) scales PAT is employed. PAT is increasingly more used for gastrointestinal imaging and mammography. Reduction of the cost of PA imaging systems can facilitate its usage and improve the diagnostic capabilities.

The two main cost factors of PA systems are the PA excitation (laser) with about 10k US\$ and the PA detection (US transducers) with about 2k US\$ for 8 element transducers and 10k US\$ for 128 element phased arrays [111]. As mentioned in 1.2.1 PLDs can be used for cost-reduction of the laser used for PA excitation [40]–[47]. Furthermore, especially for PAT, LEDs can also be employed to reduce system costs [48], [49]. Miniaturisation of the US detectors using MEMS technology and especially with a PMUT approach, shows promises for low-cost systems [112], [113]. Additionally, as shown in 1.2.3 MEMS technology leads to reduced transducer sizes and an increase in variety of transducer morphologies, increasing their effectiveness [70]–[80].

In the course of this work, MEMS technology will be employed to both the excitation and the detection side of a PA system with the goal of improving performance and increasing cost-efficiency. Firstly, a PA scanning system comprised of commercially available components will be introduced. This system is then used to compare the changes against. Secondly, custom-designed PMUT arrays manufactured using a cost-efficient multi-user process are used to replace the commercial US transducers. Thirdly, a MEMS Q-switched micromirror is used to greatly increase the PRF of the excitation laser. Lastly, a novel PA scanning technique is introduced.



## Chapter 2

# Simulations of Photoacoustic Signals

In this chapter the influence of the laser parameters (focal spot size and pulse width), the distance from the source to the detector and the acoustic attenuation on the frequency content and signal strength of a detected PA wave are discussed. To this end acoustic field are simulated using the open source MATLAB toolbox k-Wave. A PA wave generated in a medium with negligible acoustic attenuation (e.g. water with an attenuation coefficient  $\alpha = 2.2 \cdot 10^{-3} \frac{dB}{cm \cdot MHz}$ ) retains its initial pulse shape and thus its frequency spectrum [114], [115]. The initial frequency spectrum can be approximated as the Fourier transform of the laser pulse. This can be derived from the initial pressure pulse  $p_0$ , which can be described in terms of  $\Gamma$  and the heating function  $H_{max} = F_{max} \cdot \mu_a$ , as well as the spatial and temporal profiles  $S(x)$  and  $I(t)$ , as described in eq. 1.8:

$$p_0(x, t) = \Gamma H_{max} S(x) I(t) \quad (2.1)$$

The frequency content of the initial pressure  $p_0(x, t)$ , which is its PSD  $P_0(x, f)$ , is calculated as the Fourier transform of the initial pressure pulse  $P_0(x, f) = \mathfrak{F}\{p_0(x, t)\}$ . Substituting equation 1.8 for  $p_0(x, t)$ , the frequency content can be calculated from:

$$\begin{aligned} P_0(x, f) &= \mathfrak{F}\{\Gamma H_{max} S(x) \cdot I(t)\} \\ P_0(x, f) &= \Gamma H_{max} S(x) \cdot \mathfrak{F}\{I(t)\} \end{aligned} \quad (2.2)$$

Here, the only term the temporal Fourier transform needs to be calculated of is the laser pulse shape term ( $I(t)$ ), as it is the only term that is a function of  $t$ . As the other parameters ( $\Gamma$ ,  $H_{max}$ ,  $S(x)$ ) are only scaling the shape of the frequency response of the generated PA wave. Its frequency spectrum is solely defined by the laser pulse shape for circular focal points or the absorber shape (in case of e.g. PAT). Judging from equation 2.2 the approximation of the laser pulse as a Dirac-pulse leads to an overestimation of the bandwidth of the initially generated PA wave. Furthermore, it shows that the main bandwidth limiting parameter here is the pulse width  $\tau$ . A shorter laser pulse thus generates a higher bandwidth PA signal. As the bandwidth can thus be easily increased and the wave front shape easily manipulated, laser

induced acoustic waves are used for characterisation of high frequency and high bandwidth ultrasound transducers such as hydrophones [116].

In media with non-negligible acoustic attenuation (e.g. soft tissue with an attenuation coefficient  $\alpha = 7.5 \cdot 10^{-1} \frac{dB}{cm \text{ MHz}}$ ) the initially large bandwidth spectrum of a PA wave is quickly reduced and the wavefront broadened. This low-pass filter behaviour reduces the spatial information and thus the resolution of PA imaging applied in e.g. a biomedical medium [117]. The understanding of the effects of different experimental parameters, such as distance of the transducer to the source, pulse width  $\tau$  and laser spot size, on the frequency content of a PA wave in a medium with acoustic attenuation were investigated using simulations done using k-wave, an acoustic field simulation software utilising MATLAB [118]. As described in equation 1.8 the generation of the photoacoustic wave can be described numerically and is linearly dependent on the laser intensity  $I(t)$  and the absorption rate  $\mu_a$ , as well as the Grüneisen factor  $\Gamma$  of the irradiated medium. As the latter two were constant, k-wave simulations were used to evaluate the impact of the distance from the source, the pulse width  $\tau$  and the laser spot size  $d_S$  on the frequency content of the generated PA wave. The profile of the laser intensity  $I(t)$  was modelled after data recorded from the two laser sources used throughout this thesis.

## 2.1 Introduction to k-wave

With the relative initial pressure distribution modelled using the data from the two laser sources (the pulse shapes  $I(t)$ ) and assuming a Gaussian beam profile ( $S(x)$ ), the acoustic propagation is modelled using k-Wave. The propagation of a pressure wave through a medium can be described by three governing equations, namely conservation of momentum and mass, and the relationship between pressure and density (see equations 2.3, 2.4, 2.5 respectively):

$$\frac{\partial u}{\partial t} = -\frac{1}{\rho_0} \nabla p \quad (2.3)$$

$$\frac{\partial p}{\partial t} = -\rho_0 \nabla u \quad (2.4)$$

$$p = c_0^2 \rho \quad (2.5)$$

with the acoustic particle velocity  $u$ , the acoustic density  $\rho$ , the equilibrium density  $\rho_0$ , the speed of sound  $c_0$  and the acoustic pressure  $p$  [119]. k-Wave uses this set of first order equations rather than the combined second order equation. This allows for the inclusion of acoustic force and mass source as well as the implementation of a perfectly matched layer (PML), as well as the direct computation of the vector components of the acoustic intensity [30]. The PML formulation incorporated into the first order equations can readily be transformed onto a discrete (rather than continuous) time-grid using the time-staggered scheme [120]. This discretization is

not trivial for second-order equations. The PML prevents reflections of the US wave from the boundaries of the simulated grid. As a homogeneous volume with dimensions larger than the penetration depth of the US wave is assumed, the PML acts as a way of simulating this attenuation outside of the measurement volume. This especially hold true for clinical US applications, where the US penetration depths is usually smaller than the patient.

Rather than using a finite element, finite difference approach to solve these equations, k-wave is built upon pseudo-spectral method and a k-space approach to reduce complexity and increase speed of the simulation [118]. Rather than fitting a high order polynomial to a number of nodes, requiring up to 10 per wavelength, as in finite difference, a Fourier series is fitted to all data points when using the pseudo-spectral (PS) method. This can be efficiently calculated using the FFT series and reduces the number of required points to two per wavelength, thus improving spatial efficiency. The k-space pseudo spectral method allows for the use of larger time steps compared to conventional FD approaches. However, the use of this method, caused by the application of the FFT on the finite simulation grid, generates pressure waves on the opposite domain boundary to which they exited the grid. That phenomenon is called wave wrapping and is suppressed using the PML, a thin anisotropic absorbing layer surrounding the simulation grid. The effects of this layer can be seen on the edges in Fig. 2.1.

## 2.2 Setting up the simulations

The simulations were performed on a grid of 16384 x 729 points with a element size of  $dx = 1 \mu m$ . The medium was chosen as homogeneous as for these media the k-space method is temporally exact [120]. The simulations were performed with a speed of sound  $v_S = 1500 m/s$  and the attenuation  $\alpha$ . The medium is modelled as an absorbing fluid in terms of ultrasound using a power law as described in eq. 1.11[119]:

$$\alpha = \alpha_0 \cdot \omega^y \quad (2.6)$$

with  $y = 1.5$ ,  $\alpha_0 = 0.75 \frac{dB}{MHz^{1.5}cm}$  and  $\omega$  as the angular frequency. As the medium was homogeneous the Grüneisen parameter – relating the induced heat by the laser to the generated initial pressure gradient – was kept constant too. To emulate the cylindrical wave resulting from the elongated focal point due to its Rayleigh lengths 2D simulations were used. In 3D simulations the wavefront would also experience a curvature in the perpendicular (as shown in Fig. 2.1) direction. This increases the rate of amplitude decrease from  $\frac{1}{x}$  to  $\frac{1}{x^2}$ . This increased amplitude deterioration does not have an effect on the frequency content, which is investigated here. As only the behaviour of the pressure wave and its frequency content during the propagation through the medium were of interest, the laser pulse energy and the absorption coefficients (and with it the wavelength  $\lambda$ ) were modelled as having a unit value,

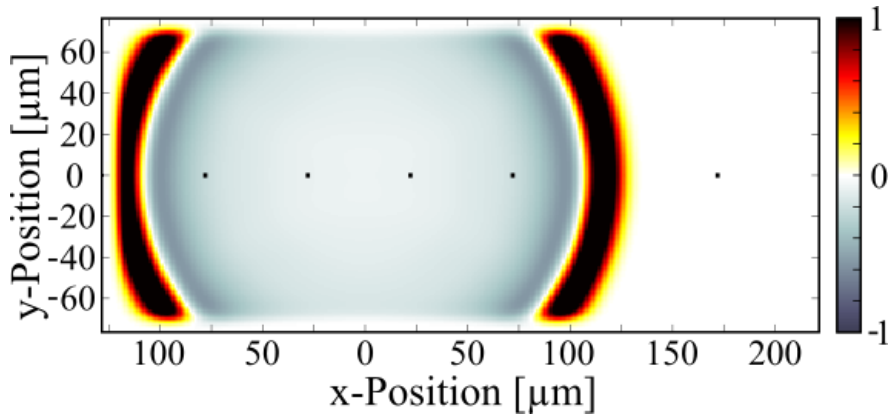


FIGURE 2.1: The simulation during running shows the propagation of the pressure wave (here as relative pressure) through the simulation grid. The detector elements (black dots, enlarged for visibility) are spaced equidistant through the mid-line. The dimension of the simulation grid have been cropped to  $351 \times 151$  for visibility. Near the border of the simulation grid, the effects of the PML can be clearly seen as gradual attenuation. The pressure mapped here is normalised.

resulting in a unit scaling factor  $H_{max}$ .

The simulation was done over  $13 \mu s$  comprising of 65000 time steps with a step length of  $dt = 200 ps$ . The initial pressure was simulated spatially ( $S(x)$ ) using a Gaussian profile and temporally ( $I(t)$ ) using the recorded laser pulse shapes of the Brilliant B and the MEMS laser, for pulse widths of 10 ns and 50 ns, respectively. The centre point of the initial pressure area was placed asymmetrically on the grid to save on computational time as the propagation of the acoustic wave is symmetrical. The centre point was placed at a distance of 128 pixels from the border in x-direction with 64 pixels to the grid end on either side in y-direction to prevent the PML to affect the initial pressure pulse. The amplitude of the pressure was recorded for 320 transducer elements, spaced at intervals of  $\Delta d_{dte} = 50 \mu m$ , positioned in a line through the midpoint of the source (see Fig. 2.1) for every time step. The simulation was run for each laser profile. The PSD was calculated at each detector point by windowing over the recorded PA wave using a Hamming window and applying the FFT. The simulations were evaluated by comparing the PSDs over the distances for the different parameters, i.e. pulse width  $\tau$  and spot size.

### 2.2.1 Influence of Pulse Width

As the frequency content of the initial pulse is heavily influenced by the temporal profile of the laser pulse  $I(t)$ , the frequency content was simulated for several pulse widths  $\tau$  at several positions with varying distance to the source. The distance to the

source was calculated as difference of the x-positions of the transducer element and the centre point of the initial pressure pulse, as the transducer elements are spaced equidistant along the x-axis (see Fig. 2.1, black dots). This was done for pulse widths of 2 ns, 10 ns and 50 ns (see Fig. 2.2, a). The laser pulse with  $\tau = 2$  ns was simulated by down sampling the recorded temporal profile of the MEMS laser. This was done by taking only every 25th element and then normalising the profile. The laser spot was modelled as a Gaussian profile with a spot diameter of  $d_s = 20$   $\mu\text{m}$  (FWHM).

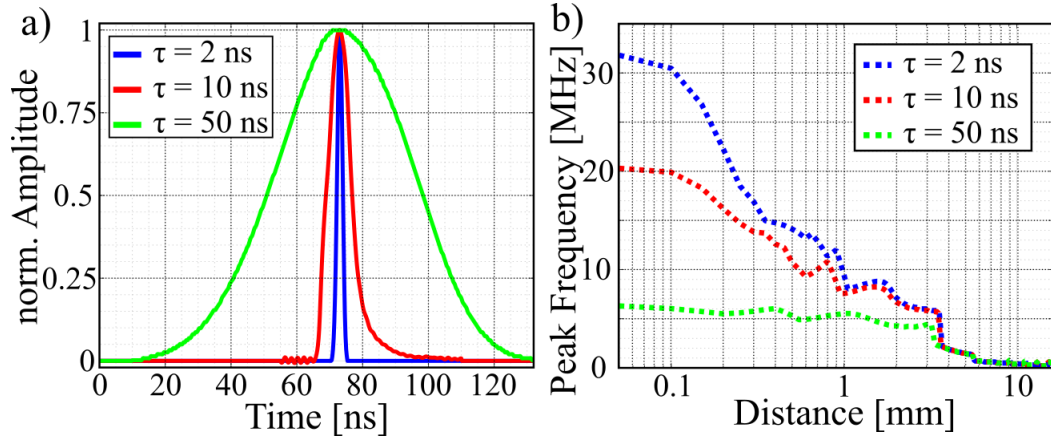


FIGURE 2.2: The pulse shapes used for the simulation (a) are shown for 2 ns (blue), 10 ns (red) and 50 ns (green). The pulse width was calculated as FWHM. The peak frequency of each detector element (b) is compared to its distance to the source for the three pulse width - 2 ns (blue), 10 ns (red) and 50 ns (green) - is different for distances  $d < 2$  mm.

The peak frequency - the maximum frequency - of each detector element was compared to its distance to the source for all three laser profiles (see Fig. 2.2, b). This graph shows that close to the source the main frequency is dependent on the laser pulse width, but for distances  $d > 0.2$  mm the dependency on the pulse widths of the laser vanishes. Here, the peak frequency is determined by the distance to the source due to frequency dependent attenuation.

This only partial dependency can be seen in the spectral maps (see Fig. 2.3 a, c, e) and the PSDs (see Fig. 2.3 b, d, f) of the simulations. The PSDs are shown near the initial pressure pulse (at 0.2 mm, blue), at the transition from laser parameter dominated region to the distance dominated region (2.2 mm, red), where the secondary peak is visibly developing (6.2 mm, green) and where the secondary peak is distinctly developed and became the primary peak (13.7 mm, black). They show that with an increase in distance a secondary peak increases in magnitude (6.2 mm) and eventually levels with the main peak frequency (13.7 mm). The spectral maps show the normalised (for each detector position) PSDs at each detector position. The region dominated by the influence of the pulse width is clearly seen as broad peak up to a

distance of  $d \approx 2 \text{ mm}$  for  $\tau = 2 \text{ ns}$  and  $\tau = 10 \text{ ns}$ . The bandwidth of the initial peak increases with decreasing pulse widths. This shows that very short laser pulses can be assumed to be a delta function with an almost uniform spectral response close to the source. The maximum frequency for the developing secondary peak is limited by its point of onset at  $d \approx 4 \text{ mm}$  with a peak frequency of  $f = 2 \text{ MHz}$ . For greater distances the distinct levels of the peak frequency and the secondary peak are clearly visible showing less dependency on the pulse width  $\tau$  as the influence of the distance grows more dominant.

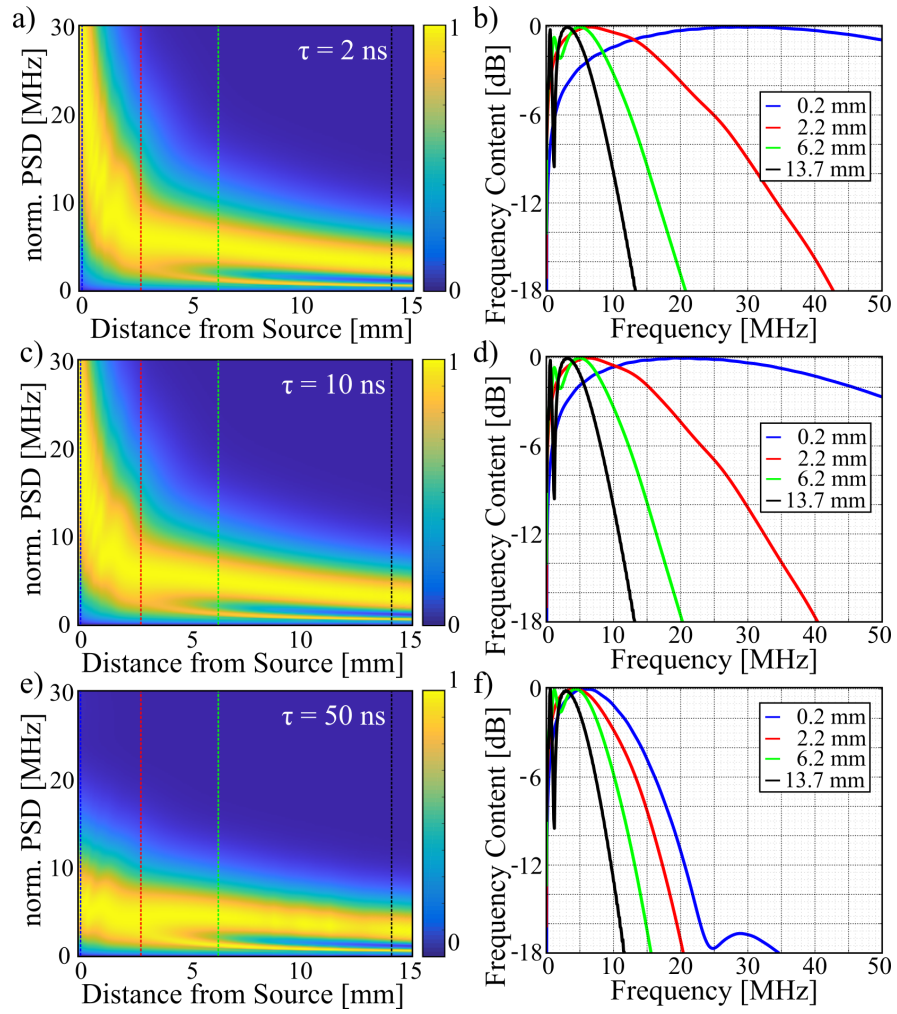


FIGURE 2.3: The spectral maps (a, c, e) and PSDs (b, d, f) are shown for pulse widths of 2 ns, 10 ns and 50 ns. The spectral map show the normalised frequency content at each distance on a linear scale. They clearly visualise the laser-parameter-dominated region and the distance dominated region. The PSDs are shown near the initial pressure pulse (at 0.2 mm, blue), at the transition from laser parameter dominated region to the distance dominated region (2.2 mm, red), where the secondary peak is visibly developing (6.2 mm, green) and where the secondary peak is distinctly developed and became the primary peak (13.7 mm, black). They illustrate the development of peak frequency and the secondary peak.

### 2.2.2 Influence of the Spot Size of the Laser

In eq. 2.2 the assumption was made that the spatial profile of the laser pulse  $S(x)$  does not effect the frequency content. Here, this assumption is tested by investigating

the influence of the laser spot size  $d_s$ . This was simulated at varying distances as described above, for spot sizes (FWHM) of  $10\ \mu\text{m}$ ,  $20\ \mu\text{m}$ ,  $40\ \mu\text{m}$  and  $80\ \mu\text{m}$  (see Fig. 2.4, a), at a pulse width of  $\tau = 10\ \text{ns}$ . These laser spot diameters were modelled using a Gaussian profile on a grid of  $101 \times 101$  pixels with standard deviations of  $\sigma = 4.2\ \mu\text{m}$ ,  $\sigma = 8.6\ \mu\text{m}$ ,  $\sigma = 16.5\ \mu\text{m}$  and  $\sigma = 34.5\ \mu\text{m}$ , respectively.

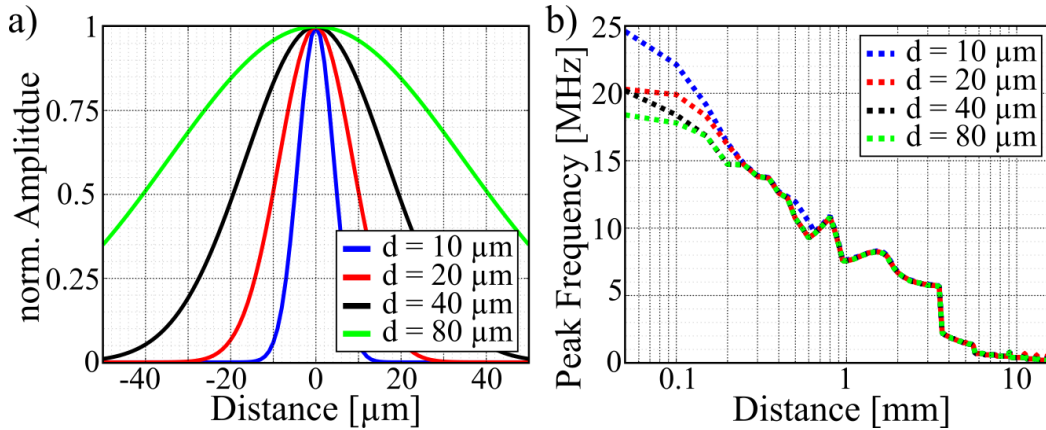


FIGURE 2.4: The laser spot sizes used in the simulations with a FWHM widths of  $10\ \mu\text{m}$  (blue),  $20\ \mu\text{m}$  (red),  $40\ \mu\text{m}$  (black) and  $80\ \mu\text{m}$  (green). The peak resonance frequencies (b) relating to the spot sizes differ only for distances  $d < 300\ \mu\text{m}$ .

Comparing the peak frequencies over the distance from the source for all laser spot sizes (see Fig. 2.4, b) shows that close to the source the main frequency is dependent on the laser spot size, but for distances  $d \geq 300\ \mu\text{m}$  this dependency vanishes. At these distances the peak frequencies for the different spot sizes are the same, thus dominated by distance. Comparing the PSDs of the different spot sizes (see Fig. 2.5) shows that the main and secondary peaks are the same for distances  $d > 2.2\ \text{mm}$ , only the 0.2 mm (blue) PSD shows small differences in peak frequency. The peak frequencies are 21 MHz, 20 MHz, 19 MHz and 19 MHz for spot sizes of  $10\ \mu\text{m}$  to  $80\ \mu\text{m}$ , respectively. This shows that the spot size has a only a small effect on the frequency content of the generated PA wave compared to the pulse width and that only near the initial pressure pulse. The spectral maps (see. Fig. 2.6) reinforce this hypothesis as they similar for all spot sizes. As described above, the laser dominated region is clearly visible for distances  $d < 2\ \text{mm}$  by the characteristic wide bandwidth. For greater distances the peak frequency and the secondary frequency develop clearly.



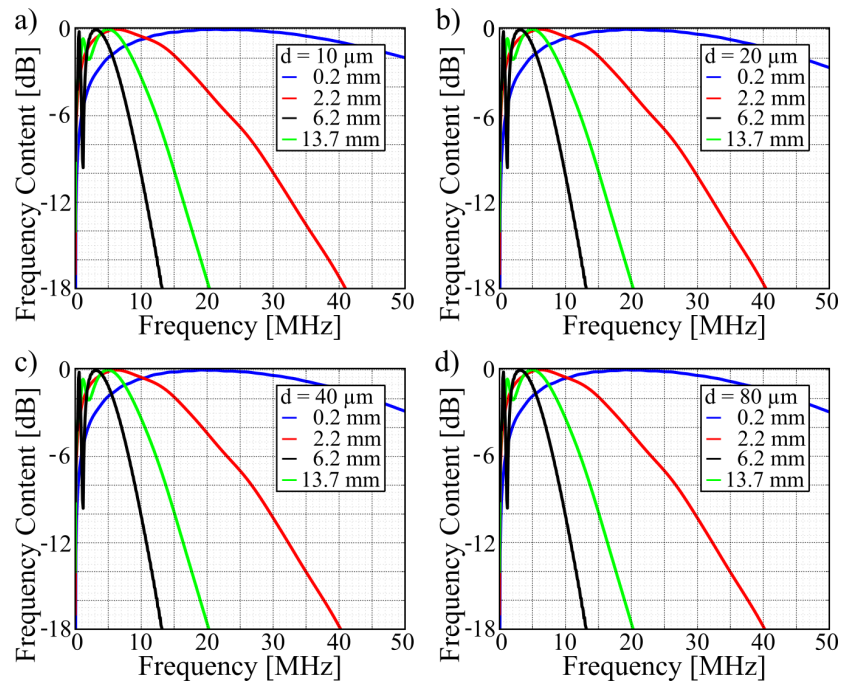


FIGURE 2.5: The PSDs are shown for spot sizes of  $10 \mu\text{m}$  (a),  $20 \mu\text{m}$  (b),  $40 \mu\text{m}$  (c) and  $80 \mu\text{m}$  (d) at distances of 0.2 mm (blue), 2.2 mm (red), 6.2 mm (black) & 13.7 mm (green). The PSDs are shown near the initial pressure pulse (at 0.2 mm, blue), at the transition from laser parameter dominated region to the distance dominated region (2.2 mm, red), where the secondary peak is visibly developing (6.2 mm, green) and where the secondary peak is distinctly developed and became the primary peak (13.7 mm, black). They show the development of the peak frequency and the secondary peaks. Furthermore, they show that except for the peak frequency at 0.2 mm the PSDs are similar independent of the spot size.

### 2.3 Near Field Distance for Detection

The size of the transducer (here diameter) and its distance to the US source have a strong impact on scaling the amplitude of the detected impinging US wavefront. For a point (or spherical) source the US wave propagates as a spherical wavefront. Using planar US detectors it impinges at different times over the length of the detector, as shown in Fig. 2.7. While the wavefront has mostly passed the transducer at its centre, it has not yet hit the transducer at its edges (see Fig. 2.7, a). Thus, the transducer is subjected to both the maximum of the wavefront and the minimum of its wake simultaneously. This leads to an overall reduction in signal strength as that is calculated as the integral of the signal over the length of the transducer.

The effects of the detector size and its distance to the source were simulated using a

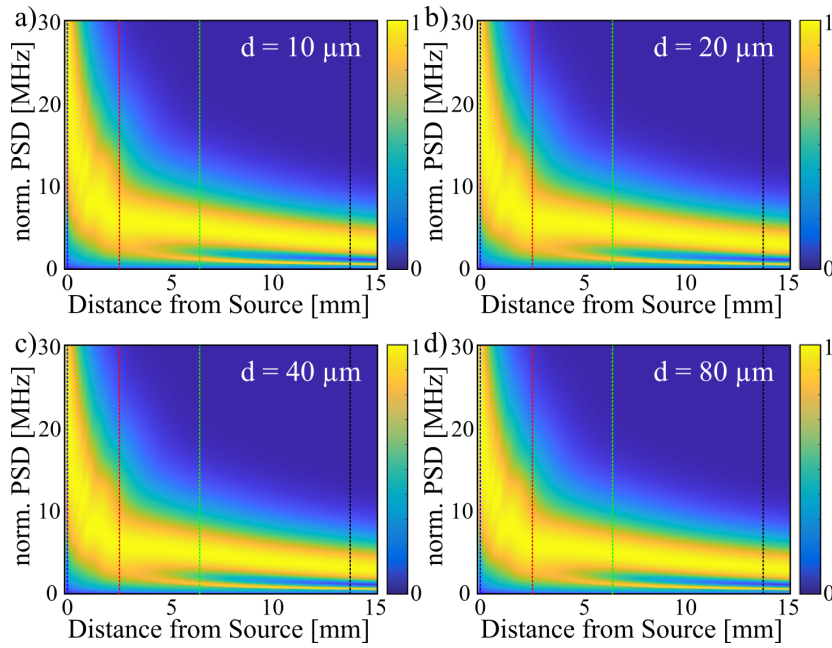


FIGURE 2.6: The spectral maps for the simulations of different spot sizes -  $10 \mu\text{m}$  (a),  $20 \mu\text{m}$  (b),  $40 \mu\text{m}$  (c) and  $80 \mu\text{m}$  (d) - clearly show the region dominated by the laser parameters (for  $d < 2 \text{ mm}$ ) and the distance dominated region (for  $d > 2 \text{ mm}$ ). The dashed lines show the position of the respective PSDs near the initial pressure pulse (at  $0.2 \text{ mm}$ , blue), at the transition from laser parameter dominated region to the distance dominated region ( $2.2 \text{ mm}$ , red), where the secondary peak is visibly developing ( $6.2 \text{ mm}$ , green) and where the secondary peak is distinctly developed and became the primary peak ( $13.7 \text{ mm}$ , black).

grid of  $2187 \times 6144$  pixels at a pixel width of  $dx = 1 \mu\text{m}$ . The simulation ran over 25000 time steps at  $dt = 0.2 \text{ ns}$ , thus over  $5 \mu\text{s}$ . Six detectors consisting of 1901 elements (maximum diameter  $d_{max} = 1.9 \text{ mm}$ ) were placed at distances of  $100 \mu\text{m}$ ,  $200 \mu\text{m}$ ,  $500 \mu\text{m}$ ,  $1000 \mu\text{m}$ ,  $2000 \mu\text{m}$  and  $5000 \mu\text{m}$ . These simulations were run for a medium with no attenuation and with soft-tissue like attenuation of  $\alpha = 0.75 \frac{\text{dB}}{\text{cm MHz}}$ . The PA waves were generated with Dirac-like pulses with pulse widths ranging from  $\tau_1 = 1 \text{ ns}$  to  $\tau_6 = 200 \text{ ns}$ .

For each detector at each distance and pulse widths, the normalised (by number of detector elements) signal strength was calculated for detector sizes ranging from  $3 \mu\text{m}$  to  $1901 \mu\text{m}$ . This resulted in the trend of the normalised signal strength for increasing detector diameters at a fixed distance as shown in Fig. 2.8. The FWHM (red) of the resulting trends were chosen as the maximum diameter  $d_{max}$  for the respective distances  $r_{NFD}$ . Thus, a transducer with a diameter  $d_{max}$  has a NFD of  $r_{NFD}$ , as the signal is reduced to  $-6 \text{ dB}$ . The normalised (per detector element) signal strength is reduced to 25 % (green) for a detector twice the diameter.

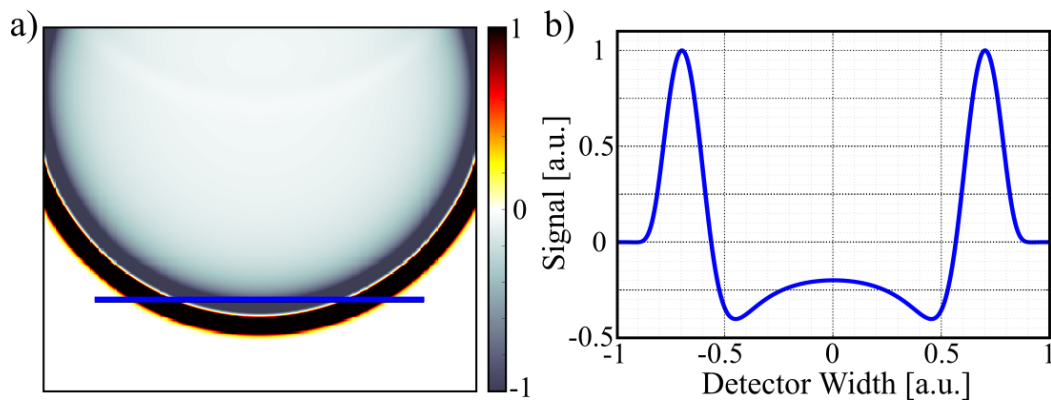


FIGURE 2.7: A spherical wavefront impinges at different times over the length of a planar transducer (blue) (a). While the wavefront has mostly passed the transducer at its centre, it has not yet impinged on the transducer edges. This causes the detector to be subjected to both the minimum and the maximum of the wavefront simultaneously (b). Thus, the detected signal is weakened.

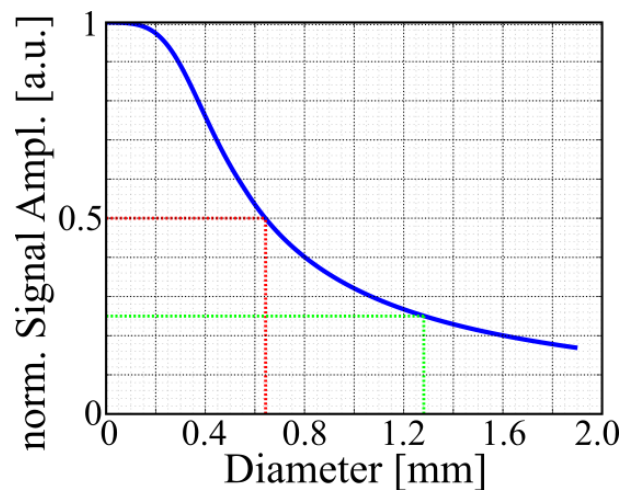


FIGURE 2.8: The normalised (per detector element) signal amplitude of a transducer decreases with its diameter. The NFD (red) is calculated as its FWHM. The signal strength is reduced to 25 % (green) for a detector twice the diameter.

The diameter of the transducers and their respective near-field distances (NFDs) are shown for media with a soft-tissue like attenuation and without attenuation in Fig. 2.9, a and b, respectively. The NFDs decrease with increasing pulse widths and attenuation coefficient. Both variables cause a lower rate of change of the amplitude

of the wave-front. Extrapolating from the data (dash-dotted lines in both graphs) the NFD for a detector with a diameter of 20 mm ranges from 12 mm to 30 mm, for a soft-tissue like attenuation, and 45 mm to 130 mm for no attenuation. Thus, the NFD in a non-attenuating medium is 4-fold the NFD in an attenuating medium such as soft-tissue.

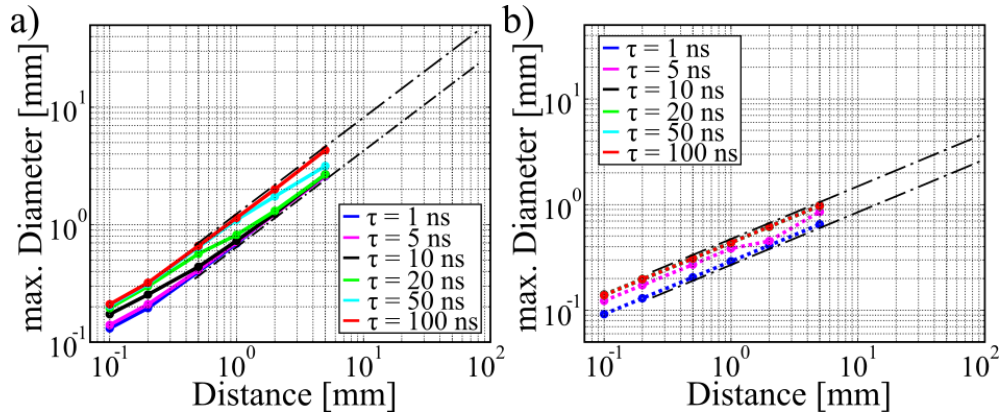


FIGURE 2.9: The simulated maximum diameters for transducers at various distances are shown for pulse widths ranging from 1 ns to 100 ns and attenuation coefficients of  $\alpha = 0.75 \frac{\text{dB}}{\text{cm MHz}}$  (a) and  $\alpha = 0 \frac{\text{dB}}{\text{cm MHz}}$  (b). The maximum diameter increases with increasing pulse width and attenuation coefficient.

## 2.4 Discussion

The simulation showed that the PSD of the generated PA signal can be divided into two regions over its distance to the source. Firstly, a region that is dominated by the influence of the laser parameters, mostly by the pulse shape  $I(t)$  and to a lesser degree by the spatial shape  $S(x)$ , characterised by a single peak with a wide bandwidth. The bandwidth and centre frequency are determined by the pulse width  $\tau$  of the laser. It is however not dependent on the spot size of the laser. This means that for PA imaging the spot size does need to be known to make correct assumptions about the frequency content of the detected PA signal. This can prove a challenge especially in turbid media such as soft tissue. Thus, the real spot size, enlarged by repeated scattering events has no effect in the PA imaging outcome. In the second region the frequency content of the PA pulse is determined by its distance to the source. Here, the original wide and uniform band is joined by a low frequency side band. The centre frequency and bandwidth of this peaks depend mostly on the distance from the transducer to the source. As the first region only expands for  $d \approx 2 \text{ mm}$ , the following experiments will be conducted in the second region.

The simulations were performed as 2D simulations to emulate the cylindrical wave resulting from the elongated focal point due to its Rayleigh lengths. In 3D simulations the wavefront would also experience a curvature in the perpendicular direction. This increases the rate of amplitude decrease from  $1/x$  to  $1/x^2$ . However, this increased amplitude deterioration does not have an effect on the frequency content, which was investigated here.

The observed low-pass filtering of the PA wave is comparable to the observations in [121], [122]. Here, the effect of the acoustic attenuation was measured using transducers with centre frequencies of 3.5 MHz and 7.5 MHz in [122] and 50.6 MHz in [121]. For the 7.5 MHz and the 50.6 MHz transducers, the measured centre frequencies, even when only weakly attenuated by water, lead to centre frequencies lower than the transducers. The centre frequency is further reduced by either increasing the thickness of the acoustic attenuator [122] or by increasing the distance of the transducer to the source [121]. Additionally, these experiments show the generated ridges (see frequency maps) in the high frequency transducer (7.5 MHz and 50.6 MHz) experiments. They are not visible in the 3.5 MHz experiment, potentially due to a too small window size, which reduces the resolution of the spectrum.

A signal feature that has not been modelled in the simulations but which has been observed in real-life - most notably in high pulse energy PA wave generation - is signal ringdown. This feature is caused by over-saturation of the transducer. The ringdown contributes to the lower frequency spectrum [123], thus increasing the spectrum in the lower frequency regions.

The simulations of the NFD showed that a shorter pulse width and a higher attenuation decrease the NFD. Thus, the SNR loss caused by placing a transducer closer to the target can be reduced by altering either the transducer, i.e. its centre frequency and its diameter, or by increasing the attenuation of the medium. The lower rate of change caused by decreasing  $\tau$  and increasing  $\alpha$  reduces the amplitude difference over the length of the transducer and thus increases the signal strength.



## Chapter 3

# Preliminary Photoacoustic Setup

The first step towards developing a PA imaging system containing miniaturised components was to set up a system using conventional and commercially available components, which is later used to compare the performance of this miniaturised PA setup against. In this chapter, the preliminary PA imaging system and its components will be presented. Furthermore, its application to PA imaging and scanning will be shown and its optimisation potential highlighted.

### 3.1 Photoacoustic test setup

The preliminary setup shown in figure 3.1 consists of a laser, a gelatin target phantom (see section 3.3 for more information on the phantoms) on a two-axis translation stage and an ultrasound transducer. The US transducer is acoustically coupled to the gelatin target phantom using US gel. The laser is a Nd:YAG laser (Brilliant B, Quantel with  $\tau = 8.15 \text{ ns}$ ,  $PRF = 10 \text{ Hz}$ ) frequency-doubled to  $\lambda = 532 \text{ nm}$  (see Fig. 3.1, a) with a maximum average power of  $P_{max} = 2.78 \text{ W}$  (at  $\lambda = 532 \text{ nm}$ ). The output beam, the power of which can be adjusted using the variable attenuator disk, is redirected using a laser line mirror (NB1-K13, Thorlabs,  $R = 98.5 \%$  ( $\lambda = 532 \text{ nm}$ )) and focused onto a target phantom using a  $f = 70 \text{ mm}$  plano-convex lens to a focal spot diameter of  $d \leq 20 \mu\text{m}$  (see 3.2.1). The distance between the output of the second harmonic generator and the dichroic mirror was variable as the mirror was mounted on a micrometer stage. This allowed adjustment of the focal spot position of the laser in  $y$ -direction. A photodiode (AEP X55, Panasonic) placed behind the dichroic mirror was used as a trigger for the recording system. This was possible as the dichroic mirror is 98.5 % reflective. No saturation of the photodiode was observed as the laser spot was still unfocused and had a diameter of  $d \approx 6.6 \text{ mm}$  (see Table 3.1).

Two different configurations were used for the ultrasound detector (see 3.4 for more characterisation of the transducers) and the gelatin phantom on the translation stage. In the first (see Fig. 3.1, b), both the detector and the phantom were fixed on the motion stage, which moved through the focal spot of the laser in  $x$ - &  $y$ - direction, thus the detector altered its distance to the laser spot. This caused the PA signal strength to also depend on the  $x$ - &  $y$ - position due to the attenuation through the gelatin. This decreased the signal power of the PA wave according to the

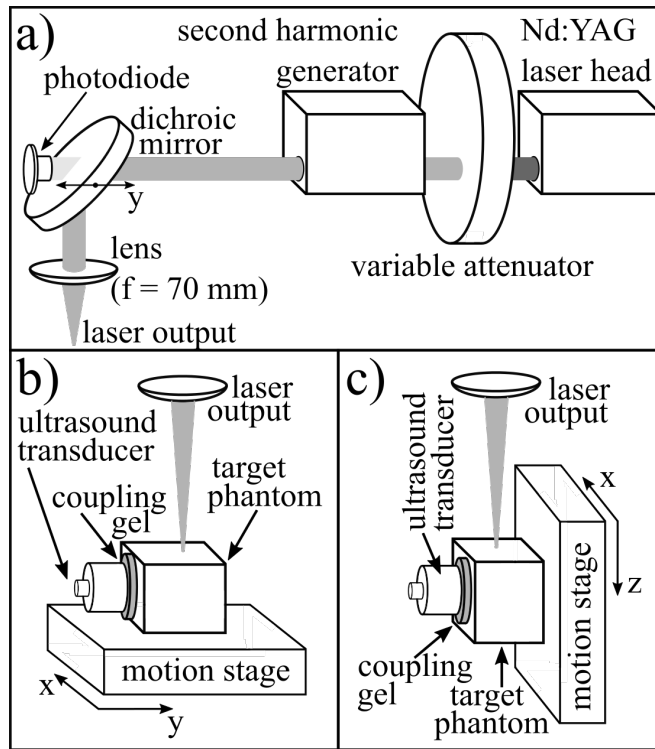


FIGURE 3.1: (a) The commercial Nd:YAG laser setup and its individual components are shown with the laser output and beam steering. (b) The first detector setup had the ultrasound transducer fixed on the motion stage, resulting in a non-fixed distance between the transducer and the laser spot and a dependency of the signal power on the distance between transducer and laser spot. This was remedied by tilting the motion stage by  $90^\circ$  and fixing the ultrasound transducer to the optical table (c). Thus, the distance between transducer and laser spot remained constant.

inverse-square law. The ultrasound transducer was acoustically coupled to the phantom using coupling gel (Ultrasound Gel, Healthlife). The setup was altered to the second design (see Fig. 3.1, c). This removed the dependency by fixing the detector to the table and thus fixing its distance to the laser spot. Furthermore, it enabled an additional degree of freedom as the motion stage was tilted by  $90^\circ$ . This allowed for fine control in the  $z$ -direction while reducing the  $y$ -direction control to coarser movement with the micrometer stage (see  $y$  in Fig. 3.1, a). The  $y$ -directional micrometer stage was not used during experiments, but during their setup. In both cases, the phantom was placed on a stage moved by two 1-axis motion actuators (850 F Actuator, Newport, encoder resolution  $\partial x = 0.05 \mu m$ , repeatability  $1 \mu m$ ) controlled by a motion control unit (motion controller model MM 4005, Newport) via a LabVIEW program. The motion stages had a minimum step length of  $\Delta x_{min} = 5 \mu m$ .



## 3.2 Laser characteristics

The pulsed laser source used in this setup was a commercial Nd:YAG (Brilliant B, Quantel, France), frequency doubled to  $\lambda = 532 \text{ nm}$ . The laser was characterised by measuring its output parameters such as maximum laser power, pulse to pulse repeatability, pulse width and beam spot size.

### 3.2.1 Maximum laser power and beam spot size

The Brilliant B has an inbuilt adjustable neutral density filter. The optical density of which was turned to a minimum to measure the maximum achievable power. The Brilliant B trigger settings were set to a pulse repetition rate of  $f_{PRF} = 10 \text{ Hz}$  and the laser was warmed up for  $t = 30 \text{ min}$ . A powermeter (Gentec E0 Solo PE, Gentec Electro-Optics, Canada) with a high-power meter head (UP19K-15s-VM-DO, Gentec Electro-Optics, Canada) was placed in the beam path. The power meter was set to measure the power over a time of  $t = 5 \text{ min}$  at a sampling rate of  $f_S = 1 \text{ Hz}$  and evaluate the measured data to give the average output power  $\bar{P}$  as well as its standard deviation  $\sigma_P$ .

The beam spot size was measured using laser alignment paper. It was placed in the beam's path at two locations; firstly, a piece of laser alignment paper was positioned at the frequency doubler's output and secondly, a piece of laser alignment paper was positioned at the lens holder. The alignment paper was then exposed to a single pulse using an OD 0 attenuation. The dimensions of the acquired beam spots were measured in the x- direction ( $x_1$  &  $x_2$ ) and the y- direction ( $y_1$  &  $y_2$ ) using a caliper. The average output power at an OD 0 attenuation setting  $\bar{P}$  and its standard deviation  $\sigma_P$  were measured as:

$$\bar{P} = 2.78 \text{ W} \quad \text{and} \quad \sigma_P = 27.3 \text{ mW}$$

From this the maximum pulse energy  $E_{pl}$  can be estimated, when simplified as a square wave pulse, as:

$$\begin{aligned} E_{pl} &= \frac{\bar{P}}{f_{PRF}} & (3.1) \\ E_{pl} &= \frac{2.78 \text{ W}}{10 \text{ Hz}} \\ E_{pl} &= 278 \text{ mJ} \end{aligned}$$

The minimum power was measured similarly to the maximum achievable, with difference that the adjustable neutral density filter was turned to maximum attenuation. The minimum achievable power was measured as  $\bar{P} = 15.4 \text{ mW}$  and  $\sigma_P = 1.17 \text{ mW}$ . Therefore, the power is adjustable over a range of OD 0 to OD 2.25.

The beam spot size was measured from the laser spot marks on the laser alignment paper in x- & y-direction (see table 3.1). The spots were measured with a ruler, thus giving a measurement uncertainty of  $\sigma = \pm 0.1 \text{ mm}$ . From these values it can be seen that the laser output, which initially is circular, has become slightly elliptic over the distance from the output of the frequency doubler to the lens  $d_L$  of  $d_L = 750 \text{ mm}$ . The measured ellipticity was potentially caused by thermal lensing in the Nd:YAG crystal.

As shown in the simulations with varying beam spot diameters, the spot size influences the frequency content of the received PA signal only for a detector-source distance of  $< 300 \mu\text{m}$ . The following experiments are performed at distances  $> 4 \text{ mm}$ , so well beyond the  $300 \mu\text{m}$  mark. The influence of the beam spot diameter is thus negligible. A better method to measuring the beam spot diameter and its properties would be to use a beam profile. This would allow the measurement of the  $M^2$  parameter. As the laser power and its pulse energies were too high, the knife-edge method was chosen.

TABLE 3.1: The measured dimensions of the marks on the laser alignment paper in x- & y- direction of the beam spots.

	Location 1	Location 2
x [mm]	$6.6 \pm 0.1$	$6.6 \pm 0.1$
y [mm]	$6.7 \pm 0.1$	$6.3 \pm 0.1$

Using these values the minimum achievable focal spot diameter  $2\omega_0$  can be calculated from the focal length of the lens  $f$ , the diameter of the spot on the lens  $d_l$  and the wavelength  $\lambda$  as:

$$2\omega_0 = \frac{4 \lambda f}{\pi d}$$

$$2\omega_0 = \frac{4 \cdot 532 \text{ nm} \cdot 70 \text{ mm}}{\pi \cdot 6.6 \text{ mm}}$$

$$2\omega_0 = 7.184 \mu\text{m}$$

The focal spot diameter was measured by my colleague Craig Murdoch (Ph.D. student at CMP, University of Strathclyde, Glasgow) using the knife edge method. Here, the power of the laser beam is measured while a the edge of a razor blade is moved through the beam. The FWHM of the beam is measured by measuring the distances at which 25% and 75% of the initial beam power are reached. This is explained more in-depth in subsection 5.4. The results (see Fig. 3.2) show that the commercial Nd:YAG laser has a focal spot size of  $d_{spot} \leq 20 \mu\text{m}$ . The measured focal spot diameter is up to 2.8-times larger than the calculated theoretical value and thus in the range of the expected diameter.

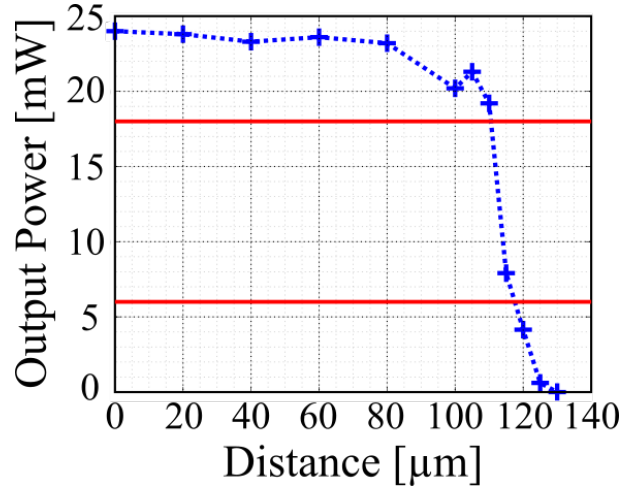


FIGURE 3.2: The power measurements taken during the knife edge experiment show a spot size of  $\leq 20 \mu\text{m}$ . The red lines denote the 25% and 75% of the initial beam power.

### 3.2.2 Pulse width & Pulse to pulse repeatability

The pulse width and pulse to pulse repeatability were measured by diverting the laser beam on to a screen of white paper using another laser line mirror. A high speed photodiode (S9055-01, Hamamatsu,  $f_{-3dB} = 1.5 \text{ GHz}$ ) was positioned at a distance of  $400 \text{ mm}$  from the screen and connected to an oscilloscope (Agilent Infiniium 54845 AR,  $Z_{in} = 50 \Omega$ , DC,  $f_s = 4 \frac{\text{GSa}}{\text{s}}$ ). The Brilliant B laser was externally triggered by a signal generator (TTi, TGA1230 30 MHz synthesised arbitrary function generator) at a repetition frequency of  $f_{PRF} = 10 \text{ Hz}$ . The laser was turned on, attenuated and warmed up for  $t = 30 \text{ min}$ . The laser output power was measured as described above. The average output power was  $\bar{P} = 72.4 \text{ mW}$  and its standard deviation was  $\sigma_P = 1.18 \text{ mW}$ . At this laser power 75 consecutive laser pulses were recorded. The pulse width  $\tau$  was calculated as the full-width half-maximum (FWHM) of the pulse. The pulse to pulse repeatability was quantified as the mean and standard deviation of the maximum photodiode voltage as well as pulse width.

The averaged recorded laser pulse is shown in Fig. 3.3, a. It shows the averaged laser pulse shape recorded with the photodiode (solid line) and the FWHM line (dotted line). The average pulse width  $\bar{\tau}$  and its standard deviation  $\sigma_\tau$  were measured as:

$$\bar{\tau} = 8.15 \text{ ns} \quad \text{and} \quad \sigma_\tau = 0.411 \text{ ns}.$$

The maximum amplitude of the laser pulse  $\bar{V}_{max}$  and its standard deviation  $\sigma_{V_{max}}$  were measured as:

$$\bar{V}_{max} = 319.2 \text{ mV} \quad \text{and} \quad \sigma_{V_{max}} = 2.52 \text{ mV}.$$

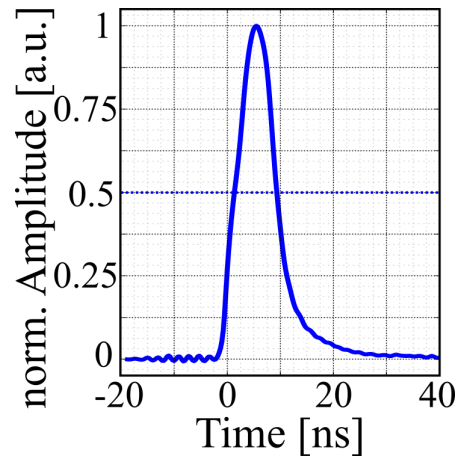


FIGURE 3.3: The shape of the laser pulse averaged over 75 samples (solid line) is shown with the FWHM line (dotted line). The pulse width is determined as  $\tau = 8.15 \text{ ns}$ .

### 3.3 Phantom preparation

The photoacoustic tests were done either on targets embedded in a matrix, such as carbon fibres or polyimide coated fibres, or by using the matrix itself as a target by adding an absorber. The matrix was made from gelatin. Gelatin was used as a phantom material as it is a readily-available, highly customizable and safe material which is easy to produce and handle. Additionally, acoustic waves in a gelatin matrix behave similar to soft tissue [124]. The drawback of using gelatin based phantoms is that water evaporates from the phantom resulting in dried out phantoms. The phantoms usually lasted 12 hours before drying out. Later experimental setups see the phantom immersed in an oilbath for acoustic coupling. This prevented the phantoms from drying out as they were protected from the air.

In order to make a clear gelatin phantom with a mass-to-mass concentration  $c$ , a clean and empty glass beaker was put on a scale and the scale re-zeroed. The beaker was filled with water and the mass of the water  $m_W$  was measured using the scale. The required mass of gelatin  $m_G$  was calculated with the total mass  $m_{tot}$  as:

$$m_G = \frac{m_W}{1 - c} - m_W \quad (3.2)$$

$$m_G = m_W \cdot \left( \frac{1}{1 - c} - 1 \right)$$

with the concentration  $c = \frac{m_g}{m_{tot}}$ . A small glass beaker was put on the scales and, after re-zeroing, a mass of  $m_G$  of gelatin powder (Gelatine general purpose grade, Fisher Scientific UK Ltd.) was poured into it. A water bath was prepared on a combined

magnetic stirrer and hotplate. The water bath was heated to 60 °C measured using a Pt-100 thermistor and its thermometer (TES 1312A, TES Electric Corp.). The glass beaker with the water was placed in the water bath. A magnetic stir bar was put into the water. A second thermistor was used to measure the water temperature in the glass beaker, once the temperature reached 50 °C the thermistor was taken out and the gelatin powder poured in. A lid was put on the beaker, the water-gelatin-concoction was stirred for  $t_{mix} = 30 \text{ min}$  and the heat was turned down to the lowest setting while still heating. When clear gelatin was required the solution was now poured into a casting mould (40 mm x 40 mm x 40 mm) and allowed to cool in a refrigerator at 2.4 °C for 3 hours. This hardened the gelatin. If alteration of the optical properties of the gelatin was required, an absorbing or a scattering agent, such as India Ink (0.4 %  $m/m$ , Drawing Ink: India Ink, Jackson's) or milk were added and the solution was stirred for another  $t = 5 \text{ min}$  before the solution was poured into a mould and allowed to cool down. In the case of phantoms made from multiple layers, the first layer of gelatin (with or without additives) would be poured into the mould chilled in the refrigerator for an hour before the next layer could be added. This was repeated until all layers were added.

A 1 % solution of India ink and water was prepared to facilitate easy and exact adding of the correct amount of absorber. The solution was produced by mixing undiluted India ink (Drawing Ink: India Ink, Jackson's) and water at a mass-to-mass ratio calculated using a modified version of equation 3.2:

$$m_I = m_W \cdot \left( \frac{1}{1 - c} - 1 \right) \quad (3.3)$$

Here,  $m_I$  is the mass of the added India ink,  $m_W$  is the mass of the water and  $c$  the desired concentration. The 1 % solution was prepared by adding  $m_I = 2.05 \text{ g}$  of India Ink to  $m_W = 207.8 \text{ g}$  of water. This results in a consecration  $c$  of:

$$\begin{aligned} c &= \frac{m_I}{m_W + m_I} \\ c &= \frac{2.05 \text{ g}}{209.85 \text{ g}} \\ c &= 0.977 \% \end{aligned}$$

### 3.3.1 Estimation of Speed of Sound in Gelatin

The speed of sound in an 8 % gelatine phantom was measured by exciting PA waves (pulse energy  $E = 172 \mu\text{J}$ ) at three relative distances to the transducer, i.e.  $d_1 = 0 \text{ mm}$ ,  $d_2 = 5 \text{ mm}$  and  $d_3 = 10 \text{ mm}$ . The distance was changed by moving the dichroic mirror mounted on the micro-meter stage (see y-stage in Fig. 3.1 a). This moved both the laser line mirror and the lens. The phantom consisted of two layers, an absorbing (0.4 % India Ink) and a clear layer. The PA wave was generated on the interface of the clear and the absorbing layer. It was recorded using an Olympus 2.25 MHz immersion transducer. It was aligned perpendicular to the direction of movement of

the laser spot (spot size  $d_s \approx 50 \mu m$ ) and positioned so that its midpoint was at the height of the interface of the layers. The transducer's output was amplified by +60 dB (HVA-10M-60B, FEMTO), averaged over 64 samples and recorded using an oscilloscope (DS 1104, Rigol) at a sampling frequency of  $f_s = 50 \frac{MSa}{s}$ . The recorded traces were then filtered using a high-pass filter with a cut-off frequency of  $f_{cut} = 50 kHz$ .

The traces for the three distances are shown in Fig. 3.4. The time difference between the "0 mm" and the "5 mm" and between the "5 mm" and the "10 mm" is  $\Delta t_5 = 3.36 \mu s$ . The time difference between the "0 mm" and the "10 mm" is  $\Delta t_{10} = 6.72 \mu s$ , twice the value of  $\Delta t_5$  for twice the distance. From the time difference  $\Delta t_{10}$  at a distance  $d_3 = 10 mm$  the speed of sound  $v_s$  in the gelatine matrix can be calculated using:

$$\begin{aligned} v_s &= \frac{d_3}{\Delta t_{10}} \\ v_s &= \frac{10 mm}{6.72 \mu s} \\ v_s &= 1488 \frac{m}{s} \end{aligned} \quad (3.4)$$

The calculated speed of sound in an 8 % (m/m) gelatine phantom is  $v_s = 1488 \frac{m}{s}$  and thus similar to the speed of sound in soft tissue (ranging from  $v_s = 1435 \frac{m}{s}$  to  $v_s = 1595 \frac{m}{s}$  [125]). The influence on the speed of sound of the added absorbent agent (India Ink) is negligible due to its small quantities. The signal at the time of the initial laser pulse is investigated in the following chapter.

### 3.3.2 Electromagnetic Interference

The electromagnetic interference (EMI) recorded in the transducer signal traces (see Fig. 1.3, red box) was investigated using filter paper (CalColor, Rosco Laboratories Inc., USA). The commercial Nd:YAG laser was fired into a clear gelatine phantom, which scattered the light. The transducer was placed as shown in Fig. 3.1, c but not acoustically coupled to the phantom, i.e. no coupling gel and an air gap between transducer and phantom. Traces of the transducer signal were recorded using a sampling rate of  $f_s = 1 \frac{GSa}{s}$ . Five different filter papers were used: transparent (Rosco CalColor 00), Lavender 60 (4960), Lavender 90 (4990), Bright Blue (79) and Moss Green (89), with their respective transmission values at  $\lambda = 532 nm$  of 0.93, 0.11, 0.07, 0.06 and 0.73. The filter papers were inserted into the air gap and 16 traces recorded, additionally 16 traces were recorded without filter paper before and after the insertion as control group. The signal power was calculated for each traced and averaged over all 16 traces.

The experimental results (see Fig. 3.5) show a good correlation between signal power and transmissivity. The pre- and post-experimental control groups show a 13 % variation of the signal strength during the experiment. Nevertheless, the correlation between transmission and EMI signal strength still holds. As it is dependent on the

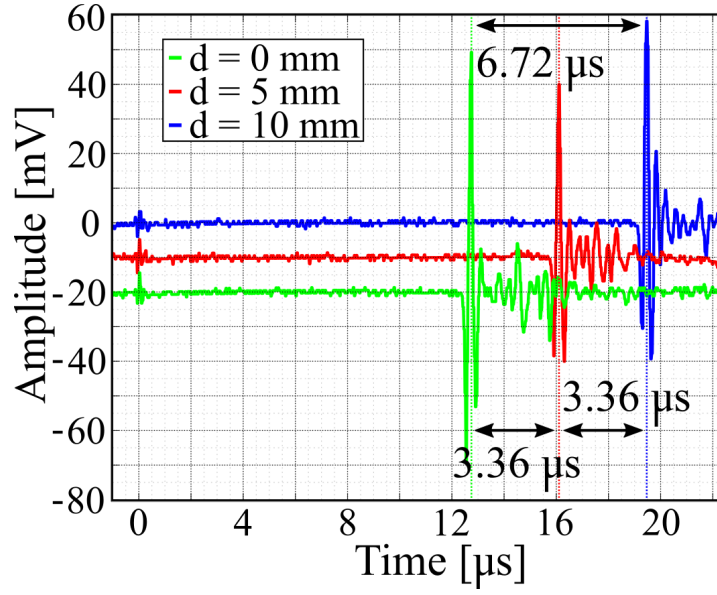


FIGURE 3.4: The traces recorded for an excitation point at different relative distances from the ultrasound transducer (offset by 10 mV each for visibility). The time difference in arrival time increases by  $\Delta t = 3.36 \mu\text{s}$  for every 5 mm distance.

light impinging the transducer surface the EMI could either be caused by photoacoustic or photoelectric mechanisms. The light generating the EMI is the laser light (532 nm) rather than the broadband flash lamps ( $750 \text{ nm} < \lambda < 900 \text{ nm}$ ). For the flash lamp light the transmission of the Lavender 60 and the Lavender 90 filter paper are higher, 0.8 and 0.75, respectively. Thus, the generated EMI signal power would also be higher. Whereas if it was EMI from the high voltage discharge during flash lamp triggering, there would be no correlation between filter cards and EMI signal power.

### 3.4 Commercial Ultrasound Transducers

Two commercially available immersion US transducer were used in this work, with centre frequencies of 2.25 MHz (I8-0216-S, Olympus) and 10 MHz (A315S, Olympus). The sensor element of the 2.25 MHz transducer had a diameter of  $d_{2.25} = 25.4 \text{ mm}$  and a total area of  $A_{2.25} = 506.7 \text{ mm}^2$ , the sensor element of the 10 MHz transducer had a diameter of  $d_{10} = 19.1 \text{ mm}$  and a total area of  $A_{10} = 286.5 \text{ mm}^2$ . Using these transducers PA waves with a broad bandwidth (see Fig. 3.3, b) were recorded, thus measuring the transducers' frequency content and sensitivity. A more in depth explanation will be given in 4.3.

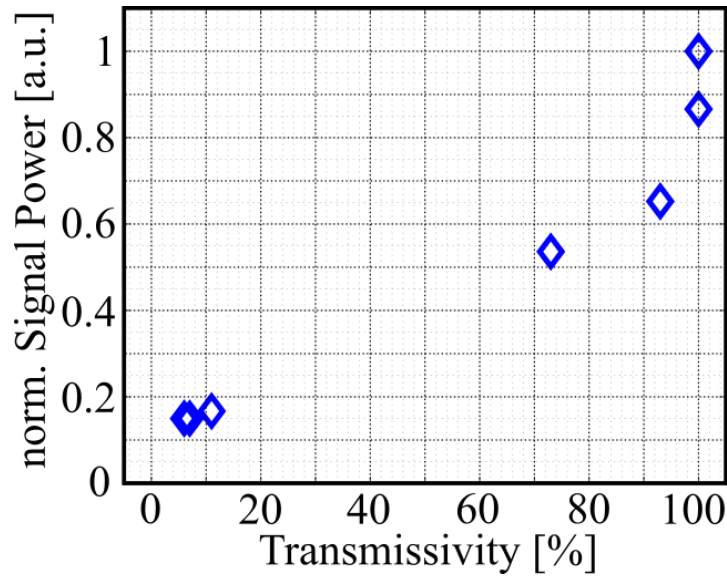


FIGURE 3.5: The graph shows the normalised signal power of the electromagnetic interference for different transmission values of the gap between transducer and gelatine phantom. A good correlation between signal power and transmissivity can be seen.

The PA waves were generated in an absorbing 8 % (m/m) gelatine phantom using the short pulsed Nd:YAG laser with a pulse energy  $E = 2.2 \text{ mJ}$  and a spot size  $d_s \approx 50 \mu\text{m}$ . The pulse energy was reduced to pulse energies ranging from  $220 \mu\text{J}$  to  $220 \text{ nJ}$  using neutral density filters (NEK01, Thorlabs). The phantom and the respective transducer were immersed in an oilbath for acoustic coupling (see Fig. 3.6). The transducers' output was amplified by +60 dB (DHPVA-200, FEMTO), averaged over 1024 samples and recorded using an oscilloscope (Agilent Infiniium) at a sampling frequency  $f_s = 500 \frac{\text{MSa}}{\text{s}}$ . The signal power  $P$  and the noise power  $N$  were calculated as described in 1.4.2. The sensitivity was measured by calculating the signal-to-noise ratio (SNR) of the recorded traces.

The trace of the PA wave recorded using the commercial 2.25 MHz transducer is shown in Fig. 3.7, a. Its PSD (see Fig. 3.7), b) shows a main peak at 2.4 MHz and a secondary peak at 7.5 MHz, with respective -6 dB bandwidths of 2.2 MHz and 2.25 MHz. For the first reduction in pulse energy (see Fig. 3.7, b, blue and red) the frequency content does not change in amplitude, for the following each reduction in pulse energy causes an equal relative reduction in the frequency content. The black line shows the averaged noise floor of the frequency content measurements. The noise floor was calculated similarly to the PSDs of the signals, by windowing over a part of the trace without signal (here: starting from  $t = 15 \mu\text{s}$ ). The FFT was then applied to this part resulting in the PSD of the noise floor. The calculated SNR is shown in Fig. 3.7, c for all measured pulse energies. The SNRs calculated range from 5 to 260 for the 2.25 MHz peak (blue) and 3 to 240 for the 7.5 MHz peak (red). As



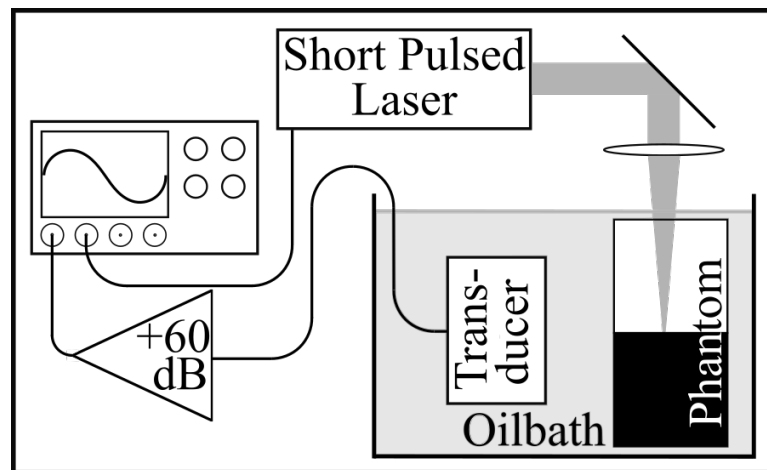


FIGURE 3.6: The output of a short-pulsed laser is focused on a gelatin target phantom and generated a PA signal. This is detected by the commercial transducer. The phantom and the array are acoustically coupled in an oilbath. The output of the latter is amplified and recorded using an oscilloscope.

stated previously the SNRs for pulse energies of  $E = 220 \mu\text{J}$  and  $E = 22 \mu\text{J}$  are similar. This is caused by non-linear effects such as ablation of the gelatine at the higher pulse energy. The graphs for the 2.4 MHz peak and the 7.5 MHz peak show the SNR linearly increasing with pulse energies. The low SNR at a pulse energy of  $E = 6.07 \mu\text{J}$  for 7.5 MHz is due to fluctuations in the spectral composition of the respective peak.

The trace of the PA wave recorded using the commercial 10 MHz transducer is shown in Fig. 3.8, a. It shows the initial PA response followed by a ring-down of the transducer. The frequency spectrum of the trace (see Fig. 3.8, b) shows a main peak at 8.5 MHz with a -6 dB bandwidth of 6.2 MHz. The spectrum is shown for the different pulse energies with the black line as the noise floor. As with the 2.25 MHz transducer the frequency content of the highest pulse energy ( $E = 220 \mu\text{J}$ ) is similar to the frequency content at  $E = 22 \mu\text{J}$  but slightly higher in this case. This can also be seen in the calculated SNRs (see Fig. 3.8, c), which range from 12 to 760. The SNR is shown to increase with the pulse energy up to a pulse energy of  $E = 22 \mu\text{J}$ , after which the SNR changes only slightly, potentially due to saturation of the sensor.

### 3.5 Photoacoustic scans

After the characterisation of the subsystems, the PA scanning system was used first to scan an injection of India ink in a clear gelatine matrix and then to image polyimide coated optical fibres in the x-y and x-z plane.

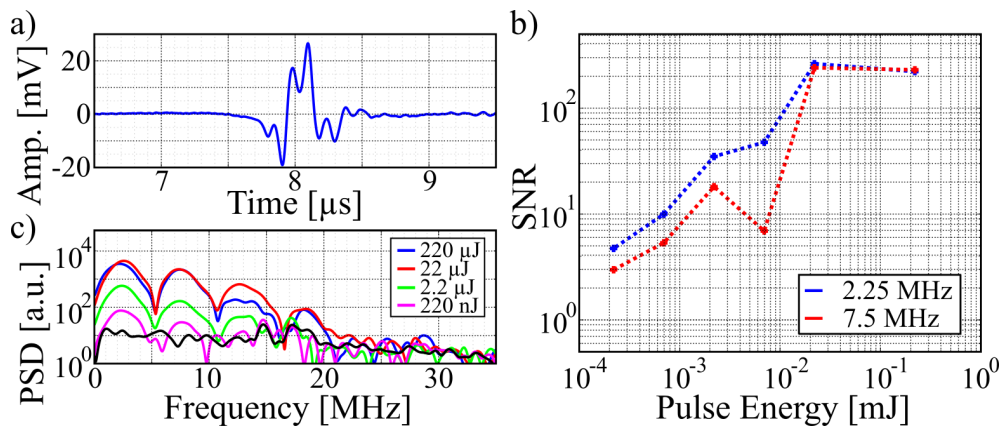


FIGURE 3.7: A trace (a) recorded using the Olympus 2.25 MHz transducer shows the superposition of two frequencies. These are also visible in the PSD (b) at 2.4 MHz and 7.5 MHz. The black line denotes the noise floor. The SNRs (c) calculated from the PSD ranges at the different pulse energy levels range from 3 to 260.

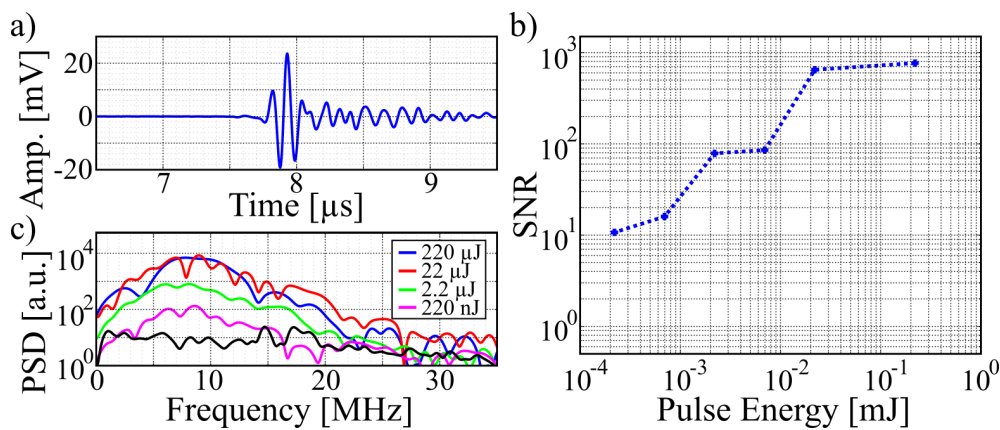


FIGURE 3.8: A trace (a) recorded using the Olympus 10 MHz transducer shows the initial PA response with a subsequent ring-down event. The PSD (b) shows a peak with a centre frequency of 8.5 MHz and a - 6 dB bandwidth of 6.2 MHz. The black line denotes the noise floor. The SNRs (c) calculated from the PSD ranges at the different pulse energy levels range from 12 to 760.

### 3.5.1 Ink Targets

The first test of the PA system was to scan over an injection of a known absorber, i.e. India Ink. A hollow needle (Microlance 0.6  $\times$  25 mm, Becton Dickinson) was used to inject a carbon particle solution (India Ink, Johnsons) into a clear gelatine matrix to show the application of the PA system to target scanning. India Ink has been shown

to work as absorber in PA experiments using wavelengths ranging from  $532\text{ nm} - 1064\text{ nm}$  at pulse energies of up to  $E = 190\text{ mJ}$  [126]–[128]. The localisation of the absorber by using a needle had some difficulties as the India ink was prone to bleed into the surrounding gelatine. The ink was injected into the phantom by manually puncturing the phantom and manually applying pressure to the syringe while simultaneously removing the needle from the phantom. This caused – probably by injecting too great a volume - the India ink to bleed into the surrounding gelatin. An improved ink injection method of using an x-y-stage and a syringe pump was dismissed in favour of changing to polyimide-coated fibres (see section 3.5.2). The phantom was placed on the motion controlled stage and acoustically coupled to the 10 MHz transducer using coupling gel at a distance of 6 mm to the focal spot (as shown in Fig. 3.1, c). The laser ( $E = 5.1\text{ mJ}$ ) was focused on the injected ink. Using the motion controller at a step size of  $\Delta x = 50\text{ }\mu\text{m}$  51 traces were recorded at a sampling frequency of  $f_s = 1\text{ }\frac{\text{GSa}}{\text{s}}$ . The signal power for each trace was calculated as stated in 1.4.2.

The normalised results of scanning over the injected ink are shown in Fig. 3.9. It shows a  $FWHM = 500\text{ }\mu\text{m}$ . This is smaller than the nominal diameter of the needle ( $d_N = 600\text{ }\mu\text{m}$ ) as it does not produce a circular hole but rather an elongated cut, which then is enclosed by the gelatine. The bleeding caused the generated PA signal to be blurred when scanned over compared to the expected sharp step if no bleeding was present. The blurring effect is caused by a gradual increase in absorber concentration due to the bleeding. Comparing the signal power at the target and the background noise power the system produced a scan with an SNR of 10. This shows that the presented PA system can be used to differentiate between an absorbing medium and a non-absorbing medium.

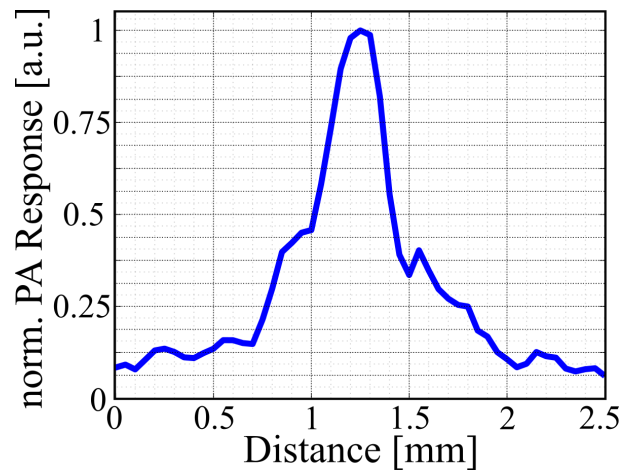


FIGURE 3.9: The normalised results of scanning over the ink injection show a  $FWHM = 500\text{ }\mu\text{m}$  and an SNR of 10.

### 3.5.2 Scans of polyimide coated Fibre

The problem with the ink injection was that the ink bleed into the surrounding gelatine matrix and that the ink injection process did not allow for a defined target diameter. Thus, polyimide coated fibre (PCF) was chosen as target material. Firstly, as the diameter of the PCF was unknown, it had to be measured. Afterwards, the PCF was embedded in a gelatine matrix and imaged over its cross-section as well as along the length of the fibre.

Firstly, the diameter of the unknown PCF  $d_{PCF}$  was measured optically by comparing the PCF to a single-mode fibre of known diameter ( $d_{SM} = 125 \mu m$ ). Both fibres were simultaneously imaged under a microscope (Axioplan 2 imaging, Zeiss) using a 20x objective (20x, 0.40 NA, 2D Epiplan). The image (see Fig. 3.10) was loaded into an image and graphics editor programme (INKSCAPE, Inkscape Project). The width of the fibre was measured (in pixels) at three locations to compensate for image distortions near the edge of the image. These optical aberrations can be avoided when the fibres would have been cleaved and their diameters compared. The diameter of the fibre was calculated from the pixel values and the known diameter of the second fibre. The results show that the width ranges from  $d_{PCF} = 98 \mu m$  to  $d_{PCF} = 100 \mu m$ . A diameter of  $d_{PCF} = 99.33 \pm 0.94 \mu m$  matches commercially available polyimide coated fibre with a cladding diameter of  $d_{CD} = 80 \mu m$  and a coating diameter of  $d_{PCF} \approx 100 \mu m$ .

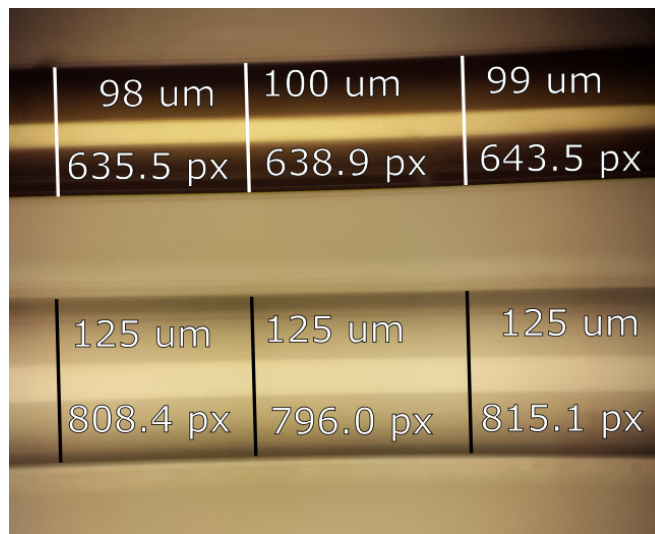


FIGURE 3.10: A microscope picture comparing a  $125 \mu m$  single-mode fibre (bottom) to the PCF (top) of unknown diameter. From this the diameter of the polyimide coated fibre was measured as  $d_{PM} = 100 \mu m$ .

With the diameter of the PCF known, the first application of the PA system was to

scan its cross-section. For this, a 30 mm long piece of PCF was embedded in a clear 8 % gelatine phantom ( $40 \times 40 \times 25 \text{ mm}^3$ ). The phantom was placed on the motion controller which was actuated using the LabVIEW programme with a step-length of  $\Delta x = 20 \text{ }\mu\text{m}$  and  $\Delta z = 40 \text{ }\mu\text{m}$ , with a total of  $51 \times 26$  steps. The ultrasound transducer (10 MHz centre frequency) was acoustically coupled to the phantom using coupling gel. The laser focal plane was adjusted so that it was close to the embedded PCF with a pulse energy of  $E_{PLS} = 5 \text{ mJ}$  and a pulse-repetition-frequency of  $PRF = 10 \text{ Hz}$ . The transducer was positioned at a distance of 15 mm to the laser spot. The trace of the US transducer was recorded at every scan-point using a MATLAB script to automatically read from the oscilloscope (Agilent Infiniium,  $f_S = 500 \frac{\text{MSa}}{\text{s}}$ ). It was then filtered using a high-pass filter at  $f_{cut} = 50 \text{ kHz}$ . The signal power was calculated as described in 1.4.2 by using  $f_{low} = 6 \text{ MHz}$  as the lower boundary and  $f_{high} = 9 \text{ MHz}$  as the upper boundary at each scan position. The resulting power was normalised, and interpolated (using spline interpolation) to increase the resolution of the resulting image from  $51 \times 26$  to  $451 \times 226$ .

The scan image (Fig. 3.11) shows only the semi-elliptical cross-section as it was only partially imaged but it would extend past the imaged FoV. It shows the diameter (FWHM) of the embedded PCF to be of  $d_x = 250 \text{ }\mu\text{m}$  in the x-direction and  $d_z = 500 \text{ }\mu\text{m}$  (estimated from symmetry condition) in the z-direction. The signal degrades faster in the x-direction ("Width") compared to the z-direction due to the longer Rayleigh length ( $l_R \approx 2 \text{ mm}$ ) of the focal spot compared to its spot size. The blue and red cross denote the origin of the "on-target" and "off-target" traces in Fig. 3.12 (top), respectively. The former shows an amplitude of  $V_{PP} = 300 \text{ mV}$ . The FFT of the traces windowed over the PA response are shown in Fig. 3.12 (bottom). This shows the signal of the centre of the PCF to have an SNR of 300.

### PCF - Scan along the Length

The limitations of the PA system were tested by scanning over a wider field of interest, while evaluating the time it takes to perform this scan. To test the limits of this PA system, a large area of  $6 \text{ mm} \times 6 \text{ mm}$  of a PCF embedded in a gelatine phantom ( $40 \times 40 \times 30 \text{ mm}^3$ ) was scanned. The step size in both direction was  $\Delta x = \Delta y = 75 \text{ }\mu\text{m}$ . The focal plane of the focused laser was brought near the target. The pulse energy was set to  $E_{PLS} = 5.2 \text{ mJ}$ . The US transducer ( $f_{centre} = 10 \text{ MHz}$ ) was acoustically coupled to the phantom using coupling gel. The amplified (+60 dB) trace of the US transducer was recorded at every scan-point using a MATLAB script to automatically read from the oscilloscope (Agilent Infiniium) with a sampling frequency of  $f_S = 500 \frac{\text{MSa}}{\text{s}}$ . Before the signal power was calculated as described in 1.4.2, it was filtered using a high-pass filter at  $f_{cut} = 50 \text{ kHz}$ . The normalised signal power was then plotted as an image. Additionally, the time difference between each recorded trace was measured and recorded.

The normalised scan image (see Fig. 3.13, a) shows the PCF crossing the field of view. The change in signal strength is caused by the PCF crossing in and out of the focal

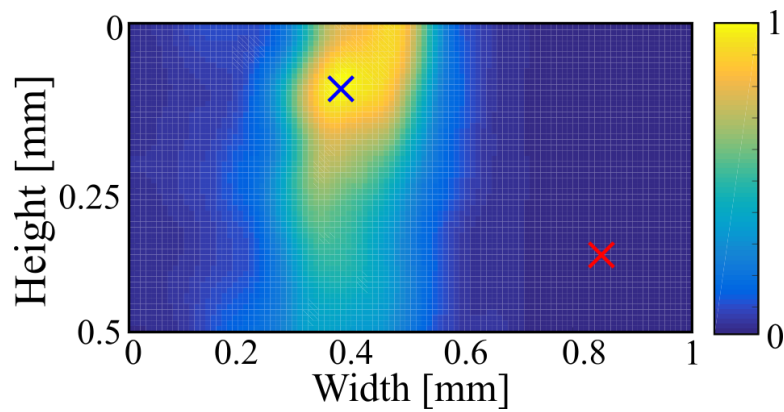


FIGURE 3.11: The scan over the cross-section of the PCF shows only the semi-elliptical cross-section as it was only partially imaged. It extends past the FoV (for  $h < 0$  mm) symmetrically to the imaged part of the cross-section. The cross-section would be elliptical as the Rayleigh length of the focal spot causes elongation in the "Height" dimension. Thus, it shows x-z dimensions (FWHM) of  $250 \mu\text{m}$  and  $500 \mu\text{m}$ , in the "Width" and "Height" dimensions respectively. The blue cross marks the origin of the "on-target" trace and the red cross the origin of the "off-target" trace shown in Fig. 3.12.

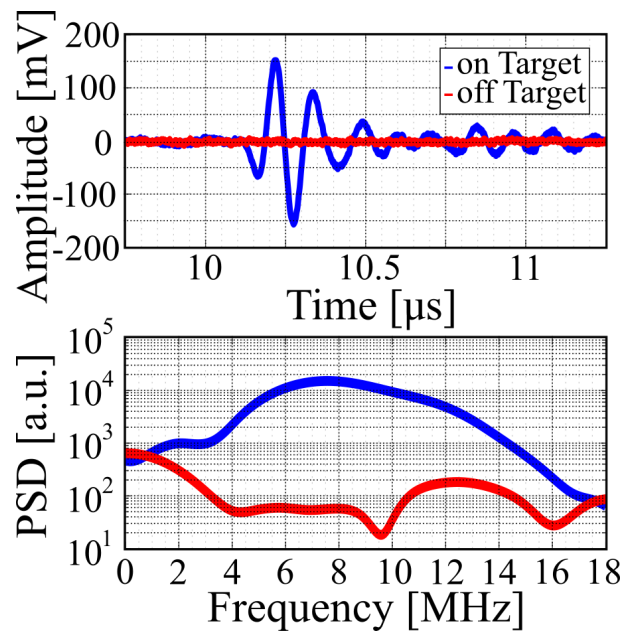


FIGURE 3.12: The trace recorded in the centre of the fibre (blue) has an amplitude of  $300 V_{PP}$ . This results in an SNR of 300 compared to the off-target trace (red).

plane, as it was not perfectly parallel to the focal plane. As no averages were taken the scan shows a prominent bright spot caused by noise. The on- and off-target traces taken from the markers (blue and red, respectively) in Fig. 3.13, a are shown in Fig. 3.13, b with an amplitude of  $700\text{ mV}_{pp}$ . The resulting PSDs show an SNR of 70. Evaluating the time recorded, the full scan over a  $6\text{ mm} \times 6\text{ mm}$  ( $81\text{ steps} \times 81\text{ steps}$ ) field of view (FoV) took  $t = 594\text{ min}$ , i.e.  $t \approx 10\text{ h}$ .

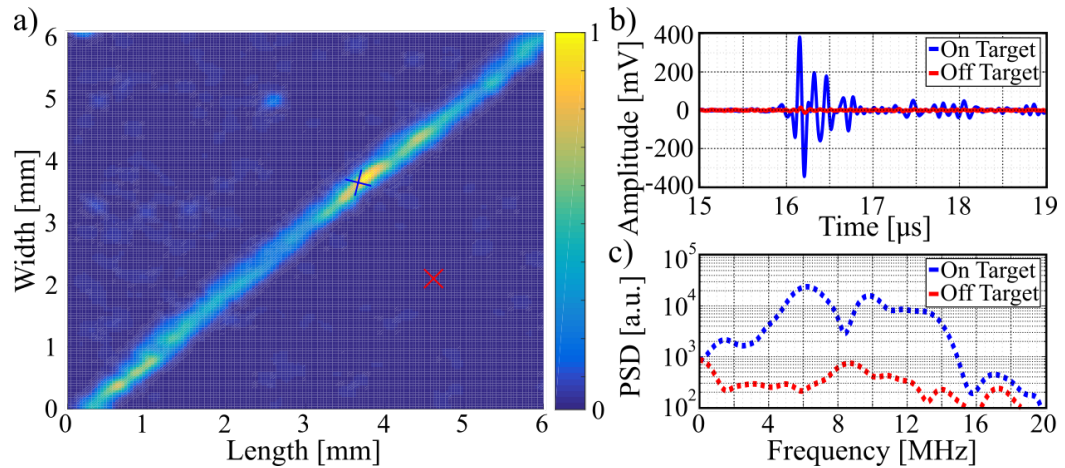


FIGURE 3.13: The recorded scan image (a) shows the fibre crossing the FoV with some noise signals (e.g. at width = 5 mm, length = 3 mm) due to lack of averaging. Furthermore, the origin of the traces for on-target and off-target (b, blue & red) are marked. The on-target traces shows an amplitude of  $700\text{ mV}_{pp}$ . From the PSD an SNR of 70 can be calculated. As the fibre was oblique to the focal plane the signal strength changed over the course of the FoV, where the fibre enters and exits the focal plane (around point marked with blue cross).

### 3.6 Discussion

This chapter presented the preliminary PA system, which was used to evaluate how PA responses could be generated, recorded and evaluated. This included building and optimising the test stand, writing software for automation of micro-meter stage movements, signal acquisition and data evaluation in LabVIEW and MATLAB. The scan of the ink injection showed the ability of the system to differentiate between absorbing and non-absorbing materials. Furthermore, it showed that the injected ink bleeds into the surrounding gelatine matrix delocalising the target. The process of injecting the ink can be improved by moving from a manual process to using an x-y-stage and a syringe pump to inject a controlled volume over a controlled distance. As the syringe creates an elongated cut rather than a hole a good starting point for the injected volume would be a fraction (such as 25 %) of a cylinder with a

diameter of the needle diameter. For the above used  $600 \mu\text{m}$  needle this would e.g. be  $0.7 \frac{\mu\text{l}}{\text{cm}}$ . Additionally, the bleeding can be reduced by concentrating the injected India Ink e.g. by reducing the water content by evaporation. Using polyimide fibre proved feasible for localising the target absorber in a PA scan experiment. The scan over a larger FoV along the top of the fibre showed a potential need for averaging. It also made clear that the system needs to be heavily improved as the acquisition time of  $t = 10 \text{ h}$  is far too great.

The laser system has a short pulsewidth of  $\tau = 8.15 \text{ ns}$ . This results in a PA response with a quasi-constant PSD for frequencies  $f < 25 \text{ MHz}$  near the source. Farther away the frequency content of the generated wave reduces as shown in Chapter 2. The low PRF of  $10 \text{ Hz}$  is problematic as any averaging would greatly increase the already long acquisition times. With an unattenuated output of  $E_{Pl}^{max} = 278 \text{ mJ}$  per pulse, the laser needs heavy attenuation to stay within the MPE of  $E_{MPE} = 0.1 \frac{\text{J}}{\text{cm}^2}$ . Thus, for a focal point with a spot size of  $20 \mu\text{m}$  the maximum permissible pulse energy is  $E = 1.256 \mu\text{J}$ . The laser output power would therefore require an attenuation of a factor of 2000, which is approximately equal to an OD 3.3 optical density filter.

The commercial ultrasound transducers showed centre frequencies of 2.4 and 8 MHz with -6 dB bandwidths of 2.4 and 6.5 MHz, respectively. Due to their large diameters of  $d_{2.25} = 25.4 \text{ mm}$  and  $d_{10} = 19.1 \text{ mm}$  these ultrasound transducers have large near field distances (according to Fig. 2.9) of  $N \approx 40 \text{ mm}$  and  $N \approx 30 \text{ mm}$ , respectively. The near-field distance for detecting US transducers denotes the distance where the destructive interference is negligibly small. This destructive interference is caused by impinging of a radial pressure wave on the detection surface of a transducer with finite diameter. Their size and their near-field distance limit the use of these commercial transducers as a greater distance from the PA source relates to more signal losses due to attenuation.



## Chapter 4

# Miniaturisation of Piezoelectric Ultrasound Transducers

The first step towards a miniaturised PA system focuses on the miniaturisation of the ultrasound detectors. To achieve this thin-film AlN based PMUTs were chosen. These were chosen due to their ease of production and high degree of customisation. Three custom PMUT arrays were designed by the author of this thesis and fabricated using PiezoMUMPS (MEMSCAP, Inc.) a cost-effective multi-user MEMS process. The PMUT arrays were characterised prior to being incorporated into the existing PA test setup, where their overall performance and that of their individual subgroups were tested. Additionally, they were deployed in phantom experiments similar to the ones shown in the previous chapter. Finally, the performance of the PMUT arrays was compared against the commercial transducers (2.25 MHz & 10 MHz).

### 4.1 Design of the PMUT arrays

Three PMUT array types were designed. The first, the single-type PMUT array, was designed as an array of 8-by-8 membrane transducers with a diameter of 240  $\mu\text{m}$ . These are grouped in differently sized subgroups which can be electrically addressed in groups of 4, 16 and 32. The second design, multi-type array, consists of membrane transducers with diameters ranging from 235  $\mu\text{m}$  to 500  $\mu\text{m}$ , resulting in multiple centre frequencies and an overall increased bandwidth of the entire array. The subgroups with their respective diameters can be addressed individually. The third array, the bar-type array, consist of differently sized bar transducers to test transducers of a different geometry. Each subgroups consisted of several transducers of the same geometry (shape, diameter) to increase the sensing area at a chosen resonance frequency. This enables production of transducers at frequencies higher than achievable with the membrane design using the same fabrication process. The mechanical resonance frequencies of the different base elements, thin discs for the single-type and the multi-type array and a bar suspended over a rectangular hole for the bar-type array, were simulated using COMSOL for different values of the main dimension. The results were used to choose compatible dimensions. For the second and the third design the results were also used to compensate for different surface areas and expected in-medium attenuation by altering the number of transducer

elements.

The designs were then fabricated using PiezoMUMPS, a cost-efficient multi-user process offered by MEMSCAP, Inc. In this process a 500 nm piezoelectric layer of AlN ( $d_{33}$  crystall orientation) is brought onto a doped 10  $\mu\text{m}$  silicon-on-insulator (SOI) device layer. This device layer acts as a bottom electrode for the piezoelectric AlN layer. The top electrode is a 1  $\mu\text{m}$  thick aluminium layer deposited onto the AlN layer using a 20 nm layer of chrome as interface. An oxide mask can be defined to electrically insulated the signal route from the top electrode from the doped SoI layer. This multi-user process restricted the design, as etching dimensions through the device layer were restricted to a minimum of  $d_{min} = 200 \mu\text{m}$  with a stated undercut of  $r_{cut} < 50 \mu\text{m}$ . A more in-depth explanation of the PMUT fabrication is described in 4.1.4.

#### 4.1.1 Design of single-element membrane transducers

The single-type transducer array was designed as a PMUT array of 8 x 8 membrane transducer elements. The diameter was chosen by simulating the resonance frequencies of a single transducer element with a height of 11.5  $\mu\text{m}$  in water using COMSOL. The transducer elements were modelled as clamped disks consisting of a  $d = 10 \mu\text{m}$  Si - layer, a  $d = 1.0 \mu\text{m}$  Al - layer and a  $d = 0.5 \mu\text{m}$  AlN - layer immersed in water. Here, only the Si - layer was clamped. The results of the first resonance frequency was mapped compared to the diameter as shown in Fig. 4.1. It shows the decline of the first resonance frequency with increasing diameter for diameters ranging from 150  $\mu\text{m}$  to 550  $\mu\text{m}$ . From this graph it can be seen that the frequency of a membrane transducer with diameters ranging from 200  $\mu\text{m}$  to 300  $\mu\text{m}$  ranges from 1.6 MHz to 0.7 MHz. An element size of  $d_{el} = 240 \mu\text{m}$  was chosen, so as to get a comparably high frequency from the minimum design rule backside etch diameter (200  $\mu\text{m}$ ), including an expected undercut of  $r_{ex} = 20 \mu\text{m}$ . This results in a centre frequency of  $f_c = 1.25 \text{ MHz}$ .

The array was designed with 64 elements of 240  $\mu\text{m}$  diameter. The layout in Fig. 4.2 shows the grouping of the individual elements in four groups with four elements each (see Fig. 4.2, A), one group with 16 elements (see Fig. 4.2, B) and another with 32 elements (see Fig. 4.2, C). This way the total transducer area can be easily varied by addressing different groups. Furthermore, this allows the testing of the subgroups of the array for phased array applications. Each group is addressed by three bond pads. This number was required as in previous tests - on older, different designs from MEMSCAP, Ltd. - showed that there was a possibility of the bond wires unbonding or breaking (about 1 in 7). The bright blue triplet of bond pads is for the grounding of the transducer elements. The total active area  $A_{tot}$  of the single-type PMUT array can be calculated using equation 4.1:

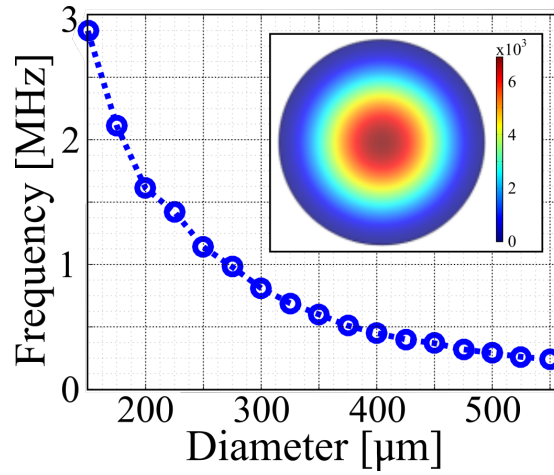


FIGURE 4.1: The resonance frequency of the mode shape shown in the inset of a clamped disc was simulated for different diameters using COMSOL. The displacement is colour-coded in the inset.

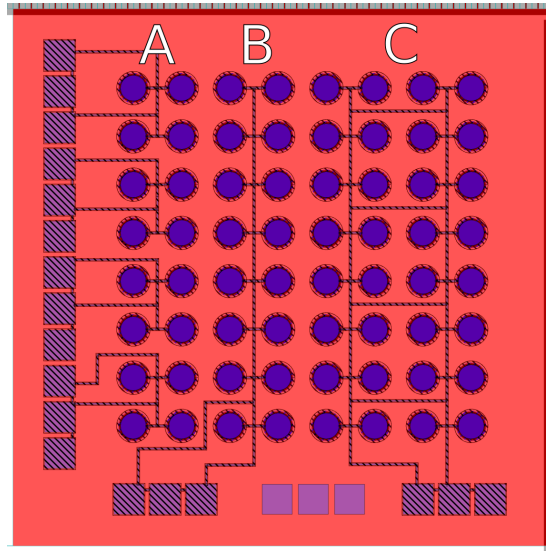


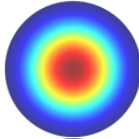
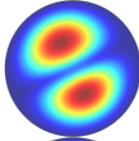
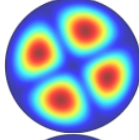
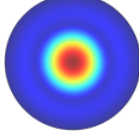
FIGURE 4.2: The finalised design of the single-type transducer array shows the 64 transducer elements grouped in sub-groups of 4 elements (A), 16 elements (B) and 32 elements (C).

$$\begin{aligned}
 A_{tot} &= n \cdot A_{ind} \\
 A_{tot} &= n \cdot d_{ind}^2 \cdot \frac{1}{4} \cdot \pi \\
 A_{tot} &= 64 \cdot (0.24 \cdot mm)^2 \cdot \frac{1}{4} \pi \\
 A_{tot} &= 64 \cdot 4.373 \cdot 10^{-2} mm^2 \\
 A_{tot} &= 2.895 mm^2
 \end{aligned} \tag{4.1}$$

with the total number of transducer elements  $n$ , the area  $A_{ind}$  and the diameter  $d_{ind}$  of an individual element. The total active area of the single-type array is  $A_{tot} = 2.895 \text{ mm}^2$ . The 4 mm x 4 mm array chip has an area of  $A_{chip} = 16 \text{ mm}^2$ . The fill factor is 18.1 %. The low fill factor is limited by the strict design limitations of the multi-user process. This was done to ensure fabrication success in a process that is not optimised for the transducer geometries.

The simulations of the designed membrane transducers in water show a first resonance frequency of 1.18 MHz and a second modal frequency of 3.21 MHz (see Table 4.1). The third and fourth modal frequency are very close with frequencies of 5.69 MHz and 5.77 MHz, respectively. The bandwidth of these modal frequencies will cause the peaks to merge and widen due to overlap. The table shows opposite phases of displacement for adjacent peaks for numbers 2 and 3. Thus, this combination of phase and anti-phase reduces the resulting electric signal. The effects of this can be seen in the photo-acoustic characterisation of this array (see subsection ), where the main frequency responses are of type  $\langle 0,1 \rangle$  and  $\langle 0,2 \rangle$ , see numbers 1 and 4, respectively.

TABLE 4.1: The resonance frequencies are shown for the different modes and their respective shapes.

No.	Mode Shape	Image	Resonance Frequency [MHz]
1	$\langle 0,1 \rangle$		1.18
2	$\langle 1,1 \rangle$		3.21
3	$\langle 2,1 \rangle$		5.69
4	$\langle 0,2 \rangle$		5.77

The relative frequencies of higher order modes compared to the first resonance mode can be derived using the Bessel equations. Fig. 4.3 shows the tension forces resulting on an infinitesimal small element of a thin (constant thickness  $t$ ), limp (material shows no flexural rigidity) membrane. The element is at a distance  $r$  from the centre of the membrane, has a length of  $dr$  and spans over an angle  $d\theta$ . The tension force on

each side of the parallelogram is calculated with the tension per unit length  $\mathfrak{T}$ . The surface density is introduced to avoid confusion between the  $t$  for time and the  $t$  for thickness, with  $\rho_s = \rho t$  [129]. The transverse wave propagation speed is calculated from the surface density as  $\sqrt{\frac{\mathfrak{T}}{\rho_s c}}$  [129].

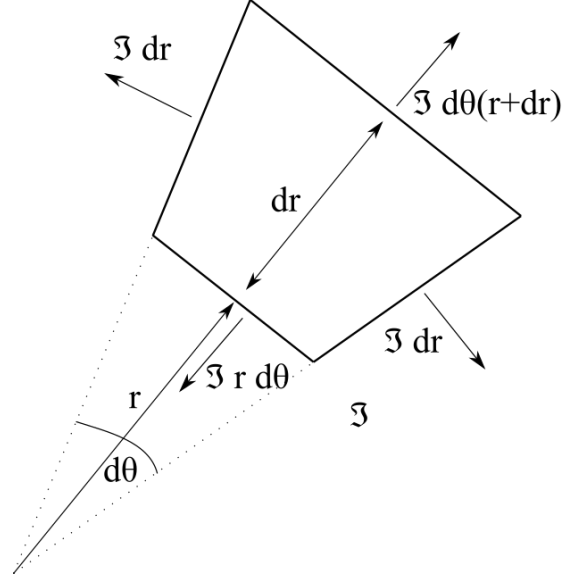


FIGURE 4.3: The resulting tension forces resulting on an infinitesimal small element of a thin, limp membrane are depicted.

The resulting vertical force in the radial direction  $F_{z,r}$  and perpendicular to the radial direction  $F_{z,\theta}$  can be calculated as [129]:

$$\begin{aligned} F_{z,r} &= \frac{\mathfrak{T}}{r} \frac{\partial}{\partial r} \left( r \frac{\partial z}{\partial r} \right) r dr d\theta \\ F_{z,\theta} &= \frac{\mathfrak{T}}{r^2} \frac{\partial^2 z}{\partial \theta^2} r dr d\theta \end{aligned} \quad (4.2)$$

Combining equations 4.2 and equating it to the vertical acceleration times the mass of the infinitesimal small element  $\rho_s dA = \rho_s(r d\theta) dr$ , while converting the second-order differential equations and imposing a harmonic time dependence  $z(r, \theta, t) = R(r) \Theta(\theta) e^{j\omega t}$ . This gives two normal independent differential equations, that are connected by  $k^2$  [129]:

$$\frac{r^2}{R} \left( \frac{d^2 R}{dr^2} + \frac{1}{r} \frac{dR}{dr} \right) + k^2 r^2 = -\frac{1}{\Theta} \frac{d^2 \Theta}{d\theta^2} \quad (4.3)$$

From the angular dependence, i.e.  $\frac{d^2\Theta}{d\theta^2} + m^2\Theta = 0$ , it can be derived that the solution is periodical with  $2\pi$  and thus with  $n = 0, 1, 2, \dots$  of [129]:

$$\Theta_m(\theta) = \Theta_m(2\pi n \theta) \quad (4.4)$$

The radial dependence can be calculated from substituting  $\frac{d^2\Theta}{d\theta^2} + m^2\Theta = 0$  in eq. 4.3, resulting in [129]:

$$\frac{d^2R}{dr^2} + \frac{1}{r} \frac{dR}{dr} \left( k^2 - \frac{m^2}{r^2} \right) R = 0 \quad (4.5)$$

Applying the Frobenius method creating solutions of a power series type to eq. 4.5, one for each integer  $m$ , results in the Bessel's equations [129]. The solutions to which are known as Bessel's functions  $J_m(k_{m,n} r)$ , where the script  $m$  refers to the respective  $\Theta_m(\theta)$ . As described by the parameter  $k_{m,n}$  it is described by two integers; the azimuthal variation  $m$  and the number of successive zero-crossings  $n$  [129]. For a circular membrane the radial boundary condition dictates that there is zero displacement at its radius  $a$ , i.e.  $J_m(k_{m,n} a) = 0$ . Thus, the modal frequency  $f_{m,n}$  can be estimated from the Bessel's functions zero-crossing  $j_{m,n}$  and the speed of the transverse waves  $c$  as [129]:

$$f_{m,n} = \frac{j_{m,n} c}{2\pi a} \quad (4.6)$$

Table 4.2 shows the Bessel's functions zero-crossing  $j_{m,n}$  and the relative (to the first mode) resonance frequency is shown for the first four modes. The relative frequencies show that e.g. the resonance frequency for mode  $\langle 1,1 \rangle$   $f_{1,1}$  would be  $f_{1,1} = 1.59 \cdot f_{0,1}$ . For the simulated resonance frequencies of the single-type array (see Table 4.1) this does not hold true as the following resonance frequencies are all under-estimated. This could be caused by the disregard of the surrounding medium of the membrane.

TABLE 4.2: The Bessel's functions zero-crossing  $j_{m,n}$  and the relative (to the first mode) resonance frequency is shown for the first four modes.

No.	Mode	$j_{m,n}$	$f_{m,n} / f_{0,1}$
1	0,1	2.4048	1
2	1,1	3.8317	1.593
3	2,1	5.1536	2.136
4	0,2	5.5200	2.295

#### 4.1.2 Design of multi-type transducer array

The multi-type transducer array was designed as an array of four subgroups of membrane transducers with different diameters, resulting in a larger overall bandwidth when combined in this customised arrangement. The array diameters

were chosen so that the overall active surface area in the sub-arrays is similar. Equally, the ratio between the resonance frequencies was kept constant to achieve equally spaced resonance peaks. The biggest membrane diameter was set to  $d = 500 \mu m$  as resulting in a resonance frequency for the first sub-array of  $f_1 = 300 \text{ kHz}$  (see Fig. 4.1). Using equation 4.1 with  $n = 1$ , the surface area of each transducer element is  $A_{500} = 0.196 \text{ mm}^2$ . The diameter of the smallest transducer was chosen as the minimally achievable (design specifications)  $d = 235 \mu m$ , resulting in a larger resonance frequency for the fourth sub-array comparable to the single-type array with  $f_4 = 1.4 \text{ MHz}$ . This gives a ratio of the resonance frequencies of  $RF_{tot} = \frac{f_4}{f_1} = 4.666$ . The resonance frequencies of the other two sub-arrays are chosen so that all resonance frequencies are spaced evenly (logarithmic). Therefore, the ratio between elements of subsequent diameters for the four different sub-arrays should be:

$$RF_{ind} = \frac{RF_{tot}}{3}$$

$$RF_{ind} = 1.556$$

The resonance frequencies for the second (equation 4.7) and third (equation 4.8) sub-array are calculated as:

$$f_2 = RF_{ind} \cdot f_1$$

$$f_2 = 467 \text{ kHz} \quad (4.7)$$

$$f_3 = RF_{ind} \cdot f_2$$

$$f_3 = 731 \text{ kHz} \quad (4.8)$$

The membrane diameter for the sub-arrays 2 and 3 were chosen as  $d_2 = 395 \mu m$  and  $d_3 = 310 \mu m$ , with a surface of  $A_2 = 0.123 \text{ mm}^2$  and  $A_3 = 0.0755 \text{ mm}^2$ , respectively. The values simulated for these diameters (see Fig. 4.1) are  $f_2 = 0.45 \text{ MHz}$  and  $f_3 = 0.75 \text{ MHz}$ . The overall surface area was adjusted by changing the number of transducer elements in each sub-array. The number of transducer elements was increased for the first and second sub-array to increase the overall fill-factor of the multi-type PMUT array (see Fig. 4.4). This increases the overall active area of the sub-arrays with larger diameters to about 1.5x the area of the other two sub-arrays. The resulting total active area is  $A_{tot} = 2.57 \text{ mm}^2$ , resulting in a fill-factor of 16.1 %. The sub-arrays with a diameter of  $d_1 = 500 \mu m$  was additionally designed to have an adjustable focus. They were designed to heat up and alter their curvature by applying a DC-voltage through the SOI layer of the membranes, thus, changing the focus. This sub-array was electrically isolated from the rest of the chip as shown in Fig. 4.4, D. The DC-voltage would be applied to the elongated, light blue bond pads, one of which would also function as ground pad for the piezoelectric signal.

The simulated mode shapes and their respective frequencies of the transducer of this design are shown in Table 4.3. The main resonance frequencies are at 1.25 MHz, 0.61 MHz, 0.32 MHz and 0.16 MHz for diameters of  $d = 235 \mu m$ ,  $d = 310 \mu m$ ,

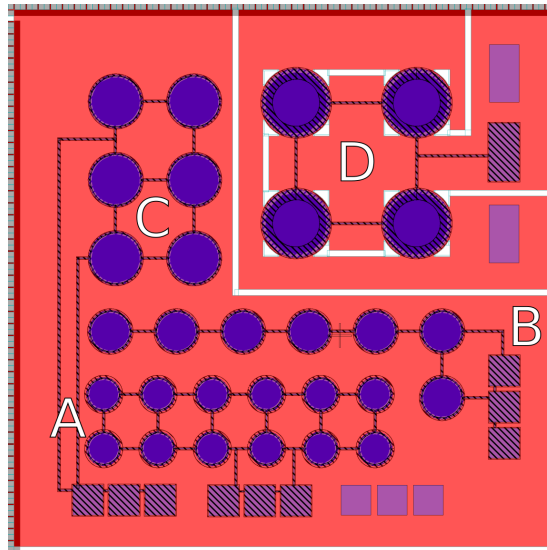
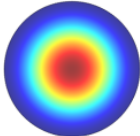
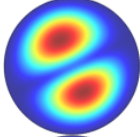
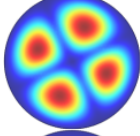
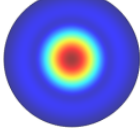


FIGURE 4.4: The finalised design of the multi-type transducer array shows the sub-arrays of membrane transducer elements of different diameters. The sub-arrays have 12 elements with a diameter of  $d = 235 \mu\text{m}$  (A),  $d = 310 \mu\text{m}$  (B),  $d = 395 \mu\text{m}$  (C) and  $d = 500 \mu\text{m}$  (D).

$d = 395 \mu\text{m}$  and  $d = 500 \mu\text{m}$ , respectively. As with the single-element transducer array, the modal frequencies number 3 and 4 are very close to each other, potentially causing a broad frequency response due to overlap. As for the single-type design, the adjacent phase and anti-phase displacement peaks result in reduced signal strength for these modes. While sub-arrays A, C and D are designed in a rectangular setup. Sub-array B is arranged in a line due to spatial constraints. This however should not negatively impact the detected signal if the array is used for detecting signals at distance of  $> 5 \text{ mm}$ . This is the NFD for arrays with a longest dimension of  $4 \text{ mm}$  (length of line). Comparing the resonance frequencies to the relative values evaluated from the Bessel's function (see Table 4.2) it again shows that the values do not hold true. The higher order resonance frequencies are all under-estimated potentially due to the disregard of the surrounding medium of the membrane.



TABLE 4.3: The resonance frequency, surface area for each element and in total and the number of elements are shown for each transducer sub-array.

No.	Mode Shape	Image $d = 235 \mu m$	f in MHz $d = 310 \mu m$	f in MHz $d = 395 \mu m$	f in MHz $d = 500 \mu m$	f in MHz
1	<0,1>		1.25	0.61	0.32	0.16
2	<1,1>		3.36	1.76	0.95	0.51
3	<2,1>		5.93	2.93	1.86	1.03
4	<0,2>		6.00	2.99	2.14	1.20

### 4.1.3 Design of bar transducers

The two previously presented arrays are made from membrane transducer elements with resonance frequencies of  $f_{res} \leq 1.4 \text{ MHz}$ . As these transducers are already designed very close to design restrictions of the multi-user fabrication process, another approach to design higher frequency ( $f \geq 2 \text{ MHz}$ ) is required. These design restrictions require minimum through hole dimensions of  $> 200 \mu m$  in all directions. For the third array, the membrane disc approach is replaced by utilising bars as resonating elements. These bars (shown in Fig. 4.5, red) are suspended over the through-hole at an angle of  $45^\circ$  enabling change in length and thus resonance frequency. The width of the bar  $H_2 = 50 \mu m$ , while the height of the triangle shaped through hole  $H_1$  is altered, changing the effective length of the bar and with that the resonance frequency. This structure (see Fig. 4.5) was simulated for different values of  $H_1$  using COMSOL. The resonance frequency decreases with the distance of the bar to base,  $H_1$  (see Fig. 4.6).

The bar array consists of three individually addressable sub-arrays with varying sizes of  $H_1$ . The first was chosen with the lowest centre frequency of  $f_1 = 3.65 \text{ MHz}$  at  $H_1 = 65 \mu m$ . The highest centre frequency was set at  $f_3 = 7.11 \text{ MHz}$  with  $H_1 = 28.5 \mu m$ .  $H_1$  was capped at that value as smaller values would potentially have made production unfeasible due to the small dimensions as well as the uncertainty of the undercut. The second frequency  $f_2$  was set at a resonance frequency in the

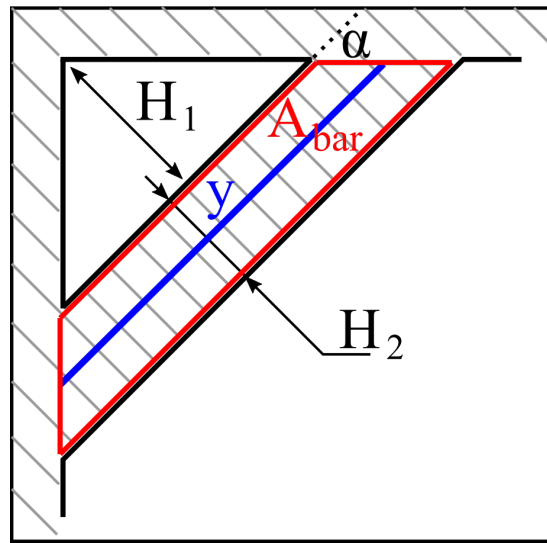


FIGURE 4.5: The device layer (grey lines) is suspended over the through hole (white), patterned to create a beam structure of width  $H_2 = 50 \mu\text{m}$  at a distance of  $H_1$  from the corner of the hole.

middle between  $f_1$  and  $f_3$ , with  $f_2 = 5.09 \text{ MHz}$ .

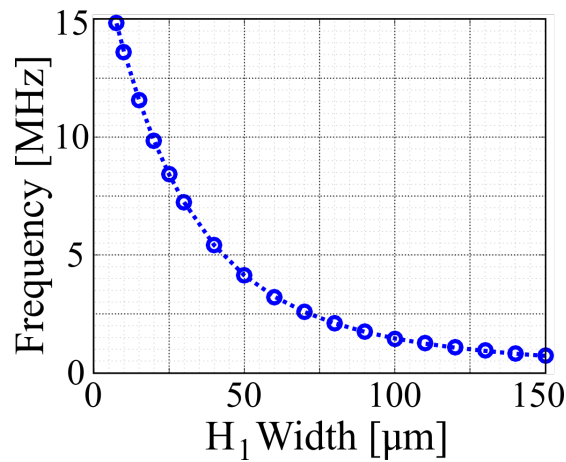


FIGURE 4.6: The resonance frequency of a suspended bar was simulated for different values for  $H_1$  using COMSOL.

The  $H_1$  dimension for the second sub-array was set to  $H_1 = 43 \mu\text{m}$  resulting in a frequency of  $f_2 = 5.18 \text{ MHz}$ . The active area of the bar transducers can be calculated as the area of the parallelogram  $A_{bar}$  (see Fig. 4.5) with the mid-line length  $y$  and the height  $H_2$  using:

$$A_{bar} = H_2 \cdot y \quad (4.9)$$

The mid-line length  $y$  can be calculated from the length of the side of the triangular through-hole  $x$ , half the length of the beam along the edge of the through-hole  $\frac{\sqrt{2}}{2}H_2$  and the angle of the triangular through-hole  $\alpha = 45^\circ$ . With  $\cos(\alpha) = \frac{\sqrt{2}}{2}$ , the length can be calculated as:

$$\begin{aligned} y &= \sqrt{2 \left[ \frac{\sqrt{2}}{2} \cdot H_2 + x \right]^2} \\ y &= \sqrt{2 \left[ \frac{\sqrt{2}}{2} \cdot H_2 + H_1 \cos(\alpha) \right]^2} \\ y &= \sqrt[4]{2} \cdot H_2 + H_1 \end{aligned} \quad (4.10)$$

Using eq. 4.10 in eq. 4.9 the active area of the bar transducer elements can be calculated as shown in equation 4.11:

$$A_{bar} = \sqrt[4]{2} \cdot H_2 \cdot [H_2 + H_1] \quad (4.11)$$

As with the multi-type array it was attempted to keep the active surface area of the sub-arrays of the bar-array equal by changing the amount of transducer elements in each sub-array. Every through-hole has multiple transducer elements, as the bars are at an angle of  $45^\circ$ . There are two bars with an  $H_1$  dimension of  $H_1 = 65 \mu m$  and four for the  $H_1 = 43 \mu m$  and  $H_1 = 28.5 \mu m$  per hole, resulting in individual surface areas of  $A_1 = 6.84 \cdot 10^{-3} mm^2$ ,  $A_2 = 5.53 \cdot 10^{-3} mm^2$  and  $A_3 = 4.67 \cdot 10^{-3} mm^2$ , respectively and a total area for all bar transducers of  $A_{tot} = 880 \cdot 10^{-3} mm^2$ . Further elements were added to populate all  $8 \times 8$  through holes (see Fig. 4.7), as in the single-type array, to increase the overall fill factor. From this the fill factor can be calculated as 5.5 %. The low fill factor is due to the large amount of not-utilised space in the through-holes. The active area for the smallest bars is 36 % bigger than the biggest bars, which should result in a comparably bigger signal.

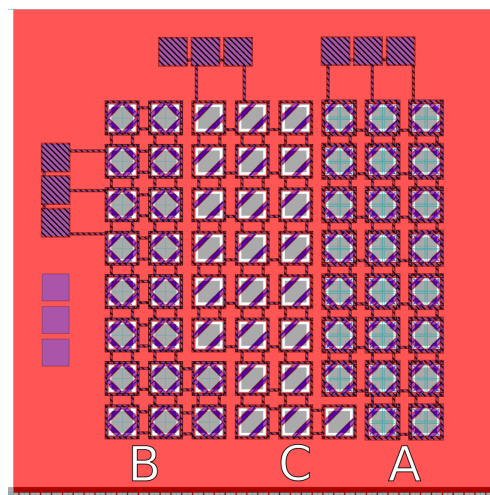


FIGURE 4.7: The finalised design of the bar-type transducer array shows the sub-arrays of bar-type resonance elements with varying values for  $H_1$ :  $H_1 = 28.5 \mu\text{m}$  (A),  $H_1 = 43 \mu\text{m}$  (B) and  $H_1 = 65 \mu\text{m}$  (C).

#### 4.1.4 Fabrication of the PMUT arrays

The PMUT chip (see Fig. 4.8) were fabricated using the cost-effective multi-user PiezoMUMPS process offered by MEMSCAP, Inc. One run cost 4200 US\$, which yielded 15 chips comprised of four sub-chips. Thus one die of transducer elements cost  $\frac{4200 \text{ US\$}}{15.4} = 70 \text{ US\$}$ . In this process a layer of aluminium nitride with a thickness of  $d = 0.5 \mu\text{m}$  is deposited on to a  $10 \mu\text{m}$  doped silicon device layer. After delivery, the transducer array chips were inspected visually and using an SEM. Furthermore, the crystal orientation in the different layers was investigated using X-ray diffraction analysis.

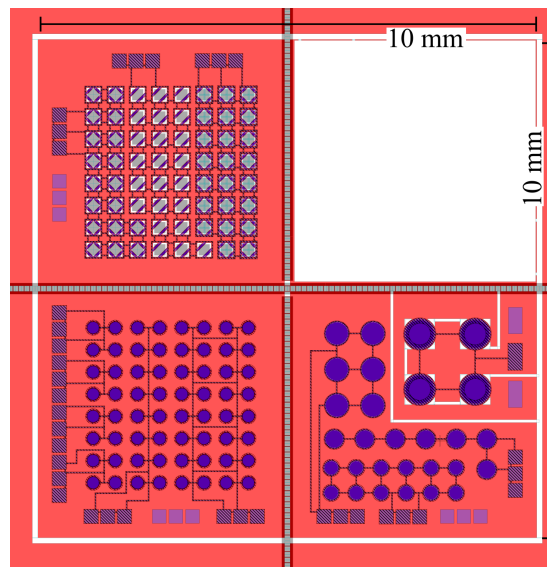


FIGURE 4.8: The combined design shows the chip with the three PMUT array designs. The chip is 10 mm x 10 mm. The "whited" out part of the design was used in another project.

#### 4.1.5 Fabrication Process

The PiezoMUMPS process is used to manufacture the PMUT array die from a stack SOI wafer (see Fig. 4.9, a) consisting of a 10  $\mu\text{m}$  device layer, on top of a 1  $\mu\text{m}$  buried oxide layer and a 400  $\mu\text{m}$  handle wafer in 5 steps. In the first step (see Fig. 4.9, b), a 200 nm oxide layer is grown on the device layer. The desired mask is then created using a photo-resist mask, which is then wet-etched to remove the oxide. This layer acts as an insulator to any added layers. In the second step (see Fig. 4.9, c), a 500 nm thin film of piezoelectric AlN is deposited on the wafer by reactive sputtering. The design mask is etched into the AlN layer using wet etching. Any additional electrical connections on top of the device layer are added in the third step (see Fig. 4.9, d), by first depositing a 20 nm layer of chrome and a subsequently depositing a 1000 nm thick layer of aluminium on the layer. Using a photo-resist mask the desired pattern is then etched into the layer. In the fourth step (see Fig. 4.9, e) parts of the device layer are electrically insulated from each other by developing the mask on the layer. The oxide layer (see first step) is removed using reactive ion etching. The subsequent deep reactive ion etching removes the device layer down to the buried oxide layer. For the fifth step (see Fig. 4.9, f) the wafer needs to be turned over. Therefore, the top of the wafer is protected by a layer of polyimide. The handle wafer etch mask is lithographically patterned. The Si-substrate is locally removed using deep reactive ion etching down to the buried oxide layer. The undercut - a side-effect of the etching process - causes the hole diameter to increase with etch depth. This layer is then removed using a wet etch process. This step creates a full backside release. The

device then consists only of the device layer, the AlN layer and the Al layer. The protective polyimide layer is finally removed by a wet etch process.

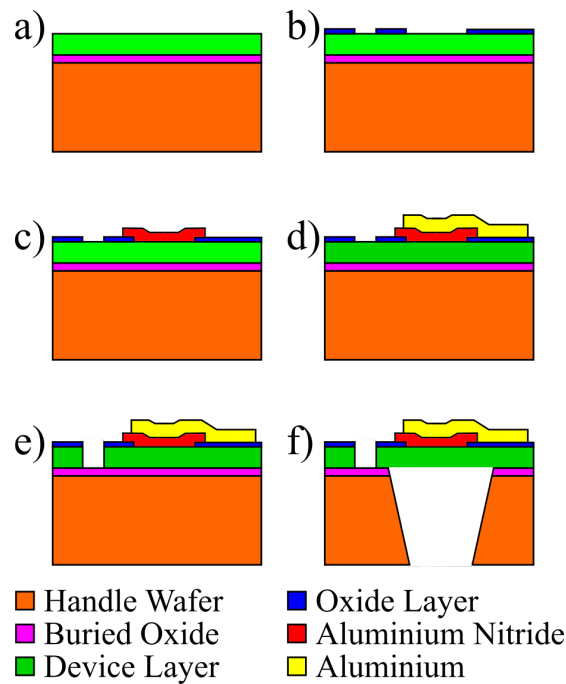


FIGURE 4.9: This shows the steps of the PiezoMUMPS process. Starting with a stack SOI wafer (a), oxide (b), the piezoelectric AlN (c) and Aluminium are deposited (d). Afterwards, the device layer is etched to the buried oxide (e) and finally the handle wafer and buried oxide layer are etched (f). The sloping etch walls symbolise the increasing diameter due to the undercut. The thickness of the handle wafer (orange) is  $t = 400 \mu\text{m}$ , the buried oxide layer  $t = 1 \mu\text{m}$ , the device layer  $t = 10 \mu\text{m}$ , the oxide layer  $t = 200 \text{nm}$ , the piezoelectric AlN layer  $t = 500 \text{nm}$  and the Al layer  $t = 1 \mu\text{m}$  with a  $t = 20 \text{nm}$  Cr interface layer.

## 4.2 Inspection of microfabricated PMUT arrays

The delivered MEMS die were examined using a scanning electron microscope (SEM), an optical profiler and by X-ray diffraction analysis.

### 4.2.1 SEM results

For the first inspection the PMUT die were investigated under an SEM. For a first overview over the individual arrays, they were imaged at a x30 magnification, 5 keV and an angle of  $\alpha = 45^\circ$ . The SEM of the single-type sub-array shows the differently sized sub-arrays as designed (see Fig. 4.10, left and right, respectively). Some minor

defects are visible along the oxide layer electrically insulating the Al connections from the SOI bottom electrode (see Fig. 4.10, inset). Additionally, particle contamination is visible on the devices, these should however not effect the performance of the PMUT array.

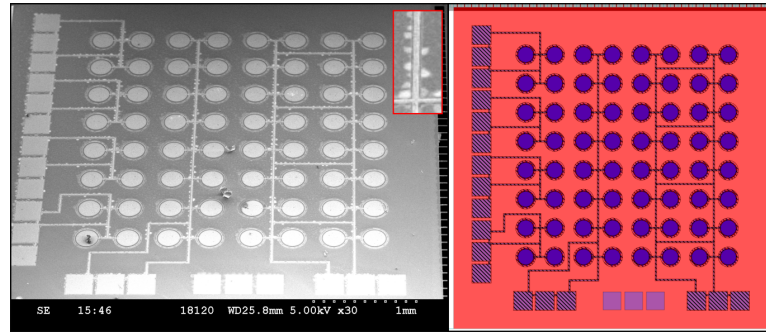


FIGURE 4.10: The SEM of Single-type transducer (left) shows good agreement with the designed masks (right). Minor defects, such as residue on the SOI along the oxide layer tracks (see inset, magnification 120x) and particle contamination should not be effecting the performance of this PMUT array.

The SEM of the multi-type arrays shows good agreement with the design mask (Fig. 4.11, left and right, respectively). Minor defects in the Si-device layer are visible along the etch lines, electrically isolating the largest diameter  $d = 500 \mu\text{m}$  sub-arrays from the other three. The through-hole etches separating the  $500 \mu\text{m}$  sub-array from the rest of the array, as well as the inner part of this sub-array from its surrounding are shown in white in the mask design (right). In the SEM image these are shown as dark tracks. Additional defects are visible on the top left transducer element of this sub-array (see Fig. 4.11, inset). Here, conductive material was potentially deposited outside its mask. This could cause potential problems if the top electrode of the transducer element is directly connected to the ground electrode, made up by the Si-device layer.

The SEM of the beam-type arrays shows the different sub-arrays are as per the design mask (Fig. 4.12, left and right, respectively). The resonant beams and electrical connections are clearly visible. Furthermore, the triangular through-holes defined by the  $H_1$ -dimension are visible for the sub-arrays with  $H_1 = 65 \mu\text{m}$  and  $H_1 = 43 \mu\text{m}$ . For the  $H_1 = 28.5 \mu\text{m}$  sub-array these through-holes appear very small. Here, the holes are not clearly visible (see inset), which will impede the performance of these transducers.

Furthermore, the undercut which was expected to be of  $r_{cut} < 50 \mu\text{m}$  is investigated using SEM images. The beam transducer with the smallest  $H_1$ -size (see Fig. 4.13, a) show no visible through-hole in the triangular etch. There are indications that the

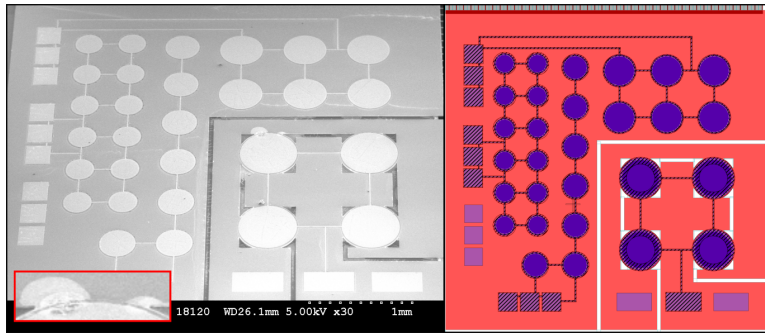


FIGURE 4.11: The SEM of the multi-type transducer (left) shows good agreement with the designed masks (right). Defects are visible on the top left  $d = 500 \mu m$  disc. Here, it looks like some conductive material was deposited outside the mask directly onto the SOI layer. However, that deposition is electrically isolated from the transducer disk (see inset, magnification 120x). The through-hole etches separating the  $500 \mu m$  sub-array from the rest of the array, as well as the inner part of this sub-array from its surrounding are shown in white in the mask design (right). In the SEM image these are shown as dark tracks. Similarly, the triangular darker shapes around the circular  $500 \mu m$  transducer elements are through-hole etches.

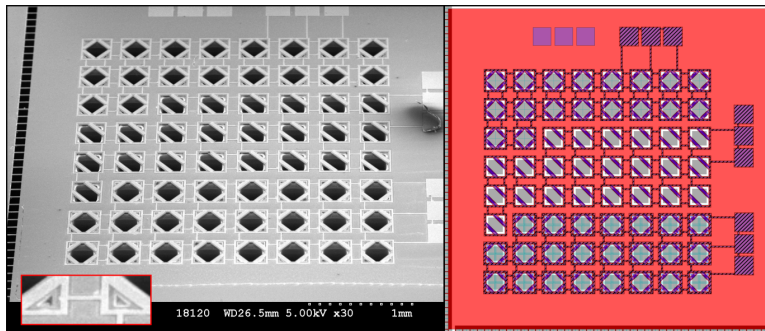


FIGURE 4.12: The SEM of Bar-type transducer (left) shows good agreement with the designed masks (right). The holes of the shortest bars ( $H_1 = 28.5 \mu m$ ) are not visible (see inset). This will strongly impede the performance of these transducers.

beam is free hanging over some length at least. The medium sized beam (see Fig. 4.13, b) show clearly defined through-holes. These are however of uneven size over the area of the chip and appear to reduce the overall beam size by around  $10 \mu m$ . The undercut for the biggest beams (see Fig. 4.13, c) show that the undercut here reached the estimated value giving the beam the designed length. The bright areas are the plateaus created by the undercut as shown in Fig. 4.13, d. Here, it can also be seen that the undercut reduces under the beam structure. From this it can be conjectured that



the undercut under the membrane transducer elements is also minimal with  $r_{cut} \approx 5 \mu m$ .

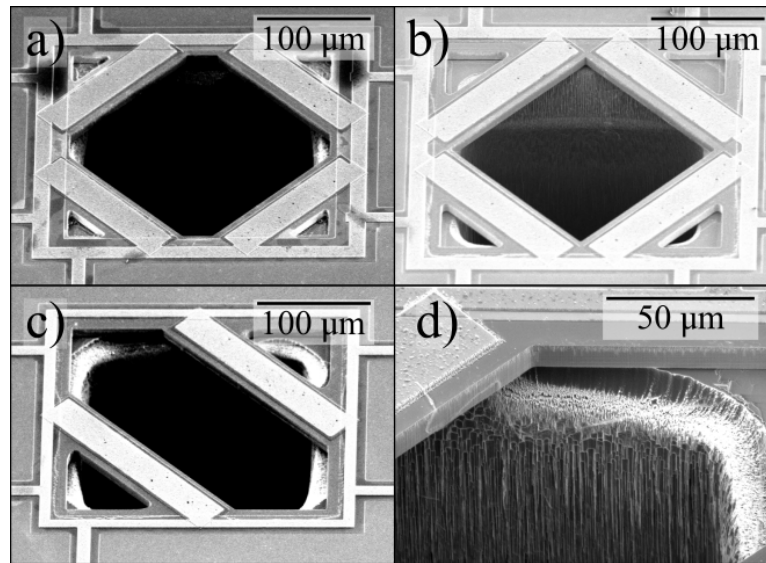


FIGURE 4.13: The undercut shown on the different elements of the beam-type array. The elements with the smallest  $H_1$ -dimension (a) shows no visible triangular through-hole. The bar with  $H_1 = 43 \mu m$  (b) show through-holes of varying sizes. The through holes for the  $H_1 = 65 \mu m$  bars (c) are of the designed size. The close up of the etch border (d) shows the created undercut.

#### 4.2.2 Optical Profiler Examination

The curvature of the multi-type array was investigated using an optical profiler (NT-1100, Veeco / Wyko). The multi-type array was chosen because of its multitude of different transducer diameters. The optical profiler is a white light interferometer system. The interference fringes are created only near the focus of the interferometre as the coherence length of white light is short. The focus region is automatically moved through the specimen at user defined step widths by moving the reference mirror. The fringe contrast is measured at each height and the height of the maximum contrast mapped. The resulting image shows the surface map of the sample. Four multi-type array were investigated using this system. The magnification was set to  $\times 2.5$  and the measurement was set to VSI (vertical scanning interferometry, VSI offers vertical resolution of  $\geq 3 \text{ nm}$ ) using a total scan length of  $h = 5 \mu m$  over a total of 150 steps. The curvature of the membranes was then measured in x- and y-direction for all transducers on four chips using the system's software.

The average and the standard deviation were calculated from the measured radii of curvature (ROCs) (see Table 4.4). All ROCs measured on chips 1 and 2 are negative, meaning the curvatures are concave. While the transducer elements with  $d \leq 395 \mu m$  show a large ROC compared to their diameter, the largest transducer ( $d = 500 \mu m$ ) have comparatively small ROCs, resulting in strong curvatures. Chip 3 shows convex curvatures for all sub-arrays with  $d \geq 395 \mu m$ . The largest sub-array shows flatter transducer elements than chips 1 and 2, with the with  $d = 395 \mu m$  showing comparable flatness. For this sub-array the standard deviation of the ROCs is bigger than the average, because of elements with very large ROC, i.e. these elements are very flat. The elements of the sub-arrays with  $d \leq 310 \mu m$  show both concave and convex curvatures on the same chip. Thus, the standard deviations are larger than their respective averages. This can also be seen in the  $d = 235 \mu m$  sub-array of chip 4. The  $d = 500 \mu m$  and  $d = 310 \mu m$  sub-array show convex curvatures and the  $d = 395 \mu m$  shows concave curvatures. Chip 4 shows the best overall flatness with  $ROC > 1000 mm$  for three sub-arrays.

TABLE 4.4: The average and standard deviation of the measured ROCs (in  $mm$ ) of the sub-arrays. The sub-arrays exhibit both convex and concave curvatures.

Chip	$d = 500 \mu m$	$d = 395 \mu m$	$d = 310 \mu m$	$d = 235 \mu m$
1 - avg	-411.7	-1625.8	-746.3	-510.6
std	131.4	793.7	445.8	365.4
2 - avg	-340.0	-951.3	-476.3	-376.2
std	92.1	463.1	143.8	242.2
3 - avg	593.7	1243.7	133.0	193.2
std	267.8	1482.9	823.3	778.4
4 - avg	1082.5	-3093.8	1253.8	111.5
std	868.0	2275.7	929.6	1550.1

The great variation of the ROCs could be caused by the different positions of the examined chips on the wafer in the multi-user process. The smallest measured ROC was  $75 mm$ . Considering the small diameters of  $\leq 500 \mu m$  the transducer elements were considered flat. The presence of both convex and concave elements is potentially caused by different stress originating from the different chip positions on the wafer during the multi-user process. The shape difference would cause concave transducer elements to act like focussed transducers while convex transducer elements would yield a wider detection angle. Due to the large ROCs these effects can be considered to be minimal.

Since large curvature values denote flat membranes the measured curvature was turned into a flatness factor by calculating the inverse of the curvature with the unit  $\frac{1}{m}$ . The inversed values - the flatness factors - were calculated over the four chips according and grouped by the transducer elements' diameter. These flatness value show low variations for the transducer elements with diameters of  $d = 500 \mu m$ ,

$d = 395 \mu\text{m}$  and  $d = 310 \mu\text{m}$  (see Fig. 4.14). The smallest transducer elements show the largest variation in flatness. This was potentially caused by imperfection during the manufacturing process - especially of the AlN layer - which results in non-uniform stresses.

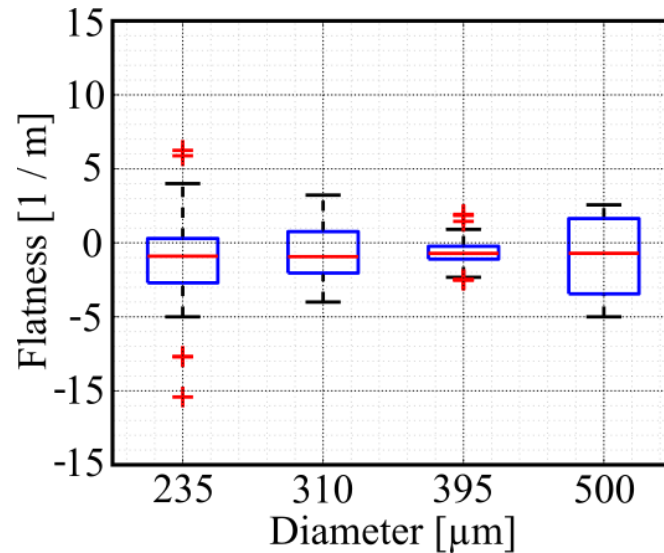


FIGURE 4.14: The calculated flatness of the membrane transducer elements with sizes of  $d = 500 \mu\text{m}$ ,  $d = 395 \mu\text{m}$ ,  $d = 310 \mu\text{m}$  and  $d = 235 \mu\text{m}$ . The smallest transducer elements show the largest variation in flatness.

### 4.2.3 X-Ray Diffraction results

A multi-type sub-array was sent to Johannes Enslin (Institute of Solid State Physics, TU Berlin) for X-ray diffraction analysis. Here, an X-ray tube emits monochromatic collimated onto the sample. The sample, placed on a tip-tilt stage, diffracts the X-rays and if the Bragg-equation is fulfilled a maximum peak is recorded using an X-ray detector. This process is repeated for different angular settings of the tip-tilt stage.

The results of the X-ray diffraction analysis (see Fig. 4.15) show a prominent double peak for Si. The doubled peak is potentially caused by the two Si-layers, i.e. the handle layer and the device layer. Both the AlN-peak and the Al-peak are broadened and flattened due to the membrane curvature. The sample geometry, i.e. the curvature, influences the  $2\theta$ -value as it locally changes the Bragg-conditions. The results show that the AlN-layer is a mono-crystalline structure and in the c-plane. This is shown by the typical spike at  $36^\circ$  for c-plane AlN. A non-mono-crystalline structure would show several additional spikes, e.g. at  $33^\circ$ ,  $50^\circ$  and  $66^\circ$  for the (100), (102) and (103) orientation, respectively [130], [131]. These additional orientations result in a lower

piezoelectric constant. The mono-crystalline structure is especially important for the piezoelectric AlN-layer as multiple crystal-orientations would reduce the piezoelectric efficiency.

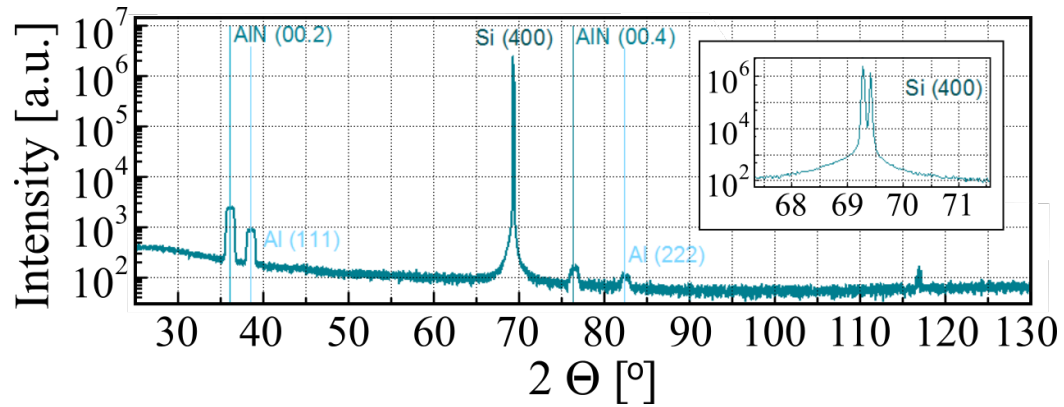


FIGURE 4.15: The X-Ray diffraction results of the sub-array show the composition of its layers. A prominent sharp double peak for Si, and broadened peaks for AlN and Al and its reflections.

### 4.3 Characterisation of the PMUT arrays

After the initial inspection the arrays were characterised using the Pitch-and-Catch technique (PCT), Laser-Doppler-Vibrometry (LDV) and Photoacoustic Excitation (PE). The centre frequency and bandwidths were measured for in oil immersed PMUT arrays. The oil was used as a non-conductive acoustic coupling agent. Here, vegetable oil was used as it was safe, cost-efficient and readily available. The change of immersion fluid from water in the FEM simulations to oil in the characterisation experiments results in an underestimation of resonance frequency of  $\approx 4\%$  [132].

#### 4.3.1 Characterisation using LDV

Laser Doppler vibrometry (LDV) uses an interferometric monochromatic setup to measure the displacement. A laser beam is split with one part going through a reference arm and a second part is emitted onto the target. The beam is reflected off the target back into the LDV apparatus and the two beams are recombined and the interference fringes detected on a photo-detector. As LDV measures the velocity using the Doppler effect, the displacement was calculated. The derived spectrum of the transducers is the bandwidth of its emission, i.e. its emission spectrum  $BW_{TX}$ .

The transducer array chips were mounted and wire-bonded onto a PCB board. The transducer elements were immersed in an oil-bath. They were then actuated by the amplified ( $\times 20$ , Voltage Amplifier A400, FLC electronics) output of a signal generator (Agilent 33250A, Agilent) with a peak-to-peak voltage of  $50 V_{PP}$  at an offset voltage of  $25.5 V$  to prevent negative voltages on the devices (see Fig. 4.16, a). The signal generator put out a train of five sinusoids at an actuation frequency  $f_A$  windowed by Hamming function (see Fig. 4.16, b). The laser Doppler vibrometer (OFV-302 head with OFV-2700 controller, Polytec, 2 MHz bandwidth) output was focused onto an individual transducer element. The LDV sensing head was then positioned in such a manner as to maximise the light, reflected from the transducer element, impinging on the sensor of the LDV system. Upon getting the best signal the actuation frequency was swept from  $f_A = 100 \text{ kHz}$  to  $f_A = 2.0 \text{ MHz}$ . This was done first for a preliminary scan to identify regions of interest. Then a second scan was performed at decreased measuring intervals. The step widths ranged from  $\Delta f = 0.01 \text{ kHz}$  to  $\Delta f = 0.25 \text{ kHz}$ . Only the single-type and the multi-type PMUT arrays could be tested, as the reflection of the bar-type PMUT array proved to be too small, generating a signal of insufficient power. The output of the LDV controller's 20 MHz channel was digitised using an oscilloscope (Agilent infinium,  $f_s = 250 \frac{MSa}{s}$ ). The signal strength was calculated as the frequency content of the recorded trace at the actuation frequency.

The spectrum measured for the single-type array (see Fig. 4.17) shows the resonance frequency for actuation to be  $f_R = 1.1 \text{ MHz}$  with a FWHM bandwidth of  $BW = 0.8 \text{ MHz}$ . This results in a relative bandwidth of  $BW_{rel} = 72.7\%$ . The spectrum also shows high displacement for low frequencies  $f < 0.5 \text{ MHz}$ . This is

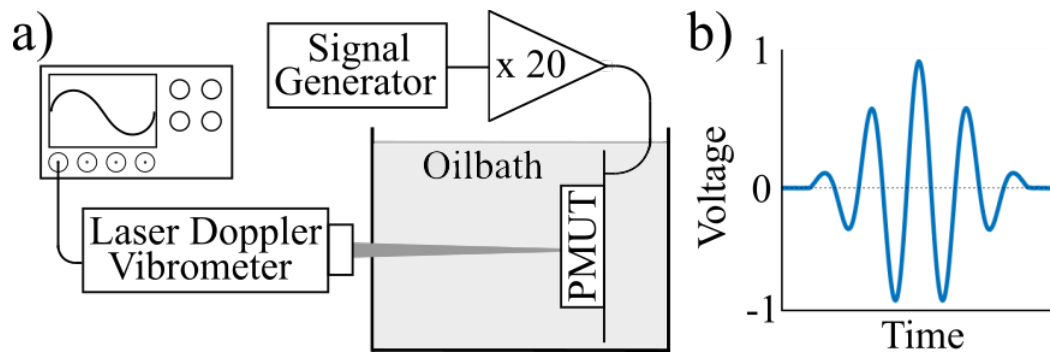


FIGURE 4.16: The setup of the LDV characterisation experiments (a) consists of an amplified signal generator actuating the PMUT array with a waveform shown in b). A laser Doppler vibrometer is used to measure the displacement.

potentially caused by quasi-static displacement at low frequencies.

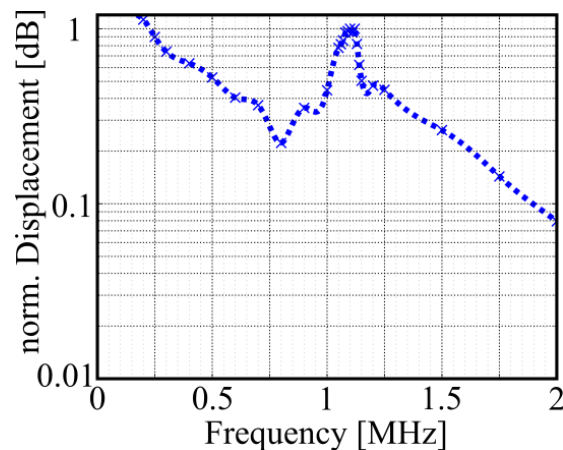


FIGURE 4.17: The spectrum of the single-type arrays shows a centre frequency of  $f = 1.1 \text{ MHz}$  and higher displacement for lower frequencies  $f < 0.5 \text{ MHz}$ . The displacement is normalised to the maximum of the peak. The dotted line is interpolated (cubic spline) between the measured data points (x).

The LDV spectra recorded for the multi-type PMUT sub-arrays (see Fig. 4.18) show the same increase in displacement at low frequencies. The effect is stronger for smaller diameters of the disks. Thus, this effect does not show for the transducer with  $d = 500 \mu\text{m}$ , as its first resonance frequency at  $f_2 = 0.2 \text{ MHz}$  shows prominently. Its second resonance frequency at  $f_2 = 1.25 \text{ MHz}$  is shown to have a much smaller frequency content. For the sub-arrays with diameters of  $d = 395 \mu\text{m}$

and  $d = 310 \mu\text{m}$  the first and second resonance frequencies are visible with  $f_1 = 0.4 \text{ MHz}$  &  $f_2 = 1 \text{ MHz}$  and  $f_1 = 0.7 \text{ MHz}$  &  $f_2 = 1.75 \text{ MHz}$ , respectively. For the  $d = 235 \mu\text{m}$  sub-array only the first resonance frequency with  $f = 1.25 \text{ MHz}$  is visible. A comparison of the first resonance frequencies and bandwidths (FWHM) is shown in Table 4.5. From this it can be seen that the relative bandwidths for all sub-arrays are around 75 %. Here, the bandwidths of the  $500 \mu\text{m}$  sub-array is difficult to precisely estimate.

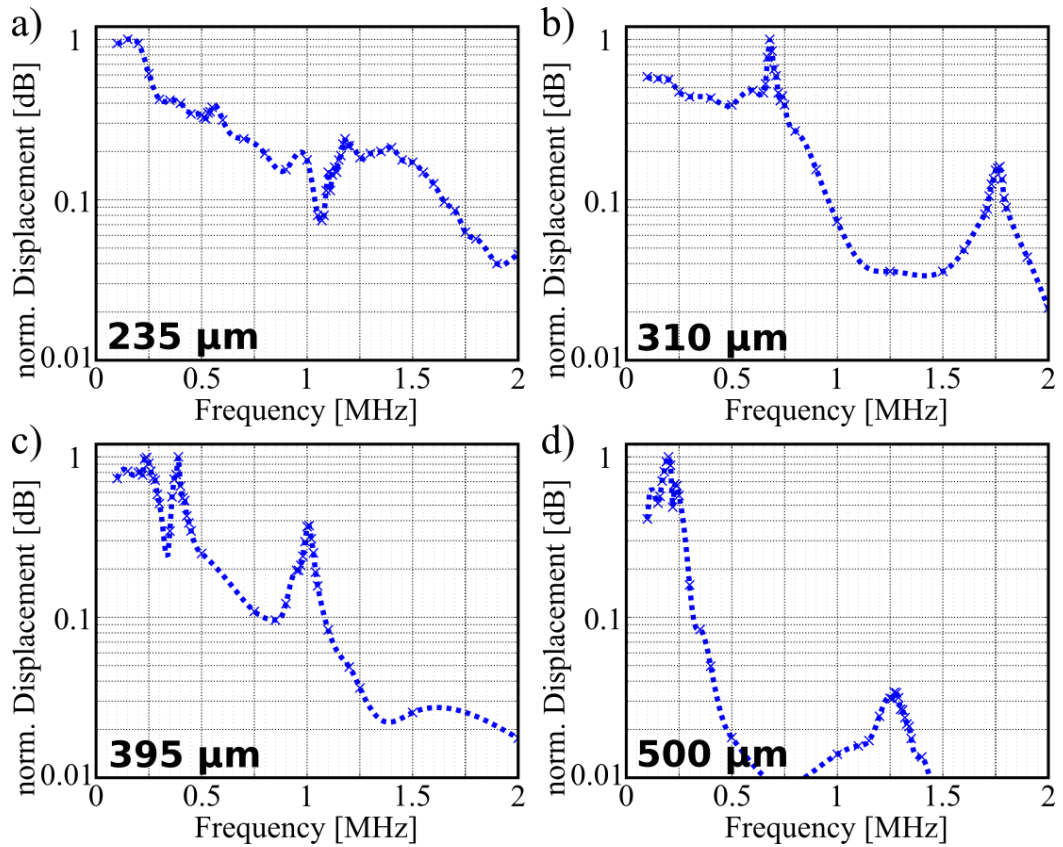


FIGURE 4.18: The spectra measured for the sub-arrays of the multi-type PMUT array with diameters of  $d = 235 \mu\text{m}$  (a),  $d = 310 \mu\text{m}$  (a),  $d = 395 \mu\text{m}$  (a) and  $d = 500 \mu\text{m}$  (a) show the response measured using LDV. The derived resonance frequencies and bandwidths are shown in Table 4.5. The displacement is normalised to the maximum of the peak. The dotted line is interpolated (cubic spline) between the measured data points (x).

TABLE 4.5: The table shows the centre frequencies and bandwidths (FWHM), as well as the relative bandwidth for the different transducer groups of the single-type PMUT array as well as the multi-type array.

Diameter [ $\mu\text{m}$ ]	Main Frequency [MHz]	Bandwidth Frequency [MHz]	relative Bandwidth
240	1.1	0.8	72.7 %
235	1.25	0.9	75.0 %
310	0.7	0.5	71.4 %
395	0.4	0.3	75.0 %
500	0.2	0.15	75.0 %

### 4.3.2 Characterisation using PCT

An alternative to LDV is the pitch-and-catch technique (PCT). It too is based on actuating a transducer array but instead of measuring the displacement, the emitted acoustic wave is detected using a second transducer array of the same type. Here, the resulting bandwidth  $BW_{PCT}$  depends on the convolution of the bandwidth of the receiver  $BW_{RX}$  and the bandwidth of the pulse  $BW_{PLS}$ :

$$BW_{PCT} = BW_{RX} * BW_{PLS} \quad (4.12)$$

If the bandwidth of the acoustic pulse is given by the bandwidth of the transmitter  $BW_{TX}$  then the overall bandwidth of the transducer is:

$$BW_{PCT} = BW_{RX} * BW_{TX} \quad (4.13)$$

In PCT, two PMUT array chips of the same design are acoustically coupled by positioning them opposite one another and immersing them in an oilbath (see Fig. 4.19, a). One of the arrays is actuated using an amplified (x20, Voltage Amplifier A400, FLC electronics) signal generator (Agilent 33250A, Agilent) with a total peak-to-peak voltage of 60  $V_{pp}$ . The output consists of five windowed (Hamming) sinusoids (see Fig. 4.19, b) at an actuation frequency  $f_A$ . The ranges of interest for the actuation frequencies of the individual transducer sub-arrays were identified prior to this experiment by running over a larger range using larger step-widths. The identified ranges for the multi-type PMUT array were 50  $\text{kHz}$  – 550  $\text{kHz}$  for the 500  $\mu\text{m}$  sub-array, 100  $\text{kHz}$  – 1.6  $\text{MHz}$  for the sub-arrays with diameters of 395  $\mu\text{m}$  & 310  $\mu\text{m}$  and 550  $\text{kHz}$  – 2  $\text{MHz}$  for the 235  $\mu\text{m}$  sub-array. The actuation frequency for the PCT characterisation of the single-type arrays ranged from 500  $\text{kHz}$  – 1.8  $\text{MHz}$ . For all experiments a step width of  $\Delta f = 22.5 \text{ kHz}$  was used. The emitted acoustic waves were detected using the second array and averaged over  $n = 256$  samples. The output of which was amplified by +60 dB (DHPCA-100, FEMTO Messtechnik GmbH) and recorded using an oscilloscope (Agilent infinium,  $f_s = 100 \frac{\text{MSa}}{\text{s}}$ ). The Fast-Fourier-Transformation (FFT) was applied to the recorded signal and its power



was calculated as the amplitude of the FFT at the actuation frequency.

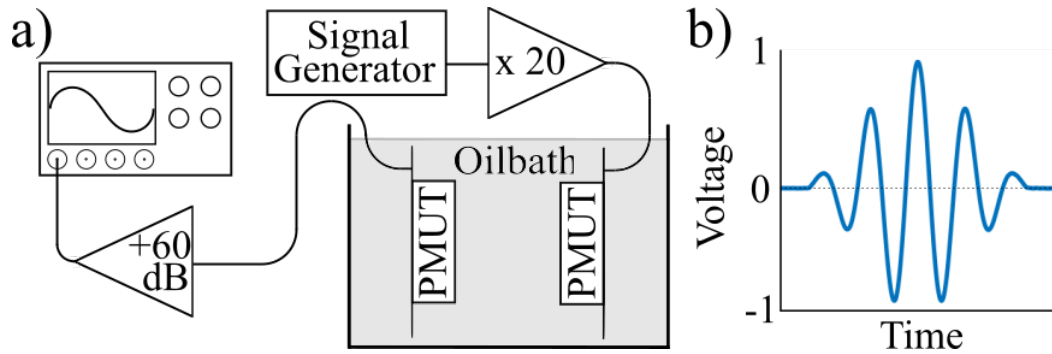


FIGURE 4.19: The setup of the PCT characterisation experiments (a) consists of an amplified signal generator actuating the PMUT array with a waveform shown in b). The excited PMUT array emits acoustic waves at an actuation frequency  $f_a$ . These are detected using a second array, the output of which is amplified and digitised using an oscilloscope.

The results of the PCT characterisation of the single-type PMUT array (see Fig. 4.20, a) shows a centre frequency of  $f = 1.2 \text{ MHz}$  and a -6 dB bandwidth of  $BW = 0.6 \text{ MHz}$ , resulting in a relative bandwidth of  $BW_{rel} = 50.0 \%$ . The characterisation of the multi-type array (4.20, b) showed for the  $395 \mu\text{m}$  sub-array that both the its first ( $f_1 = 0.4 \text{ MHz}$ ) and its second modal frequencies ( $f_2 = 0.75 \text{ MHz}$ ) can be measured. The first modal resonance frequency is similar to the one measured using LDV, but the secondary frequency is 25 % lower. This is potentially caused by fluctuations in the AlN -layer fabrication, causing a mismatch of the generated and detected bandwidths. The resonance frequency measured for the  $500 \mu\text{m}$  membranes was  $f = 200 \text{ kHz}$ , for the  $395 \mu\text{m}$  membranes was  $f = 400 \text{ kHz}$ , for the  $310 \mu\text{m}$  membranes was  $f = 650 \text{ kHz}$  and for the  $235 \mu\text{m}$  membranes was  $f = 1.2 \text{ MHz}$ , with respective bandwidths of  $BW_{500} = 150 \text{ kHz}$ ,  $BW_{310} = 700 \text{ kHz}$  and  $BW_{235} = 950 \text{ kHz}$ . This results in relative bandwidth of  $BW_{500} = 75 \%$ ,  $BW_{310} = 107.7 \%$  and  $BW_{235} = 79.2 \%$ . The bandwidths measured using PCT are larger compared to the ones measured by LDV. This is due to the above explained convolution of the transmitting bandwidth  $BW_{TX}$  and the receiving bandwidths  $BW_{RX}$ , indicating they are not equal.

### 4.3.3 Characterisation using PE

4.1.1 In the previous sections characterisation methods that are based on actuating the transducer elements were performed, i.e. the transducer arrays' parameters were recorded for transmission mode only (LDV) or for both transmission and receiving mode (PCT). In order to obtain the parameters for receiving mode only photoacoustic

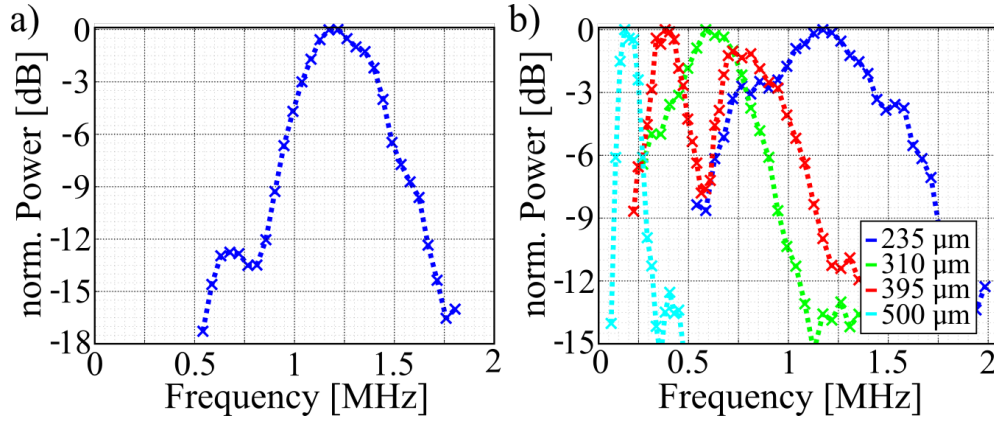


FIGURE 4.20: The trace of the signal power for the single-type PMUT array (a) shows a centre frequency of  $f = 1.2 \text{ MHz}$  and a  $-6 \text{ dB}$  bandwidth of  $BW = 0.6 \text{ MHz}$ . For the multi-type array it shows the first resonance frequencies at  $1.2 \text{ MHz}$  ( $235 \mu\text{m}$ , cyan),  $650 \text{ kHz}$  ( $310 \mu\text{m}$ , cyan),  $400 \text{ kHz}$  ( $395 \mu\text{m}$ , cyan) and  $200 \text{ kHz}$  ( $500 \mu\text{m}$ , cyan). A higher order resonance is visible for the  $395 \mu\text{m}$  membranes at  $f_{II} = 750 \text{ kHz}$ . The signal power is normalised to the maximum of the corresponding signal. The dotted line is interpolated (cubic spline) between the measured data points (x).

excitation (PE) is applied. In PE, PA waves generated using a short pulsed laser the PA wave assumes the pulse shape of the laser pulse (see eq. 2.2). The pulse width of the laser  $\tau_L$  needs to be much smaller than the pulse width of the transducer  $\tau_{XD}$ , i.e.:

$$\tau_L \ll \tau_{XD} \quad (4.14)$$

Thus, the PA wave impinges the transducer as a quasi-Dirac impulse  $\delta_L$ . Therefore, equation 4.12 can be changed to:

$$BW_{PE} = BW_{RX} * \mathfrak{F}(\delta_L) \quad (4.15)$$

Since the Fourier transform of a Dirac-impulse is  $\mathfrak{F}(\delta_L) = 1$ , equation 4.15 simplifies to:

$$BW_{PE} = BW_{RX} \quad (4.16)$$

Thus, PE can be used to measure the receiving bandwidth of the examined transducer under the condition that  $\tau_L \ll \tau_{XD}$ . The short pulsed laser used in the following experiments with a pulse width of  $\tau_L = 8.15 \text{ ns}$  fulfils this condition, compared to the minimum pulse-widths of the PMUT arrays:

$$\begin{aligned}
\tau_{MIN} &= \frac{1}{f_{res}} \\
\tau_{MIN} &= \frac{1}{7.11 \text{ MHz}} \\
\tau_{MIN} &= 140.6 \text{ ns}
\end{aligned} \tag{4.17}$$

Thus, the condition ( $\tau_L \ll \tau_{MIN}$ ) holds even for the highest expected frequency, with  $8.15 \text{ ns} \ll 140.6 \text{ ns}$ . As shown in the simulation (see Chapter 2) the generated PA wave can only be assumed to have a broad bandwidth close to the source. The transducers' response will nonetheless give insight into the transducer and the frequency content it is able to record. The expected frequency content can be seen in Chapter 2.

For this purpose a short pulsed frequency-doubled ( $\tau = 8.15 \text{ ns}$ ,  $\lambda = 532 \text{ nm}$ ,  $E_{pls} = 22 \text{ } \mu\text{J}$ ,  $PRF = 10 \text{ Hz}$ ) Nd:YAG laser (Brilliant B, Quantel) is used for generating short pulsed PA waves (see Fig. 4.21). The laser beam is focused onto a strongly absorbing (0.4% m/m India Ink, Jackson's) gelatin (8% m/m) phantom using a plane-convex lens ( $f = 70 \text{ mm}$ ). The phantom is immersed in an oilbath (Sunflower Oil) for acoustic coupling and electric insulation of the bare PMUT array chip. The chip is positioned at a distance of  $d = 15 \text{ mm}$  from the focal point of the laser on the phantom. This distance matches the one used for characterising the commercial transducers. According to the simulations, the generated PA spectrum at this distance is suitable for frequencies  $f < 7 \text{ MHz}$ . The PMUT's output is amplified by +60 dB (DHPCA-100, FEMTO Messtechnik GmbH) and digitised and stored using an oscilloscope (Agilent infiniium,  $f_s = 250 \text{ MSa/s}$ ). The spectral information is then extracted from the temporal traces by windowing (Hanning) over the PA signal and applying the FFT to it.

The PSDs from the recorded traces show the resonance frequencies and bandwidths of the characterised PMUT (sub-)arrays. Figure 4.22 shows a first resonance frequency of  $f = 1.25 \text{ MHz}$  and an according -6 dB bandwidth of  $BW = 1.05 \text{ MHz}$ . A second resonance frequency is observed at 5.75 MHz with an according -6 dB bandwidth of 1.05 MHz. While the magnitude of the first resonance mode is comparably constant at a set total active area, the magnitude of the second resonance frequency varies widely, as can be seen for the "singles" sub-arrays (4.22, bottom, black). The secondary resonance frequency coincides with the simulated mode numbers 3 and 4 (see Table 4.1). As the resonance frequencies for both modes are similar, this change in magnitude of the frequency content might be caused by the number of transducers resonating in each mode. The spectra with larger magnitude have more elements resonating mode number 4 as the deformation is bigger, thus creating a larger signal.

The spectra for the multi-bandwidth array were measured for the individual sub-arrays (see Fig. 4.23, top), i.e. the groups of transducer elements with diameters

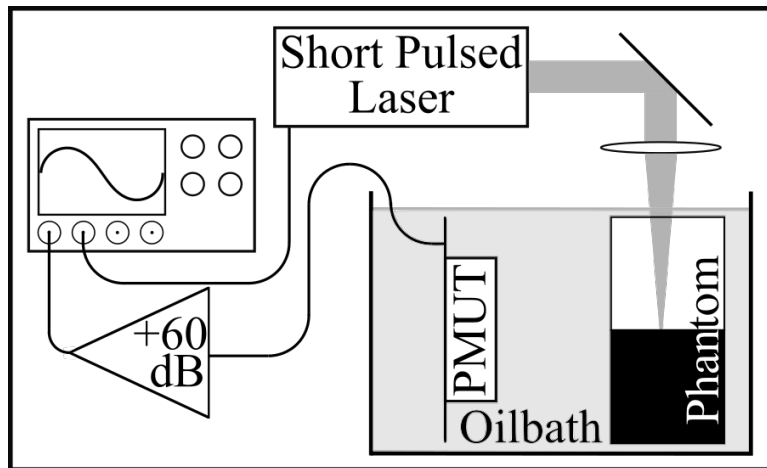


FIGURE 4.21: In PE the output of a short-pulsed laser is focused on a target phantom. The generated PA signal is detected by a PMUT array. The phantom and the array are acoustically coupled in an oilbath. The output of the latter is amplified and recorded using an oscilloscope.

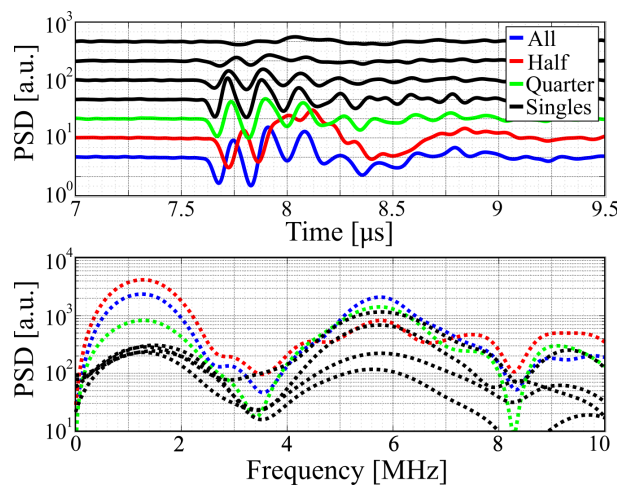


FIGURE 4.22: The signal traces (top) of the PE experiments are shown for all sub-arrays of the single-type PMUT array, as well as the whole array. The PSDs of the recorded PA signals (bottom) show a first resonance frequency of  $f = 1.25 \text{ MHz}$  and a second resonance frequency of  $f = 5.75 \text{ MHz}$  for all sub-arrays. For the "single" sub-array the frequency content varies greatly for the second resonance frequency but is comparably constant for the first resonance frequency.

of  $500 \mu\text{m}$  (cyan),  $395 \mu\text{m}$  (green),  $310 \mu\text{m}$  (red) and  $235 \mu\text{m}$  (blue). From Fig. 4.23 (top) it can be seen that the lower order modes are of lower intensity. Furthermore, the peak of the first resonance frequency of the  $500 \mu\text{m}$  membrane is barely visible

and its frequency content is about five times lower than the other sub-arrays. Fig. 4.23 (bottom) shows the spectrum of a PA response recorded using the whole multi-type PMUT array, i.e. all sub-arrays were electrically connected. The recorded signal has a spectrum with three distinct peaks at a  $f_I = 5.8 \text{ MHz}$ ,  $f_{II} = 3.4 \text{ MHz}$  and  $f_{III} = 1.6 \text{ MHz}$ . The first peak  $f_I$  is caused by the mode number 4 (see 4.3) of the  $235 \mu\text{m}$  sub-array. The second peak  $f_{II}$  is mainly caused by mode number 4 of the  $310 \mu\text{m}$  sub-array. The third peak is a superposition of the  $1.25 \text{ MHz}$  peak ( $235 \mu\text{m}$  sub-array) and mode number 4 of the  $500 \mu\text{m}$  sub-array. Thus, the combined bandwidth of the multi-type array is mainly a combination of the bandwidths of the  $235 \mu\text{m}$ ,  $310 \mu\text{m}$  &  $395 \mu\text{m}$  sub-arrays. A comparison of the measured resonance frequencies for the multi-type and the single-type PMUT arrays is shown in Table 4.6. As expected the frequencies for the elements with larger diameter are lower. Here, it can be seen that the values for the centre frequencies measured using PE agree well with the ones measured by PCT.

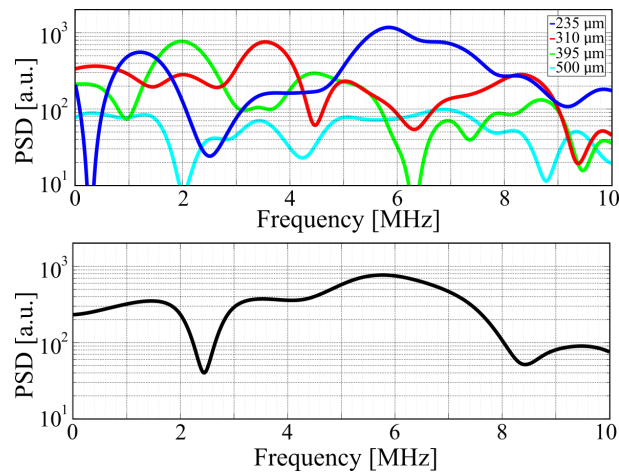


FIGURE 4.23: The spectra recorded for the individual sub-arrays of the multi-type array (top) show the mode frequencies for the  $235 \mu\text{m}$  sub-array (blue),  $310 \mu\text{m}$  sub-array (red),  $395 \mu\text{m}$  sub-array (green) and  $500 \mu\text{m}$  sub-array (cyan). Using the whole PMUT array (bottom), i.e. connecting all sub-arrays, three peaks in the spectrum are visible at  $f_I = 5.8 \text{ MHz}$ ,  $f_{II} = 3.4 \text{ MHz}$  and  $f_{III} = 1.6 \text{ MHz}$ .

TABLE 4.6: The resonance frequencies of the single-type and the multi-type PMUT arrays.

diameter [ $\mu m$ ]	1 <sup>st</sup> resonance frequency [MHz]	2 <sup>nd</sup> resonance frequency [MHz]	3 <sup>rd</sup> resonance frequency [MHz]
single-type 240	1.25	5.75	
multi-type 235	1.25	5.75	
310	0.8	2.1	3.4
395	0.45	1.95	4.2
500	0.3	1.1	3.0

PE experiments were performed for all sub-arrays of the bar-array as well as the array as a whole. Figure 4.24 (top) shows the spectra of the recorded PA response of the individual sub-arrays. The beam with the largest  $H_1$ -dimension (with  $H_1 = 65 \mu m$ ) has a main peak at  $f = 2.4 \text{ MHz}$  and side peaks at  $f = 4.2 \text{ MHz}$  and  $f = 5.8 \text{ MHz}$ . The sub-array with  $H_1 = 28.5 \mu m$  has a main peak at  $f = 4.5 \text{ MHz}$  with side peaks at  $f = 2.4 \text{ MHz}$  and  $f = 5.8 \text{ MHz}$ . When using the array as a whole, i.e. combining the individual sub-arrays, the spectrum of recorded PA signal shows several peaks; they are showing at  $f = 2.6 \text{ MHz}$ ,  $f = 4.4 \text{ MHz}$  and  $f = 5.6 \text{ MHz}$ . Additionally, it shows a peak at  $f = 1.5 \text{ MHz}$ .

Comparing the first resonance frequencies measured in the characterisation experiments with the designed values (see Table 4.7) shows good agreement for all techniques for the small transducer elements ( $235 \mu m$  and  $240 \mu m$ ). For larger elements the error increased drastically for the PE technique. Here, the resonance frequency was always over-estimated (compared to the other techniques and the design). PCT and LDV yielded similar results. PE is good for estimation of resonance frequencies larger than 1 MHz. The measurement is quick and estimates all resonance frequencies simultaneously, i.e. in one (averaged) recorded signal. Here, the distance between the PA source and the transducer should be kept minimal, i.e. at its NFD to reduce the decrease of the PA spectrum due to attenuation. While PCT and LDV yield more accurate results for lower frequencies ( $f < 1 \text{ MHz}$ ) these techniques are more time-consuming. Here, a signal has to be recorded for each discrete frequency point. Additionally, as elements get smaller it gets increasingly more difficult to receive a signal using the laser vibrometer. For PCT a decrease in active surface area reduces signal in two fashions. Firstly, the emitted signal is decreased and secondly the lower surface area yields a lower detected signal. Thus, due to recording the whole frequency response of the transducer elements and its ease of use PE is a good technique to characterise (small) transducer elements with first resonance frequencies  $f_1 > 1 \text{ MHz}$ .

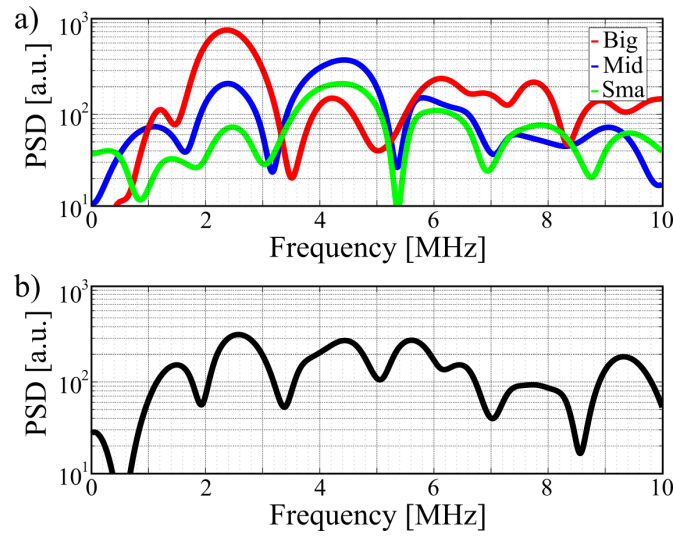


FIGURE 4.24: The spectra of the PA signal recorded using the individual sub-arrays (top) show a main peak at  $f = 2.4$  MHz for the  $H_1 = 65 \mu\text{m}$  (red) sub-array with side peaks at  $f = 4.2$  MHz and  $f = 6.1$  MHz. The elements with  $H_1 = 43 \mu\text{m}$  (blue) show their main peak to be at  $f = 4.5$  MHz with side peaks at  $f = 2.4$  MHz and  $f = 5.8$  MHz. The smallest elements ( $H_1 = 28.5 \mu\text{m}$ , green) show a main peak at  $f = 4.4$  MHz, too. PA signals recorded using the (electrically) combined bar-type array have a spectrum with peaks at  $f_2 = 1.5$  MHz,  $f_1 = 2.6$  MHz and  $f_2 = 4.3$  MHz

TABLE 4.7: The designed 1<sup>st</sup> resonance frequencies of the single-type and the multi-type PMUT arrays are compared with the results from the characterisation. The bracketed number shows the error compared to the designed values.

diameter [ $\mu\text{m}$ ]	Design Freq. [MHz]	PE Freq. [MHz]	PCT Freq. [MHz]	LDV Freq. [MHz]
single-type 240	1.18	1.25 (5.9%)	1.2 (1.7%)	1.1 (−6.8%)
multi-type 235	1.25	1.25 (0.0%)	1.2 (4.0%)	1.25 (0.0%)
310	0.61	0.8 (31.1%)	0.65 (6.6%)	0.7 (14.8%)
395	0.32	0.45 (28.9%)	0.4 (17.8%)	0.4 (17.8%)
500	0.16	0.3 (46.7%)	0.2 (−13.3%)	0.2 (−13.3%)

## 4.4 SNR measurements

After the initial inspection (Section 4.2) and characterisation (Section 4.3) of the PMUT arrays, their performance was tested. Here, the received signal is compared to the noise floor, the SNR. It describes the signal strength achieved with the transducers to its noise. Thus to choose a good transducer the detected signal should be maximal while the detected should be minimal. The noise is caused by thermal and shot noise in the electrical equipment, as well as environmental causes. While the experimental stage was vibrationally separated from the environment (i.e. the building) by using an optical table, sources of vibration such as the laser could still cause noise in the recorded signals. The results of the performance tests of the PMUT arrays were compared against the commercially available single-element transducers used in the previous chapter.

### 4.4.1 Estimation of the SNR of the PMUT arrays

The signal-to-noise ratios (SNR) achievable with custom-made AlN thin-film PMUT arrays were measured by recording and analysing PA waves generated at varying pulse energies as described in Section 3.4. Here, the output of a short pulsed frequency-doubled ( $\tau = 8.15 \text{ ns}$ ,  $\lambda = 532 \text{ ns}$ ,  $E_{max} = 2.2 \text{ mJ}$ ,  $PRF = 10 \text{ Hz}$ ) Nd:YAG laser (Brilliant B, Quantel) generates PA signal in an absorbing (0.4 % (m/m) India Ink) 8 % (m/m) gelatine matrix. The pulse energies were reduced to pulse energies ranging from  $220 \mu\text{J}$  to  $220 \text{ nJ}$  using neutral density filters (NEK01, Thorlabs). The starting pulse energy was set to the lowest, i.e.  $E_1 = 220 \text{ nJ}$  to avoid damaging the phantom ( $40 \times 40 \times 30 \text{ mm}^3$ ). The phantom consisted of two layers of equal height with a clear top layer and an absorbing bottom layer (see Fig. 4.21). The phantom and the PMUT array were acoustically coupled in an oilbath. The PMUT array was positioned at a distance of  $d \approx 11 \text{ mm}$  from the focal spot of the laser. Its output, amplified by +60 dB (DHPVA-200, FEMTO), was recorded using an oscilloscope (Agilent Infiniium,  $f_s = 500 \frac{\text{MSa}}{\text{s}}$ ) and averaged over 1024 samples. Then, the recorded traces were analysed by calculating the signal and noise power as described in Section 1.4.2. From this the SNR was calculated for each pulse energy setting as described in Section 3.4.

A trace of a PA signal generated at a pulse energy of  $22 \mu\text{J}$  recorded with the single-type array is shown in Fig. 4.25, a. The FFT over a selection of PA signal traces, their PSDs (Fig. 4.25, c), show the first and second resonance frequencies at  $f_1 = 1.2 \text{ MHz}$  and  $f_2 = 5.75 \text{ MHz}$ . The amplitude of these peaks increases with increasing pulse energy. The rate of increase decreases for higher pulse energies. This can also be seen when comparing the calculated SNR at the different pulse energies (see Fig. 4.25, b). Here, the SNR graph for the  $1.2 \text{ MHz}$  peak (blue) shows linear behaviour and the graph for the  $5.75 \text{ MHz}$  peak a sigmoidal shape, indicating that the PMUT sensor array might be saturating. At high pulse energies of  $E = 220 \mu\text{J}$  the SNR is calculated as  $SNR = 310$ . For low pulse energies of  $E = 220 \text{ nJ}$  the SNR is 6 and 7.7 for the



1.25 MHz and the 5.75 MHz frequency bands, respectively. The noise floor (black line Fig. 4.25, c) has a near uniform frequency content.

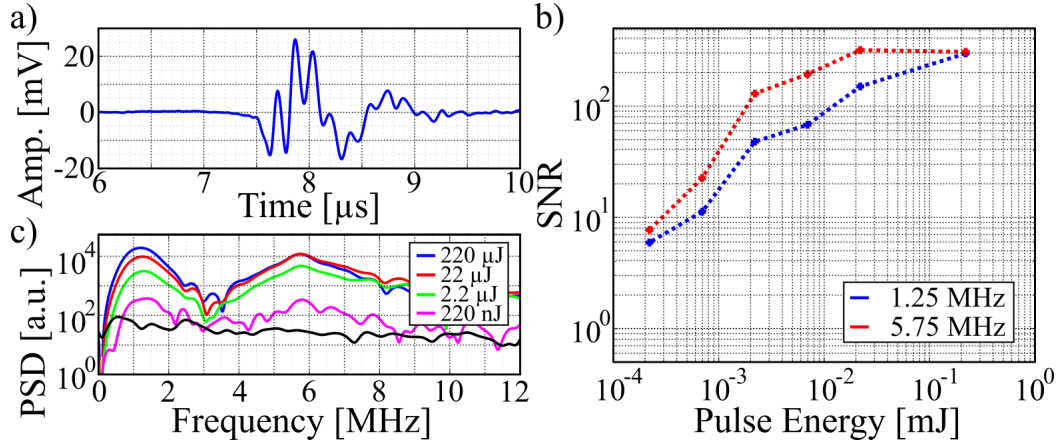


FIGURE 4.25: The PA signal (a) recorded at  $E = 22 \mu\text{J}$  using all elements of the single-type array shows an amplitude of  $38 \text{ mV}_{PP}$ . The SNR of the generated signals (b) range from 6 to 310 for the 1.25 MHz peak (blue) and from 6 to 310 for the 5.75 MHz peak (red). The PSDs of the PA signal (c) at selected pulse energies show two main peaks, at  $f_1 = 1.2 \text{ MHz}$  and  $f_2 = 5.75 \text{ MHz}$ . The black line shows the averaged noise power spectrum.

Fig. 4.26 (a) shows a typical trace of a PA signal detected at a pulse energy of  $E = 22 \mu\text{J}$  using the multi-bandwidth PMUT array. Fig. 4.26 (c) shows the PSD of traces at selected pulse energies. Three main peaks are visible at  $f_1 = 1.3 \text{ MHz}$  (blue),  $f_2 = 3.4 \text{ MHz}$  (red) and  $f_3 = 5.7 \text{ MHz}$  (green). The frequency content of these peaks decreases as the pulse energy decreases. The average noise power (black line in Fig. 4.26, c) is near uniform over the whole spectrum, decreasing with increasing frequency. The SNRs at 1.4 MHz (blue) and 3.4 MHz (red) range from 2 for low pulse energies to 105 for high energies, showing fairly linear behaviour. The SNR of the 5.7 MHz band ranges from 4 to 170. It increases suddenly at a pulse energy of  $E = 2.2 \mu\text{J}$  potentially due to broadening of its frequency content. This can be seen by comparing the shapes of the peak at  $E = 2.2 \mu\text{J}$  and  $E = 220 \text{ nJ}$  in Fig. 4.26, c (green and magenta, respectively). Additionally, from the PSDs it can be seen that the multi-bandwidth PMUT array offers a wide bandwidth for pulse energies  $E \geq 2.2 \mu\text{J}$ .

From the trace (pulse energy  $E = 22 \mu\text{J}$ ) shown in Fig. 4.27 (a) it is visible that the bar-type PMUT array has less signal power at a given pulse energy than the single-type or multi-type PMUT array, with a maximum peak-to-peak voltage of  $3.9 \text{ mV}_{PP}$  compared to  $38 \text{ mV}_{PP}$  and  $29 \text{ mV}_{PP}$  for the single-type or multi-type PMUT array, respectively. The decrease in signal power is also visible in the PSDs (see Fig. 4.27, c). Here, three main peaks are visible at  $f_1 = 2.2 \text{ MHz}$ ,  $f_2 = 4.3 \text{ MHz}$  and  $f_3 = 6.1 \text{ MHz}$ . In general, the peaks increase with increasing pulse energy. However,

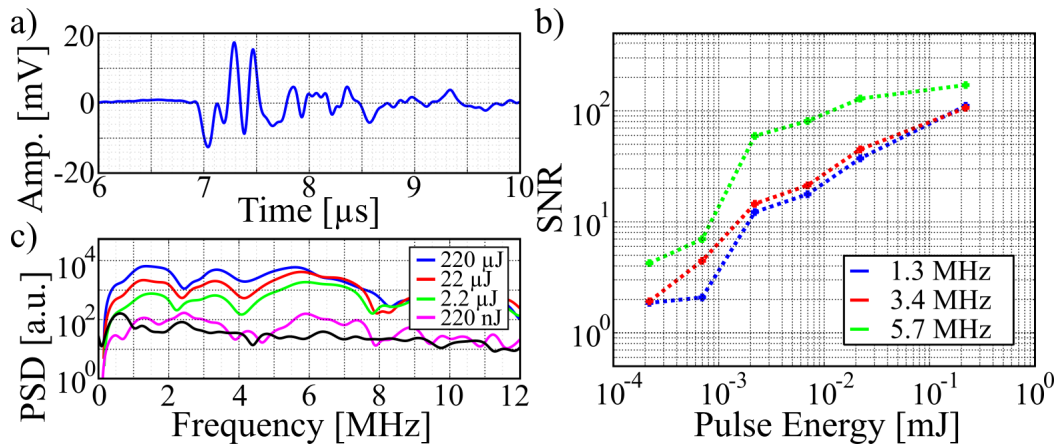


FIGURE 4.26: A typical PA traces (a) recorded using the multi-bandwidth PMUT array at a pulse energy of  $E = 22 \mu\text{J}$  with a signal amplitude of  $29 \text{ mV}_{PP}$ . The calculated SNRs (b) range from 2 to 170. The PSDs (c) are shown for selected pulse energies shows three main frequency bands, centred around  $f_1 = 1.3 \text{ MHz}$  (blue),  $f_2 = 3.4 \text{ MHz}$  (red) and  $f_3 = 5.7 \text{ MHz}$  (green). The black line shows the averaged noise power spectrum.

measuring at  $E = 22 \mu\text{J}$  compared to  $E = 220 \mu\text{J}$  the SNRs (Fig. 4.27, b) only increase for the  $6.1 \text{ MHz}$  band (green), but stays constant for the  $2.2 \text{ MHz}$  (blue) band and decreases for the  $4.3 \text{ MHz}$  band (red). In the  $2.2 \text{ MHz}$  band the SNR increases linearly with the pulse energy up to a maximum of  $\text{SNR} = 35$  at  $E = 22 \mu\text{J}$ . The SNR for the  $4.2 \text{ MHz}$  band increases up to a maximum of  $\text{SNR} = 28$  for a pulse energy of  $E = 22 \mu\text{J}$  afterwards the SNR decreases, as the signal power in that band decreases. In the  $6.1 \text{ MHz}$  band the SNR increases linearly with the pulse energy up to a maximum of  $\text{SNR} = 32$ . The simultaneous increase and decrease in the  $6.1 \text{ MHz}$  and the  $4.3 \text{ MHz}$  band at the change from  $22 \mu\text{J}$  to  $220 \mu\text{J}$ , while the  $2.2 \text{ MHz}$  band stays constant indicates that the energy is transferred to higher resonance modes. As all bar transducers show responses in all of these bands (see Fig. 4.24) the saturation at these high pulse energies might have lead to this transference for all element sizes. Thus, using a laser with more powerful pulses will not increase the overall SNR, especially as with increasing pulse energy the risk of ablation of the target increases.

#### 4.4.2 Comparison of the PMUT arrays and the commercially available single-element transducers

The performance of the custom-made AlN thin-film PMUT arrays is compared against performance of the commercially available ultrasound transducer presented in the previous chapter. This is done by comparing the measured SNRs and their active area. The measured SNRs (see Fig. 4.28) for the different ultrasound transducers show

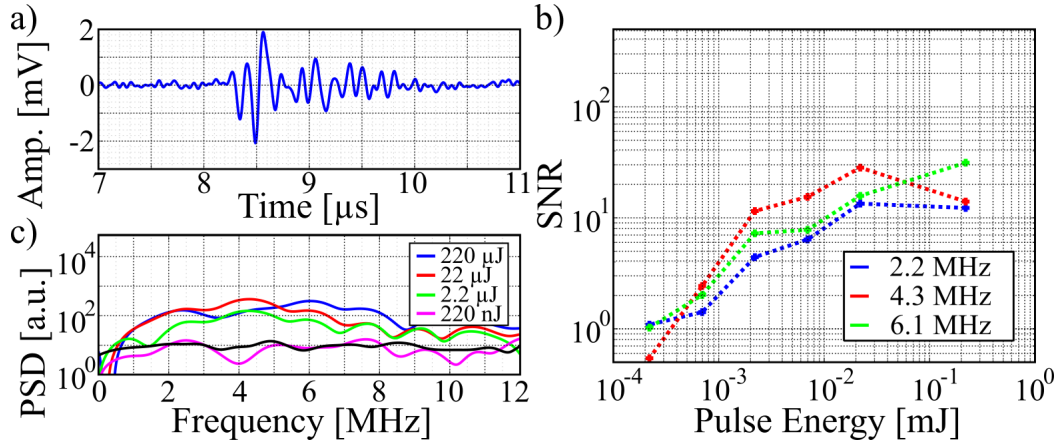


FIGURE 4.27: The PA signal (a) recorded at  $E = 22 \mu\text{J}$  using the bar-type PMUT array shows an amplitude of  $3.9 \text{ mV}_{pp}$ . The SNR of the generated signals (b) range from 1 to 12 for the 2.2 MHz peak (blue), 0.5 to 14 for the 4.3 MHz peak (red) and from 1 to 32 for the 6.1 MHz peak (green). The PSDs of the PA signal (c) at selected pulse energies show quasi-broad bandwidths spectra ranging from 1.5 MHz to 6.5 MHz. The black line shows the averaged noise power spectrum.

two groups; a group with a high SNR, consisting of the commercial transducers, with centre frequencies at  $10 \text{ MHz}$  (green, A315S, Olympus) and  $2.25 \text{ MHz}$  (blue, I8-0216-S, Olympus), and the single-type PMUT array (red). The multi-type (black) and the bar-type (magenta) PMUT array have on average a 4 to 8 times lower SNR. The single-type PMUT array slightly outperforms the commercial  $2.25 \text{ MHz}$  transducer. Its SNR is slightly less ( $\approx 75 \%$ ) of the SNR of the commercial  $10 \text{ MHz}$  transducer for pulse energies  $E \leq 7 \mu\text{J}$ . The results of the SNR measurements are to be taken in context with the overall active area (see Table 4.8). Here, it can be seen that the active area of the commercial US transducers is two orders of magnitude greater than that of the PMUT arrays. Due to their greater dimensions, the commercial US transducers also have greater NFDs. Thus, they are subject to near-field effects to a greater degree, which results in a reduction of the received signal strength.

TABLE 4.8: The active surface areas of the custom-made PMUT arrays and the commercial transducers are shown.

Transducer	single-type	multi-type	bar-type	2.25 MHz	10 MHz
Active Area [ $\text{mm}^2$ ]	2.895	2.564	0.961	506.7	286.5

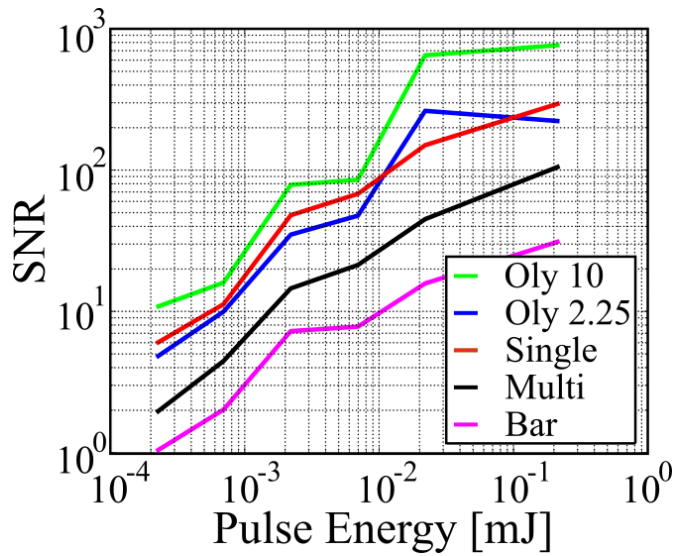


FIGURE 4.28: A comparison of the SNRs of the various US transducers and arrays shows the commercially available transducers to have a better SNR compared to the custom-made PMUT arrays. The SNR of the single-type PMUT array is up to 2.5 times lower at high pulse energies ( $E > 2.2 \mu\text{J}$ ) and matches that of the commercial transducers at lower pulse energies ( $E < 2.2 \mu\text{J}$ ).

## 4.5 Application of PMUT arrays to PA detection

The ability of the smallest sub-arrays of the single-type PMUT array were tested for their application in phased array sensing. The output of a short pulsed doubled ( $\tau = 8.15 \text{ ns}$ ,  $\lambda = 532 \text{ ns}$ ,  $E_{max} = 2.2 \text{ mJ}$ ,  $PRF = 10 \text{ Hz}$ ) Nd:YAG laser (Brilliant B, Quantel) was focused onto a layered target. The top layer was made from clear 8 % (m/m) gelatine and the bottom layer was made from absorbing (0.4 % (m/m) Inida Ink) 8 % (m/m) gelatine (see Fig. 4.29, a). The laser generated PA waves at the boundary of the two layers. The phantom and a single-type PMUT array were immersed in an oilbath for acoustic coupling. The PMUT array faced the PA source and was tilted at an angle to the axis focal spot - PMUT array of  $\alpha = 5^\circ \pm 1^\circ$  (see Fig. 4.29, a) at a distance of  $d_1 = 24 \text{ mm}$ . The output of two of the smallest sub-arrays of the single-type PMUT array were amplified by +60 dB (DHPVA-200, FEMTO) and recorded using an oscilloscope (Agilent Infiniium,  $f_s = 500 \frac{\text{MSa}}{\text{s}}$ ) using an average size of 1024 samples. The distance between the centre points of the two sub-arrays was  $x = 800 \mu\text{m}$ . Using a reduced sketch (see Fig. 4.29, b), the path difference of the recorded signals can be calculated as:

$$\Delta d = d_2 - d_1 \quad (4.18)$$

Here,  $d_2$  consists of  $d_2 = d_1 + y$ .  $d_2$  can be calculated from  $d_1$  and  $h$ . The latter of which

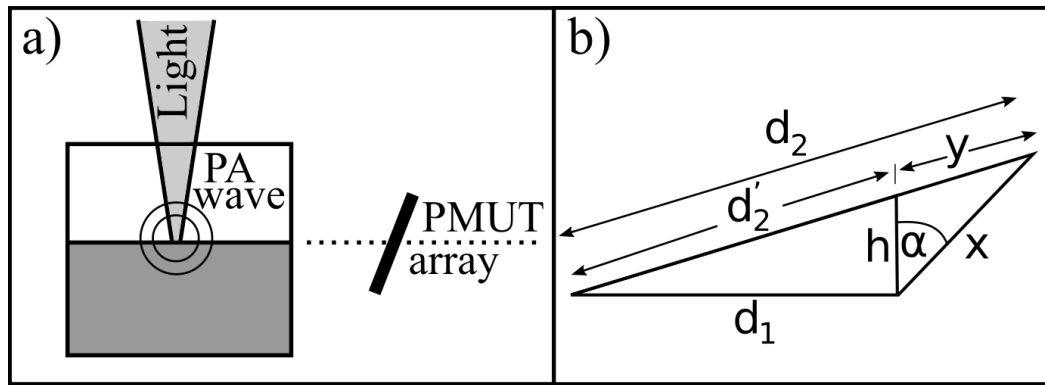


FIGURE 4.29: The sketch of the phased array experiment (a) shows the tilted PMUT array in relation to the excited PA wave. The PA wave propagates in all directions. The reduced sketch (b) shows the variables used in the theoretical calculation of the path difference and the time delay.

can be approximated as  $h = x \cdot \cos \alpha$  for small angles. Thus, using the given values it can be calculated as:

$$\begin{aligned}
 d'_2 &= \sqrt{d_1^2 + h^2} \\
 d'_2 &= \sqrt{d_1^2 + (x \cdot \cos \alpha)^2} \\
 d'_2 &= \sqrt{(24\text{mm})^2 + (0.8\text{mm} \cdot \cos 5^\circ)^2} \\
 d'_2 &= 24.013 \text{ mm}
 \end{aligned} \tag{4.19}$$

The length  $y$  is calculated using the given values as:

$$\begin{aligned}
 y^2 &= h^2 + x^2 - 2hx \cos \alpha \\
 y &= \sqrt{h^2 + x^2 - 2hx \cos \alpha} \\
 y &= \sqrt{(0.8\text{mm} \cdot \cos 5^\circ)^2 + (0.8\text{mm})^2 - 2(0.8\text{mm} \cdot \cos 5^\circ) \cdot 0.8\text{mm} \cos 5^\circ} \\
 y &= 69.7 \mu\text{m}
 \end{aligned} \tag{4.20}$$

Using this result the length  $d_2$  is calculated to:

$$\begin{aligned}
 d_2 &= d'_2 + y \\
 d_2 &= 24.013 \text{ mm} + 0.0697 \text{ mm} \\
 d_2 &= 24.083 \text{ mm}
 \end{aligned} \tag{4.21}$$

The path difference is thus:

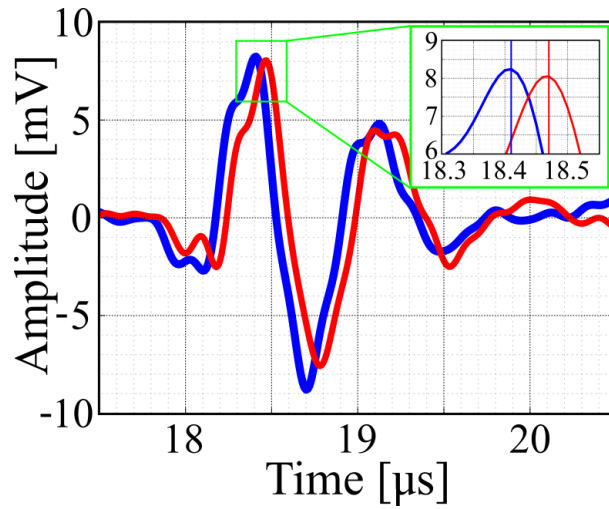


FIGURE 4.30: The PA signal recorded for the two sub-arrays shows on arriving later than the other. As the delay is too small to measure on the big time scale, the inset shows a smaller time scale and a delay of  $\Delta t = 60 \text{ ns}$  can be seen.

$$\begin{aligned}\Delta d &= d_2 - d_1 \\ \Delta d &= 24.083 \text{ mm} - 24 \text{ mm} \\ \Delta d &= 83 \text{ } \mu\text{m}\end{aligned}\tag{4.22}$$

The expected time difference  $\Delta t$  of the signal can be derived using the speed of sound in the medium  $v_s = 1450 \frac{\text{m}}{\text{s}}$  and the calculated path difference  $\Delta d = 83 \text{ } \mu\text{m}$  as:

$$\begin{aligned}\Delta t &= \frac{\Delta d}{v_s} \\ \Delta t &= \frac{83 \text{ } \mu\text{m}}{1450 \text{ m/s}} \\ \Delta t &= 57.2 \text{ ns}\end{aligned}\tag{4.23}$$

The recorded traces are shown in Fig. 4.30. Both are of similar amplitude with a peak-to-peak voltage of  $17 \text{ mV}_{pp}$ . The inset plot shows close up of the peaks and the time difference  $\Delta t$  of the two peaks can be estimated as  $\Delta t = 60 \text{ ns}$ . This is well within the calculated value for an angle of  $\alpha = 5^\circ \pm 1^\circ$  resulting in a time delay of with  $\Delta t = 57.2 \pm 9.4 \text{ ns}$ .

## 4.6 Verification of Simulation

The simulations reported in chapter 3 show that the frequency content of the generated PA wave is dependent on the distance from the source. PA waves were

generated in a phantom with an absorbing layer to verify the simulation results for the commercial laser ( $\tau = 10 \text{ ns}$ ,  $E \approx 5.1 \mu\text{J}$ ). The PA waves were recorded using the multi-type PMUT array. This PMUT array was chosen as it offered the widest low-frequency bandwidths of the available transducers. The PA waves were recorded at two distances: 4.7 mm and 5.7 mm. Finally, the FFT was applied over a windowed part of the recorded trace. The calculated spectra were then normalised to the maximum of the 4.7 mm trace.

Figure 4.31 shows the frequency map (a) simulated for a pulse width of 10 ns and the frequency spectra (b) of the traces recorded at distance of 4.7 mm (blue) and 5.7 mm (red). The black lines in the frequency map correspond to the distances and denote the strength of the spectra normalised to the 4.7-mm spectra. The spectra have three main peaks, at 1.5 MHz, 3.4 MHz and 5.8 MHz. The frequency map shows the main lobe with a maximum at around 6 MHz (for a distance of 4.7 mm) declining in relative amplitude with increasing distance. Separated from this is the side lobe with a maximum at around 1.75 MHz (for a distance of 4.7 mm).

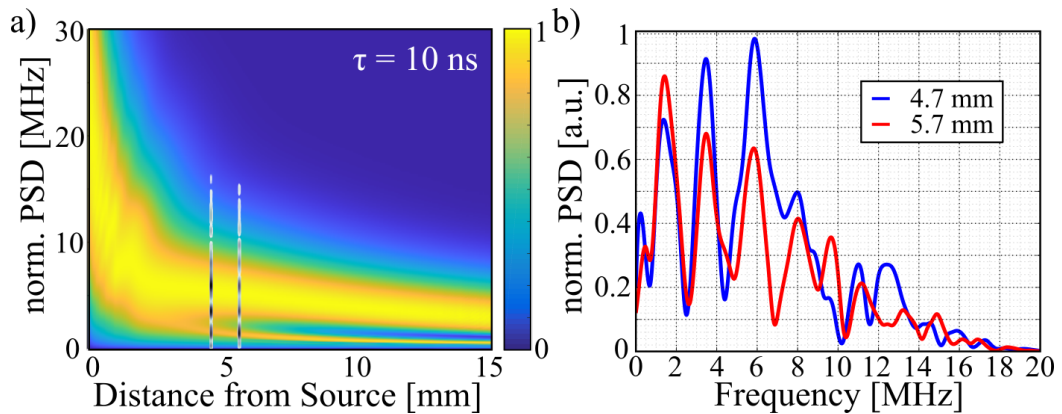


FIGURE 4.31: The frequency map shows (a) the simulation results for a laser pulse widths of  $\tau = 10 \text{ ns}$  for a distance of up to 15 mm. The PSDs (b) show the experimentally derived frequency content at distances of 4.7 mm (blue) and 5.7 mm (red). These were superimposed onto the frequency map as well. On the superimposed picture the maxima are black and the minima white.

The measured spectra agree well with the simulated frequency map. The main peak of the 4.7 mm spectra, at 5.8 MHz is near the centre of the main lobe and thus has the highest amplitude. As the other peaks, at 1.5 MHz and 3.4 MHz move towards the edge of the main lobe (the latter) and into the developing side lobe (the former) their frequency contents are reduced. At a distance of 5.7 mm the side lobe has developed sharper and the 1.5 MHz peak is now the highest measured frequency peak. The peaks at 3.4 MHz and 5.8 MHz are on either side of the maximum of the main lobe and are thus reduced in their frequency content. In general, the simulation seemed to

underestimate the low frequency content and the development of the secondary lobe. Furthermore, the measurements indicate a stronger reduction of the peak frequency of the main lobe compared to the simulation.

## 4.7 Discussion

Three PMUT arrays were designed to comply with the design rules and specification of PiezoMUMPS, a cost-efficient multi-user process offered by MEMSCAP Inc. Here, thin-film AlN is used as a piezoelectric material for the ultrasound transducer elements. The single-type array was designed as an array of 8 by 8 membrane transducer elements with a diameter of  $d = 240 \mu\text{m}$ . The elements are addressable in groups of 4, 16 and 32. The simulated centre frequency for this array was  $f_c = 1.25 \text{ MHz}$  with a total active area of  $A = 2.895 \text{ mm}^2$ . The multi-type PMUT array was designed as an array of membrane transducers with diameters ranging from  $d_1 = 235 \mu\text{m}$  to  $d_4 = 500 \mu\text{m}$ , resulting in a broader overall bandwidth. The sub-arrays of the membrane transducers of the different diameters are individually addressable to allow for more in-depth analysis of the PMUT array's behaviour. The simulated centre frequencies range from  $f_1 = 1.25 \text{ MHz}$  to  $f_4 = 0.16 \text{ MHz}$  with a total active area of  $A = 2.564 \text{ mm}^2$ . The bar-type array was designed to achieve higher centre frequencies, while still adhering to the design specifications. This meant changing the transducer element design from membranes to bars, with the length of the bars influencing the resonance frequency. Three sub-arrays were designed with resonance frequencies ranging from  $f_1 = 3.65 \text{ MHz}$  to  $f_4 = 7.11 \text{ MHz}$  with a total active area of  $A = 0.961 \text{ mm}^2$ . The smaller active area is due to the required small width of the transducer elements, resulting in a considerable quantity of unused space. This can be improved by choosing the bar length so that several different types can be used per through-etch hole, maximising the used space.

SEM images were taken of the delivered PMUT array chips. These showed that the chips were manufactured without major defects. The inspection of the delivered PMUT arrays revealed that the undercut, which was expected to be  $r_{exp} < 50 \mu\text{m}$ , was smaller with  $r_{real} < 5 \mu\text{m}$ . The undercut estimation used in the design process was  $r_{exp} < 20 \mu\text{m}$ , with this new data any newly designed PMUT arrays should be designed accordingly. Additionally, an optical profiler was used to measure the curvature of the membrane transducer elements upon delivery. Here, it was seen that the flatness, the inverse of the curvature, varied not only in size but also direction, i.e. whether the curved surface was convex or concave. The curvatures themselves were caused by the deposition and releases processes during manufacture. Fluctuations in the parameters of the deposition of the piezoelectric AlN -layer is the main reason for these fluctuations, as the fabrication of the other layers is fairly consistent. Lastly, the orientation of the crystal structures of the silicon, aluminium and aluminium nitride were measured using X-ray diffraction analysis by TU Berlin. This showed that the piezoelectric AlN was present in only one crystal-orientation (c-plane). The presence of multiple crystal orientations adversely affects the energy conversion abilities of the



AlN piezoelectric layer.

The characterisation of the PMUT arrays was done using three techniques: LDV, PCT and PE. Here, LDV measures the centre frequency and bandwidth of the emission spectrum, while PE measures both for the PMUT arrays as receiver. In PCT a convolution of both is measured. The results of the centre frequencies are similar for all three, while the bandwidths of the PMUT arrays in receiving, i.e. measured using PE, is larger. While it proved more difficult to measure the first resonance frequency and its bandwidth for low frequency elements (with  $f < 0.5 \text{ MHz}$ , such as the  $500 \mu\text{m}$  sub-array of the multi-bandwidth array) using PE, it proved much easier to measure higher order resonance modes. Furthermore, small and high frequency transducer elements, such as the bar-type PMUT array, could not be characterised using LDV or PCT due to their small features (LDV) and weak emission profile (PCT). The measured centre frequency values for the membrane transducer elements, i.e. the elements of the single-type and the multi-type PMUT arrays, show good agreement to the simulated values with an error of  $\pm 10 \%$ .

This error was not only caused by the unknown undercut dimension, but also potential device layer errors. This indicates that the undercut under the membranes, which could not be measured, was approximately as expected prior to the manufacture. The centre frequency values measured for the bar-type PMUT array are consistently lower than the simulated values with errors of  $\epsilon < 34.5 \%$ . The lower undercut seen in the SEM pictures (see Fig. 4.13) causes the length of the bar to decrease and thus the frequency to increase. Therefore, the more complex geometry (compared to the membrane transducers) potentially caused the development of different resonance modes, resulting in the lower frequencies.

The performance of the PMUT arrays was tested by measuring the SNR at various pulse energies ranging from  $E = 220 \mu\text{J}$  to  $E = 220 \text{ nJ}$ . Here, the tests showed that the array with the overall highest active surface area (single-type array,  $A = 2.895 \text{ mm}^2$ ) had the best SNR over the whole pulse energy range. It yielded minimum and maximum SNRs of  $\text{SNR}_{\min} = 6$  and  $\text{SNR}_{\max} = 300$ . The SNR showed linear behaviour. The multi-type transducer array ( $A = 2.564 \text{ mm}^2$ ) had a high SNR for high pulse energies ( $\text{SNR}_{220 \mu\text{J}} = 106$ ) decreasing to  $\text{SNR} \approx 2$  for  $E = 220 \text{ nJ}$ . Furthermore, comparing the SNRs and the signal power in the different bands, it seems that the SNR is higher for higher frequencies. This trend was seen across all investigated transducers and is possibly caused by the decrease of the noise floor with increase in frequency. The bar-type PMUT array with an overall active area of  $A = 0.961 \text{ mm}^2$  has a maximum SNR of  $\text{SNR} = 32$ .

Comparing the performance of the custom-made thin-film PMUT arrays to the commercial US transducers shows that the Olympus 10 MHz transducer's SNR is better by a factor of 2 (compared to the single-type PMUT array) at high pulse energies, down to a factor of 1.4 for low energies. The other commercial transducer is

outperformed by the single-type PMUT array. Comparing the overall active areas of the commercial and custom-made transducers shows that the area of the former is two orders of magnitude larger than those of the PMUT arrays. Thus, the SNR of the commercial US transducers should be even better, but they are adversely effected by the close proximity to the PA source resulting in signal reduction due to near-field effects. As shown in chapter 2.3 the NFD for the commercial 2.25 MHz transducer is  $NFD \approx 40 \text{ mm}$ ,  $NFD \approx 30 \text{ mm}$  for the commercial 10 MHz transducer and  $NFD \approx 5 \text{ mm}$  for the PMUT arrays due to their 4 mm side length. Thus, the SNR of the commercial transducers needs increased by a 4- fold and a 2.5-fold, for the 2.25 MHz and the 10 MHz transducer, respectively. The 10 MHz yields a 20 % better SNR than the 2.25 MHz transducer. The latter in turn yields an SNR up to 4 times better than the single-type PMUT array. The low NFD of the PMUT arrays is an advantage, especially in high attenuation media, as less signal strength is attenuated.

Two sub-arrays of the single-type transducer arrays were successfully applied to phased array measurements. The path difference and the resulting time delay were theoretically calculated and confirmed experimentally.

## Chapter 5

# Miniaturisation of the Laser Source using MEMS micromirrors

As shown in chapter 3 the PRF of the commercial system was too low, resulting in high acquisition times, even at low averaging sizes. This resulted in decreased SNRs. Simultaneously, the pulse energy of the commercial system was too high, requiring heavy attenuation. To overcome the problems, the excitation side of the PA system was miniaturised and the commercial pulsed Nd:YAG laser, which has been used in all the experiments described in previous chapters, replaced with a custom-made MEMS Q-switched Nd:YAG laser. The design, operation and general characterisation of the MEMS Q-switched laser are described in [38], [39]. The full assembly, alignment and technical details are not discussed here and can be found in the aforementioned references. In this Chapter, the potential for this custom-made MEMS based Nd:YAG laser as a PA excitation source is investigated. This custom-made laser produced an increase in PRF of three orders of magnitude and a reduction in size, while reducing the pulse energy compared to the previously used Nd:YAG system. Unfortunately, the PRF increase could not yet be taken advantage of fully, as the DAQ system was too slow.

The MEMS Q-switched Nd:YAG laser (see Fig. 5.1) emitting at a wavelength of  $\lambda = 1064 \text{ nm}$  consists of a planar 80 % (at  $\lambda = 1064 \text{ nm}$ ) reflective output coupler, a diode-side-pumped Nd:YAG gain medium (RBAT24/34 Pump Diode Module, Northrop Grumman) and a fast-scanning MEMS micromirror. The power input in to the pumping diodes was controlled using a diode controller module. The gold-coated MEMS micromirror has a reflectivity of  $R = 96 \%$ . It rotates, at resonance frequencies ranging from of 2 kHz to 22 kHz, in and out of alignment with the output coupler and the gain medium, thus closing and opening the laser cavity. The MEMS mirrors were designed by Ralf Bauer (CMP, University of Strathclyde, Glasgow) and fabricated by MEMSCAP, Inc.

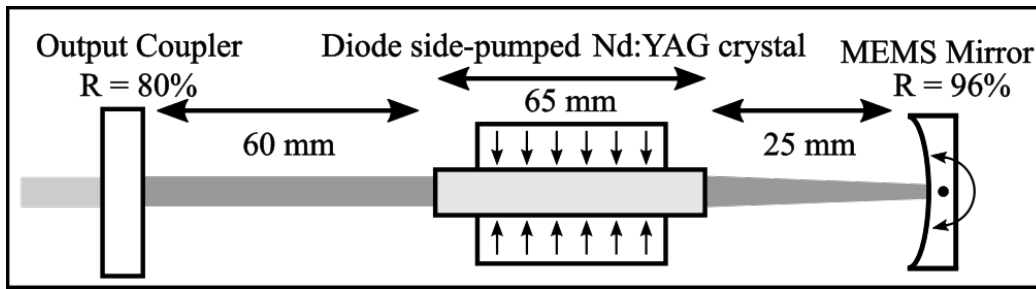


FIGURE 5.1: The MEMS Q-switched laser consists of a MEMS micromirror ( $R = 96\%$ ), a diode-side pumped Nd:YAG gain crystal and an output coupler ( $R = 80\%$ ).

## 5.1 MEMS Micromirrors

The mirror disc (see Fig. 5.2, red box) is mounted on a torsion spring and actuated by an electro-static comb-drive (see Fig 5.2, green box). The comb-drive consists of 10 interleaved Si-finger with a thickness of  $\tau = 10 \mu\text{m}$  and a length of  $l = 120 \mu\text{m}$ . The combs on the torsion spring and the side-wall combs have a gap of  $6 \mu\text{m}$ . They form the electrodes of the capacitor, that drives the electrostatic actuation. The comb-drive is actuated using a signal generator (DG1022Z, Rigol) with a square wave output with an amplitude of  $V_{out} = 10 V_{PP}$ , amplified by  $\times 20$  (A400 voltage amplifier, FLC electronics) and current limited by a  $R = 10 \text{ k}\Omega$  resistor.

As shown in Fig. 5.2 each MEMS device consists of four mirrors. Four of these devices were available and the resonance frequencies of the mirrors were tested by reflecting the output of a HeNe laser of the mirror onto a screen. Three micromirrors were not functional due to mechanical damage. The screen was at a distance of  $d_S = 245 \text{ mm}$ . The actuation frequency of the mirror was swept from  $2 \text{ kHz}$  to  $25 \text{ kHz}$  in  $\Delta f = 10 \text{ kHz}$  steps. By measuring the length of the generated line  $d_{in}$ , the maximum deflection angle was calculated as  $\beta = 2 \tan^{-1}(\frac{0.5 d_{in}}{d_S})$ . The results in table 5.1 show the measured maximum deflection angles.

For the mirrors 2, 3 and 4 the frequency range, in which the other mirrors had their first resonance frequency showed, no response. Mirror 1 and 10 show a double peak for their second and first resonance frequency, respectively. The line created by deflecting the laser beam off the micromirror did not create a straight line for mirrors 11 and 12 at their second resonance frequency, but a line superimposed with a sinusoidal function. This was potentially caused by a resonance mode perpendicular to the torsion-spring. Thus, these mirrors were not used. Fig. 5.3 (a) shows the double peaked resonances for mirrors 1 (blue) and 10 (green) compared to mirror 9 (red). As the peaks are clearly separated, there are two distinct resonances present. The maximum deflection angle of mirror 13 was dependent on the direction of the frequency sweep, i.e. whether the frequency was increased (see Fig. 5.3, b, red) or decreased (see Fig. 5.3, b, blue). For the first resonance frequency decreasing the

frequency achieved a deflection angle almost three times compared to increasing the frequency (green inset). For the second resonance frequency the deflection angle profile was near-Gaussian (cyan inset) when increasing, while a sharp drop of the deflection angle - about 2 degrees larger - showed when the frequency was decreased. This meant that, when using this mirror for Q-switching the frequency needed to be carefully adjusted from the right direction as otherwise the deflection angle might abruptly drop to 0 when heat-induced changes changed the mechanical properties and thus the resonance frequency. This would cause the cavity to be closed and the mirror to be destroyed due to thermal damage.

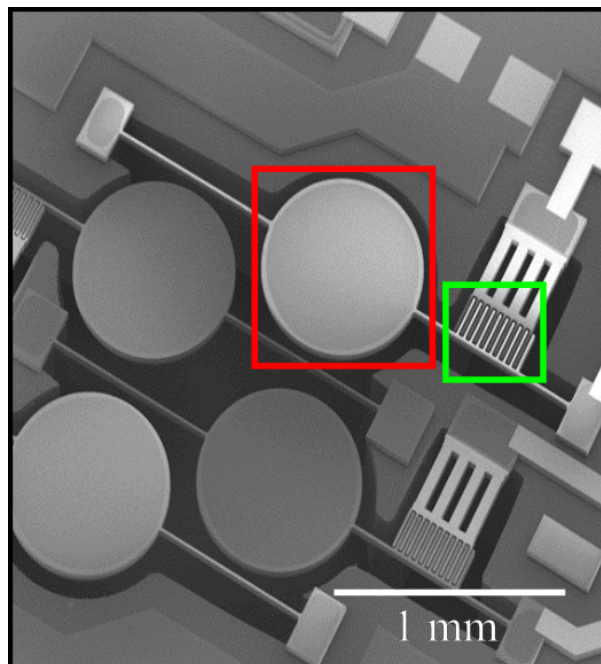


FIGURE 5.2: The SEM image of a group of four micromirrors shows the comb-drive (green) connect to the torsion-spring mounted mirror plate (red).

TABLE 5.1: The table shows the maximum deflection angle of the micromirror at their first and second resonance frequency.

\* These values were measured at a separate experiment

No.	1 <sup>st</sup> Res. Freq [kHz]	Deflection Angle [°]	2 <sup>nd</sup> Res. Freq [kHz]	Deflection Angle [°]	comments
1	2.499	6.6	11.74 / 12.46	11.34 / 24.8	double peak
2	12.16	41.5	48.64*	77.3*	used in Chapter 7
3			16.86	43.6	used in 6.1
4			10.91	9.9	
5	2.587	4.7	10.34	38.0	
6	8.954	6.6	17.89	57.8	
7	3.214	8.1	11.91	39.4	used in 6.2
8	9.73	9.5	19.46	53.8	used in 6.3.1
9	8.937	8.1	17.89	51.1	burnt
10	8.953 / 9.613	8.4 / 8.4	17.88	52.5	double peak
11	10.33	35.5	22.05	57.5	not used
12	10.31	17.6	20.6	43.5	not used
13	9.78	8.8	16.24	32.5	

The micromirrors showed two resonances. Two types of resonance modes cause large changes in the deflection angle. Firstly, the tilt mode, where the mirror surface rotates around torsion spring, causing a change in deflection orthogonal to the torsion spring (see Fig. 5.4, a, taken from [133]). Secondly, a micromirror on a torsion spring can resonate along the axis of the torsion spring (see Fig. 5.4, b), this mode is called the flexural mode [133]–[135]. Here, the deflection angle is along the axis of the torsion spring. The flexural mode shown in Fig. 5.4, b is the second flexural mode. The first resonance mode creates a piston-like movement. This is caused by the comb-drives displaced in the same direction from the normal position (unlike shown in Fig. 5.4, where they are displaced in opposite directions).

As the resonance modes measured on the micromirrors were deflecting in the same direction, they can only be either of type a or type b, not mixed. As the tilt mode does not lend itself to higher resonance modes, the first resonance measured with the micromirrors is the one shown in Fig. 5.4, b, which is really the second flexural mode. The secondary resonance mode is thus the fourth resonance mode, resulting in larger deflection angles.

## 5.2 Pulse Width and PRF

The first step towards integrating the miniaturised MEMS Q-switched Nd:YAG laser into the PA setup was to characterise the laser output. The laser pulse shape and

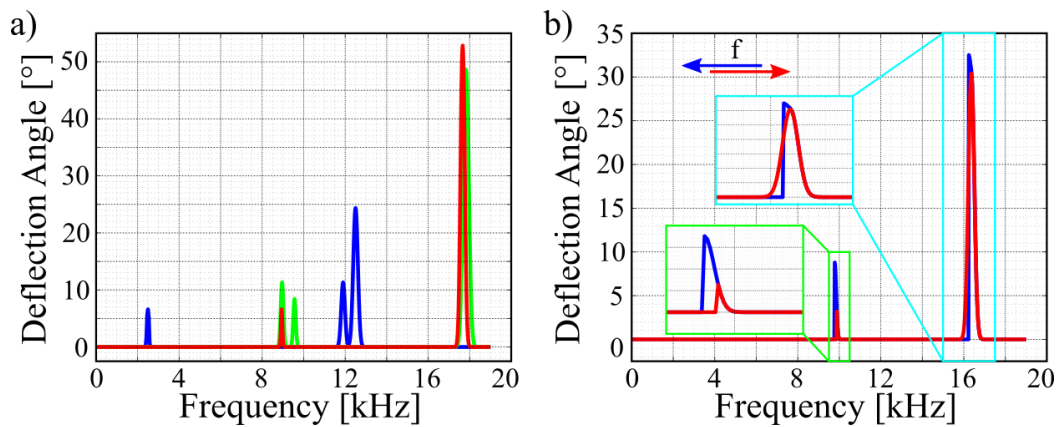


FIGURE 5.3: The deflection angle is shown for actuation frequencies ranging from 2 kHz to 25 kHz in  $\Delta f = 10$  kHz steps. In general, the micromirrors had two resonance frequencies (see a, shown for mirror 9, red). Mirrors 1 (see a, blue) and 10 (see a, green) showed double peaks for the second and first resonance frequency, respectively. The shape and maxima of the deflection angles of mirror 13 (see b) were dependent on the direction of the sweep (red: increasing, blue: decreasing). The first resonance frequency (see green inset) shows the deflection angle to be three times larger when the frequency is decreased. For the second resonance frequency (cyan inset) the shape of the deflection angle over the actuation frequency changes from near-Gaussian (increase) to a drop to zero (decreasing).

a) tilt mode



b) flexural mode



FIGURE 5.4: shows the resonance modes of a micromirror on torsion springs (from [133]). For the tilt mode (a) the mirror rotates around the torsion spring and in flexural mode the resonates around the axis orthogonal to the torsion spring but in plane with the mirror surface.

pulse width of the MEMS Q-switched laser were measured to estimate its feasibility to induce PA waves. Additionally, the pulse repetition frequency was measured to be able to calculate the pulse energy and the averaging potential during data acquisition of the PA waves.

After checking all the initial alignments of the different optical components in the laser cavity, the MEMS Q-switched Nd:YAG laser was operated by electrically driving the MEMS scanning mirror at its resonance frequency of  $f_M = 16.859 \text{ kHz}$ . The micromirrors are actuated under a harmonic driving scheme. Thus, the actual movement frequency is the actuation frequency halved. As the cavity is closed twice per cycle, the PRF should equal the actuation frequency. Afterwards, the pump power of the pump diodes (see Fig. 5.1) was slowly increased using the diode-controller module, thus increasing the energy output of the laser to its continuous operating power of  $P \approx 150 \text{ mW}$ . The laser was allowed to warm up and stabilise for  $t = 45 \text{ min}$ . Afterwards, the laser beam was reflected from two consecutive microscope slides and redirected onto a photodiode (AEP X55, Panasonic). The photodiode was connected to an oscilloscope (Agilent Infiniium). An averaged ( $n = 256$ ) laser pulse was recorded with a sampling frequency of  $f_s = 2 \frac{\text{GSa}}{\text{s}}$  and a train of 11 consecutive laser pulses was recorded with a sampling frequency of  $f_s = 50 \frac{\text{MSa}}{\text{s}}$  and averaged over 256 samples.

The pulse shape of the pulsed laser output is shown in Fig. 5.5 (a). The laser pulse has a Gaussian pulse shape with a FWHM of  $\tau = 50 \text{ ns}$ . The simulation (see chapter 2) using this pulse shows that the frequency spectrum of a PA wave generated using this laser pulse has a centre frequency of 5.5 MHz and a -6 dB bandwidth of 16 MHz (see Fig. Fig. 5.5, b).

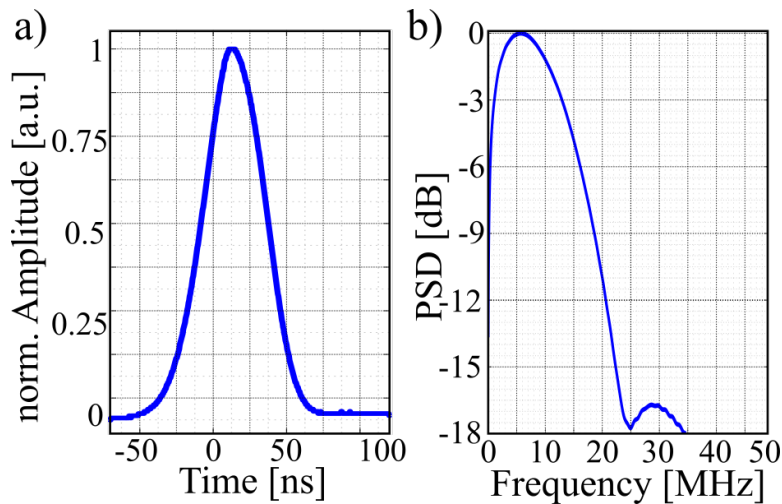


FIGURE 5.5: The recorded laser pulse (a) has a pulse width (FWHM) of  $\tau = 50 \text{ ns}$ . The simulated frequency spectrum of a generated PA wave (b) shows a centre frequency of 5.5 MHz and a -6 dB bandwidth of 16 MHz.

The PRF can be calculated from the period  $T$ . The period, measured from the recorded



pulse train (see Fig. 5.6), was  $T = 118.6 \mu\text{s}$ , thus giving a PRF of  $PRF = 8.43 \text{ kHz}$ . The calculated PRF is half of the actuation frequency of the MEMS mirror with  $f_M = 16.859 \text{ kHz}$ . This is caused by an orthogonal tilt during the movement and the way the micromirror was aligned. The amplitude variation of the recorded pulse train is caused by a non-suppressible 100 Hz noise of the pump diode driver. According to Fig. 5.5 (a) this resulted in a minimum value of 80 % of the maximum amplitude.

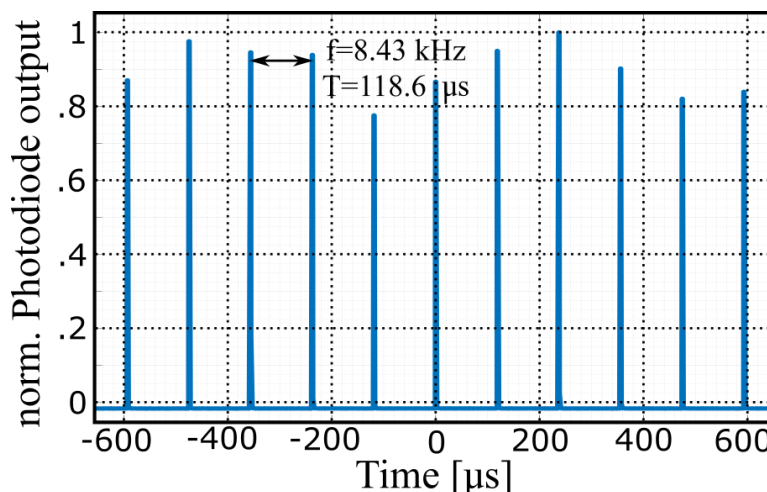


FIGURE 5.6: The recorded laser pulse train shows a period of  $T = 118.6 \mu\text{s}$  between the consecutive pulse, resulting in  $PRF = 8.43 \text{ kHz}$ .

### 5.3 Maximum Pulse Energy and Power

Initially, the maximum pulse power and pulse energy were recorded for the MEMS Q-switched laser system. Subsequently, the power trend over the start up period was recorded at a lower power level used for sustained long-term operation. The MEMS Q-switched laser system was started up as described above. A beam block was inserted into the beam path and the laser system was allowed to warm up for  $t = 30 \text{ min}$ . A powermeter (Gentec E0 Solo PE, Gentec Electro-Optics, Canada) with a high-power meter head (UP19K-15s-VM-DO, Gentec Electro-Optics, Canada) was placed into the beam. The power meter was set to measure the power over a time  $t = 5 \text{ min}$  and evaluate the measured data to give the average output power  $\bar{P}$  as well as its standard deviation  $\sigma_P$  ( $f_{\text{samp}} = 1 \text{ Hz}$ ). Then, the laser was turned off and let cool down for a day to correctly measure the start-up behaviour of the laser output power. Here, the laser was started up the same way as above and an averaged power reading (with an acquisition time of  $t_{ac} = 30 \text{ s}$ ) was taken every minute for 65 minutes. The average maximum output power  $\bar{P}$  and its standard deviation  $\sigma_P$  were measured as:

$$\bar{P} = 202 \text{ mW} \quad \text{and} \quad \sigma_P = 1.5 \text{ mW}$$

From this the maximum pulse energy  $E_{max}$  can be calculated as:

$$E_{max} = \frac{\bar{P}}{f_{PRF}} \quad (5.1)$$

$$E_{max} = \frac{202 \text{ mW}}{8.43 \text{ kHz}}$$

$$E_{max} = 23.96 \text{ } \mu\text{J}$$

The maximum achievable pulse energy of the MEMS Q-switched Nd:YAG laser system is  $E_{max} = 23.96 \text{ } \mu\text{J}$ , which is a 3-fold the pulse energy compared to previously reported pulse energies generated from a MEMS Q-switched laser [38], [39]. The start-up behaviour of the laser (see Fig. 5.7) shows an increase in power for the first ten minutes. Afterwards, the power decreases and approaches a steady level of  $\approx 90\%$  of the maximum at about  $t = 60 \text{ min}$ . Compared to the start, the standard deviation  $\sigma_P$  has doubled at the time point  $t = 50 \text{ min}$  and stayed constant afterwards. The change in output power is potentially caused by thermal lensing effects in the crystal.

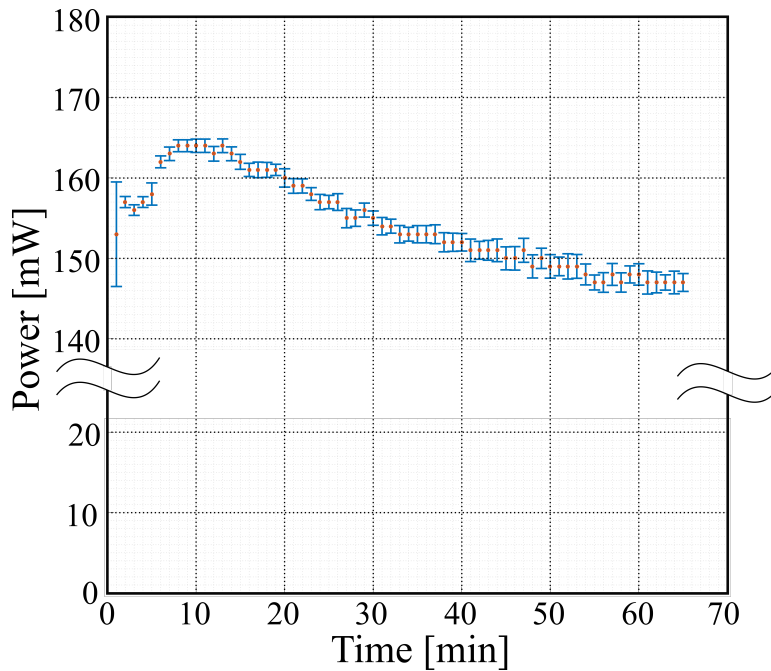


FIGURE 5.7: The average power measured each minute for the first 65 minutes of the startup phase of the laser shows an initial increase in power output. After reaching its maximum the power output decreases to a stable output of  $\bar{P} \approx 150 \text{ mW}$ .

## 5.4 Laser Spot size and Focal point size

The beam diameter near the output coupler of the MEMS Q-switched Nd:YAG laser ( $\lambda = 1064 \text{ nm}$ ) and the focal spot diameter were tested to characterise the output laser optical beam. Before the beam profile near the output coupler of the MEMS enabled laser system was measured the laser was started up and stabilised as described above. An operating power of  $\bar{P} = 157 \text{ mW}$  was measured using a powermeter (Gentec E0 Solo PE, Gentec Electro-Optics, Canada). As this power was too high for the CMOS camera used for imaging the beam profile (WinCAMD-LCM, DataRay Inc.), it was decreased using neutral density filters (NEK01, Thorlabs) with a total optical density of  $OD_{tot} = 4.1$ . This reduced the average power to  $\bar{P}_{4.1} = 12.47 \mu\text{W}$ . The CMOS camera was inserted into the beam path and its software was used to measure and image the beam profile.

The image of the beam spot captured with the CMOS camera shows high intensity spot (see Fig. 5.8, left), the base of which is bigger to one side of the x-axis. This can also be seen in the intensity graph of the x-axis (see Fig. 5.8, top right). Here, the base of is elongated in one direction. The intensity graph of the y-axis (see Fig. 5.8, bottom right) shows a quasi-Gaussian intensity distribution. The diameter (FWHM)  $d$  of the spot is  $d \approx 700 \mu\text{m}$  in both directions. This coincides with the diameter of the MEMS scanning mirror disc.

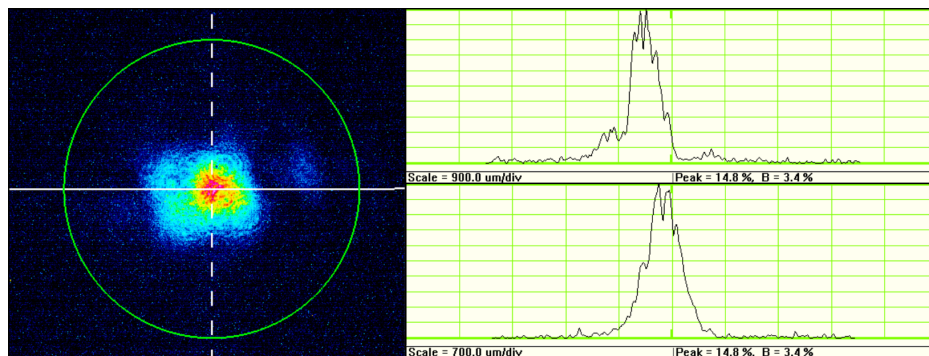


FIGURE 5.8: The image of the intensity of the beam spot (left) shows an elongation of the spot on the x-axis. This can also be seen on the x-axis intensity graph (top right) as a low-intensity plateau. The intensity on the y-axis (bottom right) follows a quasi-Gaussian curve.

The laser beam is guided to the focussing lens ( $f = 70\text{mm}$ ) using gold-coated mirrors at an optical distance of 1.5 m. The focal spot of the laser through this lens was measured using the knife edge technique. Here, a razor blade was mounted onto a motorised actuation stage (MTS50-Z8, Thorlabs). The razor blade was moved through the focused laser beam with a step length of  $\Delta x = 10 \mu\text{m}$  at different heights ( $\Delta h = 200 \mu\text{m}$ ). The laser power was measured behind the razor blade, indicating

how much of the beam's power is blocked. The power of all steps for each height were recorded. For each height the diameter was calculated as the distance between the point where the power was 25 % and 75 % of the maximum power, thus including 50 % of the power. The radius calculated from the knife edge measurements at various heights (see Fig. 5.9) shows a minimum focal spot radius  $r_f$  of  $r_f = 9 \mu\text{m}$ . Thus, the minimum measured focal spot diameter is  $d_f = 18 \mu\text{m}$ .

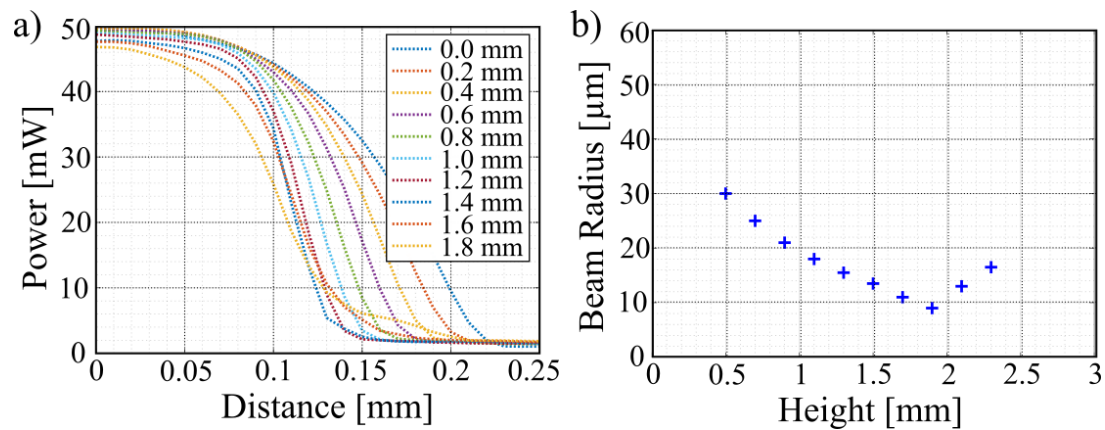


FIGURE 5.9: The data of the knife edge experiments (a) was measured at different heights ranging from 0 mm to 1.8 mm. The diameter was calculated as the distance between the 25 % and 75 % power points. The minimum measured focal spot radius is  $r_f = 9 \mu\text{m}$  (b).

## 5.5 Discussion and Conclusion

The move from the commercially available Nd:YAG (Brilliant B, see Chapter 3) to the MEMS Q-switched Nd:YAG laser resulted in changes in some of the laser parameters while other were comparable. The MEMS Q-switched laser had a Gaussian beam and the laser required a warm up period of about 30 min. The beam steering and forming resulted in a focal point diameter of  $d = 18 \mu m$ . The MEMS based Q-switching using a fast scanning MEMS micromirror to open and close the laser cavity resulted in a PRF approximately three orders of magnitudes higher than that of the commercial laser used previously. Additionally, the maximum pulse energy of the MEMS Q-switched Nd:YAG laser system was measured to be  $E_{max} = 23.96 \mu J$  - a 3-fold the pulse energy compared to previously reported pulse energies generated from a MEMS Q-switched laser.

The MEMS Q-switched Nd:YAG offered a PRF of  $8.43 kHz$ , a 843-fold increase over the previously used commercially available Nd:YAG. This offers the possibility of decreasing acquisition times. Additionally, the higher PRF yields potentially higher SNR by increasing averaging size. Thus, the presented MEMS Q-switched laser addresses both problems of the commercial Nd:YAG, i.e. the low PRF and the high pulse energy requiring heavy attenuation.



## Chapter 6

# All MEMS based PA system

The laser system based on fast scanning MEMS micromirrors presented in Chapter 6 was incorporated in to the PA system, replacing the commercial Nd:YAG laser. The performance of the different ultrasound transducers (presented in the Chapters 3 and 4) was compared using this laser as a PA excitation source. Then, using the different PMUT arrays, this all MEMS based PA system was applied to imaging of artificial targets in phantoms as part of an all-MEMS based PA imaging system. Afterwards, the shape of recorded traces over consecutive laser pulses was investigated. Finally, the all MEMS based PA scanning system was used to image artificial targets in a biological matrix. Finally, the performance of the all MEMS based PA imaging system compared to the all commercial system presented in Chapter 3.

### 6.1 Performance of the PA generation using the MEMS laser

The output of the MEMS Q-switched Nd:YAG laser ( $PRF = 8.43 \text{ kHz}$ ,  $\tau = 50 \text{ ns}$ ,  $\lambda = 1064 \text{ nm}$ ,  $E_{max} = 23.8 \text{ } \mu\text{J}$ ) was focused ( $f = 70 \text{ mm}$ ) onto an absorbing (0.4 % (m/m) India Ink) gelatine (8 % (m/m)) target to a focal spot size of  $d_f = 18 \text{ } \mu\text{m}$ . The laser was started up and its output power set to  $P_0 = 162 \text{ mW}$ , resulting in a pulse energy of  $E = 9.7 \text{ } \mu\text{J}$ . The generated PA waves were recorded using first the PMUT arrays and then the commercial US transducers. The target and the array in use were immersed in an oilbath (vegetable oil) for acoustic coupling. The relevant transducer was then positioned facing the laser spot, which was made visible using an Near-Infrared sensor card (F-IRC1, Newport) at a distance of  $l \approx 10 \text{ mm}$ . The laser was turned on and its power output reduced using the neutral density filters. The transducer output was amplified (+60 dB, HVA-10M-60B, FEMTO) and recorded using an oscilloscope (Agilent Infiniium) at sampling frequency of  $f_s = 500 \frac{\text{MSa}}{\text{s}}$ . For the PMUT arrays the output of all sub-arrays was combined giving the output of the whole array. The PA responses of five pulse energies were recorded for every transducer. The pulse energy was altered using neutral density filters ranging from  $OD = 0$  to  $OD = 2$ , resulting in pulse energies of  $E_{min} = 97 \text{ nJ}$  to  $E_{max} = 9.7 \text{ } \mu\text{J}$ . The first PA trace recorded was at  $E_{min} = 97 \text{ nJ}$  for all transducers to decrease the influence of potential ablation of the target material altering the subsequent results. The frequency spectra of the recorded PA waves was calculated by applying the FFT over a windowed (Hamming) part of the signal. The SNR was then calculated as

described in Section 3.4. Due to spatial and size constraints the commercial 2.25 MHz transducer had to be placed further away from the laser focal spot compared to the other smaller transducers. This increased distance was compensated for by multiplying the resulting SNR by a compensation factor  $f_{comp}$ , calculated as:

$$f_{comp} = \left(\frac{d_t}{d_{ref}}\right)^2 \quad (6.1)$$

Here,  $d_t$  and  $d_{ref}$  are the distance of the transducer and the reference distance, i.e. the distance of the other transducers to the focal spot.

### 6.1.1 Single-type Array

The PA wave induced in the target phantom at a pulse energy of  $E = 9.7 \mu\text{J}$ , averaged over 1024 samples and recorded with the single-type PMUT array is shown in Fig. 6.1 (a). It has an amplitude of  $130 \text{ mV}_{pp}$  and shows a superposition of two sinusoid signals. The frequencies of these can be identified in the calculated PSDs (see Fig. 6.1, c). The two peaks can be seen centred around  $f_1 = 1.3 \text{ MHz}$  and  $f_2 = 5.7 \text{ MHz}$ . They increase with increasing pulse energy; a 70 % decrease of the pulse energy results in a reduction of the frequency content to a quarter (compare blue to red). A further 90 % reduction of the pulse energy decreases the frequency content to noise level (see Fig. 6.1, bottom, black dotted line). The SNR in Fig. 6.1 (c) for both the first resonance frequency  $f_1 = 1.3 \text{ MHz}$  (blue) and the second resonance frequency  $f_2 = 5.75 \text{ MHz}$  (red) increase linearly with the pulse energy over its range. At the maximum pulse energy  $E = 9.7 \mu\text{J}$  their SNR is  $\text{SNR} \approx 150$  and  $\text{SNR} \approx 110$ , respectively. This decreases for both to noise level ( $\text{SNR} \approx 1$ ) at the lowest pulse energy of  $E = 97 \text{ nJ}$ .

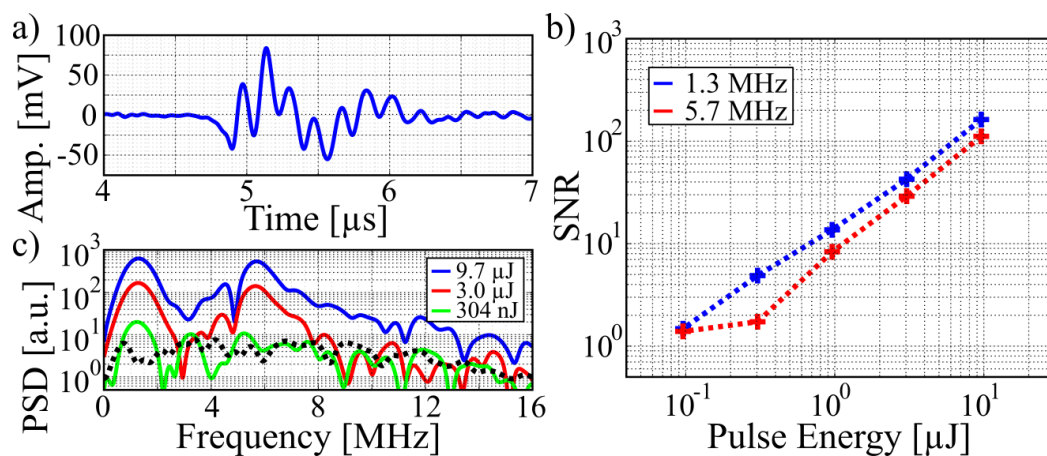


FIGURE 6.1: The trace recorded with the single-type array at a pulse energy of  $E = 9.7 \mu\text{J}$  has an amplitude of  $130 \text{ mV}_{pp}$ . The SNR (b) of the peaks increases with the pulse energy. The PSDs (c) shown at selected pulse energies show two main peaks at 1.3 MHz and 5.75 MHz. The black dotted line denotes the noise floor.



### 6.1.2 Multi-type Array

The second transducer used to record PA waves was the multi-type PMUT array. The trace shown in Fig. 6.2 (a) was recorded at a pulse energy of  $E = 9.7 \mu\text{J}$  and averaged over 1024 samples. It has an amplitude of  $75 \text{ mV}_{PP}$  and shows no clear underlying frequency, indicating a superposition of multiple resonance frequencies. This is to be expected, as the multi-type PMUT array consists of four sub-arrays with different dimensions and thus resonance frequencies (see Fig. 4.4). This can also be seen in the frequency spectra of the traces (see Fig. 6.2, c), derived by applying the FFT. Here, five peaks in the frequency content are shown. They are at  $f_1 = 1.4 \text{ MHz}$ ,  $f_1 = 3.4 \text{ MHz}$ ,  $f_1 = 5.5 \text{ MHz}$ ,  $f_1 = 8.1 \text{ MHz}$  and  $f_1 = 10.3 \text{ MHz}$ , resulting in a broad overall bandwidth. The amplitude of these peaks are decreasing with increasing frequency, but so is the noise floor (black dotted line). The amplitude of the frequency content decreases with decreasing pulse energy and reaches the noise floor at a pulse energy  $E = 304 \text{ nJ}$ . The SNR for the first three resonance frequencies  $f_1 = 1.4 \text{ MHz}$ ,  $f_1 = 3.4 \text{ MHz}$  and  $f_1 = 5.5 \text{ MHz}$  is shown in Fig. 6.2. The SNR of  $f_1$  is the highest at high pulse energies with  $\text{SNR} = 40$ , while those of  $f_2$  and  $f_3$  are  $\text{SNR} \approx 32$  and  $\text{SNR} \approx 25$ . The SNRs decrease linearly until an SNR of  $\text{SNR} \approx 1$  is reached at a pulse energy  $E = 304 \text{ nJ}$ .

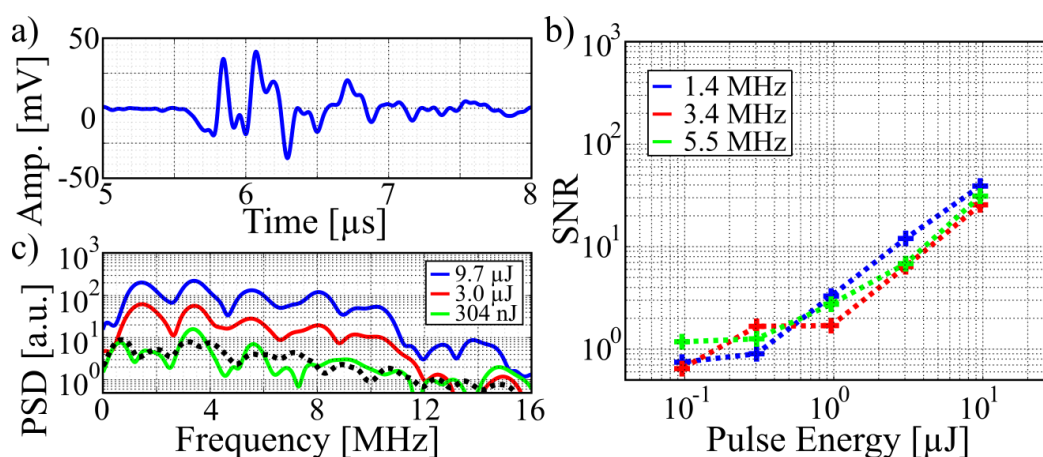


FIGURE 6.2: A trace (a) with an amplitude of  $75 \text{ mV}_{PP}$  was recorded with the multi-type array at a pulse energy of  $E = 9.7 \mu\text{J}$ . The resulting SNRs (b) of the  $1.4 \text{ MHz}$  peak (blue), the  $3.4 \text{ MHz}$  peak (red) and the  $5.5 \text{ MHz}$  peak (green) decrease linearly from  $\text{SNR} \approx 40$ ,  $\text{SNR} \approx 32$  and  $\text{SNR} \approx 25$ , respectively, to  $\text{SNR} \approx 1$  at  $E = 304 \text{ nJ}$  for these three major peaks.

### 6.1.3 Beam-Type Array

The bar-type PMUT array recorded a trace with an amplitude of  $4 \text{ mV}_{pp}$  when excited by a PA wave generated at  $E = 9.7 \mu\text{J}$  and averaged over 1024 samples (see Fig. 6.3).

The PSD derived from the signal reveals one prominent peak at 4.1 MHz. This result is comparable to the one recorded with the commercial Nd:YAG (see Fig. 4.27). Here, the 4 MHz band was the largest (3-fold higher) for pulse energies  $E_{pls} \leq 22 \mu\text{J}$ . Due to the stark decrease in sensing area, compared to the single-type and the multi-type PMUTs, the SNR is only significantly bigger than 1 for  $E = 9.7 \mu\text{J}$ , with an  $SNR = 4.2$ .

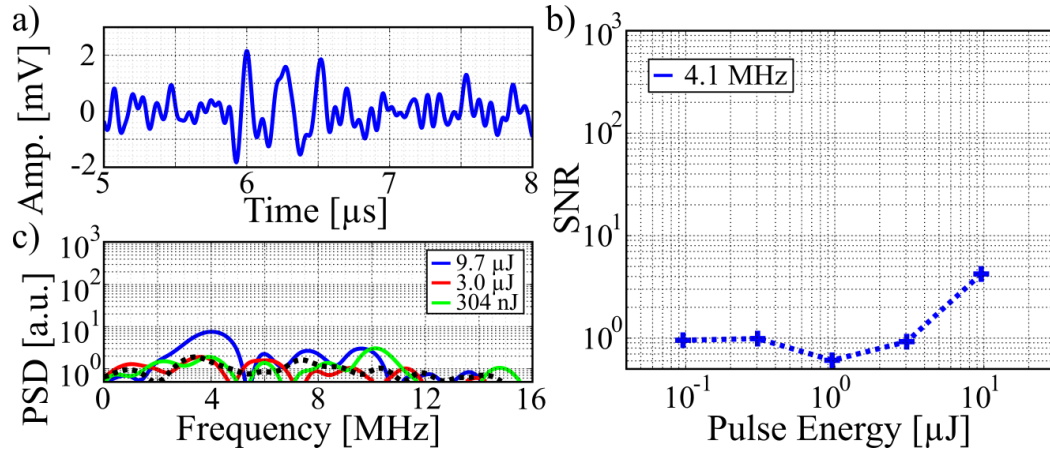


FIGURE 6.3: The trace recorded from the bar-type array (a) shows a very faint signal. This results in an  $SNR = 4.2$  for  $E = 9.7 \mu\text{J}$  while for lower pulse energies the  $SNR = 1$  (b). The faintness of the signal shows in its PSDs (c) as only for the highest pulse energy the 4.1 MHz peak is above the noise floor (black dotted line).

#### 6.1.4 Commercial Transducers

The performance of the commercial transducers was investigated again to directly compare their performance using the MEMS Q-switched laser to their PMUT counterparts. The trace recorded with the Olympus 2.25 MHz transducer (see Fig. 6.4, a) has an amplitude of  $21 mV_{pp}$ . This amplitude is much lower, compared e.g to the single-type PMUT array, as the distance of the transducer to the source is larger. This difference in distance was compensated with  $f_{comp} = 2.78$  for when calculating the SNR in accordance with eq. 6.1. The spectra of the recorded pulses (see Fig. 6.4, b) show a main peak at 2.3 MHz and a side peak at 7.3 MHz. The SNR of the main peak increases linearly with the pulse energy over its set range to a maximum of  $SNR \approx 210$ , while the SNR of the side peak saturates at a pulse energy of  $3.0 \mu\text{J}$  with an  $SNR \approx 21$ .

The trace recorded with the Olympus 10 MHz transducer (see Fig. 6.5, a) has an amplitude of  $220 mV_{pp}$ . The PSD calculated using the FFT on the recorded pulses (see Fig. 6.4, b) shows a main peak at 6.7 MHz. Its SNR increases with the pulse energy to a maximum of  $SNR \approx 320$ . With increasing pulse energy the rate of increase decreases, indicating that the sensor is nearing its saturation point. The reduction of

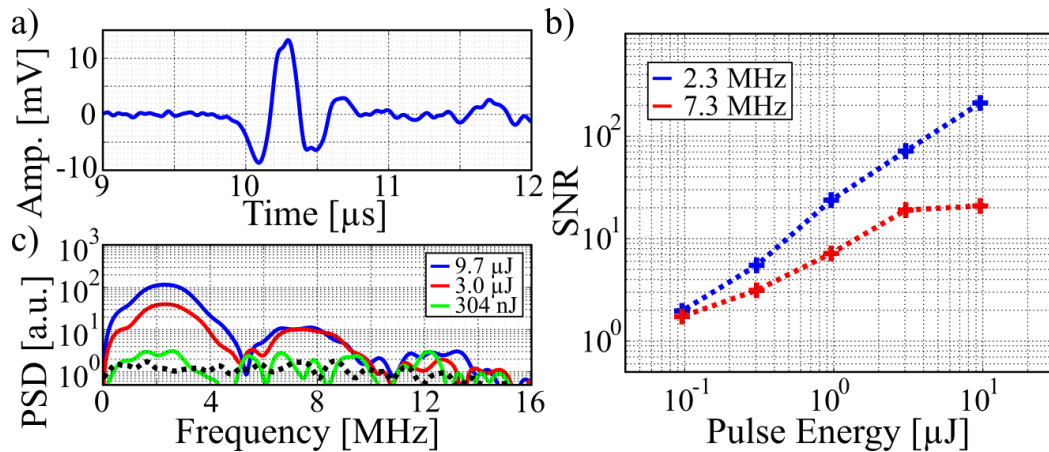


FIGURE 6.4: The trace (a) recorded using the commercial 2.25 MHz transducer at a pulse energy of  $E = 9.6 \mu\text{J}$  has an amplitude of  $21 \text{ mV}_{pp}$ . The SNR (b) of the peaks increases with the pulse energy from  $\text{SNR}_{min} \approx 2$  to  $\text{SNR}_{max} \approx 210$ . The PSDs (c) shown at selected pulse energies show two main peaks at 2.3 MHz and 7.3 MHz. The black dotted line denotes the noise floor.

the centre frequency 10 MHz centre frequency of this transducer is caused by the low-pass filtering effects described in Chapter 2.

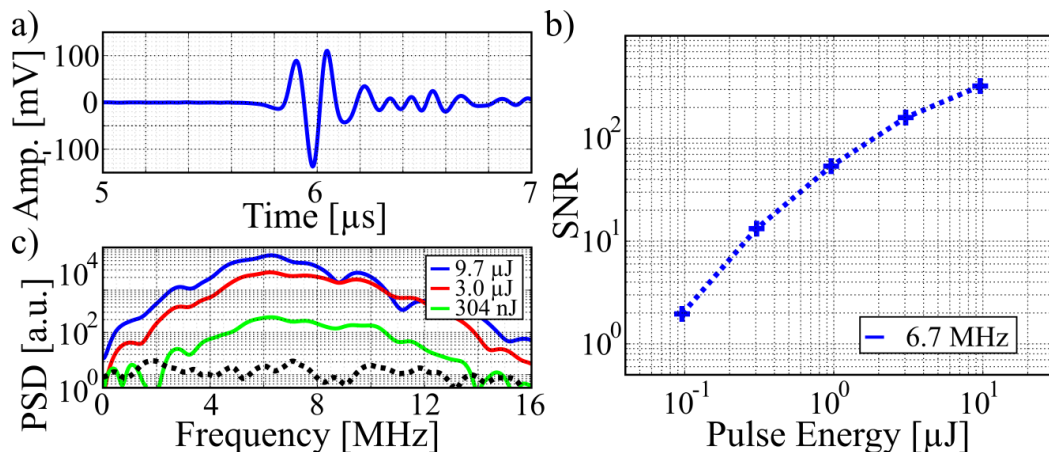


FIGURE 6.5: The trace recorded using the commercial 10 MHz transducer at a pulse energy of  $E = 9.6 \mu\text{J}$  has an amplitude of  $220 \text{ mV}_{pp}$ . The SNR (b) of the peak at 6.7 MHz increases with the pulse energy ranging from  $\text{SNR}_{min} \approx 2$  to  $\text{SNR}_{max} \approx 320$ . The PSD (c) shows a main peak at 6.7 MHz with a broad bandwidth of approximately 5 MHz. The black dotted line denotes the noise floor.

### 6.1.5 Comparison of SNRs

Comparing the SNRs of the five transducers (see Fig. 6.6) shows that the commercial 10 MHz transducer (black) achieves the best SNR with a maximum of 320, while the bar-type PMUT array yields the lowest (cyan) with a maximum of 4. The latter is followed by the multi-type PMUT array with a maximum at 35. The single-type transducer array and the commercial 2.25 MHz transducer perform similarly well, with a maximum SNR of 210. None of the presented transducers record a distinguishable signal ( $\text{SNR} > 5$ ) for pulse energies below 200 nJ. Therefore, SNR-wise the best laser-transducer combination is the MEMS Q-switched laser combined with the commercial 10 MHz transducer. This combination is followed by equally good pairings of MEMS Q-switched Nd:YAG and single-type PMUT array as well as MEMS Q-switched Nd:YAG and commercial 2.25 MHz transducer. Considering the much smaller footprint of the single-type PMUT array and thus its ability to sense from a closer distance (as the NFD is lower) and thus higher signal strength and its potential to increase the surface area by using several arrays, the single-type PMUT array can be argued to be better than the commercial 10 MHz transducer.

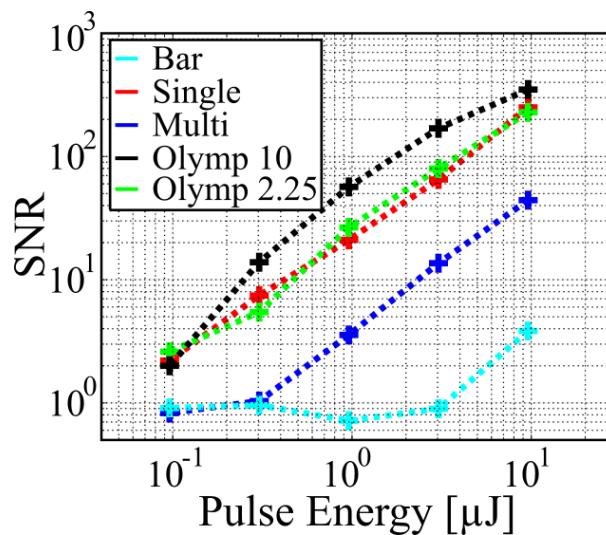


FIGURE 6.6: The figure shows the SNRs of the first main peaks of the bar-type PMUT (cyan), the single-type PMUT (red), the multi-type PMUT (blue), and the commercial 2.25 MHz (green) and 10 MHz (black) transducers. The latter performs best, while the 2.25 MHz transducer and the single-type PMUT perform equally well.

The performance of an all MEMS system, comprised of the MEMS Q-switched laser generating PA waves detected using the single-type PMUT array, was compared to an all commercial system, using the Brilliant B and the commercial 2.25 MHz transducer. To compare the performance, the influence of the repetition rate was considered as well. As the much higher repetition rate of the MEMS Q-switched laser, which was

$f_{MEMS} = 8.43 \text{ kHz}$  compared to  $f_{COM} = 10 \text{ Hz}$  for the Brillant B, allowed for a much higher sample size for averaging. This is addressed by using an averaging size of 1024 samples for the MEMS based system and an averaging size of 4 samples for the commercial components based system. The SNR data of the MEMS based PA system is compared at an averaging size of 256. This compensates for the slightly reduced real acquisition rate of this system caused by the acquisition software and hardware, i.e. the LabVIEW code and the used NI chassis. Further improving the acquisition software would cause the acquisition rate to be only limited by the repetition rate of the laser. Considering this, the all MEMS system shows an SNR of up to 10 times the SNR of the all commercial system (see Fig. 6.7).

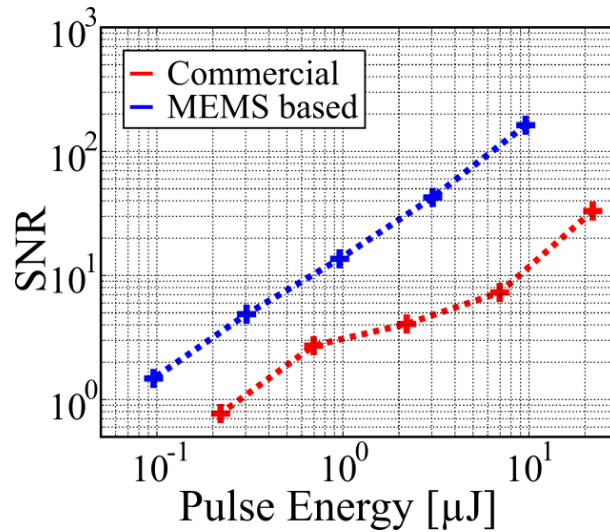


FIGURE 6.7: A comparison of a MEMS based PA-system (blue, average size of 256 elements) and a commercial components based system (red, average size of 4 elements) shows the former outperform the latter. This takes into account the different acquisition rates, due to the difference in laser repetition rates.

## 6.2 Analysis of the PA wave train

With a laser repetition frequency around three orders of magnitudes larger than the previously used commercial laser, we want to demonstrate the system's ability to detect and record PA signals at this rate. The elements of the recorded transducer traces were investigated by recording (Agilent Infiniium,  $f_s = 50 \frac{MSa}{s}$ ) consecutive PA pulses averaged over a sample size of 1024 using the single-type transducer. A different micromirror was used for Q-switching resulting in a different actuation frequency ( $f_{act} = 11.91 \text{ kHz}$ ,  $\tau = 44.3 \pm 1.23 \text{ ns}$ ) due to design variations. The PA waves were generated at an average power of  $\bar{P} = 55.1 \text{ mW}$ , resulting in a pulse energy of  $E_{PLS} = 4.63 \mu\text{J}$ . Figure 6.8 shows the recorded trace from the PMUT array

(blue), the signal recorded from the photodiode (red), showing the laser pulses, and the square wave actuation frequency (green) generated by the signal generator. Each laser cycle generated five spikes visible in the signal trace. The first spike (a) corresponds to the main Q-switching of the laser as described in Section 3.3.2, and is caused by electromagnetic interference due to the laser firing. The generated PA wave is recorded 5.3  $\mu\text{s}$  later at the second spike (b). The third and the last spikes (c & e) are generated due to electromagnetic interference from the amplified square wave actuation of the micromirror. The fourth spike (d) is caused - like the first spike - by the Q-switching of the laser. The energy recorded from this laser pulse using the photodiode is however, at 4 % of the amplitude of the initial laser pulse. This reduction in pulse energy is due to the misalignment of the micromirror during the rotation in the reverse direction. Thus, any generated PA response is not visible in the noise background. The photodiode trace is further reduced by misalignment of the photodiode with respect to the second (off-axis) pulse. The time period between the laser pulses is thus 41.95  $\mu\text{s}$  and thus twice the repetition frequency of  $f_R = 11.91 \text{ kHz}$ . This is expected due to the harmonic driving scheme of the micromirrors. The time period of the PA wave excitation pulses is 83.9  $\mu\text{s}$ .

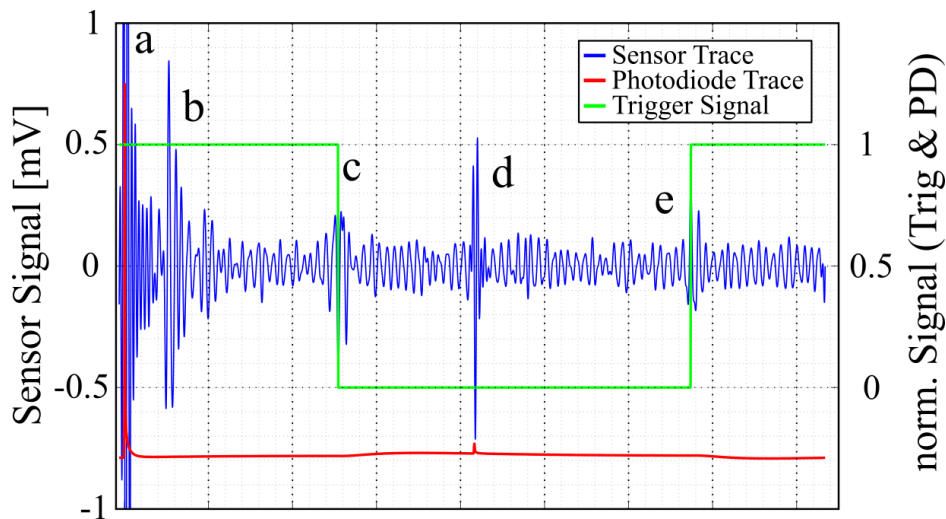


FIGURE 6.8: The signal train of the ultrasound transducer (blue), the photodiode (red) and the signal generator (green) show the recorded spikes (a-e). The first and fourth (a, d) spike coincide with signals from the photodiode and are caused by electromagnetic interference from the laser triggering (see 6.8). The second signal is the PA response. The third and fifth spike coincide with the change in the square trigger signal and are caused by electromagnetic interference. The period between the laser pulses exciting a PA response is 83.9  $\mu\text{s}$ .

### 6.3 Target imaging

With its components characterised, the all-MEMS PA scanning system was used to image targets in gelatine phantoms. The targets used were polyimide coated fibres (used previously in chapter 3.5.2) and suture threads coated with carbon particles. The system (shown in Fig. 6.9) consists of the MEMS Q-switched laser, a beam steering and forming part, and the target which was acoustically coupled to the PMUT array using an oilbath. The PMUT's output is amplified (DHPVA-200, FEMTO) and fed into an NI PXI chassis (National Instruments, NI PXIe-5122). Here, the data from the PMUT array and the photodiode are recorded and the xyz-stage, moving the target, is actuated. The laser beam is redirected onto a lens ( $f = 70 \text{ mm}$ ) using a gold-coated mirror ( $R = 99\%$ ). Before the mirror a fraction of the beam is redirected as a trigger signal for the data acquisition on the NI PXI chassis. The chassis ran a custom-written LabVIEW script triggering, recording and averaging the data, while also moving the translation stage into the relevant position.

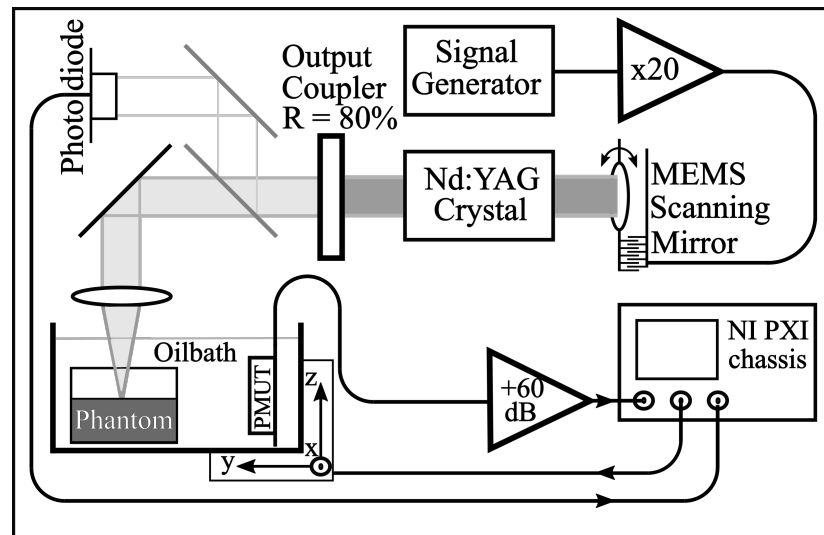


FIGURE 6.9: The all-MEMS PA scanning system used for the scanning experiments consists of the MEMS Q-switched laser, a beam steering and forming part, and a signal detection and data acquisition part. The latter consists of an amplified PMUT array, which is acoustically coupled to the target. Its output is digitised using an NI PXI chassis running a LabVIEW script actuating the translation stage and triggering the data acquisition via the photodiode input.

#### 6.3.1 Fibre scans

The cross-section of a polyimide coated fibre was imaged using the all-MEMS system. The PA waves were generated using pulse energies of  $E_S = 1.27 \mu\text{J}$  and  $E_M = 1.63 \mu\text{J}$  using the single-type and the multi-type PMUT array, respectively.

Firstly, using the single-type PMUT array the fibre cross-section was scanned over in the x-direction with 51 steps at  $\Delta x = 10 \mu m$  and in the h-direction with 43 steps at  $\Delta h = 30 \mu m$ . The PMUT array was placed at a distance of 6.5 mm from the focal point of the laser. The signal was recorded at a sampling frequency of  $f_s = 100 \frac{MSa}{s}$  and its power was evaluated for two bands with centre frequencies of 1.4 MHz and 6.3 MHz (see Fig. 6.10 a and b, respectively). The scanned images are shown in Fig. 6.10 a (1.4 MHz band) and b (6.3 MHz band). The former shows the cross-section, elongated due to the Rayleigh length of the focal spot, to be  $100 \mu m$  by  $700 \mu m$  (FWHM, x by h). Due to the modal shape of the response the size is more difficult to estimate using the FWHM for the latter. Using the three local maxima assumed to be on an ellipse the size can be estimated as  $150 \mu m$  by  $750 \mu m$ .

In the image derived from the 6.3 MHz band (see Fig. 6.10 b) the fibre cross-section displays a higher mode shaped (similar to the simulated resonating disc, see Table 4.1, 3) response. This can also be seen in the traces (6.10 c). Here, the trace from the centre (red, red cross in (a, b)) shows a sinusoidal response whereas the edge's trace (6.10 c blue, blue cross in (a, b)) shows two superimposed sinusoidal signals. The green trace shows the background noise (6.10 c green, green cross in (a, b)). This can be seen better in the respective PSD (6.10 b), while the frequency content of the first peak is roughly equal between these two traces, it is about 3 times higher for the trace recorded on the edge of the fibre. This modal response is probably caused by circumferential guided waves induced in the outer polyimide layer [136]. This means that while the low ( $f < 2$  MHz) frequency can be used to image the contour of a target, higher order acoustic effects can be used to gain information about the target composition. In this case this information is that it is a coated fibre in which the acoustic wave propagates.

Secondly, the fibre cross-section was imaged at 26 steps in the x-direction with  $\Delta x = 10 \mu m$  and 34 steps in the h-direction with  $\Delta h = 30 \mu m$  using the multi-type PMUT array. The PMUT array was positioned at a distance of 5 mm to the focal spot of the laser. The signal power of the recorded traces was evaluated for the 2.6 MHz and the 3.7 MHz peak. The former (see Fig. 6.11, a) shows the fibre to have a  $100 \mu m$  by  $400 \mu m$  (x by h) cross-section. As with the single-type PMUT array, the image evaluated from the secondary peak (see Fig. 6.11, b) shows a modal pattern. Its dimensions are estimated in a similar fashion to the modal pattern detected with the single-type PMUT array as  $200 \mu m$  by  $750 \mu m$ . Here, it is of a higher order mode shape (similar to the simulated resonating disc, see Table 4.3, 3) with the lower right peak of higher intensity. While this modal pattern cannot be easily spotted in the traces (see Fig. 6.11, c), it is clearly visible in the PSDs (see Fig. 6.11, d) where the frequency content of the secondary peak of the traces at the edge is 2.5 - fold compared to the centre traces. It is caused by circumferential guided waves induced in the outer polyimide layer [136], which offer the possibility to characterise the composition of the target for higher frequencies ( $f > 2$  MHz). The lower ( $f < 2$  MHz) frequency can be used to image the contour of a target.



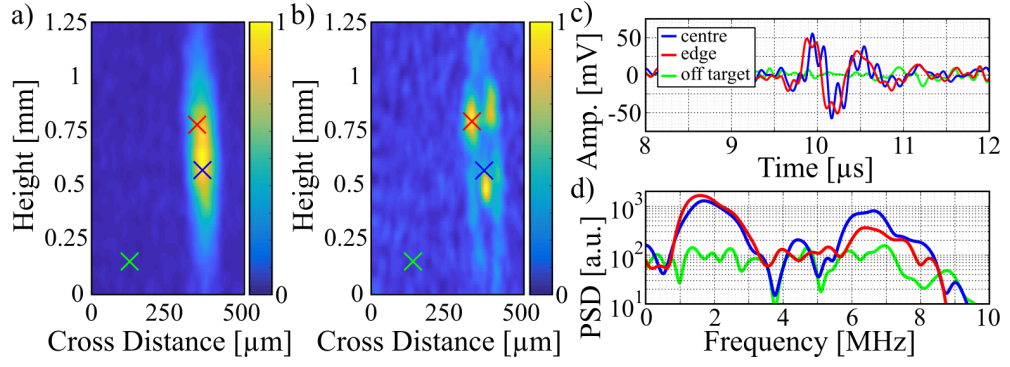


FIGURE 6.10: The scanned cross-section shown for the peak centred at 1.4 MHz (a) shows the fibre cross-section with dimensions of  $100 \mu\text{m}$  by  $700 \mu\text{m}$  (FWHM,  $x$  by  $h$ ). Using the power of the 6.3 MHz peak (b) reveals a (3,1) mode shaped response. This is also visible in the traces (c) as a sinusoid with one major frequency for traces in the centre (red, see cross in (a) for origin) and two superimposed frequencies for traces from the edge (blue, see cross in (a) for origin), while the off-target trace (green, see cross in (a) for origin) shows no signal. This can be more clearly seen in the PSDs (d) where the frequency content of these two is about the same in the first peak, but the edge-trace's is a 3-fold in the secondary peak compared to the centre's.

The cross-section of a fibre ( $d = 100 \mu\text{m}$ ) was imaged at different pulse energies to investigate at which point the received signal power would be too low to differentiate a target from the noise background. Furthermore, with these experiments the previous SNR experiments (see Fig. 6.6) can be put into relationship with the fibre scans above. A PCF was scanned at pulse energies ranging from  $372 \text{ nJ}$  to  $135 \text{ nJ}$ . The scans were done using 25 steps at  $\Delta x = 10 \mu\text{m}$  in the  $x$ -direction and 22 steps at  $\Delta h = 25 \mu\text{m}$  in the  $h$ -direction. The single-type PMUT array was placed 5 mm from the focal point of the laser. Its output was recorded at a sampling frequency of  $f_s = 100 \frac{\text{MSa}}{\text{s}}$  and averaged over 1024 samples. In between measurements the position of the fibre was altered slightly to prevent any photo-bleaching and ablation processes from occurring and falsifying the results. The traces (see Fig. 6.12, a) are shown and colour-coded relating to the energies used. The same colour can also be found surrounding the related scan image (c - g). The PSDs (see Fig. 6.12, b) show low energy content in the first resonance band (0.7 MHz - 1.7 MHz) and larger frequency content for the second resonance frequency band (5.2 MHz - 6.3 MHz). In general, the SNR decreases with decreasing pulse energy and the apparent movement of the target is due to the above mentioned repositioning. When compared to the noise floor (black) the former has an SNR ranging from 1 to 7 while the latter has one ranging from 5 to 10. Thus, the second band was used to calculate the signal power and to reconstruct the scanned images. The images show good contrast for pulse energies  $E \geq 285 \text{ nJ}$  (c - e). Afterwards the contrast starts to

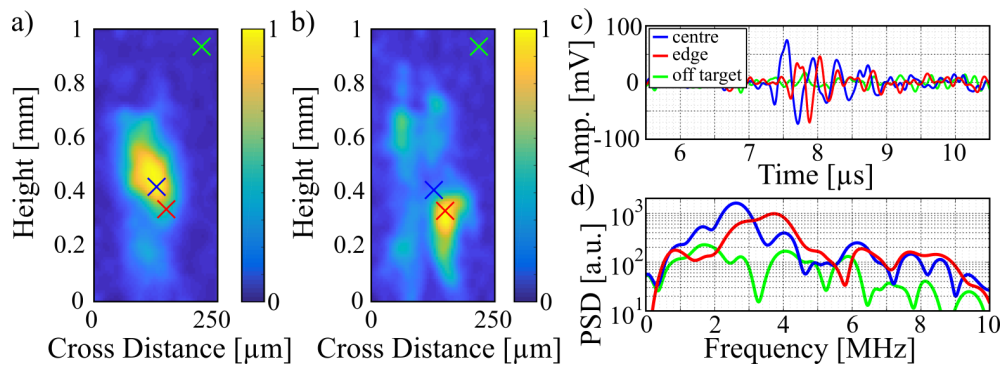


FIGURE 6.11: The cross-section scanned using the multi-type PMUT array shows the fibre cross-section with dimensions of  $100 \mu\text{m}$  by  $400 \mu\text{m}$  ( $x$  by  $h$ ) when using the first peak for calculating the signal power (a). Imaging the secondary peak's power distribution (b) reveals a 4,1 modal shape with the lower right of higher intensity. The centre and the edge traces (c, blue and red, respectively, see cross in (a) for origin) are of the same shape with the latter being of lower amplitude. The difference in power between these two can be seen from the PSD (d). Here, the edge has 2.5 - times the signal power in the secondary peak compared to the centre trace.

decrease noticeably. Even though the contrast for  $E = 175 \text{ nJ}$  (f) is noticeably lower compared to images taken at higher pulse energies, the target can still be easily distinguished. Thus, targets can be imaged with pulse energies  $E \geq 175 \text{ nJ}$  when averaging over 1024 samples. To image targets at lower pulse energies either the averaging size needs to be increased or the distance of the focal point to the transducer reduced.

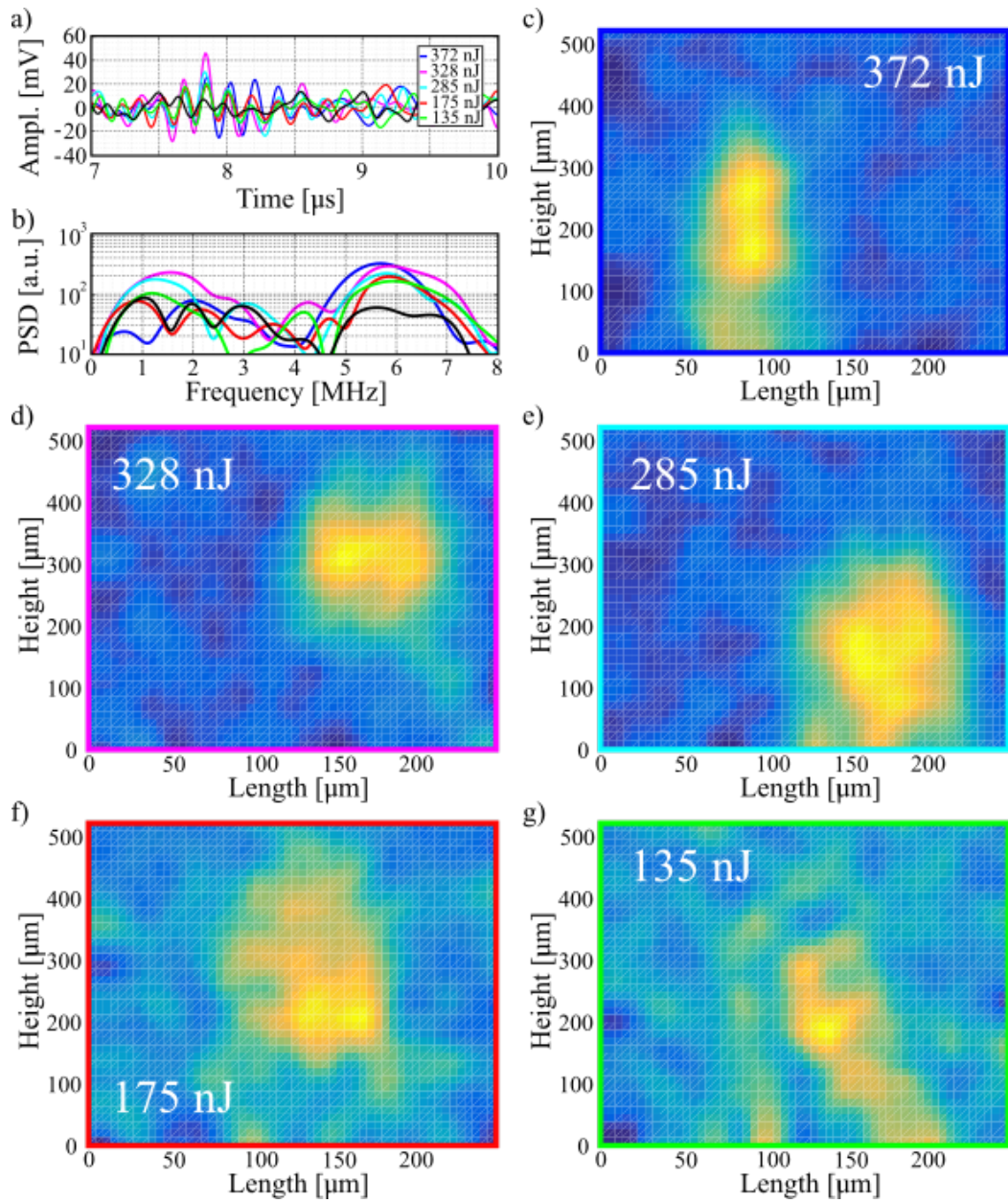


FIGURE 6.12: The traces of the cross-section of the PCF ( $d = 100 \mu\text{m}$ ) centre point (a) are shown for the used pulse energies, their amplitudes range from  $30 mV_{PP}$  to  $70 mV_{PP}$  for 135 nJ and 372 nJ, respectively. Their respective PSDs (b) show two peaks. The signal in the second resonance band at 5.2 MHz - 6.3 MHz is stronger. The scan images mapping the calculated signal power (c - g) from this band are shown with the respectively coloured edges.

An additional cross-section of a fibre was imaged to show that the presented system can image a target even through turbid media. For this a PCF ( $d = 100 \mu\text{m}$ ) was embedded in a clear gelatine matrix. This matrix was then covered with a 4.5 mm layer of gelatine mixed with 7.5% ( $m/m$ ) of milk (see Fig. 6.13, b). This resulted in an effective scattering factor of  $\mu'_s = 0.15 \text{ mm}^{-1}$  [137]. This 4.5 mm layer thus reassembles the scattering of a 1 mm layer of epidermis ( $\mu'_s = 0.6 \text{ mm}^{-1}$ ) [138], [139]. The lasers pulses were generated at a repetition frequency of  $f_R = 9.73 \text{ kHz}$  at a pulse energy of  $E = 3.47 \mu\text{J}$ . The scans were done using 51 steps at  $\Delta x = 10 \mu\text{m}$  in the x-direction and 51 steps at  $\Delta h = 50 \mu\text{m}$  in the h-direction. The output of a single-type PMUT array, placed at a distance of 8 mm from the focal point, was recorded at a sampling frequency of  $f_s = 100 \frac{\text{MSa}}{\text{s}}$  and averaged over 256 samples. The target dimensions seen from the scan image are  $0.2 \text{ mm}$  by  $1.3 \text{ mm}$  (x by h). Comparing this imaged size to the size of a PCF in a non-scattering medium (see Fig. 6.10, a) indicates, that the focal spot size and the axial resolution have doubled and the Rayleigh length tripled due to scattering effects. The image has a very good contrast between on and off-target. The broadening of the target dimensions compared to previous clear gelatine experiments is due to the broadening of the focal point caused by the increased scattering factor.

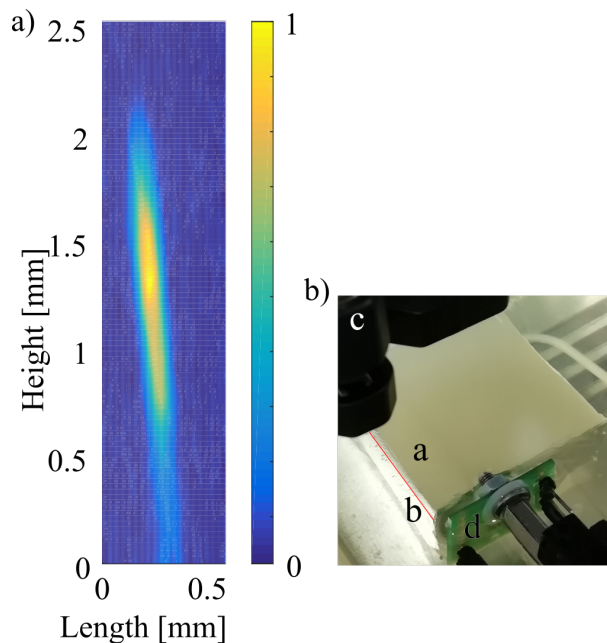


FIGURE 6.13: The image mapping the signal power (a) shows the target with dimensions of  $0.2 \text{ mm}$  by  $1.3 \text{ mm}$  (x by h). The photograph of the used phantom with the 4.5 mm high scattering layer is shown in b and consisted of a 4.5 mm scattering layer (a) and a clear layer (b). The separating line is emphasised (red line). The lens-holder (c) and the PCB-mount for the PMUT array (d) are also shown.

The recorded trace (see Fig. 6.14, a) from the fibre centre has an amplitude of 190 mV. The PSDs (see Fig. 6.14, b) and resulting signal power mapping (see Fig. 6.13, a) show a resulting  $SNR \approx 30$ . Thus showing that the all MEMS PA-scanning system can image targets under high-scattering media.

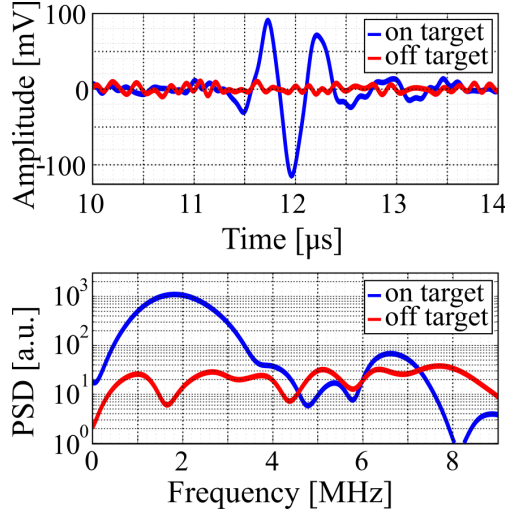


FIGURE 6.14: The recorded traces (a) show that the on-target trace (blue) has an amplitude of  $V_{PP} = 190$  mV and the off-target trace (red) one of  $V_{PP} = 20$  mV. Their respective PSDs show an  $SNR \approx 30$ .

Similarly to the all-commercial system (see 3.5.2), a scan along the length of an embedded PCF ( $d = 100$   $\mu$ m) was performed using the all MEMS based PA system. The target was scanned in x-y- direction with a step size of  $\Delta x = 10$   $\mu$ m and  $\Delta y = 50$   $\mu$ m, resulting in an imaging plane of 0.43 mm by 1.25 mm (x by y). The step size in y-direction is larger as the rate of change in the x-direction was anticipated to be larger, as the fibre was only 100  $\mu$ m in diameter but relatively well aligned in the y-direction. The scan took  $t = 59$  min. The PA waves were generated at a pulse energy of  $E = 586$  nJ and a PRF of  $f_{rep} = 8.43$  kHz. The image (6.15, a) shows that the target is not perfectly parallel to the imaging plane, thus the signal power decreases noticeably at length  $l > 1$  mm. The fibre has an imaged cross-section of  $d \approx 90$   $\mu$ m. Comparing an on-target trace (6.15, b, blue) to an off target trace (red) shows an on-target signal amplitude of 175 mV<sub>PP</sub>. The PSDs (6.15, c) show two peaks at 1.2 MHz and 5.9 MHz. Both have an  $SNR \approx 10$  compared to the off-target PSD.

When comparing the scan time to that of the commercial system the much finer grid of this scan has to be taken into account. The previous scan was done on a 75  $\mu$ m by 75  $\mu$ m grid while this was done on a 10  $\mu$ m by 50  $\mu$ m grid. The previous grid consisted of 6561 data points ( $\Sigma t \approx 10$  h) and the present of 1144 data points ( $\Sigma t \approx 1$  h), resulting in an adjustment factor of 5.73. Thus, the MEMS based PA system imaged along a target at approximately half the time it took the commercial system. This however does not yet

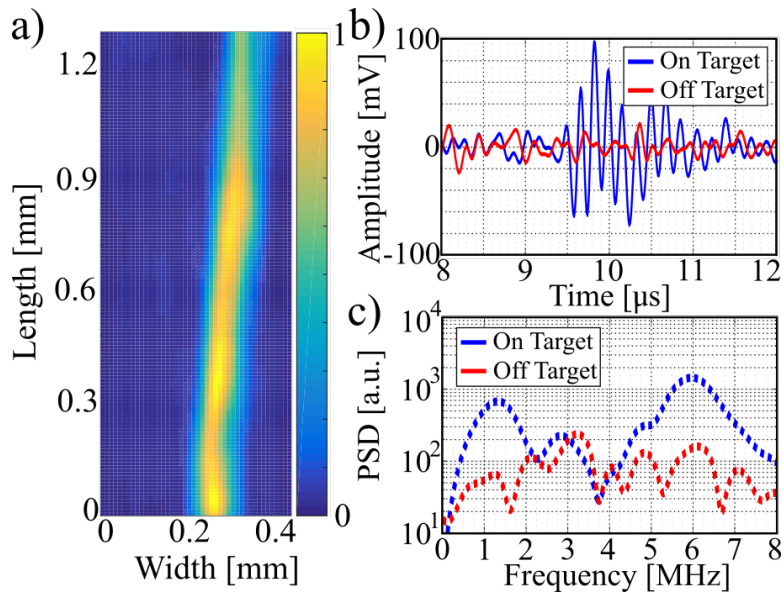


FIGURE 6.15: The reconstructed image (a) shows the PCF with an imaged cross-section of  $d \approx 90 \mu\text{m}$ . The on-target trace (b, blue) has an amplitude of  $175 \text{ mV}_{PP}$  and its PSD(c) show two peaks; at 1.3 MHz and 5.9 MHz. Both have an  $\text{SNR} \approx 10$ .

take into account the pulse energies used. The commercial system imaged the target at a pulse energy of  $5.2 \text{ mJ}$  whereas it was imaged at  $E = 586 \text{ nJ}$  using the MEMS based system, thus four orders of magnitude less. This only increased the need for averaging over a sample size of 256 compared to the previous 10, by a factor of 25.6. Furthermore, this increased averaging requirement was more than compensated for by the three orders of magnitude increase in the laser's PRF. Considering all of the points above the MEMS based system is superior to the previously presented commercial PA imaging system.

### 6.3.2 Ink soaked thread

The previously target material only allowed for two dimensional structures due to its rigidity. Furthermore, the diameter of the target was fixed by the PCF's diameter ( $d = 100 \mu\text{m}$ ). A new type of target material was found in surgical thread (SILK USP 7/0 0.5, SMI). The thread itself, while not absorbing, offers flexibility and, by unravelling of the thread, an adjustable target size. Its helical structure lends an inherent three dimensional character to the target cross-section. The absorption parameter of the suture thread was adjusted by a carbon particle (CP) based coating. This coating was applied by laying the suture threads into a CP solution and evaporating the water. This resulted in a CP film covering the entire submerged specimen. A polyimide fibre of known diameter (see Fig. 3.10) was compared to the coated and uncoated suture threads, and their diameters measured and structures

investigated (see Fig. 6.16). The suture threads, both coated and uncoated, can be seen to have a helical structure, resulting in a minimum and a maximum dimension in the image plane. The bare thread has a width ranging from  $50 \mu\text{m}$  -  $74 \mu\text{m}$ , while the coated thread's dimensions range from  $53 \mu\text{m}$  -  $82 \mu\text{m}$ . While the topographic details of the bare thread caused by its individual sub-threads are clearly visible, these details are absent on the coated suture thread. Thus indicating a coating on the entire surface.

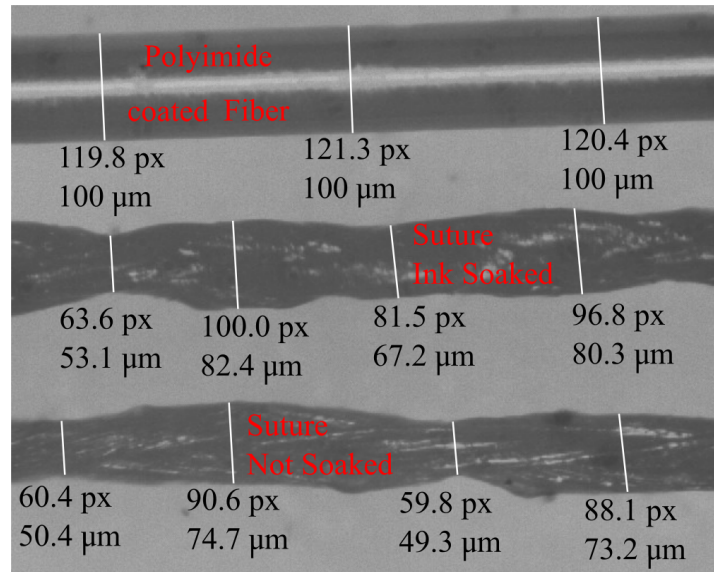


FIGURE 6.16: The image shows the comparison of a polyimide coated optical fibre with a diameter of  $100 \mu\text{m}$  (top) to a CP coated (middle) and a bare suture thread (bottom). The former's dimensions in the image plane range from  $50 \mu\text{m}$  -  $74 \mu\text{m}$  and the latter's from  $53 \mu\text{m}$  -  $82 \mu\text{m}$ . The coated thread lacks the bare one's surface detail caused by the coating covering the individual sub-threads.

The first scan using the suture as a target was to compare it to the previously used polyimide coated fibre targets. For this experiment (see Fig. 6.17, b) a polyimide coated fibre (1), a bare suture thread (2), a CP coated suture thread (3) and a CP coated sub-thread (unravalled suture thread dimension ranging from  $32 \mu\text{m}$  -  $48 \mu\text{m}$ , 4) were embedded in a gelatine matrix. The image plane (red,  $2 \text{ mm} \times 3 \text{ mm}$ ) was scanned over in 81 steps at  $dx = 25 \mu\text{m}$  in the x -direction and 31 steps at  $dz = 100 \mu\text{m}$  in the z -direction using the single-type PMUT array and at 91 steps at  $dx = 25 \mu\text{m}$  in the x -direction and 41 steps at  $dz = 100 \mu\text{m}$  in the z -direction using the multi-type PMUT array. The former was imaged plotting the signal power of the first and second peak, ranging from 0.6 MHz to 1.5 MHz and 3.75 MHz to 5.2 MHz, respectively. For the multi-type PMUT array the signal power was calculated for the 0.9 MHz - 2.5 MHz and the 2.8 MHz to 3.9 MHz band. The PMUT array was placed

at a distance of 5 mm from the focal point of the laser. The PA waves were generated using a pulse energy of  $E = 6.3 \mu\text{J}$  at a repetition frequency of  $f_{rep} = 8.43 \text{ kHz}$ . The increase in pulse energy over previous experiments was necessary to get a PA response with a good SNR ( $\text{SNR} > 10$ ).

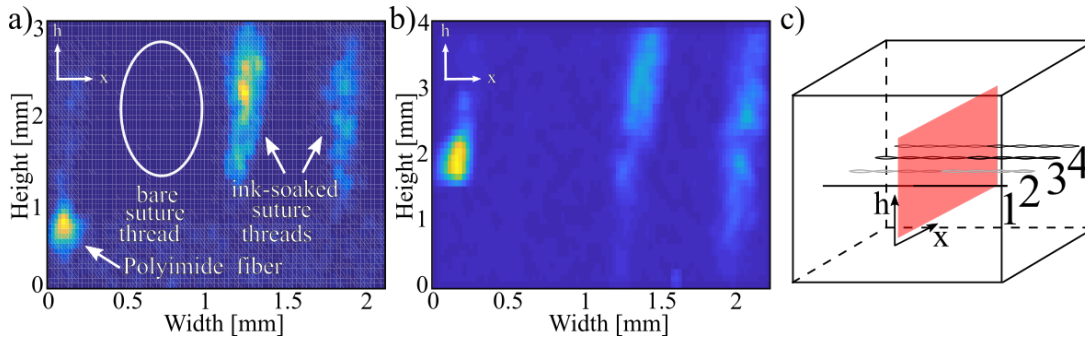


FIGURE 6.17: The reconstructed scan image using the single-type array (a) and the multi-type array (b) show that the PCF and the CP coated suture threads give a PA response, while the uncoated suture thread does not yield a detectable PA response. The schematic (c) shows the position of the PCF (1), the uncoated suture thread (2), the CP coated suture thread (3) and the CP coated sub-thread (4).

The scanned image shows that the bare thread does not yield a PA response caused by a too low absorption coefficient. The polyimide coated fibre has  $x - z$  dimensions of  $100 \mu\text{m}$  by  $350 \mu\text{m}$ . The threads show much broader  $x - z$  dimensions ( $400 \mu\text{m}$  by  $1250 \mu\text{m}$  for the full thread and  $200 \mu\text{m}$  by  $1100 \mu\text{m}$  for the unravelled thread). This is caused by bleeding of the CP coating into the gelatine matrix during the pouring process as well as during storage.

In the next setup two CP coated suture threads were crossed over in a gelatine matrix. The phantom was cast in three steps. Firstly, the base layer was cast and allowed to cool. Secondly, the ink-soaked CP coated suture threads were manually placed in the desired shape. Lastly, the top layer is cast while the threads are held in place with tweezers. The phantom was then placed in the fridge to settle. They were scanned over using a  $3 \text{ mm} \times 3 \text{ mm}$  imaging plane consisting of 101 steps at  $dx = 30 \mu\text{m}$  in the  $x$ -direction and 41 steps at  $dz = 75 \mu\text{m}$  in the  $y$ -direction. The PA waves were generated using the MEMS Q-switched laser ( $E = 12.6 \mu\text{J}$ ,  $PRF = 8.43 \text{ kHz}$ ) at a distance of 7 mm from the PMUT array. From the resulting scan image (see Fig. 6.18) it can be seen that the focal plane was closer to the suture thread which was positioned at an angle, hence its signal power is higher. This can also be seen in the traces (see Fig. 6.19, a) where the amplitude of the suture thread closest to the focal plane (blue) is  $300 \text{ mV}_{pp}$  and the one farther away (red) has one of  $90 \text{ mV}_{pp}$ . The spectra (see Fig. 6.19, b) show two main peaks at 4.7 MHz and at 1.1 MHz as well as two side peaks at 2.25 MHz and 6 MHz. The signals received from the thread closest to the imaging



plane yield  $SNR \approx 30$  and signals from the other on yield  $SNR \approx 10$  when compared to the off target signal power (green). The suture threads show a diameter of  $300 \mu m$  and the area around their point of contact shows a circular region with a diameter  $d \approx 1 mm$ . This broadening of the diameters as well as in the region of contact is caused by bleeding of the CP coating into the gelatine matrix.

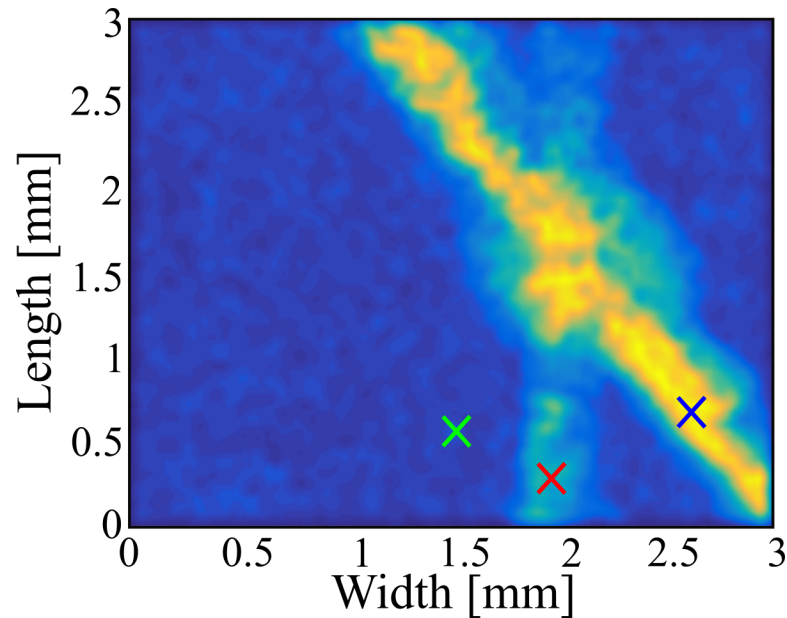


FIGURE 6.18: The scan image shows the two suture threads with different signal strengths. This is caused by unequal distances to the imaging plane, with the angled thread being the closest to that plane. They show to have a cross-section of  $300 \mu m$ ; this broadening is caused by the previously mentioned bleeding of the CP into the surrounding matrix. Furthermore, the region of contact is enlarged by a circular pattern with a diameter  $d \approx 1 mm$  caused by the same effect.

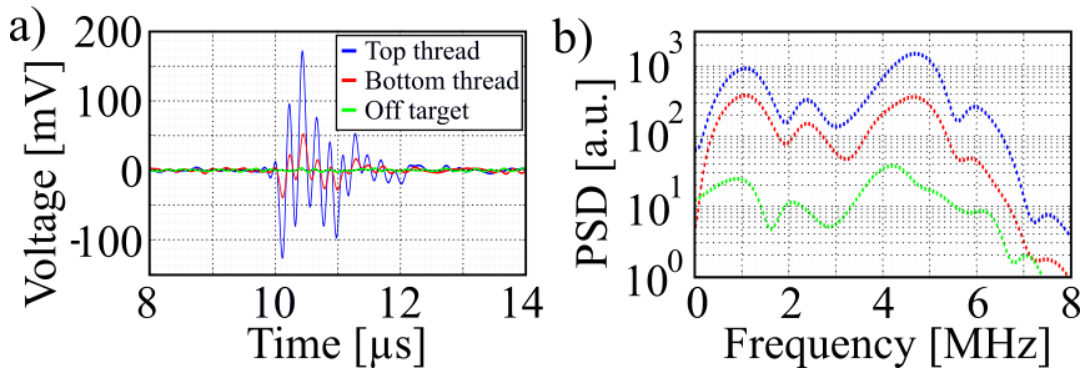


FIGURE 6.19: The traces (a) recorded from the thread closest to the imaging plane (blue), the one farther away (red) and off target (green) show amplitudes of  $300\text{ mV}_{PP}$  and  $90\text{ mV}_{PP}$  for the former two, respectively. The PSDs show two main peaks at 4.7 MHz and at 1.1 MHz and two side peaks at 2.25 MHz and 6 MHz.

## 6.4 Discussion and Conclusion

Incorporating the MEMS Q-switched laser into an all MEMS based PA system caused the laser pulse width to increase by a five-fold, but as shown in chapter 2, this had no great impact on the generated spectra for transducers placed at a distance  $d \geq 2\text{ mm}$ . The transducers in the presented experiments were always placed at larger distances. When generating PA waves using this system the recorded transducer trace consisted of five distinct spikes per micromirror period. The most prominent are interference spikes from closing the optical cavity. This happens twice per revolution of the micromirror, but the output power of the generated beam can be different on these two occasions due to an elliptical path. This path is caused by slight misalignment. The second biggest spike is that of the generated PA wave. Thirdly, two spikes are caused by EM interference of the  $200\text{ V}_{PP}$  square wave (falling and rising edge) actuating the micromirror. Here the Dirac-like alteration of the amplified driving voltage is recorded.

The SNR tests showed that this laser system can be easily used for PA wave generation and detection using the PMUT arrays. Here, the bar-type PMUT array performed worst, showing only distinguishable signals at high pulse energies, while the multi-type and the single-type PMUT arrays achieved good SNRs for pulse energies  $E > 1\text{ }\mu\text{J}$  and  $E \geq 300\text{ nJ}$ , respectively. The commercial transducers, the Olympus 2.25 MHz and the Olympus 10 MHz, both showed good SNRs pulse energies  $E \geq 300\text{ nJ}$ . For the single-type and the multi-type PMUT array the SNR was similar over their respective secondary and tertiary resonance frequencies, while that of the Olympus 2.25 MHz transducer was lower by factor of two. Comparing this all-MEMS based PA scanning system using the single-type PMUT to the previously used all commercial system with the Olympus 2.25 MHz transducer (due

to similar resonance frequencies), shows that the former outperforms the latter by a factor of up to 10. This is mostly caused by the higher averaging size made possible by the higher laser PRF, which is three orders of magnitude greater than the all-commercial system's. The limiting factor for the all-commercial system is its low PRF, while the all-MEMS based system can be improved even further by decreasing the computational time. Without this limiting factor the system could average over about 10000 samples while the commercial system averages over 10. Thus, this could potentially cause an additional  $\sqrt{10}$  - fold increase, resulting in a performance of the MEMS-based system to be up to 30 times better.

The presented system was used to image targets in a gelatine matrix using both the single-type and the multi-type PMUT array. The bar-type PMUT array was left aside due to its poor performance in the SNR trials. Imaging a PCF with these two transducers shows comparable contrast in the derived images. Their cross-resolution is comparable, while the target resulted in different height-dimensions using the two transducers. The single-type PMUT array showed almost twice the height compared to the multi-type PMUT array, 700  $\mu m$  and 400  $\mu m$ , respectively. Using the frequency content of the secondary peak the dimensions of the imaged fibre can be estimated to be 100  $\mu m$  by 700  $\mu m$  (x by h) for both PMUT types. This suggest that this second band gives a better and more comparable estimate. Furthermore, using these secondary bands the cross-section of the image shows a higher resonant mode shape (similar to the simulated resonating disc, see Table 4.1, 3). This is potentially caused by a circumferential guided waves in the outer coating layer. Using the single-type PMUT array a PCF was imaged at decreasing pulse energies to relate the effects of the SNR trials to image contrast. From the scanned images it could then be seen that this reduction still resulted in images with good contrast for pulse energies  $E \geq 175 \text{ nJ}$ . This relates well to an  $SNR \approx 5$  for  $E = 175 \text{ nJ}$  for the SNR trials. Additionally, the cross-section of a PCF under a high-scattering medium was scanned, resulting in a good contrast image ( $SNR \approx 30$ ) showing that the system works for targets in turbid media. Finally, imaging along a PCF shows the MEMS based PA system to operate at a grid point speed three times that of the commercial system, while operating at a 4 orders of magnitudes lower pulse energy and an averaging size 25 times larger.

The target material was changed from PCF to CP coated suture threads. These offered the possibility for smaller more flexible and shape-able targets. While these could be unravelled to create even smaller targets with inherent helical structure, their coating bled into the surrounding water-based gelatine matrix, thus resulting in an overestimation of the original target size and the blurring of small features. The bleeding and its effects could be prevented by using e.g. PDMS based matrix. Comparing PCFs, uncoated threads, and coated threads and sub-threads showed that the latter required higher pulse energies for PA wave generation but were also more resilient to high pulse energy than PCF. Furthermore, an uncoated suture thread did not produce a detectable PA wave.



## Chapter 7

# Scanning laser beam PA

The PA system presented in the previous chapter is based on a MEMS Q-switched laser consisting of a laser cavity which includes a fast-scanning MEMS micromirror and a diode-pumped Nd:YAG gain crystal. The gain crystal unit is very cost-intensive ( $\approx 10000$  £). Therefore, to further reduce size and cost of the system, the pulsed PA light source should be replaced or otherwise substituted. For this purpose, a new concept is introduced where generic high power CW or long pulsed laser diode and the fast-scanning MEMS micromirror are used to create a scan line consisting of a fast-moving focused laser point. Rather than using a short laser pulse, a quasi-CW laser's focal point is scanned rapidly across a target or absorbing medium to create the short temporal profile necessary to induce a PA response. This setup thus does not require a short-pulsed laser diode or complicated triggering circuitry. It only requires high power laser diodes, that can be pulsed (long pulses, to reduce thermal stress on the mirror), a fast-scanning MEMS micromirror and focussing optics. Using this concept the scan point is scanned over a line at double the resonance frequency of the micromirror, creating a pseudo 2D scanline.

### 7.1 Basic Principle

The basic principle of scanning beam PA differs from conventional PA in the way the temporal profile  $I(t)$ , necessary for the generation of the pressure wave, is created. While conventional PA systems (mostly) rely on a short pulsed laser, thus using the laser pulse shape as the temporal profile, the presented novel technique relies on the fast movement of a laser spot over the target (see Fig. 7.1). Thus each target unit distance  $\partial d$  experiences photoacoustic excitation and relaxation. The temporal profile  $I(t)$  is a convolution of the spatial profile of the beam spot  $S(x)$  and the dimensions of the light-absorbing target  $d_t$ . The pulse shape can then be estimated from the spatial beam profile divided by the speed with which the laser spot is scanned over the target  $v_{scan}$ . The normalised adjusted pulse widths of a spot scanned over a target with dimensions 2.5-times (blue) and 0.25-times (red) the spot diameter are shown in Fig. 7.1. The pulse widths were calculated as convolution of the beam spot size ( $d_{spt}$ ) and the target size ( $d = 2.5 \cdot d_{spt}$  and  $d = 0.25 \cdot d_{spt}$ , see Fig. 7.1 lower right, blue and red, respectively). Here, the pulse widths (FWHM) of the larger target is 2.5 times longer compared to the smaller target. While the pulse widths of the larger target is

influenced by both the laser beam spot size and the target size, the pulse width of the smaller target is mainly caused by the laser beam spot size. The temporal profile shows the initial amplitude of the PA response.

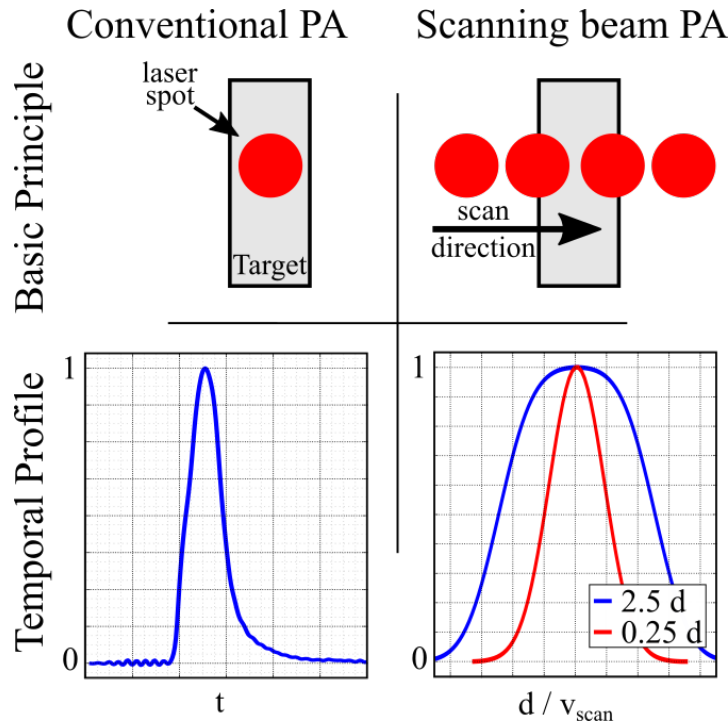


FIGURE 7.1: The basic principle of conventional PA is a (point-wise) heating of a target with a short laser pulse. Thus, the temporal profile of the heating is determined by the laser pulse shape  $I(t)$ . In Scanning beam PA the laser spot is scanned across the target. This results in a temporal heating profile in the shape of the convolution of the (Gaussian) laser profile  $S(x)$  and the target dimensions in scanning direction. The temporal profile here is shown for a target 2.5 times (blue) and a 0.25 (red) the spot diameter.

With the temporal profile depending on both the spatial profile of the beam spot and the profile of the target, the frequency content of the induced PA wave will depend on the latter (assuming a near constant spatial beam profile). This will be examined using simulations (see chapter 7.2.2). As the micromirrors are made of a thin layer of gold on top of a  $10\ \mu\text{m}$  Si layer, damage of the mirror due heating of laser power absorbed in the 96 % reflective mirror is problematic. This will be further discussed in chapter 7.4.1. The general setup consist of a high-power laser, the output of which is focused onto the phantom (see Fig. 7.2). The fast-scanning MEMS micromirror is located in the beam path before the focal point, creating the scan line.

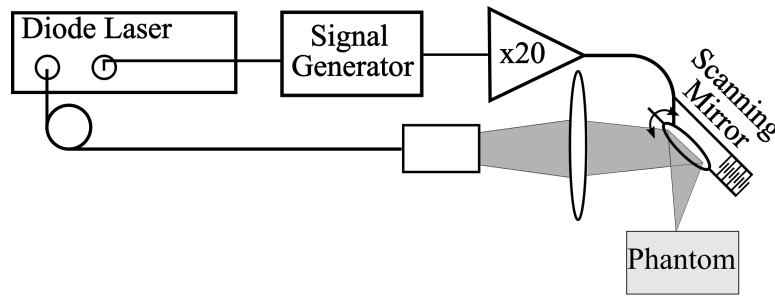


FIGURE 7.2: The scanning beam experimental setup consists of a fibre-coupled laser diode bar. The laser is triggered using a signal generator. Its second output is amplified and actuates the micromirror. The output of the fibre-coupled laser is focused onto the phantom. The fast-scanning micromirror is in the beam path before the focal point, creating the scan line.

## 7.2 Simulation

In a first step towards developing the scanning beam PA system, the expected spot velocities, pulse energies and frequency content were simulated. This was done using MATLAB calculations and its acoustic propagation tool box k-wave (see Chapter 2).

### 7.2.1 Pulse Energy and Pulse Width

The fast-scanning MEMS micromirror is used to create the scanline. The projection of the spot and its speed onto the imaging plane results in the spot velocity being different in the centre of the scanline compared to its edges (see Fig. 7.3). As the absolute spot velocity varies greatly over the whole revolution of the micro-mirror, from 0 - 2km/s, only a part of the signal should be used (see Fig. 7.3, between black dotted lines). Here, the spot velocity will be within  $2.25 \frac{km}{s} \pm 11.1\%$ . This can be achieved by reducing the duty cycle of the laser triggering to either 12.5 % (once per revolution) or 25 % (twice per revolution). The pulse width  $\tau$  and the pulse energy  $E_{pls}$  were calculated as the convolution of the Gaussian spot and the target profile and the energy deposited during that time using a laser power of  $W_0$ .

The simulations were done for a Gaussian laser spot with a diameter of  $d = 50 \mu m$  and a power of  $W_0 = 1 W$ . The resonance frequency of the scanning mirror was set to  $f_{res} = 12 kHz$  and the scanline length was set to 30 mm. Using these parameters the pulse width  $\tau$  and the pulse energy  $E_{pls}$  were calculated for three targets with dimensions of  $d_1 = 50 \mu m$ ,  $d_2 = 100 \mu m$  and  $d_3 = 200 \mu m$  (see Fig. 7.4). The values for the pulse widths and their respective pulse energies are shown in Table 7.1. The closer the target is to the centre of the scanline and the smaller the target, the shorter the induced pulse length. Additionally, changing the beam spot size alters the rise and fall times of the induced laser pulses. Judging from these values for  $W_0 = 1 W$

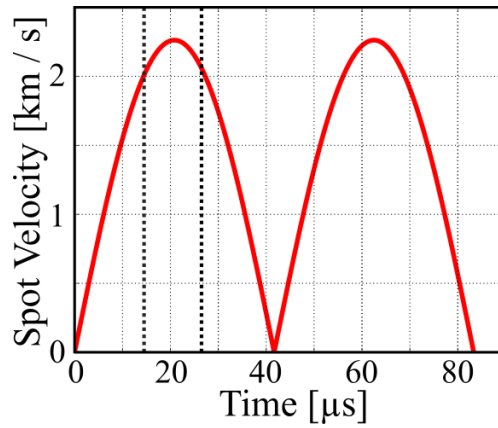


FIGURE 7.3: The absolute spot velocity of the scanned spot shows two peaks. Each peak is at the centre of the scanline, whereas the minima show the reversal of the direction of the velocity. The black dotted line denotes the envisioned time-frame used for measuring.

and considering previous SNR measurements (as in Figures 6.6 & 6.12) a laser power of  $W_0 > 2 \text{ W}$  and a large averaging size will be required for scanning a  $100 \mu\text{m}$  target (such as PCF).

TABLE 7.1: The pulse widths and the pulse energies increase with target dimensions and with distance from the centre of the scanline. The values shown here result from a simulation using a CW-laser with 1 W power output.

Position	$\tau$ in [ns]			Energy [nJ]		
	$50 \mu\text{m}$	$100 \mu\text{m}$	$200 \mu\text{m}$	$50 \mu\text{m}$	$100 \mu\text{m}$	$200 \mu\text{m}$
centre	43	87	177	40	90	180
middle	46	91	180	50	90	180
edge	43	98	190	50	90	190

## 7.2.2 Expected PA signal

The effects of a change in the target dimensions on the frequency content were simulated using k-wave. The PA wave generation was modelled as moving target with a beam spot size of  $d = 25 \mu\text{m}$  over target sizes of  $d_1 = 50 \mu\text{m}$ ,  $d_2 = 100 \mu\text{m}$ ,  $d_3 = 250 \mu\text{m}$  and  $d_4 = 500 \mu\text{m}$ . The grid was initialised with  $1024 \times 256$  elements and a step width of  $dx = 5 \mu\text{m}$  and run over  $t = 5 \mu\text{s}$  in time steps of  $dt = 1 \text{ ns}$ . The detector is positioned at a distance  $d = 2.5 \text{ mm}$  from the source has a thickness of  $15 \mu\text{m}$  and an element length of  $170 \mu\text{m}$ . The FFT is then applied to the simulated PA responses to calculate their frequency content.



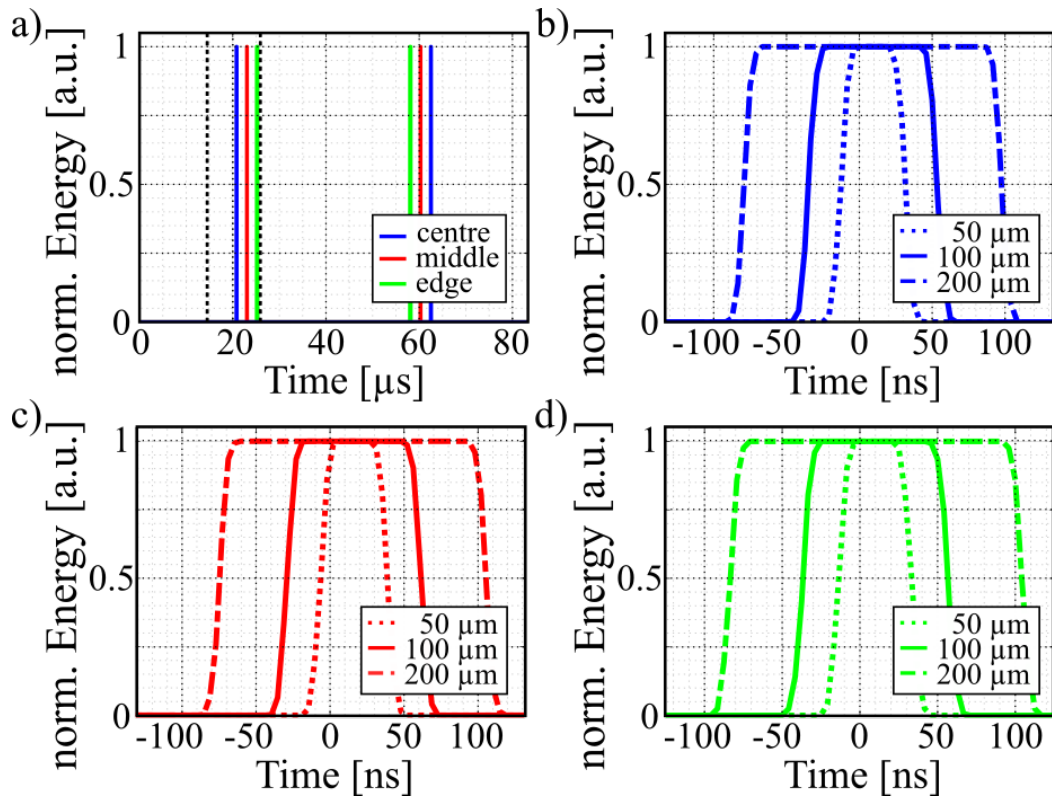


FIGURE 7.4: The effect of the different spot velocities is shown on three points spaced evenly over the measurement time-frame (a, black dotted line). In the centre of the scanline (blue, b) the simulated pulse-widths (FWHM) will be  $\tau = 43 \text{ ns}$ ,  $\tau = 87 \text{ ns}$  and  $\tau = 177 \text{ ns}$ , for  $d_1 = 50 \mu\text{m}$  (dotted),  $d_2 = 100 \mu\text{m}$  (solid) and  $d_3 = 200 \mu\text{m}$  (dashed), respectively. The pulse widths for these target diameters in the middle of scanline (red, c) was simulated as  $\tau = 46 \text{ ns}$ ,  $\tau = 91 \text{ ns}$  and  $\tau = 180 \text{ ns}$ , respectively and at the edges of the measurement frame (green, d) as  $\tau = 43 \text{ ns}$ ,  $\tau = 98 \text{ ns}$  and  $\tau = 190 \text{ ns}$ , respectively.

The pulse widths of the simulated PA responses (see Fig. 7.5, a) increases with the target width. The pulse widths (peak max to peak min) are  $75 \text{ ns}$ ,  $120 \text{ ns}$ ,  $200 \text{ ns}$  and  $450 \text{ ns}$  for target widths of  $50 \mu\text{m}$ ,  $100 \mu\text{m}$ ,  $250 \mu\text{m}$  and  $500 \mu\text{m}$ , respectively. With the increase in pulse width, the centre frequency reduces accordingly; the PSDs (see Fig. 7.5, b) show centre frequencies of  $0.75 \text{ MHz}$ ,  $1.45 \text{ MHz}$ ,  $3.0 \text{ MHz}$  and  $4.9 \text{ MHz}$  for target widths of  $500 \mu\text{m}$ ,  $250 \mu\text{m}$ ,  $100 \mu\text{m}$  and  $50 \mu\text{m}$ , respectively. Thus using a scanning beam PA system both position and size of the target can be determined.

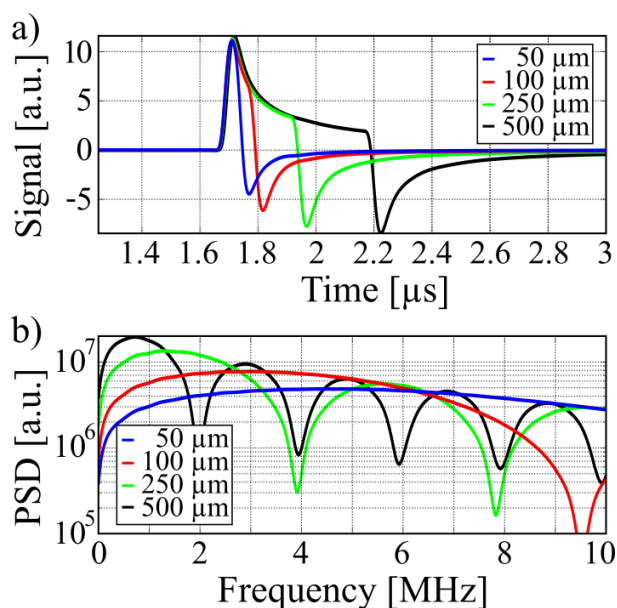


FIGURE 7.5: The simulated PA response shows that the recorded PA response is longer the larger the target. Their respective centre frequencies are lower for longer targets.

### 7.2.3 Minimum Discernible Target Distance

The minimum distance of two consecutive absorbing targets on the scanline that can be distinguished depends on the modulation depth of the signal change between the two generated PA signals. The modulation depth is influenced by the focal spot size of the scanned laser beam and the distance of the targets. This was simulated by convoluting a Gaussian distribution of size  $d_{spot}$  (FWHM) over a profile of two targets ( $d_{trgt} = 2.5 d_{spot}$ ) for several target distances  $l$ , ranging from  $l = 0$  to  $l = 2.5 d_{spot}$ . The results of the convolution (see Fig. 7.6, a) show increased modulation depth for increasing distances. The trend of the normalised signal at maximum modulation depth (see Fig. 7.6, b) shows that a modulation depth of  $1 - 1/e$  is reached at a target distance of  $l \approx 0.75 d_{spot}$ . Thus, a system scanning a focused laser beam with a focal spot size  $d_{spot}$  offers a lateral resolution of  $0.75 d_{spot}$ .

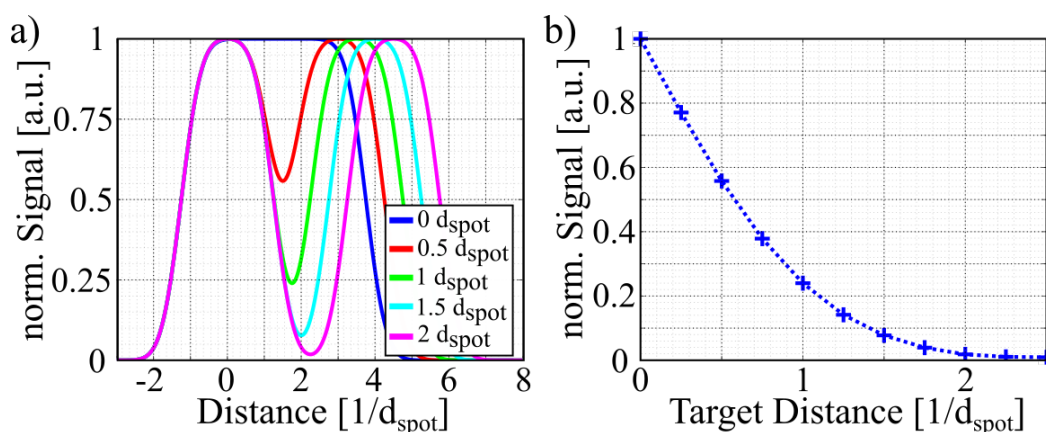


FIGURE 7.6: A Gaussian distribution of size (FWHM)  $d_{spot}$  is convoluted with two targets (each  $2.5 d_{spot}$  wide) at various target distances. The resulting signals (a) show an increasing modulation depth. The trend of which (b) shows a  $1 - 1/e$  modulation depth at a target distance of  $l \approx 0.75 d_{spot}$ .

## 7.3 Reconstruction Algorithm

Using Scanning beam PA the reconstruction algorithm is based in principle on the same as the short pulsed spot excitation and thus less computational demanding than the algorithms for volume evaluation (see Chapter 1.3.1). As the position of the point on the scanline is known from the phase of the MEMS scanning mirror actuation signal, the position of the point of origin can be determined in polar coordinates  $(r, \phi)$  from the time of flight  $t$  and the speed of sound  $v_s$ , as distance  $r$ . The angle  $\phi$  can be derived from the length of the scanline and the phase angle  $\psi$  from the MEMS scanning mirror actuation signal.

## 7.4 Experiments

A test setup was assembled to verify the initial considerations and simulations. Firstly, the laser pulse widths with considerations to the position on the scanline were examined. Secondly, the pulse power was measured and the CW - laser diode pulsed using long pulses ( $\tau > 1 \mu s$ ) to reduce thermal stress on the micromirrors. Lastly, the scanning beam PA system was used to generate a PA response on a PCF target.

### 7.4.1 Pulse width

As was shown in the earlier simulations, the pulse width of a scanned over target depends on the position of the target. Furthermore, it depends on the mirror actuation frequency and the distance from the target to the mirror. Here, the micromirror (see Table 5.1, 2) was actuated using a sinusoidal wave at

$f_{act} = 48.64 \text{ kHz}$ . A CW HeNe laser beam was bounced off this micromirror and projected onto a screen at a distance  $l = 150 \text{ mm}$ , resulting in a scanline with a length of 240 mm. The midpoint of the resulting scanline was marked by a big dot, caused by reflection on the SOI device layer rather than the moving micromirror. This point was used to position a photodiode (S1336-18BQ, Hamamatsu, length optical sensitive area  $d_{opt} = 1.1 \text{ mm}$ ) at four points along the scanline. Thus, the pulse widths (FWHM) were recorded for different positions starting from the midpoint and then at intervals of  $\Delta x \approx 30 \text{ mm}$  (see Fig. 7.7). Here, it can be seen that the midpoint trace (blue) gives the highest photodiode response and the shortest pulse width ( $\tau_1 = 280 \text{ ns}$ ). The photodiode amplitudes decrease and the pulse widths increase for the points at distances of  $d_2 = 30 \text{ mm}$ ,  $d_3 = 60 \text{ mm}$  and  $d_4 = 90 \text{ mm}$ , with pulse widths of  $\tau_2 = 290 \text{ ns}$ ,  $\tau_3 = 295 \text{ ns}$  and  $\tau_4 = 400 \text{ ns}$ , respectively. Thus, scanning over a target (e.g. PCF) with a diameter of  $d = 100 \mu\text{m}$  at a distance of  $l = 25 \text{ mm}$ , will result in pulse width of  $127 \text{ ns} < \tau < 175 \text{ ns}$ . With expected pulse widths only 2.5 to 3.5 times the pulse width using the MEMS Q-switched Nd:YAG laser (see Chapter 5), generation of PA responses will still be feasible.

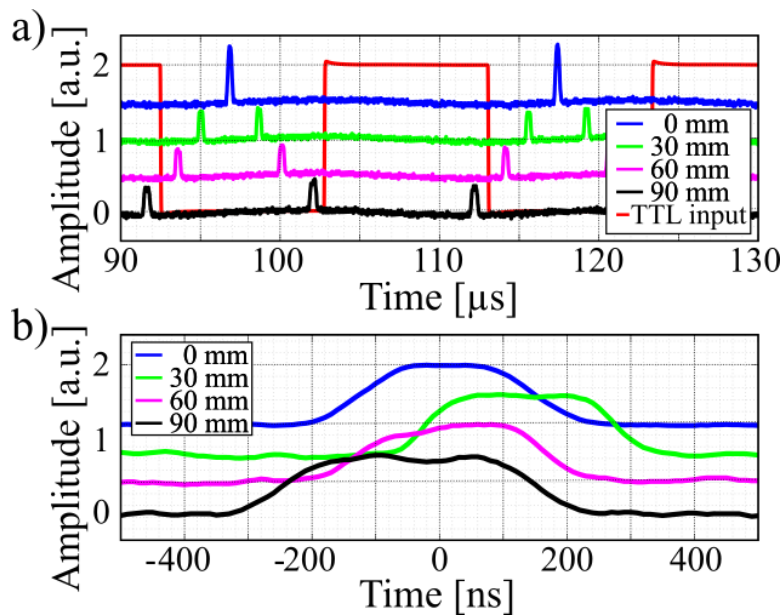


FIGURE 7.7: The pulse shapes (a) were recorded at the midpoint (blue), and at distances of  $d_2 = 30 \text{ mm}$  (green),  $d_3 = 60 \text{ mm}$  (magenta) and  $d_4 = 90 \text{ mm}$  (black) overlaid with the TTL input (red) of the signal generator. Comparing the pulse widths (b) shows a decrease with increased distance from the midpoint.

### 7.4.2 Output Power

PA generation requires not only short laser pulses but also high enough pulse energies. For this reason a high power, pulseable (long pulses  $\tau > 1\mu\text{s}$ ) diode laser bar (BWDT-16, BW-TEK). This diode laser bar consisted of 8 individual fibre-coupled laser diodes and emitted light at  $\lambda = 808\text{ nm}$ . The output can be changed from CW to pulsed by adjusting the input frequency and duty cycle off the TTL input. Its output power can be adjusted by altering the driving current  $I_{dr} \leq 5.5\text{ A}$ . The CW output power is shown in Fig. 7.8 for currents ranging from 1 A to 5.5 A.

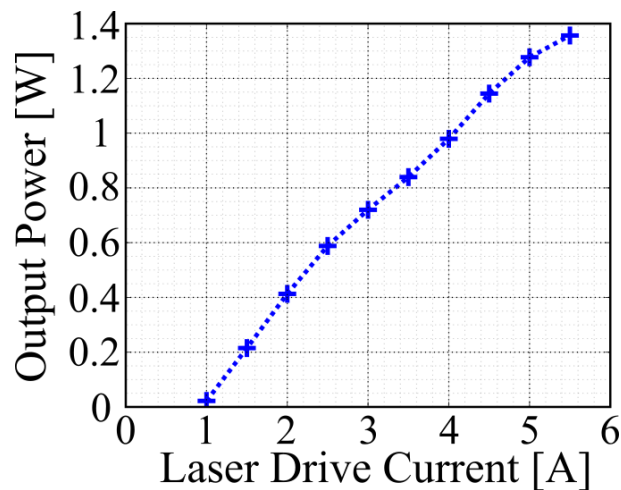


FIGURE 7.8: The output of the laser diode is shown for drive currents ranging from 1 A to 5.5 A.

The pulse energies were measured using a powermeter (Gentec E0 Solo PE plus power meter head UP19K-15s-VM-DO, Gentec Electro-Optics, Canada). Initial experiments showed, that using the CW-laser output at a power of  $P = 491\text{ mW}$  was damaging the micromirror due to thermal stress. Thus, the laser's duty-cycle was decreased to  $DC = 25\%$ . The duty cycle of the laser was also reduced to keep the velocity profile of the spot within limits of  $\pm 11\%$  (as discussed in section 7.2.1). This was done by using a two-output signal generator (Agilent, 33502A). One output was used to actuate the scanning mirror, while the other was used as a trigger signal for the laser diode bar (see Fig. 7.9). The outputs were frequency matched. Moving from CW laser output to a pulse output caused only a part of the original scanline to be active. Utilising this, the phase shift of the two output channels of the signal generator was adjusted to separate the active scanline from the midpoint. This midpoint was caused by the laser reflecting of the SOI substrate rather than the actuated mirror. Unfortunately, it was not possible to remove the spot by properly matching the laser spot size on the micromirror as this reduced the distance of the focal point and the micromirror and thus the length of the scanline too much. The power meter head was positioned so, that the scanline was incident on the sensing

area while the midpoint was not. The power was then measured for several current inputs.

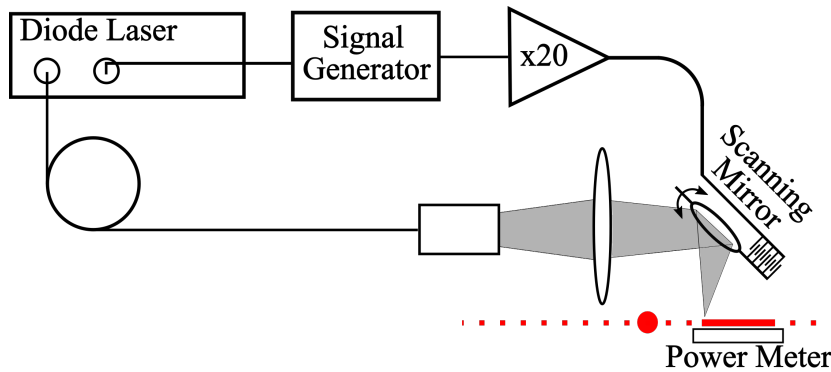


FIGURE 7.9: The power measurements were conducted using the diode bar laser actuated by a two-output signal generator. The other output was amplified and used to actuate the micromirror. The output of the fibre-coupled laser was focused and bounced off the micromirror. The focal point (after the micromirror) formed the scanline. As the laser was operated at a 25 % DC the original length of the scanline (red dotted line) was reduced (red solid line). The stationary reflection of the SOI substrate is shown as an enlarged red dot. The phase shift was adjusted to separate the active scanline from the midpoint. The active part was measured using a powermeter.

The measured output power of the scanline is shown in Fig. 7.10 (blue). The measured power ranges from 23 mW to 199 mW for diode drive currents of 1 A to 5.5 A. Its CW  $P_{CW}$  equivalent (red) was calculated from the measured power  $P_M$  and the duty cycle  $DC$  as  $P_{CW} = \frac{P_M}{DC}$ . Thus, it ranges from 92 mW to 796 mW. The energy deposited  $E_{CW}$  onto a target with diameter of  $d = 100 \mu m$  at a distance of  $l = 25 mm$ , such as a PCF, can be calculated from the pulse width over the target  $\tau$  as:

$$\begin{aligned} E_{CW} &= P_{CW} \cdot \tau \\ E_{CW} &= 799 \text{ mW} \cdot 127 \text{ ns} \\ E_{CW} &= 101.5 \text{ nJ} \end{aligned} \tag{7.1}$$

The perceived pulse energy deposited onto a  $100 \mu m$  target is 101.5 nJ and thus lower than the threshold pulse energy shown in Fig. 6.12. The lower energy in combination with the larger pulse widths indicates that heavy averaging ( $n > 4096$ ) will have to be employed to measure the generated PA responses.

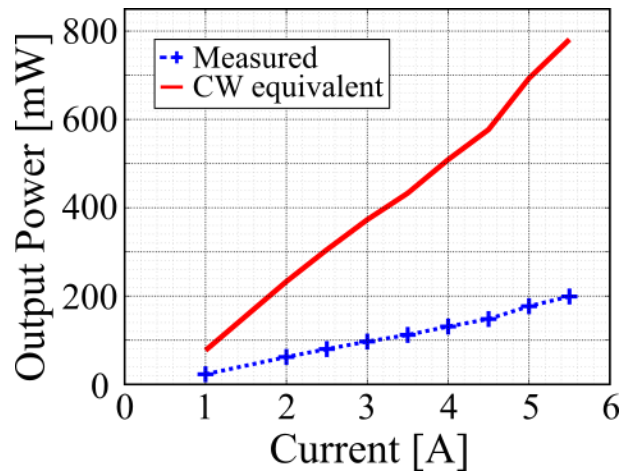


FIGURE 7.10: The measured output power (blue) ranges from 23 mW to 199 mW for diode drive currents of 1 A to 5.5 A. The equivalent a CW illumination would cause ranges from 92 mW to 796 mW.

### 7.4.3 Test setup

The scanning beam PA system (see Fig. 7.11) consists of a fibre-coupled diode laser bar (BWDT-16,  $\lambda = 808 \text{ nm}$ ), which is triggered using a signal generator with two separate outputs (Agilent, 33502A). The second output is amplified and used as an actuation signal for the scanning mirror. The two outputs are frequency matched but phase shifted, to alter the position of the active part of the scanline, to the mid-point of the "complete" scanline. The output of the fibre, coupled to the laser bar, is fed into a microscope objective (40x, NA 0.65) for collimation. The collimated beam is the de- and re-collimated using two microscope objectives (20x, NA 0.35 & 20x, NA 0.45) with an iris at the focal point to clean up the beam. Finally, the beam is focused using a plane-convex lens (focal length = 70 mm) placed at a distance  $d \approx 40 \text{ mm}$  from the scanning mirror, which is tilted at an angle of  $\alpha = 45^\circ$ . This causes the focal spot of the laser to be moved along the scanline.

### 7.4.4 Experimental Verification

The setup was tested using a PCF embedded in a gelatine matrix. The diode bar was driven at  $I = 5.5 \text{ A}$  at a duty-cycle of  $DC = 12.5 \%$  and triggered using the signal generator. The power output of the laser measured at this duty cycle (blue) and its CW-equivalent (red) are shown in Fig. 7.12. The latter actuated the MEMS micromirror using a sine input with an actuation frequency of  $f = 12.16 \text{ kHz}$ . The target was placed at  $d \approx 15 \text{ mm}$  from the micromirror and the generated PA waves were recorded using the commercial 10 MHz transducer (placed  $l \approx 20 \text{ mm}$  from target), as it achieved the best SNR in the previous SNR comparison experiments. Its output was amplified by +60 dB (HVA-10M-60B, FEMTO) and averaged ( $n = 4096$ )

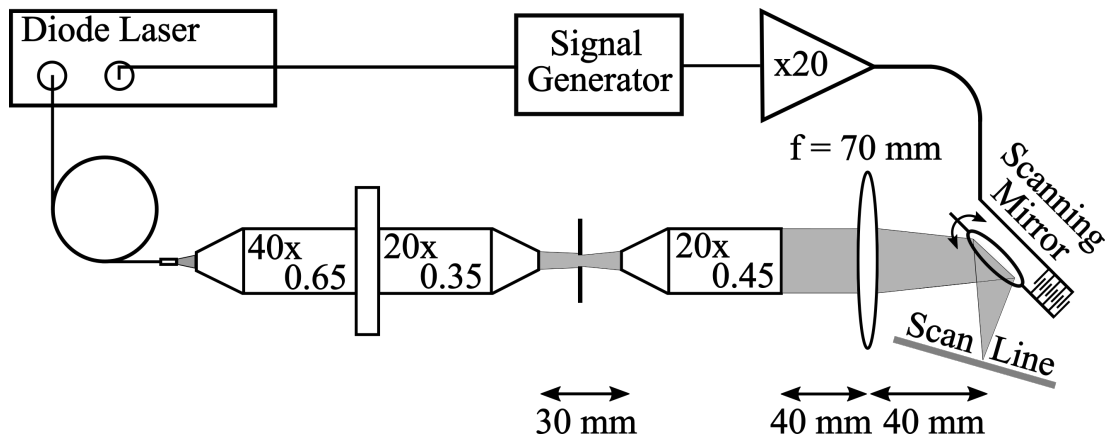


FIGURE 7.11: The scanning beam experimental setup consists of a fibre-coupled laser diode bar. It is triggered using a signal generator with two outputs. Their frequencies are matched but phase-shifted. The second output is amplified and actuates the scanning mirror. The beam shaping of the fibre output is done by three consecutive microscope objectives. The beam is shaped by a plan-convex lens with a focal length of 70 mm. The scanning mirror is at a distance of 40 mm from the focusing lens. Thus, creating the scanline from the focal point.

and recorded using an oscilloscope (Agilent Infiniium) at a sampling frequency of  $f_s = 100 \frac{MSa}{s}$ . Additionally, to observe the change in signal amplitude a second experiment was done as described above, but driving the diode bar at  $I = 5.0 A$  at a duty-cycle of  $DC = 12.5 \%$ .

Traces were recorded for a driving current of  $I = 5.5 A$  (see Fig. 7.13) for the scanline incident on the target (blue), not incident on the target (red) and the background (green, by blocking the laser). The on-target trace resulted in a clear signal with an amplitude of  $V_{pp} = 3.5 mV$ . The off-target and the blocked traces yielded no discernible signals. As the response is separate from the falling edge of the trigger signal and did not appear in neither the off-target nor the blocked trace, the observed signal is a PA response generated using the scanning beam PA method.

The traces recorded with a driving current of  $I = 5.0 A$  (see Fig. 7.14) for the scanline incident (blue) and not incident on the target (red) show a lower signal with  $V_{pp} = 1.5 mV$ . The off-target trace shows no discernible signal. As expected, the power output of the laser diode directly influences the generated PA signal.



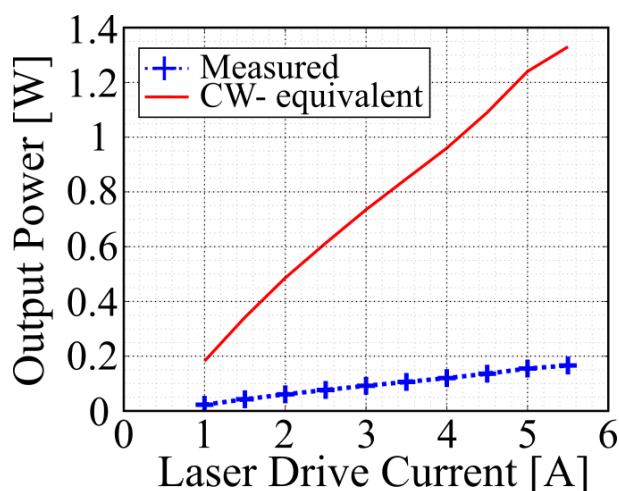


FIGURE 7.12: The output of the laser diode bar at a DC of 12.5 % (blue) and its CW equivalent (red) are shown for drive currents ranging from 1 A to 5.5 A.

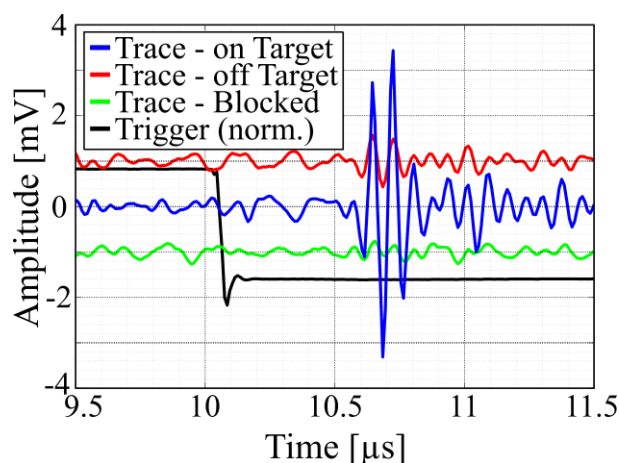


FIGURE 7.13: The trace with the scanline on target (blue) shows a  $3.5 \text{ mV}_{PP}$  signal. The off-target (red) and blocked (green) traces show no response. The trigger signal (black) is shown for reference.

## 7.5 Discussion

A novel method was shown that uses a moving focal spot to create the temporal profile  $I(t)$  required for the generation of a PA response rather than pulsing a laser. This allows for the use of CW or long-pulsed laser sources for PA imaging, while keeping both the excitation and the detection scheme simple. The test setup was shown for a MEMS micromirror with a gold coating as reflective surface, using a dielectric coating on the mirror surface as well as potentially the whole die, the

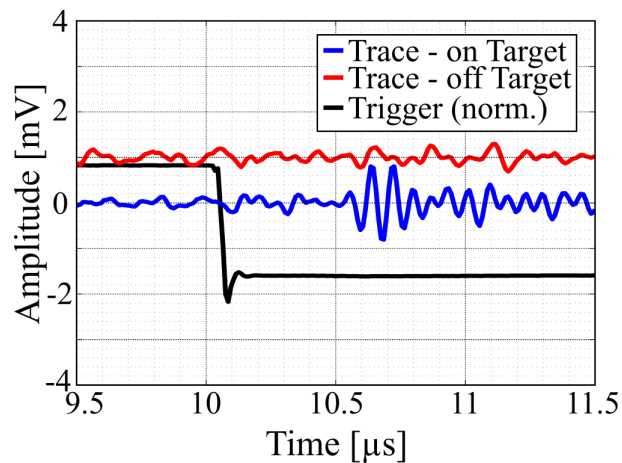


FIGURE 7.14: The trace with the scanline on target (blue) shows a  $1.5 \text{ mV}_{PP}$  signal. The off-target (red) trace shows no discernible signal. The trigger signal (black) is shown for reference.

absorbed heat can be reduced [39]. This would allow for higher laser powers to be used before the device breaks down due to thermal damage, which would generate PA signals with an improved SNR.

The scanning beam PA setup showed to produce pulse widths ranging from 127 ns to 175 ns for a  $100 \mu\text{m}$  target at a distance of 25 mm, depending on the target's distance to the centre point of the scanline. The maximum output power at a duty-cycle of 25 % - to prevent thermal damage to the die - was  $P_{max} = 796 \text{ mW}$ . Thus, a  $100 \mu\text{m}$  target is objected to a pulse energy of  $E_{CW} = 101.5 \text{ nJ}$ , indicating the need for heavy averaging. Lastly, the test setup was successfully used to generate a PA response from a  $100 \mu\text{m}$  diameter PCF as a proof of concept.

## Chapter 8

# Conclusion and Future Work

The presented work is subdivided into three parts. Firstly, theoretical considerations on the propagation of the generated photoacoustic waves, the detected signals and their frequency content were undertaken by simulating the influence of the laser parameters and the transducer source distance (see Chapter 2). Secondly, potential improvements were identified from a conventional photoacoustic system and addressed by miniaturisation of system components by applying MEMS technology (see Chapters 3 to 6). Lastly, a novel photoacoustic scanning scheme was presented, which was based on scanning a laser beam across a target and thus removing the need for short pulsed laser excitation (see Chapter 7).

### 8.1 Simulations of Photoacoustic Signals

The simulations from Chapter 2 showed that the frequency content of a detected photoacoustic signal is dependent on the distance of the transducer to the source for photoacoustic imaging in acoustically attenuating media. This can be divided into a high-frequency region, where the frequency content is dominated by the parameters of the excitation source; it is mainly influenced by the temporal profile  $I(t)$  (laser pulse width) and to a lesser degree the spatial profile  $S(x)$  (focal spot size for acoustic resolution photoacoustic microscopy and optical resolution photoacoustic microscopy and absorber size for photoacoustic tomography). These parameters set the centre frequency and the bandwidth of the photoacoustic pulse. This region with a frequency content characterised by a high centre frequency and a broad bandwidth expands to a distance  $d$  around the photoacoustic source. For media with soft tissue like attenuation this distance is  $d \approx 2 \text{ mm}$ . Past this distance the centre frequency decreases and the broad bandwidth is reduced. In its stead low frequency side bands start to develop. The photoacoustic signal loses acoustic energy due to visco-elastic effects, which are linearly dependent on frequency. Thus, this low-pass filtering effect is exhibited in acoustically attenuating media. The diameter of the high-frequency region is inversely proportional to the acoustic attenuation  $\alpha$ .

Simulating spherical acoustic wavefronts for different transducer diameter and distances to the photoacoustic source showed that signal losses are caused by the

wavefront arriving at different times over the length of the transducer surface. This can be mitigated by placing the transducer further away from the source or by deploying transducers with smaller active surface areas. Furthermore, it was shown that a higher frequency content increases the occurring losses. Thus, increasing the source transducer distance in an attenuating medium reduces the losses in two ways. Firstly, the curvature of the spherical wave on the transducer surface is reduced. Secondly, the low-pass filtering effect increases with distance reducing the frequency content. Other centre frequency reducing properties, such as longer pulse widths  $\tau$ , focal spot size (for acoustic resolution photoacoustic microscopy and optical resolution photoacoustic microscopy) and absorber size (photoacoustic tomography), similarly reduce the signal losses. According to the simulations, the near-field distance of the designed PMUT transducer arrays is  $NFD \approx 5 \text{ mm}$  when using the whole array and  $NFD \approx 800 \mu\text{m}$  for the smallest group of the single-type PMUT array. Thus, small individually addressable arrays of transducers are to be favoured for photoacoustic imaging. Going forward, these simulations should be verified using (optical) high-bandwidth ultrasound detection schemes.

## 8.2 Miniaturisation of the photoacoustic scanning system

The first step towards miniaturising a photoacoustic scanning system was to set up a system using conventional and commercially available equipment, which was later used as a comparison to the miniaturised photoacoustic system. This setup was characterised and successfully applied to photoacoustic scans. Furthermore, polyimide coated fibres were identified as suitable targets in a gelatine matrix. Three potentials for improvement were identified. Firstly, the low PRF of the used laser system was problematic as it prohibited large ( $n \geq 25$ ) averaging. Secondly, the laser system's high pulse energy required high attenuation. Thirdly, the large diameters of the commercial ultrasound transducers caused signal losses due to the acoustic wavefront arriving at different times over the length of the transducer surface as described in the Chapter 2. Placing these transducer at a greater distance reduced the signal losses due to this effect but increased losses due to US attenuation.

The first and second point, low PRF and high pulse energies, were addressed by replacing the commercial laser system with a MEMS Q-switched Nd:YAG laser. Here, a fast scanning MEMS micromirror is used to align and disalign the laser cavity. This resulted in a laser system offering a PRF three orders of magnitude higher ( $PRF_{MEMS} = 10 \text{ kHz}$ ) than the commercial laser system ( $PRF_{com} = 10 \text{ Hz}$ ). The new laser system ( $E_{max} = 23.96 \mu\text{J}$ ) offered a pulse energy four orders of magnitude lower compared to the commercial laser ( $E_{com} = 278 \text{ mJ}$ ). This lower maximum pulse energy meant that the laser output required less attenuation for photoacoustic scanning without damaging the target, addressing the second point. Additionally, it was a 3-fold increase of the pulse energy compared to previously reported pulse energies generated from a MEMS Q-switched laser. Furthermore, the

MEMS Q-switched laser had a larger pulse widths of  $\tau = 50 \text{ ns}$ . As the transducer source distance was larger than  $2 \text{ mm}$  for all measurements this did not cause any adverse effects.

The third point – the bulkiness of the commercial US transducers – was addressed by designing PMUT arrays. Three types were designed a single-type, a multi-type and a bar-type PMUT array. The single-type PMUT array consisted of 64 elements of  $200 \mu\text{m}$  diameter grouped in individually addressable sets of 4, 16 and 32 elements. This array had a total active surface area of  $A = 2.895 \text{ mm}^2$ . The multi-type array consisted of transducer elements grouped according to their diameters, which ranged from  $200 \mu\text{m}$  to  $500 \mu\text{m}$ , giving it a broader overall bandwidth but also reduced SNR. This resulted in a total active surface area of  $A = 2.564 \text{ mm}^2$ . The minimum through hole size - and thus the upper limit for the centre frequencies achievable with clamped disc transducer elements - was set by the design limitations. Thus, the bar-type PMUT array was designed to increase the centre frequency by suspending a bar over the etched through hole at an angle. Due to the design this PMUT array had the lowest fill factor and an active surface area of only  $A = 0.961 \text{ mm}^2$ . The commercial US transducers had active surface areas two orders of magnitude larger,  $A = 507 \text{ mm}^2$  for the 2.25 MHz transducer and  $A = 286 \text{ mm}^2$  for the 10 MHz transducer. Additionally, the smaller size of the PMUT arrays resulted in smaller near-field distance ( $NFD \approx 5\text{mm}$ ) compared to the commercial US transducers ( $NFD \geq 30\text{mm}$ ). This is advantageous especially in highly attenuating media, as the signal is less attenuated. Furthermore, the signal is not subject to such strong low-pass filtering improving the lateral resolution.

The multi-user fabrication process offers a good and cost-efficient way of fabricating PMUT arrays. The PMUT die were inspected using SEM and no major defects were found. The crystals of the piezoelectric AlN layer were orientated only in the c-plane and thus the energy conversion was not hindered by additional crystal orientations. Comparing the performance of all US transducers (commercial transducer and PMUT arrays) using the commercial laser showed that for high-pulse energies ( $E = 220 \mu\text{J}$ ) the single-type array achieved  $SNR = 300$ , the multi-type array  $SNR = 106$  and the bar-type array  $SNR = 32$ . The commercial transducer achieved at this pulse energy  $SNR = 260$  for the 2.25 MHz transducer and  $SNR = 760$  for the 10 MHz transducer. Thus, despite an active surface area two orders of magnitudes smaller the single-type PMUT array outperformed the commercial 2.25 MHz transducer while the 10 MHz transducer shows a 2.5 times better SNR. Similarly, the multi-type PMUT array shows an SNR of only 2.5 times lower compared to the 2.25 MHz transducer despite its much smaller active area. This shows the great potential miniaturisation using this cost-efficient multi-user process offers for detection of photoacoustic waves.

Addressing all three improvement potentials identified in the preliminary system lead to the development of an all MEMS based photoacoustic system. The

incorporation of the MEMS Q-switched laser increased the pulse widths to  $\tau = 50 \text{ ns}$ . This did not adversely affect the generated spectra as the transducers were placed at a distance  $d \geq 2 \text{ mm}$ . The SNRs of the single-type and the multi-type PMUT array were compared to the commercial transducers using this laser as an excitation source. Despite a surface area smaller by two orders of magnitude the single-type PMUT array performed equally well as the 2.25 MHz commercial transducer, and the 10 MHz transducer showed only a 2-fold higher SNR. Compared to the multi-type PMUT array the 2.25 MHz and 10 MHz transducer had a 6 times and 10 times better SNR, respectively. The all MEMS based photoacoustic system was used to image PCF and carbon particle coated suture threads. Comparing cross-sectional scans at different pulse energies showed that the lower bound for pulse energies for this system lies at  $E = 175 \text{ nJ}$ . Additionally, the system was successfully applied to imaging targets under a high-scattering medium. Finally, a comparative scan along a PCF showed that this system can perform scans at twice the speed and pulse energies four orders of magnitudes lower compared to the all commercial system presented in Chapter 3. This was enabled by its three orders of magnitudes higher PRF, while its data acquisition rate was limited by the acquisition software to  $\approx 1000 \text{ kHz}$ .

Going forward, the data acquisition software should be improved to take full advantage of the high PRFs provided by the fast scanning MEMS micromirrors. The pulse energies provided by a MEMS Q-switched laser can be increased by changing from gold-coating to a dielectric coating on the micromirror surface as well as potentially the whole die. This would increase its reflectivity and thus reduce the absorbed heat, which would allow for higher laser powers - by up to 550 % - to be used before the device breaks down due to thermal damage [39].

A re-design of the PMUT arrays should consist of an array maximising the sensing area by maximising the fill factor. A second generation design with an increased bandwidth and utilising the inherent array abilities, such as phased array focusing techniques is shown in Fig. 8.1. The design shows an array of sub-arrays consisting of four transducer elements of different diameters (two each) for increased bandwidth. These designs could either be manufactured over a quarter die (same as was used in the previously presented experiments) or a half or full die, resulting in a  $1.5 D$  and  $2 D$  array, respectively. Alternatively, the layout could be designed, so that any number of dice could be combined to form a large array, resulting in a custom-built low-cost  $1.5 D$  array of arbitrary size. A design similar to the one presented in Fig. 8.1 could be used, but needs to be adjusted by moving the bond pads to the top / bottom. Additionally, an extra row of sub-arrays should be added to minimise the pitch to the sub-arrays of the next die. Thus, e.g. a  $100 \times 4$  element array would result in an array of approximately  $100 \text{ mm} \times 4 \text{ mm}$ .

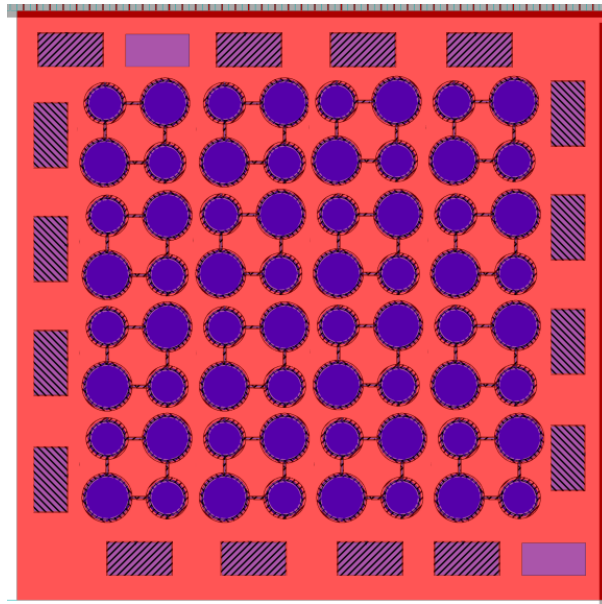


FIGURE 8.1: A second generation low-cost PMUT array offering a large bandwidth and phased-array capabilities should comprise of an array of sub-arrays. These sub-array consist of four transducer elements of two diameters.

### 8.3 Scanning laser beam photoacoustic

A novel scanning method was developed. Here, the temporal profile  $I(t)$  is not created by a laser pulse but by scanning a CW laser beam over an absorber using fast MEMS scanning micromirrors. This scanning laser beam photoacoustic system can be used to increase acquisition speed for photoacoustic microscopy setups as the scanning dimension would be reduced by one dimension. The size information of a target manifests itself by an altered photoacoustic response pulse width, i.e. a difference in the frequency content of the pulse. Thus, smaller targets result in higher frequencies and larger targets in lower. It is currently limited by a low pulse energy, which potentially limits the minimum detectable target size. The system was used to generate a photoacoustic response from a PCF as a proof of concept.

Advancing the scanning laser beam photoacoustic system, the fast scanning micro-mirrors coating should be changed from a gold-coating to a dielectric coating, thus increasing the laser power that can be used without damaging the MEMS device. Additionally, the large PMUT array could be used for simultaneous imaging over the scan-line using an optical resolution photoacoustic microscopy setup. The duty-cycle of the long pulsed laser can be adjusted so that it matches the length of the phased array and to reduce thermal stress on the MEMS device.

PA systems can be used for medical imaging and sensing, such as mammography, and dermal and vascular diagnostics, as well as non-destructive testing. PA systems do not require long acquisition times or use harmful radiation, such as MRI and CT. A PA systems contrast is based upon the difference in absorptivity of the wavelength of the laser. The absorbed light generates acoustic waves via the PA effect. The acoustic waves are detected using an ultrasound detector. PA systems pair well with US diagnostic systems as their information (spectral for PA, elasticity for US) complements one another.

PA systems can be used in attenuating and in non-attenuating media. The former results in a decrease in frequency in the detected signal, resulting in a lower resolution scan. Additionally, PA imaging cannot be done for targets embedded in non-transparent media, as the interrogation beam will not reach the target and thus no PA will be generated.

In the course of this work a cost-efficient custom-designed MEMS-based PA system was presented as a way towards a cost-efficient miniaturised photoacoustic imaging systems. Additionally, a novel photoacoustic excitation scheme based on CW - laser excitation and a MEMS based fast-scanning micro-mirror was presented. This new PA technique shows can potentially be applied in real-time PAM.



# Bibliography

- [1] G. Di Leo, R. M. Trimboli, T. Sella, and F. Sardanelli, "Optical imaging of the breast: Basic principles and clinical applications," *American Journal of Roentgenology*, vol. 209, no. 1, pp. 230–238, 2017, ISSN: 15463141. DOI: [10.2214/AJR.16.17220](https://doi.org/10.2214/AJR.16.17220).
- [2] G. Diot, S. Metz, A. Noske, E. Liapis, B. Schroeder, S. V. Ovsepian, R. Meier, E. Rummeny, and V. Ntziachristos, "Multispectral Optoacoustic Tomography (MSOT) of human breast cancer," *Clinical Cancer Research*, vol. 23, no. 22, pp. 6912–6922, 2017, ISSN: 15573265. DOI: [10.1158/1078-0432.CCR-16-3200](https://doi.org/10.1158/1078-0432.CCR-16-3200).
- [3] T. Kitai, M. Torii, T. Sugie, S. Kanao, Y. Mikami, T. Shiina, and M. Toi, "Photoacoustic mammography: initial clinical results," *Breast cancer*, vol. 21, no. 2, pp. 146–153, 2012. DOI: [10.1007/s12282-012-0363-0](https://doi.org/10.1007/s12282-012-0363-0).
- [4] M. Heijblom, D. Piras, W. Xia, J. van Hespén, J. Klaase, F. van den Engh, T. van Leeuwen, W. Steenbergen, and S. Manohar, "Visualizing breast cancer using the Twente photoacoustic mammoscope: What do we learn from twelve new patient measurements?" *Optics Express*, vol. 20, no. 11, p. 11 582, 2012, ISSN: 1094-4087. DOI: [10.1364/oe.20.011582](https://doi.org/10.1364/oe.20.011582).
- [5] M. Heijblom, D. Piras, F. M. van den Engh, M. van der Schaaf, J. M. Klaase, W. Steenbergen, and S. Manohar, "The state of the art in breast imaging using the Twente Photoacoustic Mammoscope: results from 31 measurements on malignancies," *European Radiology*, vol. 26, no. 11, pp. 3874–3887, 2016, ISSN: 14321084. DOI: [10.1007/s00330-016-4240-7](https://doi.org/10.1007/s00330-016-4240-7). [Online]. Available: <http://dx.doi.org/10.1007/s00330-016-4240-7>.
- [6] L. Lin, P. Hu, J. Shi, C. M. Appleton, K. Maslov, L. Li, R. Zhang, and L. V. Wang, "Single-breath-hold photoacoustic computed tomography of the breast," *Nature Communications*, vol. 9, pp. 1–9, 2018, ISSN: 20411723. DOI: [10.1038/s41467-018-04576-z](https://doi.org/10.1038/s41467-018-04576-z).
- [7] R. Li, P. Wang, L. Lan, F. P. Lloyd, C. J. Goergen, S. Chen, and J.-X. Cheng, "Assessing breast tumor margin by multispectral photoacoustic tomography," *Biomedical Optics Express*, vol. 6, no. 4, p. 1273, 2015, ISSN: 2156-7085. DOI: [10.1364/boe.6.001273](https://doi.org/10.1364/boe.6.001273).
- [8] J. Aguirre, M. Schwarz, D. Soliman, A. Buehler, M. Omar, and V. Ntziachristos, "Broadband mesoscopic optoacoustic tomography reveals skin layers: publisher's note," *Optics Letters*, vol. 44, no. 21, p. 5116, 2019, ISSN: 0146-9592. DOI: [10.1364/ol.44.005116](https://doi.org/10.1364/ol.44.005116).

- [9] S. J. Ford, P. L. Bigliardi, T. C. Sardella, A. Urich, N. C. Burton, M. Kacprowicz, M. Bigliardi, M. Olivo, and D. Razansky, "Structural and Functional Analysis of Intact Hair Follicles and Pilosebaceous Units by Volumetric Multispectral Optoacoustic Tomography," *Journal of Investigative Dermatology*, vol. 136, no. 4, pp. 753–761, 2016, ISSN: 15231747. DOI: [10.1016/j.jid.2015.09.001](https://doi.org/10.1016/j.jid.2015.09.001). [Online]. Available: <http://dx.doi.org/10.1016/j.jid.2015.09.001>.
- [10] A. Breathnach, E. Concannon, J. J. Dorairaj, S. Shaharan, J. McGrath, J. Jose, J. L. Kelly, and M. J. Leahy, "Preoperative measurement of cutaneous melanoma and nevi thickness with photoacoustic imaging," *Journal of Medical Imaging*, vol. 5, no. 01, p. 1, 2018, ISSN: 2329-4302. DOI: [10.1117/1.jmi.5.1.015004](https://doi.org/10.1117/1.jmi.5.1.015004).
- [11] S. Y. Chuah, A. B. Attia, V. Long, C. J. Ho, P. Malempati, C. Y. Fu, S. J. Ford, J. S. Lee, W. P. Tan, D. Razansky, M. Olivo, and S. Thng, "Structural and functional 3D mapping of skin tumours with non-invasive multispectral optoacoustic tomography," *Skin Research and Technology*, vol. 23, no. 2, pp. 221–226, 2017, ISSN: 16000846. DOI: [10.1111/srt.12326](https://doi.org/10.1111/srt.12326).
- [12] Y. Zhou, S. V. Tripathi, I. Rosman, J. Ma, P. Hai, G. P. Linette, M. L. Council, R. C. Fields, L. V. Wang, and L. A. Cornelius, "Noninvasive Determination of Melanoma Depth using a Handheld Photoacoustic Probe," *Journal of Investigative Dermatology*, vol. 137, no. 6, pp. 1370–1372, 2017, ISSN: 15231747. DOI: [10.1016/j.jid.2017.01.016](https://doi.org/10.1016/j.jid.2017.01.016).
- [13] I Stoffels, S Morscher, I Helfrich, U Hillen, J Leyh, N. C. Burton, T. C. Sardella, J Claussen, T. D. Poeppel, H. S. Bachmann, A Roesch, K Griewank, D Schadendorf, M Gunzer, and J Klode, "Metastatic status of sentinel lymph nodes in melanoma determined noninvasively with multispectral optoacoustic imaging.[Erratum appears in Sci Transl Med. 2015 Dec 23;7(319):319er8 Note: Lehy, Julia [corrected to Leyh, Julia]; PMID: 26702088]," *Science Translational Medicine*, vol. 7, no. 317, 317ra199, 2015, ISSN: 1946-6242. [Online]. Available: <http://ovidsp.ovid.com/ovidweb.cgi?T=JS{\&}CSC=Y{\&}NEWS=N{\&}PAGE=fulltext{\&}D=med8{\&}AN=26659573>.
- [14] J. Aguirre, M. Schwarz, N. Garzorz, M. Omar, A. Buehler, K. Eyerich, and V. Ntziachristos, "Precision assessment of label-free psoriasis biomarkers with ultra-broadband optoacoustic mesoscopy," *Nature Biomedical Engineering*, vol. 1, no. 5, pp. 1–8, 2017, ISSN: 2157846X. DOI: [10.1038/s41551-017-0068](https://doi.org/10.1038/s41551-017-0068).
- [15] B. Zabihian, J. Weingast, M. Liu, E. Zhang, P. Beard, H. Pehamberger, W. Drexler, and B. Hermann, "In vivo dual-modality photoacoustic and optical coherence tomography imaging of human dermatological pathologies," *Biomedical Optics Express*, vol. 6, no. 9, p. 3163, 2015, ISSN: 2156-7085. DOI: [10.1364/boe.6.003163](https://doi.org/10.1364/boe.6.003163).
- [16] A. Dima and V. Ntziachristos, "Non-invasive carotid imaging using optoacoustic tomography," *Optics Express*, vol. 20, no. 22, p. 25 044, 2012, ISSN: 1094-4087. DOI: [10.1364/oe.20.025044](https://doi.org/10.1364/oe.20.025044).

- [17] C. V. Bourantas, F. A. Jaffer, F. J. Gijsen, G. Van Soest, S. P. Madden, B. K. Courtney, A. M. Fard, E. Tenekecioglu, Y. Zeng, A. F. Van Der Steen, S. Emelianov, J. Muller, P. H. Stone, L. Marcu, G. J. Tearney, and P. W. Serruys, "Hybrid intravascular imaging: Recent advances, technical considerations, and current applications in the study of plaque pathophysiology," *European Heart Journal*, vol. 38, no. 6, 400–412b, 2017, ISSN: 15229645. DOI: [10.1093/eurheartj/ehw097](https://doi.org/10.1093/eurheartj/ehw097).
- [18] J. W. Baik, J. Y. Kim, S. Cho, S. Choi, J. Kim, and C. Kim, "Super Wide-Field Photoacoustic Microscopy of Animals and Humans in Vivo," *IEEE Transactions on Medical Imaging*, vol. 39, no. 4, pp. 975–984, 2020, ISSN: 1558254X. DOI: [10.1109/TMI.2019.2938518](https://doi.org/10.1109/TMI.2019.2938518).
- [19] A. Horiguchi, M. Shinchi, A. Nakamura, T. Wada, K. Ito, T. Asano, H. Shinmoto, H. Tsuda, and M. Ishihara, "Pilot Study of Prostate Cancer Angiogenesis Imaging Using a Photoacoustic Imaging System," *Urology*, vol. 108, pp. 212–219, 2017, ISSN: 15279995. DOI: [10.1016/j.urology.2017.07.008](https://doi.org/10.1016/j.urology.2017.07.008). [Online]. Available: <http://dx.doi.org/10.1016/j.urology.2017.07.008>.
- [20] M. J. Waldner, F. Knieling, C. Egger, S. Morscher, J. Claussen, M. Vetter, C. Kielisch, S. Fischer, L. Pfeifer, A. Hagel, R. S. Goertz, D. Wildner, R. Atreya, D. Strobel, and M. F. Neurath, "Multispectral Optoacoustic Tomography in Crohn's Disease: Noninvasive Imaging of Disease Activity," *Gastroenterology*, vol. 151, no. 2, pp. 238–240, 2016, ISSN: 15280012. DOI: [10.1053/j.gastro.2016.05.047](https://doi.org/10.1053/j.gastro.2016.05.047). [Online]. Available: <http://dx.doi.org/10.1053/j.gastro.2016.05.047>.
- [21] F. Knieling, C. Neufert, A. Hartmann, J. Claussen, A. Urich, C. Egger, M. Vetter, and S. Fischer, "Multispectral Optoacoustic Tomography for Assessment of Crohn's Disease Activity," *The New England Journal of Medicine*, pp. 29–31, 2017. DOI: [10.1056/NEJMc1612455](https://doi.org/10.1056/NEJMc1612455).
- [22] R. R. Jones, D. C. Hooper, L. Zhang, D. Wolverson, and V. K. Valev, "Raman Techniques: Fundamentals and Frontiers," *Nanoscale Research Letters*, vol. 14, no. 1, pp. 1–34, 2019, ISSN: 1556276X. DOI: [10.1186/s11671-019-3039-2](https://doi.org/10.1186/s11671-019-3039-2).
- [23] V. Tuchin, "Tissue optics," in. Bellingham, Washington: SPIE Press, 2004, pp. 3–11.
- [24] B. B. J. Patterson, "Multiple light scattering - tables, formulas, and applications," in. New York: Academic Press, 1980, pp. 149–191.
- [25] S. T. Flock, M. S. Patterson, B. C. Wilson, and D. R. Wyman, "Monte Carlo Modeling of Light Propagation in Highly Scattering Tissues—I: Model Predictions and Comparison with Diffusion Theory," *IEEE Transactions on Biomedical Engineering*, vol. 36, no. 12, pp. 1162–1168, 1989, ISSN: 15582531. DOI: [10.1109/TBME.1989.1173624](https://doi.org/10.1109/TBME.1989.1173624).
- [26] P. Beard, "Biomedical photoacoustic imaging," *Interface Focus*, vol. 1, no. 4, pp. 602–631, 2011, ISSN: 20428901. DOI: [10.1098/rsfs.2011.0028](https://doi.org/10.1098/rsfs.2011.0028).

- [27] B. B. J. Patterson, "Solid-state physics introduction to the theory," in. Berlin: Springer, 2010, pp. 41–108.
- [28] L. V. Wang, "Photoacoustic microscopy and computed tomography," *Biomedical Optics, BIOMED 2008*, vol. 14, no. 1, pp. 171–179, 2008. DOI: [10.1364/biomed.2008.bma1](https://doi.org/10.1364/biomed.2008.bma1).
- [29] J. Xia, J. Yao, and L. V. Wang, "Photoacoustic tomography: Principles and advances," *Progress in Electromagnetics Research*, vol. 147, pp. 1–22, 2014, ISSN: 15598985. DOI: [10.2528/PIER14032303](https://doi.org/10.2528/PIER14032303).
- [30] B. Treeby, J. Jaros, A. Rendell, and B. T. Cox, "Modeling nonlinear ultrasound propagation in heterogeneous media with power law absorption using a k-space pseudospectral method," *The Journal of the Acoustical Society of America*, vol. 131, no. 6, pp. 4324–4336, 2012.
- [31] T. L. Szabo, *Diagnostic ultrasound imaging inside out*. Amsterdam: Elsevier/Academic Press, 2004.
- [32] J. T. Bushberg, J. A. Seibert, E. M. Leidholdt, and J. M. Boone, *The essential physics of medical imaging*. Philadelphia: Lippincott Williams and Wilkins, 2020.
- [33] B. Lashkari and A. Mandelis, "Comparison between pulsed laser and frequency-domain photoacoustic modalities: Signal-to-noise ratio, contrast, resolution, and maximum depth detectivity," *Review of Scientific Instruments*, vol. 82, no. 9, pp. 1–14, 2011, ISSN: 00346748. DOI: [10.1063/1.3632117](https://doi.org/10.1063/1.3632117).
- [34] M. E. Khosroshahi and S. Valizadeh, "Measurement of pulse Nd: YAG laser-induced stress and analysis of dental tissue and amalgam plume using uniaxial polyvinylidene fluoride-based photoacoustic sensor and plasma spectroscopy," *Optics and Laser Technology*, vol. 128, no. September 2019, pp. 1–11, 2020, ISSN: 00303992. DOI: [10.1016/j.optlastec.2020.106239](https://doi.org/10.1016/j.optlastec.2020.106239).
- [35] N. Nyayapathi, R. Lim, H. Zhang, W. Zheng, Y. Wang, M. Tiao, K. W. Oh, X. C. Fan, E. Bonaccio, K. Takabe, and J. Xia, "Dual Scan Mammoscope (DSM) - A New Portable Photoacoustic Breast Imaging System with Scanning in Craniocaudal Plane," *IEEE Transactions on Biomedical Engineering*, vol. 67, no. 5, pp. 1321–1327, 2020, ISSN: 15582531. DOI: [10.1109/TBME.2019.2936088](https://doi.org/10.1109/TBME.2019.2936088).
- [36] Y. Wang, Y. Zhan, L. M. Harris, S. Khan, and J. Xia, "A portable three-dimensional photoacoustic tomography system for imaging of chronic foot ulcers," *Quantitative Imaging in Medicine and Surgery*, vol. 9, no. 5, pp. 799–806, 2019, ISSN: 22234306. DOI: [10.21037/qims.2019.05.02](https://doi.org/10.21037/qims.2019.05.02).
- [37] D. Wang, Y. Wang, W. Wang, D. Luo, U. Chitgupi, J. Geng, Y. Zhou, L. Wang, J. F. Lovell, and J. Xia, "Deep tissue photoacoustic computed tomography with a fast and compact laser system," *Biomedical Optics Express*, vol. 8, no. 1, pp. 112–123, 2017, ISSN: 2156-7085. DOI: [10.1364/boe.8.000112](https://doi.org/10.1364/boe.8.000112).
- [38] R. Bauer, W. Lubeigt, and D. Uttamchandani, "Dual Q-switched laser outputs from a single lasing medium using an intracavity MEMS micromirror array," *Optics Letters*, vol. 37, no. 17, pp. 3567–3569, 2012, ISSN: 0146-9592. DOI: [10.1364/ol.37.003567](https://doi.org/10.1364/ol.37.003567).

- [39] R. Bauer, A. Paterson, C. Clark, D. Uttamchandani, and W. Lubeigt, "Output Characteristics of Q-switched Solid-State Lasers Using Intracavity MEMS Micromirrors," *IEEE JOURNAL OF SELECTED TOPICS IN QUANTUM ELECTRONICS*, vol. 21, no. 1, pp. 1–8, 2015, ISSN: 0146-9592. DOI: [10.1109/JSTQE.2014.2345700](https://doi.org/10.1109/JSTQE.2014.2345700).
- [40] K. Daoudi, P. van den Berg, O. Rabot, A. Kohl, S. Tisserand, P. Brands, and W. Steenbergen, "Handheld probe integrating laser diode and ultrasound transducer array for ultrasound/photoacoustic dual modality imaging," *Optics Express*, vol. 22, no. 21, pp. 1–10, 2014, ISSN: 1094-4087. DOI: [10.1364/oe.22.026365](https://doi.org/10.1364/oe.22.026365).
- [41] A. Kohl, C. Canal, A. Laugustin, and O. Rabot, "An ultra compact laser diode source for integration in a handheld point-of-care photoacoustic scanner," *Photons Plus Ultrasound: Imaging and Sensing 2016*, vol. 9708, pp. 1–6, 2016, ISSN: 0277-786X. DOI: [10.1117/12.2212560](https://doi.org/10.1117/12.2212560).
- [42] P. K. Upputuri and M. Pramanik, "Performance characterization of low-cost, high-speed, portable pulsed laser diode photoacoustic tomography (PLD-PAT) system," *Biomedical Optics Express*, vol. 6, no. 10, pp. 1–12, 2015, ISSN: 2156-7085. DOI: [10.1364/boe.6.004118](https://doi.org/10.1364/boe.6.004118).
- [43] S. K. Kalva, P. K. Upputuri, and M. Pramanik, "High-speed, low-cost, pulsed-laser-diode-based second-generation desktop photoacoustic tomography system," *Optics Letters*, vol. 44, no. 1, pp. 81–84, 2019, ISSN: 0146-9592. DOI: [10.1364/ol.44.000081](https://doi.org/10.1364/ol.44.000081).
- [44] L. Zeng, G. Liu, D. Yang, and X. Ji, "Portable optical-resolution photoacoustic microscopy with a pulsed laser diode excitation," *Applied Physics Letters*, vol. 102, no. 5, pp. 1–4, 2013, ISSN: 00036951. DOI: [10.1063/1.4791566](https://doi.org/10.1063/1.4791566).
- [45] M. Erfanzadeh, P. D. Kumavor, and Q. Zhu, "Laser scanning laser diode photoacoustic microscopy system," *Photoacoustics*, vol. 9, pp. 1–9, 2018, ISSN: 22135979. DOI: [10.1016/j.pacs.2017.10.001](https://doi.org/10.1016/j.pacs.2017.10.001).
- [46] J. Nissinen and J. Kostamovaara, "A 4 a peak current and 2 ns pulse width CMOS laser diode driver for high measurement rate applications," *European Solid-State Circuits Conference*, pp. 355–358, 2013, ISSN: 19308833. DOI: [10.1109/ESSCIRC.2013.6649146](https://doi.org/10.1109/ESSCIRC.2013.6649146).
- [47] A. Stylogiannis, L. Prade, A. Buehler, J. Aguirre, G. Sergiadis, and V. Ntziachristos, "Continuous wave laser diodes enable fast photoacoustic imaging," *Photoacoustics*, vol. 9, pp. 31–38, 2018, ISSN: 22135979. DOI: [10.1016/j.pacs.2017.12.002](https://doi.org/10.1016/j.pacs.2017.12.002).
- [48] A. Hariri, J. Lemaster, J. Wang, A. K. S. Jeevarathinam, D. L. Chao, and J. V. Jokerst, "The characterization of an economic and portable LED-based photoacoustic imaging system to facilitate molecular imaging," *Photoacoustics*, vol. 9, pp. 10–20, 2018, ISSN: 22135979. DOI: [10.1016/j.pacs.2017.11.001](https://doi.org/10.1016/j.pacs.2017.11.001).

- [49] W. Xia, M. K. A. Singh, E. Maneas, N. Sato, Y. Shigeta, T. Agano, S. Ourselin, S. J. West, and A. E. Desjardins, "Handheld real-time LED-based photoacoustic and ultrasound imaging system for accurate visualization of clinical metal needles and superficial vasculature to guide minimally invasive procedures," *Sensors (Switzerland)*, vol. 18, no. 5, pp. 1–13, 2018, ISSN: 14248220. DOI: [10.3390/s18051394](https://doi.org/10.3390/s18051394).
- [50] H. F. Zhang, K. Maslov, G. Stoica, and L. V. Wang, "Functional photoacoustic microscopy for high-resolution and noninvasive in vivo imaging," *Nature Biotechnology*, vol. 24, no. 7, pp. 848–851, 2006, ISSN: 10870156. DOI: [10.1038/nbt1220](https://doi.org/10.1038/nbt1220).
- [51] A. Karlas, M. Kallmayer, N. A. Fasoula, E. Liapis, M. Bariotakis, M. Krönke, M. Anastasopoulou, J. Reber, H. H. Eckstein, and V. Ntziachristos, "Multispectral optoacoustic tomography of muscle perfusion and oxygenation under arterial and venous occlusion: A human pilot study," *Journal of Biophotonics*, vol. 13, no. 6, pp. 1–9, 2020, ISSN: 18640648. DOI: [10.1002/jbio.201960169](https://doi.org/10.1002/jbio.201960169).
- [52] P. Wang, H. W. Wang, M. Sturek, and J. X. Cheng, "Bond-selective imaging of deep tissue through the optical window between 1600 and 1850 nm," *Journal of Biophotonics*, vol. 5, no. 1, pp. 25–32, 2012, ISSN: 1864063X. DOI: [10.1002/jbio.201100102](https://doi.org/10.1002/jbio.201100102).
- [53] Y. He, J. Shi, M. A. Pleitez, K. Maslov, D. A. Wagenaar, and L. V. Wang, "Label-free imaging of lipid-rich biological tissues by mid-infrared photoacoustic microscopy," *Journal of Biomedical Optics*, vol. 25, no. 10, pp. 1–7, 2020, ISSN: 1083-3668. DOI: [10.1117/1.jbo.25.10.106506](https://doi.org/10.1117/1.jbo.25.10.106506).
- [54] T. Imai, J. Shi, T. T. W. Wong, L. Li, L. Zhu, and L. V. Wang, "High-throughput ultraviolet photoacoustic microscopy with multifocal excitation," *Journal of Biomedical Optics*, vol. 23, no. 03, pp. 1–6, 2018, ISSN: 1560-2281. DOI: [10.1117/1.jbo.23.3.036007](https://doi.org/10.1117/1.jbo.23.3.036007).
- [55] D.-K. Yao, R. Chen, K. Maslov, Q. Zhou, and L. V. Wang, "Optimal ultraviolet wavelength for in vivo photoacoustic imaging of cell nuclei," *Journal of Biomedical Optics*, vol. 17, no. 5, pp. 1–7, 2012, ISSN: 1083-3668. DOI: [10.1117/1.jbo.17.5.056004](https://doi.org/10.1117/1.jbo.17.5.056004).
- [56] X. Liu, T. T. W. Wong, J. Shi, J. Ma, Q. Yang, and L. V. Wang, "Label-free cell nuclear imaging by Grüneisen relaxation photoacoustic microscopy," *Optics Letters*, vol. 43, no. 4, pp. 947–950, 2018, ISSN: 0146-9592. DOI: [10.1364/ol.43.000947](https://doi.org/10.1364/ol.43.000947).
- [57] J. Shi, L. Wang, C. Noordam, and L. V. Wang, "Bessel-beam Grüneisen relaxation photoacoustic microscopy with extended depth of field," *Journal of Biomedical Optics*, vol. 20, no. 11, pp. 1–6, 2015, ISSN: 1083-3668. DOI: [10.1117/1.jbo.20.11.116002](https://doi.org/10.1117/1.jbo.20.11.116002).

- [58] G. Langer, K.-D. Bouchal, H. Grün, P. Burgholzer, and T. Berer, "Two-photon absorption-induced photoacoustic imaging of Rhodamine B dyed polyethylene spheres using a femtosecond laser," *Optics Express*, vol. 21, no. 19, pp. 1–13, 2013, ISSN: 1094-4087. DOI: [10.1364/oe.21.022410](https://doi.org/10.1364/oe.21.022410).
- [59] V. Verrina, S. Edward, H. Zhang, A. Antoncetti, S. Witte, and P. C. Planken, "Role of scattering by surface roughness in the photoacoustic detection of hidden micro-structures," *Applied Optics*, vol. 59, no. 30, pp. 9499–9509, 2020, ISSN: 1559-128X. DOI: [10.1364/ao.397264](https://doi.org/10.1364/ao.397264).
- [60] E. Shestaev, D. Hoff, A. M. Sayler, A. Klenke, S. Hädrich, F. Just, T. Eidam, P. Jójárt, Z. Várallyay, K. Osvay, G. G. Paulus, A. Tünnermann, and J. Limpert, "High-power ytterbium-doped fiber laser delivering few-cycle, carrier-envelope phase-stable 100  $\mu$ J pulses at 100 kHz," *Optics Letters*, vol. 45, no. 1, pp. 97–100, 2020, ISSN: 0146-9592. DOI: [10.1364/ol.45.000097](https://doi.org/10.1364/ol.45.000097).
- [61] H. Stark, J. Buldt, M. Müller, A. Klenke, A. Tünnermann, and J. Limpert, "23 mJ high-power fiber CPA system using electro-optically controlled divided-pulse amplification," *Optics Letters*, vol. 44, no. 22, pp. 5529–5532, 2019, ISSN: 0146-9592. DOI: [10.1364/ol.44.005529](https://doi.org/10.1364/ol.44.005529).
- [62] H. G. Craighead, J. C. White, R. E. Howard, L. D. Jackel, R. E. Behringer, J. E. Sweeney, and R. W. Epworth, "CONTACT LITHOGRAPHY AT 157 nm WITH AN F2 EXCIMER LASER," *Journal of Vacuum Science and Technology B: Microelectronics and Nanometer Structures*, vol. 1, no. 4, pp. 1186–1189, 1983, ISSN: 0734211X. DOI: [10.1116/1.582758](https://doi.org/10.1116/1.582758).
- [63] T. Y. Chang, T. J. Bridges, and E. G. Burkhardt, "Cw submillimeter laser action in optically pumped methyl fluoride, methyl alcohol, and vinyl chloride gases," *Applied Physics Letters*, vol. 17, no. 6, pp. 249–251, 1970, ISSN: 00036951. DOI: [10.1063/1.1653386](https://doi.org/10.1063/1.1653386).
- [64] R. Weissleder, "A clearer vision for in vivo imaging: Progress continues in the development of smaller, more penetrable probes for biological imaging," *Nature Biotechnology*, vol. 19, no. 4, pp. 316–317, 2001, ISSN: 15461696. DOI: [10.1038/86684](https://doi.org/10.1038/86684).
- [65] J. E. Bertie and Z. Lan, "Infrared intensities of liquids XX: The intensity of the OH stretching band of liquid water revisited, and the best current values of the optical constants of H<sub>2</sub>O(1) at 25 °C between 15,000 and 1 cm<sup>-1</sup>," *Applied Spectroscopy*, vol. 50, no. 8, pp. 1047–1057, 1996, ISSN: 00037028. DOI: [10.1366/0003702963905385](https://doi.org/10.1366/0003702963905385).
- [66] L. A. Sordillo, Y. Pu, S. Pratavieira, Y. Budansky, and R. R. Alfano, "Deep optical imaging of tissue using the second and third near-infrared spectral windows," *Journal of Biomedical Optics*, vol. 19, no. 5, pp. 1–6, 2014, ISSN: 1083-3668. DOI: [10.1117/1.jbo.19.5.056004](https://doi.org/10.1117/1.jbo.19.5.056004).
- [67] S. Park, G. Park, J. Kim, W. Choi, U. Jeong, and C. Kim, "Bi<sub>2</sub>Se<sub>3</sub> nanoplates for contrast-enhanced photoacoustic imaging at 1064 nm," *Nanoscale*, vol. 10, no. 44, pp. 20 548–20 558, 2018, ISSN: 20403372. DOI: [10.1039/c8nr05672b](https://doi.org/10.1039/c8nr05672b).

- [68] J. Wu, L. You, L. Lan, H. J. Lee, S. T. Chaudhry, R. Li, J. X. Cheng, and J. Mei, "Semiconducting Polymer Nanoparticles for Centimeters-Deep Photoacoustic Imaging in the Second Near-Infrared Window," *Advanced Materials*, vol. 29, no. 41, pp. 1–6, 2017, ISSN: 15214095. DOI: [10.1002/adma.201703403](https://doi.org/10.1002/adma.201703403).
- [69] R. Bogue, "Recent developments in MEMS sensors: A review of applications, markets and technologies," *Sensor Review*, vol. 33, no. 4, pp. 300–304, 2013, ISSN: 02602288. DOI: [10.1108/SR-05-2013-678](https://doi.org/10.1108/SR-05-2013-678).
- [70] S. H. Pun, Y. Yu, J. Zhang, J. Wang, C. H. Cheng, K. F. Lei, Z. Yuan, and P. U. Mak, "Monolithic Multiband CMUTs for Photoacoustic Computed Tomography with In Vivo Biological Tissue Imaging," *IEEE Transactions on Ultrasonics, Ferroelectrics, and Frequency Control*, vol. 65, no. 3, pp. 465–475, 2018, ISSN: 08853010. DOI: [10.1109/TUFFFC.2018.2792784](https://doi.org/10.1109/TUFFFC.2018.2792784).
- [71] T. Takezaki, M. Kawano, H. Hasegawa, S. Machida, and D. Ryuzaki, "Ultra-narrow gap CMUT cell structure for highly sensitive photoacoustic imaging," *IEEE International Ultrasonics Symposium, IUS*, pp. 1–4, 2017, ISSN: 19485727. DOI: [10.1109/ULTSYM.2017.8091865](https://doi.org/10.1109/ULTSYM.2017.8091865).
- [72] J. Song, C. Xue, C. He, R. Zhang, L. Mu, J. Cui, J. Miao, Y. Liu, and W. Zhang, "Capacitive micromachined ultrasonic transducers (CMUTs) for underwater imaging applications," *sensors*, vol. 15, no. 9, pp. 23 205–23 217, 2015, ISSN: 14248220. DOI: [10.3390/s150923205](https://doi.org/10.3390/s150923205).
- [73] X. Zhang, F. Y. Yamanery, O. Adelegan, and O. Oralkan, "Design of high-frequency broadband CMUT arrays," *2015 IEEE International Ultrasonics Symposium, IUS 2015*, pp. 6–9, 2015. DOI: [10.1109/ULTSYM.2015.0167](https://doi.org/10.1109/ULTSYM.2015.0167).
- [74] D. Zhao, S. Zhuang, and R. Daigle, "A commercialized high frequency CMUT probe for medical ultrasound imaging," *2015 IEEE International Ultrasonics Symposium, IUS 2015*, pp. 3–6, 2015. DOI: [10.1109/ULTSYM.2015.0063](https://doi.org/10.1109/ULTSYM.2015.0063).
- [75] D. F. Lemmerhirt, X. Cheng, R. D. White, C. A. Rich, M. Zhang, J. B. Fowlkes, and O. D. Kripfgans, "A 32 x 32 capacitive micromachined ultrasonic transducer array manufactured in standard CMOS," *IEEE Transactions on Ultrasonics, Ferroelectrics, and Frequency Control*, vol. 59, no. 7, pp. 1521–1536, 2012, ISSN: 08853010. DOI: [10.1109/TUFFFC.2012.2352](https://doi.org/10.1109/TUFFFC.2012.2352).
- [76] K. K. Park, O. Oralkan, and B. Khuri-Yakub, "A comparison between conventional and collapse-mode capacitive micromachined ultrasonic transducers in 10-MHz 1-D arrays," *IEEE Transactions on Ultrasonics, Ferroelectrics, and Frequency Control*, vol. 60, no. 6, pp. 1245–1255, 2013, ISSN: 08853010. DOI: [10.1109/TUFFFC.2013.2688](https://doi.org/10.1109/TUFFFC.2013.2688).
- [77] S. Sadeghpour and R. Puers, "Optimization in the Design and Fabrication of a PZT Piezoelectric Micromachined Ultrasound Transducer (PMUT)," *Proceedings*, vol. 2, no. 743, pp. 1–5, 2018, ISSN: 2504-3900. DOI: [10.3390/proceedings2130743](https://doi.org/10.3390/proceedings2130743).



- [78] J. Joseph, S. G. Singh, and S. R. K. Vanjari, "Piezoelectric Micromachined Ultrasonic Transducer Using Silk Piezoelectric Thin Film," *IEEE Electron Device Letters*, vol. 39, no. 5, pp. 749–752, 2018, ISSN: 07413106. DOI: [10.1109/LED.2018.2816646](https://doi.org/10.1109/LED.2018.2816646).
- [79] A. Hajati, D. Latev, D. Gardner, M. Ottosson, D. Imai, M. Torrey, and M. Schoeppler, "Monolithic ultrasonic integrated circuits based on micromachined semi-ellipsoidal piezoelectric domes," *Applied Physics Letters*, vol. 103, no. 20, pp. 1–4, 2013, ISSN: 00036951. DOI: [10.1063/1.4831988](https://doi.org/10.1063/1.4831988).
- [80] T. Wang, T. Kobayashi, and C. Lee, "Micromachined piezoelectric ultrasonic transducer with ultra-wide frequency bandwidth," *Applied Physics Letters*, vol. 106, no. 1, pp. 1–5, 2015, ISSN: 00036951. DOI: [10.1063/1.4905441](https://doi.org/10.1063/1.4905441).
- [81] C. Zhang, S. L. Chen, T. Ling, and L. J. Guo, "Review of imprinted polymer microrings as ultrasound detectors: Design, fabrication, and characterization," *IEEE Sensors Journal*, vol. 15, no. 6, pp. 3241–3248, 2015, ISSN: 1530437X. DOI: [10.1109/JSEN.2015.2421519](https://doi.org/10.1109/JSEN.2015.2421519).
- [82] T. Ling, S. L. Chen, and L. J. Guo, "High-sensitivity and wide-directivity ultrasound detection using high Q polymer microring resonators," *Applied Physics Letters*, vol. 98, no. 20, pp. 1–3, 2011, ISSN: 00036951. DOI: [10.1063/1.3589971](https://doi.org/10.1063/1.3589971).
- [83] H. Li, B. Dong, Z. Zhang, H. F. Zhang, and C. Sun, "A transparent broadband ultrasonic detector based on an optical micro-ring resonator for photoacoustic microscopy," *Scientific Reports*, vol. 4, pp. 1–8, 2014, ISSN: 20452322. DOI: [10.1038/srep04496](https://doi.org/10.1038/srep04496).
- [84] S. Ashkenazi, Y. Hou, T. Buma, and M. O'Donnell, "Optoacoustic imaging using thin polymer talon," *Applied Physics Letters*, vol. 86, no. 13, pp. 1–3, 2005, ISSN: 00036951. DOI: [10.1063/1.1896085](https://doi.org/10.1063/1.1896085).
- [85] E. Zhang, J. Laufer, and P. Beard, "Backward-mode multiwavelength photoacoustic scanner using a planar Fabry-Perot polymer film ultrasound sensor," *Applied Optics*, vol. 47, no. 4, pp. 561–577, 2008.
- [86] P. V. Chitnis, H. Lloyd, and R. H. Silverman, "An adaptive interferometric sensor for all-optical photoacoustic microscopy," *IEEE International Ultrasonics Symposium, IUS*, pp. 353–356, 2014, ISSN: 19485727. DOI: [10.1109/ULTSYM.2014.0087](https://doi.org/10.1109/ULTSYM.2014.0087).
- [87] A. Hochreiner, T. Berer, H. Gru, M. Leitner, and P. Burgholzer, "Photoacoustic imaging using an adaptive interferometer with a photorefractive crystal," *Journal of Biophotonics*, vol. 10, pp. 1–10, 2012. DOI: [10.1002/jbio.201100111](https://doi.org/10.1002/jbio.201100111).
- [88] R. Shelton and B. E. Applegate, "Off-axis photoacoustic microscopy," *Photons Plus Ultrasound: Imaging and Sensing 2010*, vol. 57, no. 8, pp. 1835–1838, 2010, ISSN: 0277-786X. DOI: [10.1117/12.841082](https://doi.org/10.1117/12.841082).

- [89] J. Park, S. Jeon, J. Meng, L. Song, J. S. Lee, and C. Kim, "Delay-multiply-and-sum-based synthetic aperture focusing in photoacoustic microscopy," *Journal of Biomedical Optics*, vol. 21, no. 3, pp. 1–10, 2016, ISSN: 1083-3668. DOI: [10.1117/1.jbo.21.3.036010](https://doi.org/10.1117/1.jbo.21.3.036010).
- [90] S. Jeon, J. Kim, D. Lee, J. W. Baik, and C. Kim, "Review on practical photoacoustic microscopy," *Photoacoustics*, vol. 15, no. July, pp. 1–16, 2019, ISSN: 22135979. DOI: [10.1016/j.pacs.2019.100141](https://doi.org/10.1016/j.pacs.2019.100141).
- [91] C. Zhang, K. Maslov, and L. V. Wang, "Subwavelength-resolution label-free photoacoustic microscopy of optical absorption in vivo," *Optics letters*, vol. 35, no. 10, pp. 3195–3197, 2010, ISSN: 15378276. arXiv: [NIHMS150003](https://arxiv.org/abs/NIHMS150003).
- [92] K. Maslov, H. F. Zhang, S. Hu, and L. V. Wang, "Optical-resolution photoacoustic microscopy for in vivo imaging of single capillaries," *Optics Letters*, vol. 33, no. 9, pp. 929–931, 2008, ISSN: 0146-9592. DOI: [10.1364/ol.33.000929](https://doi.org/10.1364/ol.33.000929).
- [93] M. Jeon, J. Kim, and C. Kim, "Multiplane spectroscopic whole-body photoacoustic imaging of small animals in vivo," *Medical and Biological Engineering and Computing*, vol. 54, no. 2-3, pp. 283–294, 2016, ISSN: 17410444. DOI: [10.1007/s11517-014-1182-6](https://doi.org/10.1007/s11517-014-1182-6).
- [94] J. Yao, L. Wang, C. Li, C. Zhang, and L. V. Wang, "Photoimprint photoacoustic microscopy for three-dimensional label-free subdiffraction imaging," *Physical Review Letters*, vol. 112, no. 1, pp. 1–5, 2014, ISSN: 00319007. DOI: [10.1103/PhysRevLett.112.014302](https://doi.org/10.1103/PhysRevLett.112.014302).
- [95] B. Park, H. Lee, S. Jeon, J. Ahn, H. H. Kim, and C. Kim, "Reflection-mode switchable subwavelength Bessel-beam and Gaussian-beam photoacoustic microscopy in vivo," *Journal of Biophotonics*, vol. 12, no. 2, 2019, ISSN: 18640648. DOI: [10.1002/jbio.201800215](https://doi.org/10.1002/jbio.201800215).
- [96] D. Cai, Z. Li, and S.-L. Chen, "In vivo deconvolution acoustic-resolution photoacoustic microscopy in three dimensions," *Biomedical Optics Express*, vol. 7, no. 2, pp. 1–12, 2016, ISSN: 2156-7085. DOI: [10.1364/boe.7.000369](https://doi.org/10.1364/boe.7.000369).
- [97] D. Cai, Z. Li, Y. Li, Z. Guo, and S.-L. Chen, "Photoacoustic microscopy in vivo using synthetic-aperture focusing technique combined with three-dimensional deconvolution," *Optics Express*, vol. 25, no. 2, pp. 1421–1434, 2017, ISSN: 1094-4087. DOI: [10.1364/oe.25.001421](https://doi.org/10.1364/oe.25.001421).
- [98] R. Cheng, J. Shao, X. Gao, C. Tao, J. Ge, and X. Liu, "Noninvasive Assessment of Early Dental Lesion Using a Dual-Contrast Photoacoustic Tomography," *Scientific Reports*, vol. 6, no. November 2015, pp. 2–10, 2016, ISSN: 20452322. DOI: [10.1038/srep21798](https://doi.org/10.1038/srep21798).
- [99] T. J. Allen and P. C. Beard, "High power visible light emitting diodes as pulsed excitation sources for biomedical photoacoustics," *Biomedical Optics Express*, vol. 7, no. 4, p. 1260, 2016, ISSN: 2156-7085. DOI: [10.1364/boe.7.001260](https://doi.org/10.1364/boe.7.001260).

- [100] I. Kosik, M. Brackstone, A. Kornecki, A. Chamson-Reig, P. Wong, M. H. Araghi, and J. J. L. Carson, "Intraoperative photoacoustic visualization and surgical guidance perspective on malignancy screening of breast cancer: a new," *Journal of Biomedical Optics*, vol. 24, no. 5, pp. 1–13, 2019. DOI: [10.1117/1.JBO.24.5.056002](https://doi.org/10.1117/1.JBO.24.5.056002).
- [101] S. M. Schoustra, D. Piras, R. Huijink, T. J. P. M. op 't Root, L. Alink, W. M. Kobold, W. Steenbergen, and S. Manohar, "Twente Photoacoustic Mammoscope 2: system overview and three-dimensional vascular network images in healthy breasts," *Journal of Biomedical Optics*, vol. 24, no. 12, pp. 1–12, 2019, ISSN: 1560-2281. DOI: [10.1117/1.jbo.24.12.121909](https://doi.org/10.1117/1.jbo.24.12.121909).
- [102] X. L. Deán-Ben and D. Razansky, "Portable spherical array probe for volumetric real-time optoacoustic imaging at centimeter-scale depths," *Optics Express*, vol. 21, no. 23, pp. 1–10, 2013, ISSN: 1094-4087. DOI: [10.1364/oe.21.028062](https://doi.org/10.1364/oe.21.028062).
- [103] J. Jo, C. Tian, G. Xu, J. Sarazin, E. Schiopu, G. Gandikota, and X. Wang, "Photoacoustic tomography for human musculoskeletal imaging and inflammatory arthritis detection," *Photoacoustics*, vol. 12, no. July, pp. 82–89, 2018, ISSN: 22135979. DOI: [10.1016/j.pacs.2018.07.004](https://doi.org/10.1016/j.pacs.2018.07.004).
- [104] T. Chaigne, J. Gateau, M. Allain, O. Katz, S. Gigan, A. Sentenac, and E. Bossy, "Super-resolution photoacoustic fluctuation imaging with multiple speckle illumination," *Optica*, vol. 3, no. 1, pp. 54–57, 2016.
- [105] T. W. Murray, M. A. H. Altmeier, T. H. B. Erer, and E. L. L. E. Olzinger, "Super-resolution photoacoustic microscopy using blind structured illumination," *Optica*, vol. 4, no. 1, pp. 17–22, 2017.
- [106] C.-K. Liao, M.-L. Li, and P.-C. Li, "Optoacoustic imaging with synthetic aperture focusing and coherence weighting," *Optics Letters*, vol. 29, no. 21, pp. 2506–2508, 2004, ISSN: 0146-9592. DOI: [10.1364/ol.29.002506](https://doi.org/10.1364/ol.29.002506).
- [107] S. C. BUSHONG, "Radiologic science for technologists: Physics, biology, and protection," in Houston, Texas: ELSEVIER MOSBY, 2020, 437–465.
- [108] M. Haltmeier, T. Schuster, and O. Scherzer, "Filtered backprojection for thermoacoustic computed tomography in spherical geometry," *Mathematical Methods in the Applied Sciences*, vol. 28, no. 16, pp. 1919–1937, 2005, ISSN: 01704214. DOI: [10.1002/mma.648](https://doi.org/10.1002/mma.648).
- [109] C. G. A. Hoelen and F. F. M. D. Mul, "Image reconstruction for photoacoustic scanning of Tissue Structures," *Applied Optics*, vol. 39, no. 31, pp. 5872–5883, 2000.
- [110] M. Olofsson, "Signal theory," in Lund: Studentlitteratur, 2004, pp. 5–41.

- [111] A. Fatima, K. Kratkiewicz, R. Manwar, M. Zafar, R. Zhang, B. Huang, N. Dadashzadeh, J. Xia, and K. M. Avanaki, "Review of cost reduction methods in photoacoustic computed tomography," *Photoacoustics*, vol. 15, no. June, p. 100137, 2019, ISSN: 22135979. DOI: [10.1016/j.pacs.2019.100137](https://doi.org/10.1016/j.pacs.2019.100137). arXiv: [1902.09987](https://arxiv.org/abs/1902.09987). [Online]. Available: <https://doi.org/10.1016/j.pacs.2019.100137>.
- [112] Y. Qiu, J. V. Gigliotti, M. Wallace, F. Griggio, C. E. Demore, S. Cochran, and S. Trolier-McKinstry, "Piezoelectric micromachined ultrasound transducer (PMUT) arrays for integrated sensing, actuation and imaging," *Sensors (Switzerland)*, vol. 15, no. 4, pp. 8020–8041, 2015, ISSN: 14248220. DOI: [10.3390/s150408020](https://doi.org/10.3390/s150408020).
- [113] H. Wang, Y. Ma, H. Yang, H. Jiang, Y. Ding, and H. Xie, *Mems ultrasound transducers for endoscopic photoacoustic imaging applications*, 10. 2020, vol. 11, ISBN: 3120200697. DOI: [10.3390/mi11100928](https://doi.org/10.3390/mi11100928).
- [114] G. J. Diebold, T Sun, and M. I. Khan, "Photoacoustic Monopole Radiation in One, Two, and Three Dimensions," *Physical Review Letters*, vol. 67, no. 24, pp. 3384–3389, 1991.
- [115] Y. Hou, S. Ashkenazi, S. W. Huang, and M. O'Donnell, "Improvements in optical generation of high-frequency ultrasound," *IEEE Transactions on Ultrasonics, Ferroelectrics, and Frequency Control*, vol. 54, no. 3, pp. 682–686, 2007, ISSN: 08853010. DOI: [10.1109/TUFFC.2007.292](https://doi.org/10.1109/TUFFC.2007.292).
- [116] S. Rajagopal, T. Sainsbury, B. E. Treeby, and B. T. Cox, "Laser generated ultrasound sources using carbon-polymer nanocomposites for high frequency metrology," *The Journal of the Acoustical Society of America*, vol. 144, no. 2, pp. 584–597, 2018, ISSN: 0001-4966. DOI: [10.1121/1.5048413](https://doi.org/10.1121/1.5048413).
- [117] E. M. Strohm, E. S. Berndl, and M. C. Kolios, "High frequency label-free photoacoustic microscopy of single cells," *Photoacoustics*, vol. 1, no. 3-4, pp. 49–53, 2013, ISSN: 22135979. DOI: [10.1016/j.pacs.2013.08.003](https://doi.org/10.1016/j.pacs.2013.08.003).
- [118] B. E. Treeby and B. T. Cox, "k-Wave: MATLAB toolbox for the simulation and reconstruction of photoacoustic wave fields," *Journal of Biomedical Optics*, vol. 15, no. 2, pp. 1–12, 2010, ISSN: 10833668. DOI: [10.1117/1.3360308](https://doi.org/10.1117/1.3360308).
- [119] Bradley Treeby, Ben Cox, Jiri Jaros, *k-Wave - A MATLAB toolbox for the time domain simulation of acoustic wave fields*. London: User Manual, 2016.
- [120] M. Tabei, T. D. Mast, and R. C. Waag, "A k-space method for coupled first-order acoustic propagation equations," *The Journal of the Acoustical Society of America*, vol. 111, no. 1, pp. 53–63, 2002, ISSN: 0001-4966. DOI: [10.1121/1.1421344](https://doi.org/10.1121/1.1421344).
- [121] P. Burgholzer, J. Bauer-Marschallinger, B. Reitingner, and T. Berer, "Resolution limits in photoacoustic imaging caused by acoustic attenuation," *Journal of Imaging*, vol. 5, no. 1, pp. 1–11, 2019, ISSN: 2313433X. DOI: [10.3390/jimaging5010013](https://doi.org/10.3390/jimaging5010013).

- [122] X. L. Den-Ben, D. Razansky, and V. Ntziachristos, "The effects of acoustic attenuation in optoacoustic signals," *Physics in Medicine and Biology*, vol. 56, no. 18, pp. 6129–6148, 2011, ISSN: 00319155. DOI: [10.1088/0031-9155/56/18/021](https://doi.org/10.1088/0031-9155/56/18/021).
- [123] G. Xu, I. A. Dar, C. Tao, X. Liu, C. X. Deng, and X. Wang, "Photoacoustic spectrum analysis for microstructure characterization in biological tissue: A feasibility study," *Applied Physics Letters*, vol. 101, no. 22, pp. 1–5, 2012, ISSN: 00036951. DOI: [10.1063/1.4768703](https://doi.org/10.1063/1.4768703).
- [124] J. R. Cook, R. R. Bouchard, and S. Y. Emelianov, "Tissue-mimicking phantoms for photoacoustic and ultrasonic imaging.," *Biomedical optics express*, vol. 2, no. 11, pp. 3193–3206, 2011, ISSN: 2156-7085. DOI: [10.1364/B0E.2.003193](https://doi.org/10.1364/B0E.2.003193).
- [125] M. A. O. C. Uljat, D. A. G. Oldenberg, P. R. T. Ewari, and R. A. S. S. Ingh, "A review of tissue substitutes for ultrasound imaging," *Ultrasound in Med. & Biol.*, vol. 36, no. 6, pp. 861–873, 2010. DOI: [10.1016/j.ultrasmedbio.2010.02.012](https://doi.org/10.1016/j.ultrasmedbio.2010.02.012).
- [126] P. C. Beard, "Photoacoustic imaging of blood vessel equivalent phantoms," *Biomedical Optoacoustics III*, vol. 4618, pp. 54–62, 2002. DOI: [10.1117/12.469848](https://doi.org/10.1117/12.469848).
- [127] J. A. Viator, S. L. Jacques, and S. A. Prahl, "Depth profiling of absorbing soft materials using photoacoustic methods," *IEEE Journal on Selected Topics in Quantum Electronics*, vol. 5, no. 4, pp. 989–996, 1999, ISSN: 1077260X. DOI: [10.1109/2944.796321](https://doi.org/10.1109/2944.796321).
- [128] L. Yin, Q. Wang, Q. Zhang, and H. Jiang, "Tomographic imaging of absolute optical absorption coefficient in turbid media using combined photoacoustic and diffusing light measurements," *Optics Letters*, vol. 32, no. 17, pp. 2556–2558, 2007, ISSN: 0146-9592. DOI: [10.1364/ol.32.002556](https://doi.org/10.1364/ol.32.002556).
- [129] S. M. Garrett, "Understanding acoustics," in Cham: pringer Nature Switzerland AG, 2020, pp. 283–333.
- [130] L. Shen, T. Cheng, L. Wu, X. Li, and Q. Cui, "Synthesis and optical properties of aluminum nitride nanowires prepared by arc discharge method," *Journal of Alloys and Compounds*, vol. 465, no. 1-2, pp. 562–566, 2008, ISSN: 09258388. DOI: [10.1016/j.jallcom.2007.11.007](https://doi.org/10.1016/j.jallcom.2007.11.007).
- [131] N. Jackson, R. O'Keeffe, F. Waldron, M. O'Neill, and A. Mathewson, "Influence of aluminum nitride crystal orientation on MEMS energy harvesting device performance," *Journal of Micromechanics and Microengineering*, vol. 23, no. 7, pp. 1–9, 2013, ISSN: 09601317. DOI: [10.1088/0960-1317/23/7/075014](https://doi.org/10.1088/0960-1317/23/7/075014).
- [132] J. Lee, "The effect of liquid on the vibrational intensity of a wineglass at steady state resonance," *arXiv*, pp. 1–5, 2018, ISSN: 23318422.
- [133] R. Bauer, G. Brown, and D. Uttamchandani, "Comparison of the curvature homogeneity and dynamic behaviour of framed and frameless electrostatic X/Y scanning micromirrors," *Micro and Nano Letters*, vol. 6, no. 6, pp. 425–428, 2011, ISSN: 17500443. DOI: [10.1049/mnl.2011.0113](https://doi.org/10.1049/mnl.2011.0113).

- [134] J. C. Chiou, C. F. Kuo, and Y. J. Lin, "A micromirror with large static rotation and vertical actuation," *IEEE JOURNAL OF SELECTED TOPICS IN QUANTUM ELECTRONICS*, vol. 13, no. 2, pp. 297–303, 2007. DOI: [10.1109/omems.2006.1708300](https://doi.org/10.1109/omems.2006.1708300).
- [135] B. Jiang, M. Peng, Y. Liu, T. Zhou, and Y. Su, "The fabrication of 2D micromirror with large electromagnetic driving forces," *Sensors and Actuators*, vol. 286, pp. 163–168, 2019, ISSN: 09244247. DOI: [10.1016/j.sna.2018.12.038](https://doi.org/10.1016/j.sna.2018.12.038). [Online]. Available: <https://doi.org/10.1016/j.sna.2018.12.038>.
- [136] T. Hayashi, "Energy trapping of circumferential resonant modes at a thin-walled groove in a hollow cylinder," *The Journal of the Acoustical Society of America*, vol. 146, no. 4, EL376–EL380, 2019, ISSN: 0001-4966. DOI: [10.1121/1.5129561](https://doi.org/10.1121/1.5129561).
- [137] F. Real, A. Batou, T. Ritto, and C. Desceliers, "Broadband optical properties of milk," *Journal of Vibration and Control*, no. X, pp. 1–14, 2019. DOI: [10.1177/0003702816666289](https://doi.org/10.1177/0003702816666289).
- [138] T. Kono and J. Yamada, "In Vivo Measurement of Optical Properties of Human Skin for 450–800 nm and 950–1600 nm Wavelengths," *International Journal of Thermophysics*, vol. 40, no. 5, pp. 1–14, 2019, ISSN: 15729567. DOI: [10.1007/s10765-019-2515-3](https://doi.org/10.1007/s10765-019-2515-3).
- [139] Y. Du, X. H. Hu, M. Caiveau, X. Ma, G. W. Kalmus, and J. Q. Lu, "Optical properties of porcine skin dermis between 900 nm and 1500 nm," *Physics in Medicine and Biology*, vol. 46, no. 1, pp. 167–181, 2001, ISSN: 00319155. DOI: [10.1088/0031-9155/46/1/312](https://doi.org/10.1088/0031-9155/46/1/312).